GeoForschungsZentrum Potsdam

STIFTUNG DES ÖFFENTLICHEN RECHTS

Scientific Technical Report

Different styles of deformation of the fore-arc wedge along the Chilean convergent margin: Insights from 3D numerical experiments

_____

Dissertation

zur Erlangung des akademischen Grades

Doktor der Naturwissenschaften (Dr. rer. nat.)

in der Wissenschaftsdisziplin Geowissenschaften

eingereicht an der

Mathematisch-Naturwissenschaftlichen Fakultät

der Universität Potsdam

Antje Kellner

Potsdam, Juli 2007

Doctoral Thesis

by

Antje Kellner

supervised by

Dr. Nina Kukowski and Prof. Dr. Georg Dresen

submitted to

University of Potsdam, Germany

Reviewers   Prof. Dr. Georg Dresen

                   Prof. Dr. Kelin Wang

                   Dr. Susan Ellis

Date of oral defense   07. November 2007

Abstract

The styles of deformation of the fore-arc wedges along the Chilean convergent margin are observed to vary significantly, despite similar plate kinematic conditions. Here, I focus on the analysis of fore-arc deformation on two regions along the Chilean convergent margin at 20°-24°S and 37°-42°S. Although both regions are subjected to the oblique subduction of the oceanic Nazca plate and backstopped by the Andes mountain chain; they display different patterns of deformation.

The northern Chilean study area (20° - 24°S) is characterized by an exceptionally thick crust of about 60 km beneath the Altiplano – Puna plateau, lack of an accretionary wedge in the fore-arc due to hyperarid climate, and consequently a sediment starved trench. Two major margin parallel strike slip faults are observed in this area, the Atacama Fault Zone (AFZ) and the Precordilleran Fault System (PFS). Both strike-slip faults do not exhibit significant recent displacement.

The southern study area (37° - 42°S), compared to the northern study area, is characterized by lower topography, high precipitation rates (~2000 mm/yr), and a younger subducted oceanic plate. An active strike-slip fault, the Liquiñe-Ofqui-Fault-Zone (LOFZ), shows ~1 cm/yr recent dextral movement and shapes the surface of this area. Thus, the southern Chilean study area exhibits localized strike-slip motion. Within this area the largest earthquake ever recorded, the 1960 Valdivia earthquake, occurred with a moment magnitude of M_W=9.5.

I have constructed 2D thermal models and 3D mechanical models for both Chilean study areas to study processes related to active subduction. The applied numerical method is the finite element technique by means of the commercial software package ABAQUS.

The thermal models are focused on the thermal conditions along the plate interface. The thermal structure along the plate interface reveals the limits of coupling but also the type of transition from coupled to uncoupled and vice versa. The model results show that shear heating at the plate interface is an important mechanism that should be taken into account. The models also show that the thermal condition at the downdip limit of the coupling zone leads to a sharp decrease of friction along the interface. Due to the different geometries of the two Chilean study areas, such as the slab dip and the thickness of the continental crust, the downdip limit of the southern study area is slightly shallower than that of the northern study area. The results of the 2D thermal models are used to constrain the spatial extent of the coupling zone in the 3D mechanical models.

3D numerical simulations are used to investigate how geometry, rheology and mechanical parameters influence strain partitioning and styles of deformation in the Chilean fore-arc. The general outline of the models is based on the fore-arc geometry and boundary conditions as derived from geophysical and geological field data. I examined the influence of different rheological approaches and varying physical properties of the fore-arc to identify and constrain the parameters controlling the difference in surface deformation between the northern and southern study area.

The results of numerical studies demonstrate that a small slab dip, a high coefficient of basal friction, a high obliquity of convergence, and a high Young's modulus favour localisation of deformation in the fore-arc wedge. This parameter study helped me to constrain preferred models for the two Chilean study areas that fit to first order observations. These preferred models explain the difference in styles of deformation as controlled by the angle of obliquity, the dip of subducting slab, and the strength of wedge material. The difference in styles can be even larger if I apply stronger coupling between plates within the southern area; however, several independent observations indicate opposite tendency showing southward decrease of intensity of coupling.

The weaker wedge material of the preferred model for the northern study area is associated with advanced development of the adjacent orogen, the Central Andes. Analysis of world-wide examples of oblique subduction zones supports the conclusion that more mature subduction zones demonstrate less pronounced localization of strike-slip motion.

Kurzfassung

Die Deformationsmuster der Fore-Arc Keile entlang des chilenischen konvergenten Plattenrandes variieren beachtlich, trotz ähnlicher plattenkinematischer Randbedingungen. In dieser Arbeit konzentriere ich mich auf die Analyse der Deformation des Fore-Arcs in zwei Gebieten entlang des chilenischen konvergenten Plattenrandes zwischen 20°-24°S und 37°-42°S. Obwohl beide Gebiete durch schiefe Subduktion der ozeanischen Nazca Platte und der östlichen Begrenzung durch die Andine Gebirgskette gekennzeichnet sind, zeigen sie unterschiedliche Deformationsmuster an der Oberfläche.

Das nördliche chilenische Arbeitsgebiet (20° - 24°S) ist gekennzeichnet durch eine außergewöhnliche Krustendicke von ungefähr 60 km unterhalb des Altiplano - Puna Plateaus, dem Fehlen eines akkretionären Prismas im Fore-Arc aufgrund des trockenen Klimas und somit einer nahezu sedimentfreien Tiefseerinne. Zwei große Plattenrand-parallele Strike-Slip Störungen werden in diesem Gebiet beobachtet, die Atacama Fault Zone (AFZ) und das Precordilleran Fault System (PFS). Beide Strike-Slip Störungen zeigen keine signifikanten aktuellen Bewegungsraten.

Das südliche Arbeitsgebiet (37° - 42°S) ist im Vergleich zum nördlichen Arbeitsgebiet durch eine niedrigere Topographie, hohe Niederschlagsraten (~2000 mm/a) und eine jüngere abtauchende ozeanische Platte gekennzeichnet. Die aktive Strike-Slip Störung, Liquiñe-Ofqui-Fault-Zone (LOFZ), ist gekennzeichnet durch aktuelle dextrale Bewegungsraten von 1 cm/a und prägt die Oberflächenstruktur in dieser Region. Folglich ist der südliche Arbeitsbereich durch lokalisierte Strike-Slip Bewegung charakterisiert. Innerhalb dieses Gebietes ereignete sich das größte instrumentell aufgezeichnete Erdbeben, das 1960 Valdivia Erdbeben, mit einer Stärke von M_W=9.5.

2D thermische Modelle und 3D mechanische Modelle wurden für die beiden chilenischen Arbeitsgebiete konstruiert, um Prozesse im Zusammenhang mit aktiver Subduktion zu untersuchen. Als numerisches Verfahren wurde die Finite Elemente Methode mit Hilfe des kommerziellen Softwarepakets ABAQUS angewandt.

Die thermischen Modelle sind auf die thermischen Konditionen entlang der Plattengrenzfläche fokussiert. Die thermische Struktur entlang der Plattengrenzfläche zeigt die Grenzen der Kopplung an aber auch die Art des Überganges von gekoppelt zu nicht gekoppelt und umgekehrt. Die Modelergebnisse zeigen, dass Heizen infolge der Scherung an der Plattengrenzfläche ein wichtiger Faktor ist, der in Betracht gezogen werden sollte. Die Modelle zeigen auch, dass die thermische Struktur an der unteren Begrenzung der

Koppelzone zu einer deutlichen Abnahme der Reibung entlang der Grenzfläche führt. Aufgrund der unterschiedlichen Geometrien der zwei chilenischen Untersuchungsgebiete, z.B. Abtauchwinkel der ozeanischen Platte und Krustendicke, ist die untere Begrenzung der Koppelzone des südlichen Untersuchungsgebietes in geringerer Tiefe als die des nördlichen Gebietes. Die Ergebnisse der thermischen 2D Modelle werden genutzt, um die räumliche Ausdehnung der Koppelzone in den mechanischen 3D Modellen festzulegen.

Numerische 3D Simulationen werden genutzt, um zu verstehen, wie Geometrien, Rheologien und mechanische Parameter die Verformungspartitionierung und das Deformationsmuster im chilenischen Fore-Arc beeinflussen. Der allgemeine Aufbau der Modelle basiert auf Fore-Arc Geometrie und Randbedingungen, die aus geophysikalischen und geologischen Feldresultaten abgeleitet wurden. Ich habe den Einfluss unterschiedlicher rheologischer Ansätze und unterschiedlicher physikalischer Eigenschaften auf den Fore-Arc untersucht, um Parameter zu identifizieren und zu bestimmen, die den Unterschied des Deformationsmusters zwischen dem nördlichen und südlichen Gebiet steuern.

Die Ergebnisse der numerischen Studien stellen heraus, dass ein kleinerer Abtauchwinkel der ozeanischen Platte, ein hoher basaler Reibungskoeffizient, eine hohe Konvergenzschiefe und ein großer Elastizitätsmodul die Lokalisierung der Deformation im Fore-Arc Keil begünstigen. Basierend auf dieser Parameterstudie habe ich Modelle für die beiden chilenischen Arbeitsgebiete ausgewählt, die in Beobachtungen erster Ordnung übereinstimmen. Diese ausgewählten Modelle erklären die unterschiedlichen Deformationsmuster durch eine größere Konvergenzschiefe, einen kleineren Abtauchwinkel der ozeanischen Platte und ein härteres Keilmaterial für das südliche Untersuchungsgebiet. Der Unterschied bezüglich der Deformationsmuster kann sogar größer sein, wenn ich eine größere Reibung zwischen den Platten im südlichen Gebiet anwende; jedoch zeigen einige unabhängige Beobachtungen eine umgekehrte Tendenz: eine Abnahme der Intensität der Koppelung von Nord nach Süd.

Das schwächere Keilmaterial des ausgewählten Modells für das nördliche Untersuchungsgebiet steht im Zusammenhang mit der fortgeschrittenen Entwicklung des angrenzenden Orogens, der zentralen Anden. Die Analyse weltweiter Beispiele von schiefen Subduktionzonen unterstützt die Schlussfolgerung, dass ältere Subduktionzonen weniger ausgeprägte Lokalisierung von Strike-Slip Bewegung aufzeigen.

Resumen

Los estilos de deformación a lo largo de la cuña de ante-arco chileno son muy disímiles, a pesar de condiciones similares de la cinemática de las placas. En este trabajo yo me focalizo en el análisis de la deformación en dos regiones a lo largo del margen convergente chileno a 20°-24°S y 37°-42°S. Aunque ambas regiones están sujetas a la subducción oblicua de la placa oceánica de Nazca y detenida por la cadena montañosa andina, ellas muestran patrones distintos de deformación.

La zona de estudio del Norte de Chile (20°-24°S) se caracteriza por una corteza excepcionalmente gruesa de cerca de 60 km de espesor bajo el Altiplano – Puna Plateau, la ausencia de una cuña acrecionaria en el ante-arco debida a un clima hiper-árido, y consecuentemente una fosa sin sedimentos. En esta área se observan dos sistemas de fallas mayores paralelas al margen, la Zona de Falla Atacama (ZFA) y el Sistema de Falla de la Precordillera (SFP). Ambos sistemas transcurrentes no exhiben desplazamiento reciente significativo.

El área de estudio Sur (37°-42°S), comparada con el área de estudio Norte, se caracteriza por una topografía más baja, altas tasas de precipitación (2000 mm/a), y una placa oceánica más joven. Un sistema de fallas transcurrentes activo, la Zona de Falla Liquiñe-Ofqui (ZFLO), muestra 1 cm/a de movimiento dextral reciente y controla la morfología de esta área. Así, el área de estudio del Sur de Chile exhibe movimiento transcurrente localizado. Dentro de esta área ocurrió el terremoto de Valdivia 1960 que es el evento de mayor magnitud (Mw=9.5) registrado en la Tierra.

Con el objetivo de estudiar los procesos relacionados con la subducción activa en ambas áreas de estudio se construyeron modelos termales 2D y modelos mecánicos 3D. El método numérico aplicado es la técnica de elementos finitos, haciendo uso del paquete comercial ABAQUS.

Los modelos 2D se concentraron en las condiciones termales a lo largo de la interfaz de placas. La estructura termal a lo largo de esta interfaz revela los límites de acoplamiento pero también el tipo de transición de acoplado a desacoplado y vice-versa. Los resultados del modelo demuestran que el calentamiento por cizalle es un mecanismo importante que debería ser tomado en cuenta. Los modelos también muestran que las condiciones termales en el límite inferior de la zona de acoplamiento promueven un disminución tajante de la fricción a lo largo de la interfaz. Debido a las distintas geometrías de las dos áreas estudiadas, esto es en el ángulo de subducción y espesor de la corteza continental, el límite inferior de la zona

acoplada en el área Sur es ligeramente más somero que el del área Norte. Los resultados de los modelos termales 2D fueron usados para controlar la extensión espacial de la zona acoplada en los modelos mecánicos 3D.

Las simulaciones numéricas 3D son usadas para entender como las geometrías, reologías y parámetros mecánicos influyen en la partición del strain y los estilos de deformación en el ante-arco chileno. La estructura general de los modelos se basa en las geometrías del ante-arco y condiciones de borde derivadas de datos geofísicos y geológicos. Se examinó la influencia de distintos modelos reológicos y propiedades físicas diversas del ante-arco para identificar y restringir los parámetros que controlan las diferencias en la deformación superficial existente entre las áreas Norte y Sur.

Los resultados de estos estudios numéricos demuestran que la localización de deformación en un cuña de ante-arco se ve favorecida por un bajo ángulo de subducción, alto coeficiente de fricción basal, una alta oblicuidad de convergencia y un alto modulo de Young. Sobre la base de este estudio paramétrico se eligieron modelos preferenciales para ambas áreas, los que reproducen observaciones de primer orden. Estos modelos preferenciales explican las diferencias en los estilos de deformación por un alto ángulo de oblicuidad y bajo ángulo de subducción de la placa subductada, y un material más resistente formando la cuña en el área de estudio Sur. Las diferencias entre estos estilos podrían ser aún mayor si se aplicase mayor acoplamiento entre las placas del área Sur; sin embargo, varias observaciones independientes indican la tendencia opuesta mostrando un descenso hacia el Sur de la intensidad de acoplamiento.

La debilidad del material formador de la cuña para el área de estudio Norte se asocia con un desarrollo avanzado del orógeno adyacente, los Andes Centrales. El análisis de ejemplos similares de subducción oblicua en el mundo soportan la conclusión que zonas de subducción maduras presentan localización menos pronunciada de movimientos transcurrentes.

Contents

1   Introduction

The Andes are one of the largest and most spectacular orogenic systems on Earth formed by the subduction of the oceanic Nazca plate beneath the South American continent. The Andes extend for more than 50° of latitude along the western margin of the South American continent.

The recent kinematics of the convergence, approximately 6.5 cm/yr subduction of the Nazca plate at an azimuth of ~74° (e.g., Norabuena et al., 1998), is almost uniform along the length of the northern, central, and southern Andes. South of 18°S, the boundary between the two converging plates is an almost straight north-south line (Figure 1.1). These uniform conditions should favor a rather uniform orogenic belt. The Andean margin is notably marked by strong along-strike segmentation, varying in topography, morphostructure, tectonics, basin distribution, volcanism, subduction geometry, deep lithospheric structure, and geological history (e.g., Jordan et al., 1983, Isacks, 1988, Cahill & Isacks, 1992, Yañez & Cembrano, 2004, Tassara, 2005). Whereas the central Andes lack recent margin-parallel strike-slip motion, the southern Andes show considerable recent strike-slip motion. Strike-slip faulting reflects the impact of oblique convergence.

The Andean orogenic system inspired numerous studies; especially during the last decades (e.g., Oncken et al., 2006). However, some of the first order features, such as the along-strike variations of deformation of the Andes, are not yet fully understood.

Two areas along the Chilean margin were chosen (Figure 1.1) to analyze the variations of the style of deformation along the Chilean margin. One area in the central Andes is located in northern of Chile between 20° - 24°S, and will be referred to as the northern study area. The second area in the southern Andes is located in southern Chile between 37° - 42°S, and will be referred to as the southern study area. By comparing these areas I try to understand the variations in deformation related to the oblique subduction along the western margin of South America. The analysis of deformation caused by oblique convergence requires a 3D approach.

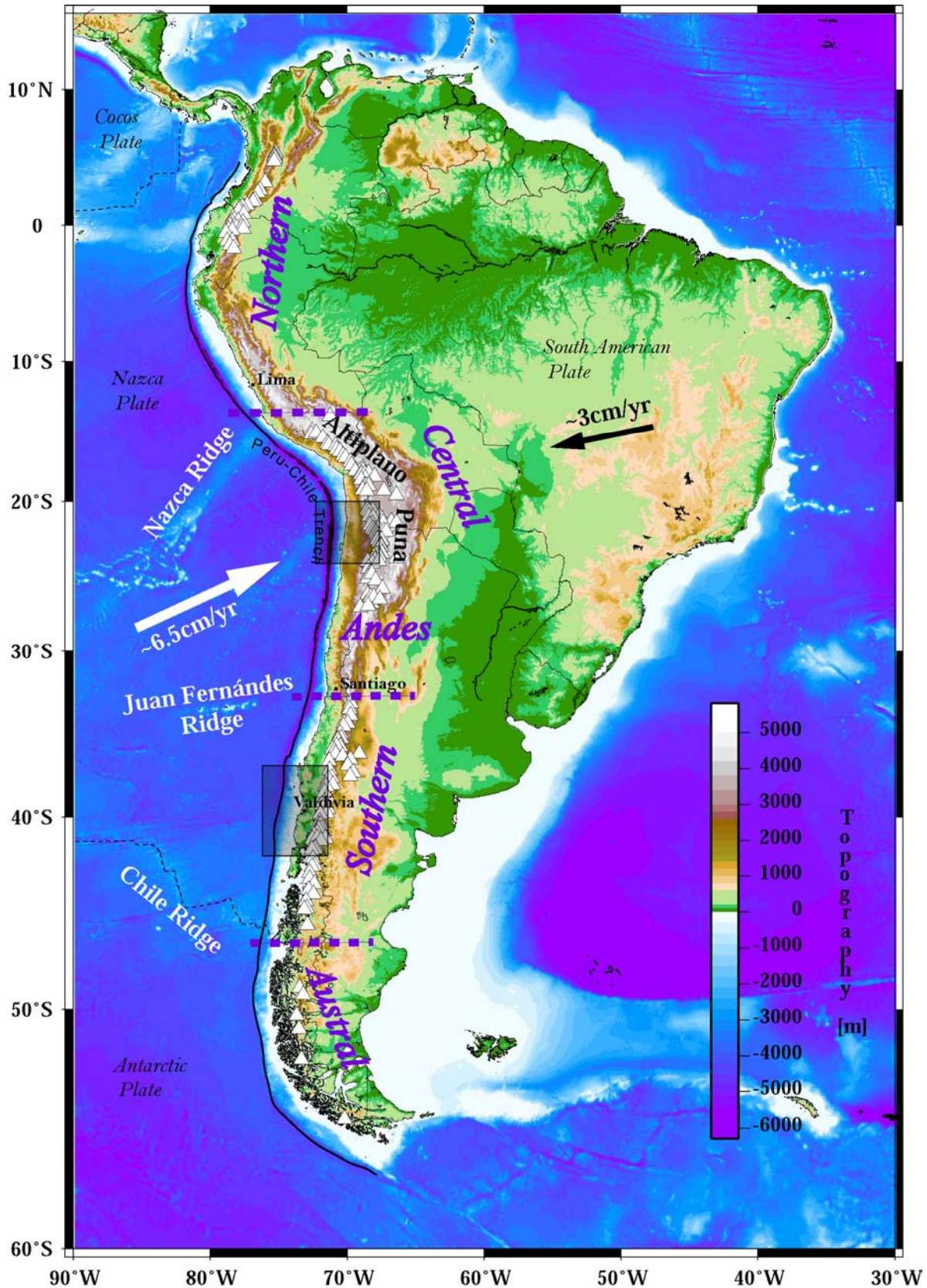**Figure 1.1**: Topography and bathymetry of the South American continent (Smith & Sandwell, 1997). Dashed purple lines indicate boundaries of first order Andean segments (Tassara, 2005). Arrows show the vectors of motion of Nazca (white) and South American (black) plates. Triangles display Holocene volcanoes (data from http://www.volcano.si.edu/gvp/world). Rectangles indicate the northern (20°–24°S) and southern (37°-42°S) study areas.

The northern study area is located in the central Andes dominated by the Altiplano-Puna plateau (Figure 1.1), the second biggest plateau in the world after the Tibet plateau. The northern study area, as part of the central Andes, is characterized by significant topographic relief, an up to 60 km thick crust (e.g., Wigger et al., 1994, ANCORP Working Group, 1999, Giese et al., 1999), and the lack of an accretionary wedge in the fore-arc due to hyperarid climate and consequently a sediment-starved trench (e.g., Scholl et al., 1970, von Huene & Ranero, 2003). Field observations do not show any major zones of active recent strike-slip motion (Hervé, 1987, Scheuber, 1987, Scheuber & Andriessen, 1990). Two margin-parallel strike slip faults are observed in this area (Figure 1.2a), the Atacama Fault Zone (AFZ) and the Precordilleran Fault System (PFS), but they do not show significant recent activities (Gonzáles et al., 2006). The GPS data (Bevis et al., 1999, Klotz et al., 2001, Khazaradze & Klotz, 2003) show that the margin-parallel motion of the fore-arc wedge due to oblique motion of subducting Nazca plate is up to 2 cm/yr near the trench and decays smoothly inland, and no partitioning of deformation is observed.
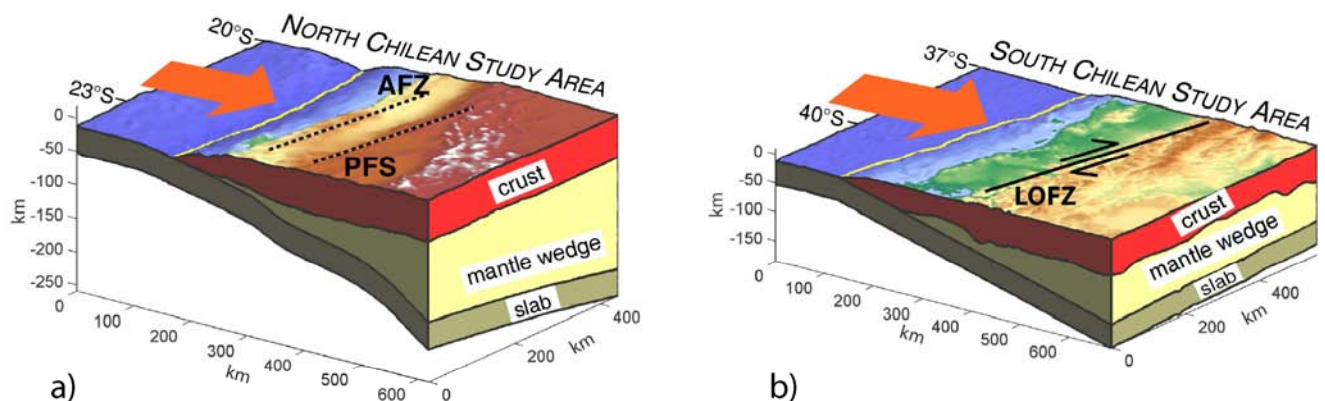
Figure 1.2: General view of two segments of the South America western margin (indicated by rectangles on Figure 1.1). a) The northern study area (20° - 24°S) is characterized by two major faults, the Atacama Fault Zone (AFZ) and the Precordilleran Fault System (PFS). b) The southern study area (37° - 42°S) is characterized by the Liquiñe-Ofqui-Fault-Zone (LOFZ). Data used to construct the 3D views: topography and bathymetry from Smith & Sandwell (1997), depth of the subducting slab from Isacks (1988) and Hoffmann-Rothe et al. (2006), Moho from Airy isostasy model (Turcotte & Schubert, 2002). Red arrows indicate the direction of subduction.

The southern study area is located in the southern Andes (Figure 1.1) and is in significant contrast with the northern study area. It has lower topography; it is characterized by high precipitation rates of ~2000 mm/yr, a narrower volcanic arc, and a younger subducting oceanic plate. The southern study area is characterized by one major margin-parallel strike-slip fault, the Liquiñe-Ofqui-Fault-Zone (LOFZ, Figure 1.2b). The LOFZ

shows 1 to 3 cm/yr recent dextral movement increasing from 38°S to 42°S (Rosenau et al., 2006). Thus, despite similar obliquity and convergence rate of the subducting Nazca plate in both study areas, the southern study area exhibits localized strike-slip motion.

Oblique convergence forces strike-parallel and strike-normal motion of the fore-arc wedge at plate margins. The partitioning of this motion depends on the obliquity of the convergence, the mechanical behavior of the fore-arc, and the degree of coupling at the plate interface. Figure 1.3 shows a cartoon illustrating the end-member styles of deformation of continental wedges subjected to oblique motion of the subducting plate. The case in which the continental margin deforms in a distributed way (Figure 1.3a) can be applied to the northern study area. If the continental fore-arc breaks into parts creating a fore-arc sliver (Figure 1.3b), elastic deformation is replaced by the evolution of strike-slip faults, similar to the behavior of the southern study area. The analysis of the partitioning demands a simulation in 3D.
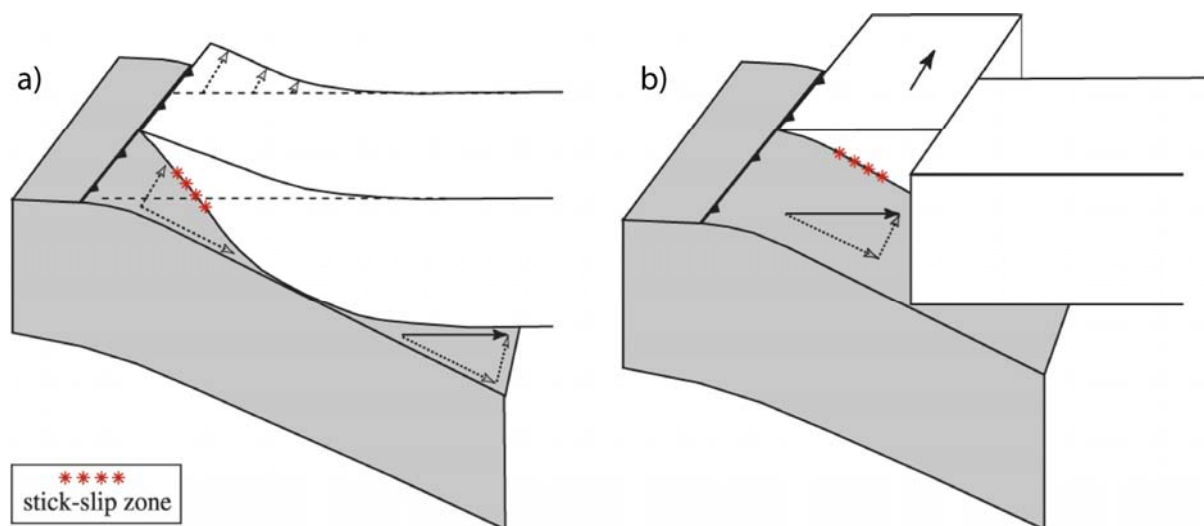
Figure 1.3: Cartoons illustrating two end-member styles of the response of the overriding plate to the oblique motion of the down-going plate (after Bevis & Martel, 2001). If the coupling between the plates is not strong enough to break the overriding plate, the resulting deformation is distributed evenly (a). If the coupling overcomes the brittle strength of the overriding plate, the overriding plate undergoes localized deformation (b).

This thesis aims to understand these changes and reasons behind by analyzing the styles of deformation of the western margin of South America, in particular the surface expression of deformation, along the Chilean convergent margin. To understand the parameters controlling the style of deformation in the chosen areas I applied 3D transient numerical modeling. This thesis represents the first real 3D study analyzing deformation caused by oblique convergence associated with a realistic composite rheology.

The advances in the numerical techniques and computational facilities give the opportunity to perform a systematic study of the dependence of the styles of deformation on different controlling parameters. As the main tool of the numerical research I used the commercial finite element software package ABAQUS (ABAQUS User's Manual, 2004) to model deformation in this 3D setup using appropriate rheologies. Chapter 2 considers the theoretical background of the numerical models including the basic equations governing deformation and their coupling with different rheological models. Basics of the finite element technique outline the main method used in the numerical calculations. The section also compares two commercial software packages available for such calculations, ABAQUS and Nisa.

My work refers to data collection covering geology, geophysics, and geodesy. I constrained the numerical models and compare results with these observations. Chapter 3 presents the field observations and geological constraints in the two chosen study areas, as well as the data available (gravity, seismic) for evaluating parameters for numerical models.

Chapter 4 presents two-dimensional thermal models of subduction focused on the thermal regime along the zone of coupling between the two plates. The thermal structure of a subduction zone plays an important role in understanding processes controlling active subduction.

Chapter 5 presents an additional study of important constraining parameters for the study areas. Using the critical wedge theory and analysis of the elastic material properties give the range of the material properties (including geometry, coupling between plates, and material properties) used in modeling the South American margin.

Chapter 6 presents the main 3D mechanical model and the results of the systematic parameter studies. The variation of basal friction, obliquity, Young's modulus, and slab dip show how these parameters control deformation. These experiments help to constrain preferred models for both study areas and to understand possible controls responsible for different styles of deformation along the Chilean margin.

Chapter 7 compares the results of this study with analogue and numerical studies of other authors. The comparison of results of this study with other subduction zones characterized by oblique convergence shows the general applicability of conclusions of my study.

2 Physical description of lithospheric deformation

2.1 Force balance

Continuous systems, as the lithosphere, relate to material bodies which continuously fill parts of space with matter. The following equations describe the balance of stresses in a 3D continuous medium:

$$\frac{\partial \sigma_{xx}}{\partial x} + \frac{\partial \sigma_{xy}}{\partial y} + \frac{\partial \sigma_{xz}}{\partial z} = 0 \tag{2.1a}$$

$$\frac{\partial \sigma_{xy}}{\partial x} + \frac{\partial \sigma_{yy}}{\partial y} + \frac{\partial \sigma_{yz}}{\partial z} = 0 \tag{2.1b}$$

$$\frac{\partial \sigma_{zx}}{\partial x} + \frac{\partial \sigma_{zy}}{\partial y} + \frac{\partial \sigma_{zz}}{\partial z} = \rho g \tag{2.1c}$$

where $\{x,y,z\}$ is the system of Cartesian coordinates (with the z-axis pointing downwards), σ is the stress tensor with its components σ_{ij}, and the last term in equation 2.1c represents the body force: ρ is the density, and g is the acceleration due to gravity. The differential equations of the stress balance describe the response of the continuum due to applied boundary conditions. This system of equations 2.1 is the main system to be solved numerically. However, to solve this system of three equations requires analyzing the relations between stresses and deformations, i.e. the rheological implementation of the model.

2.2 Rheological models

Lithospheric deformation is usually described by three types of rheological models: elastic, viscous, and plastic (brittle). Here, I briefly discuss these rheological models and outline their applicability to the numerical simulation of fore-arc deformation, the main aim of this work.

2.2.1 Elasticity

The properties of an elastic material are independent of the loading velocity and stresses are linearly proportional to strains. The elastic material behavior can be measured by laboratory mono- to triaxial compression and tensile experiments (Altenbach & Altenbach, 1994). This experimental work can be generalized to formulate the related constitutive equations. Elastic material behavior is characterized by the following properties:

- Loading and unloading follow the same way in a stress-strain diagram (Figure 2.1a).
- Deformational work is stored entirely as strain energy inside the body.
- Strain is only dependent on loading but not on rate of loading.
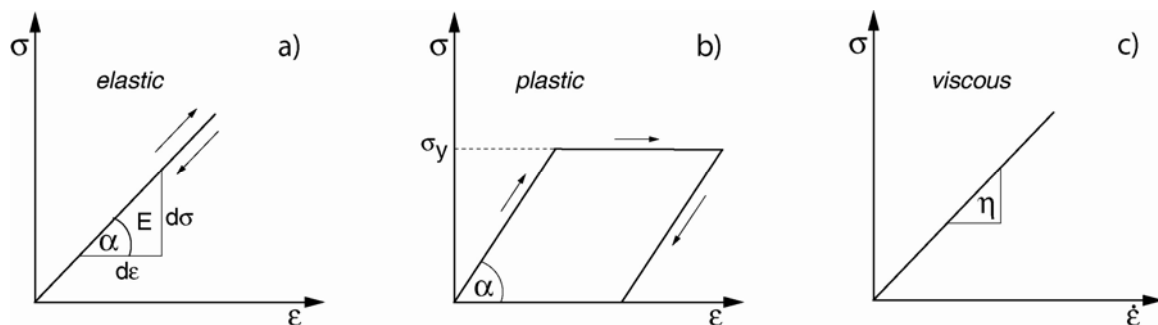
Figure 2.1: Stress σ – strain ε / strain rate $\dot{\varepsilon}$ relations in an elastic, a plastic, and a viscous body. Arrows illustrate the loading / unloading path. (a) Linear correlation between stress σ and strain ε in an elastic body. The stress-strain relationship in the elastic body does not depend on the direction of loading/unloading. (b) Relation between stress σ and strain ε in a plastic body. (c) Linear correlation between stress σ and strain rate $\dot{\varepsilon}$ in a linear viscous body. α=slope angle, σ_y=yield stress, η=dynamic viscosity

The starting point for the elastic material behavior is uni-axial Hooke's law:

$$\sigma^e = E\varepsilon^e \tag{2.2}$$

Hooke's law describes the linear relation between stress σ and strain ε, where E is the Young's modulus. In 3D, this constitutive relation can be written in the following form (Kwon & Bang, 1997):

$$\{\sigma^e\} = \mathbf{D}\{\varepsilon^e\} \tag{2.3}$$

where $\{\sigma^e\}$ and $\{\varepsilon^e\}$ are the stress and strain vectors with components from the stress and strain tensors

$$
\begin{aligned}
\{\sigma^e\} &= \{\sigma_{xx}^e \quad \sigma_{yy}^e \quad \sigma_{zz}^e \quad \sigma_{xy}^e \quad \sigma_{yz}^e \quad \sigma_{xz}^e\} \\
\{\varepsilon^e\} &= \{\varepsilon_{xx}^e \quad \varepsilon_{yy}^e \quad \varepsilon_{zz}^e \quad \varepsilon_{xy}^e \quad \varepsilon_{yz}^e \quad \varepsilon_{xz}^e\}
\end{aligned}
\tag{2.4}
$$

and D is the property matrix for isotropic material:

$$
\mathbf{D} = \frac{E}{(1+\nu)(1-2\nu)}
\begin{bmatrix}
1-\nu & \nu & \nu & 0 & 0 & 0 \\
\nu & 1-\nu & \nu & 0 & 0 & 0 \\
\nu & \nu & 1-\nu & 0 & 0 & 0 \\
0 & 0 & 0 & 1-2\nu & 0 & 0 \\
0 & 0 & 0 & 0 & 1-2\nu & 0 \\
0 & 0 & 0 & 0 & 0 & 1-2\nu
\end{bmatrix}
\tag{2.5}
$$

where ν is the Poisson ratio. In uni-axial experiments, Young's modulus, E, can be determined as the tangent of the stress-strain curve (Figure 2.1a):

$$
E = \frac{d\sigma}{d\varepsilon} = \tan\alpha
\tag{2.6}
$$

The components of the strain tensor are expressed via the displacements by $\varepsilon_{ij}^e = \frac{1}{2}\left(\frac{\partial u_i}{\partial x_j} + \frac{\partial u_j}{\partial x_i}\right)$ for $\{i,j\}=\{x,y,z\}$. Note that the above equations describe linear elastic problems, in which deformations are small.

2.2.2 Plasticity

Plasticity is a behavior of materials independent of time and velocity (Figure 2.1b, Altenbach & Altenbach, 1994). Plastic material is characterized by the following properties:

- Plastic loading procedures beyond yield are non-reversible since dissipation occurs.
- Plastic loading is dependent on the loading path.
- The loading history influences the responding material behavior.

Yield criterion

Plastic material is characterized by a yield stress. Above the yield stress deformation is irreversible and below yield stress the material deforms elastically. The general yield criterion (Zienkiewicz & Taylor, 1998) is

$$F(\sigma, \kappa) = 0 \qquad (2.7)$$

F is the yield function and it depends on the stress tensor σ and hardening parameter κ. In perfectly plastic materials the strength of the material after reaching the yield stress does not change with the amount of deformation (Figure 2.1b). The hardening parameter κ describes the plastic stress-strain behavior of work hardening materials when the strength of material is strain/work dependent after yield stress is reached. If some parts of a plastic body reach the condition 2.7, these parts deform plastically. The yield criterion should be satisfied during plastic deformation. The hardening parameter can change the plastic behavior depending, for example, on the total strain accommodated by the continuous media. Explicit expressions for F are discussed below.

The simplest example of plastic behavior is a perfectly rigid-plastic body, in which $F = \sigma - \sigma_{yield}$. Condition 2.7 states that the rigid-plastic body deforms plastically if $\sigma = \sigma_{yield}$ (Zienkiewicz, 1972). Figure 2.1b illustrates the loading-unloading process of an elasto-plastic body with a plastic potential of $F = \sigma - \sigma_{yield}$. During the first phase of loading, when stress is below yield, the body deforms elastically according to equations 2.2 and 2.6. Further deformation of a perfectly plastic body is characterized by the stress, which does not overcome yield stress and remains constant during the second phase, when deformation is plastic (Davis & Selvadurai, 2002). The unloading during the third phase ends up with finite non-reversible deformation due to plastic deformation during the second phase.

The most appropriate model of plasticity for crustal materials is considered to be Mohr-Coulomb plasticity (Davis et al., 1983, Dahlen et al., 1984) with the yield function:

$$F_{MC} = -P \sin \phi + \sqrt{J_2} \cos \theta - \sqrt{\frac{J_2}{3}} \sin \phi \sin \theta - C \cos \phi \qquad (2.8)$$

where ϕ is the angle of internal friction, $P = -J_1/3$ is the pressure, C is the cohesion. J_1 is the first invariant of the stress tensor: $J_1 = \sigma_{xx} + \sigma_{yy} + \sigma_{zz}$, J_2 is the second invariant of the deviatoric stress tensor: $J_2 = \left(\tau_{ij} \tau_{ij} / 2 \right)$ (assuming summation over repeated subscripts,

$\{i,j\}=\{x,y,z\}$), the components of the deviatoric stress tensor are $\tau_{ij} = \left(\sigma_{ij} + \delta_{ij} P \right)$ (δ_{ij} is the Kronecker delta), θ is the Lode angle (Homand & Shao, 2000; Papamichos et al., 1997; Bardet, 1990) defined as $\theta = \dfrac{1}{3} \arcsin \left[-\dfrac{3\sqrt{3}}{2} \dfrac{J_3}{\sqrt{J_2^3}} \right]$, and J_3 is the third invariant of the deviatoric stress, $J_3 \equiv \det \tau$.

Numerical models, however, often use the Drucker-Prager plastic approach (Drucker & Prager, 1952). This approach assumes a smooth yield condition and can be treated more easily numerically than Mohr-Coulomb plasticity. The singularities of the sharp vertices of the Mohr-Coulomb yield surface cause significant computational problems. In contrast to the hexagonal pyramid shape of the Mohr-Coulomb yield surface in the principle stress space, the Drucker-Prager yield surface has a conical shape (Figure 2.2). Tests with geomechanical materials show that the Drucker-Prager representation of the yield surface is not as accurate as the Mohr-Coulomb yield surface, but the significant virtue of the Drucker-Prager criterion lies in its simplicity (Davis & Selvadurai, 2002). Experimental triaxial test results for sand approximate the Mohr-Coulomb surface (Vermeer & de Borst, 1984). Test results on solid material show a more curved approximation to the Mohr-Coulomb surface (Newman, 1979) and the yield surface lies between the Mohr-Coulomb and the Drucker-Prager yield surface. It depends on the material whether it matches the Mohr-Coulomb surface or results in a more curved yield surface. Yield condition and constitutive behavior of most fore-arc materials are not well constrained. At this stage the Drucker-Prager model provides a good approximation of the yield surface for materials to be simulated in this thesis.
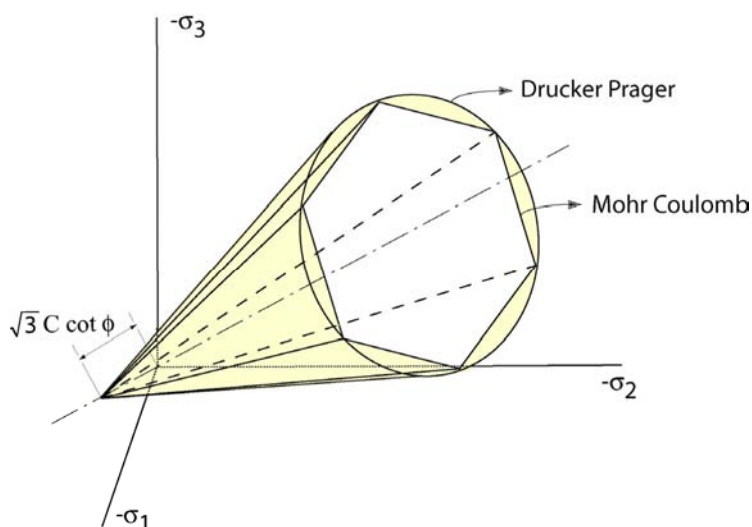

Figure 2.2: Drucker-Prager (circumscribed) and Mohr-Coulomb isotropic yield surfaces in a principal stress space (modified after Zienkiewicz & Taylor, 1998)

The yield function for the Drucker-Prager criterion is

$$F_{DP} = -3\alpha' P + \sqrt{J_2} - K \tag{2.9}$$

where $\alpha' = \dfrac{2\sin\phi_{DP}}{\sqrt{3}(3-\sin\phi_{DP})}$ and $K = \dfrac{6C_{DP}\cos\phi_{DP}}{\sqrt{3}(3-\sin\phi_{DP})}$ are constants related to the angle of

friction ϕ_{DP} and cohesion C_{DP} of the material, respectively (Ncheuguim, 2006). The angle of internal friction ϕ_{DP} and the cohesion C_{DP} in the Drucker-Prager criterion relate to the corresponding Mohr-Coulomb parameters as (ABAQUS User's Manual, 2004):

$$\tan\phi_{DP} = \frac{9\sin\phi}{\sin\phi\tan\psi + \sqrt{3(9-\tan^2\psi)}}$$
$$C_{DP} = \frac{(9-\tan\phi_{DP}\tan\psi)C\cos\phi}{\sqrt{3(9-\tan^2\psi)}} \tag{2.10}$$

where ψ is the dilatancy angle.

In the following, I will refer to the cohesion C and the angle of internal friction ϕ by the definition of Mohr-Coulomb plasticity, even though in the numerical simulations corresponding values for Drucker-Prager plasticity calculated by equation 2.10 are used. It is common practice to use the parameter definition of Mohr-Coulomb plasticity when discussing cohesion C and angle of internal friction ϕ of materials.

Plastic flow: Associated and non-associated plasticity

If a plastic material reaches condition 2.7, it flows plastically. The flow satisfies the condition:

$$d\varepsilon^{pl} = \lambda\frac{\partial Q}{\partial\sigma} \tag{2.11}$$

where Q is the plastic potential and λ is the plasticity consistency parameter (Roque & Button, 2000). The latter should be chosen such that condition 2.7 is satisfied during plastic deformation. In the special case of associated plasticity the condition

$$Q = F \tag{2.12}$$

is valid. While associated plasticity can be applied successfully to metals, it is less appropriate to be applied to materials like rock and unconsolidated sediments.

The plastic potential Q for plasticity has the same form as the yield function F (equations 2.8 or 2.9), but with the angle of internal friction ϕ replaced by the dilatancy angle ψ (Davis & Selvadurai 2002). Thus, for Mohr-Coulomb plasticity,

$$Q_{MC} = -P\sin\psi + \sqrt{J_2}\cos\theta - \sqrt{\frac{J_2}{3}}\sin\theta\sin\psi - C_{MC}\cos\psi \qquad (2.13)$$

Note, that the last term in the above equation is presented here to illustrate the similarity between F (2.8) and Q (2.13). It does not affect the plastic flow, because of the differential form of the flow law 2.11. Similarly, Drucker-Prager plasticity has

$$Q_{DP} = -3\alpha'P + \sqrt{J_2} - K \qquad (2.14)$$

with $\alpha' = \dfrac{2\sin\psi_{DP}}{\sqrt{3}(3-\sin\psi_{DP})}$ and $K = \dfrac{6C_{DP}\cos\psi_{DP}}{\sqrt{3}(3-\sin\psi_{DP})}$.

Associated plasticity is characterized by the condition $\phi = \psi$, whereas in non-associated models $\phi \neq \psi$. The specific form of the plastic potential can be substituted into equations 2.8 – 2.11 to calculate the proportionality coefficient λ and further calculate the flow of material in the plastic regime.

Vermeer & de Borst (1984) showed that associated plasticity (2.12) does not satisfactorily describe the results of triaxial experiments on dilatant materials such as sand, concrete, and rock. To account for dilatancy in non-associated plasticity a dilatancy angle ψ is introduced, which controls the inelastic volume changes. Plastic yielding is nearly always accompanied by a plastic volume increase, but the amount of dilatation differs considerably from the value that would follow from associated plasticity. The dilatancy angle is at least 20° smaller than the internal angle of friction for rock and unconsolidated sediments (Vermeer & de Borst, 1984).

Deformation of a material may involve a volume change. An increase in volume is often referred to as dilatancy, as opposed to a decrease in volume, which is commonly called compaction (Paterson & Wong, 2005). Hansen (1958) first introduced the dilatancy angle ψ as a parameter characterizing dilatant materials. The angle represents plastic volume change

over plastic shear strain. The physical meaning of ψ can be understood by considering a shear box, in which the material at the interface between the two halves of the box forms a thin rupture zone (Figure 2.3). The dilatancy angle ψ describes the uplift angle in a created shear band.
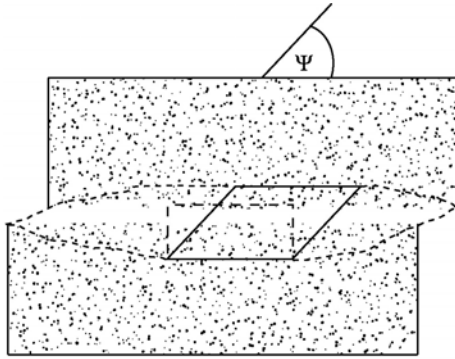

Figure 2.3: Shear box model predicting an uplift angle ψ for shear bands (modified after Vermeer & de Borst, 1984)

For soils, concrete, and rock, the dilatancy angle ψ is known to be smaller than the internal angle of friction ϕ of the material, whereas the difference between dilatancy and the angle of internal friction of soil is most significant. A range from 0 to 20° for the dilatancy angle ψ covers the values obtained for soils, concrete, and rock. A typical value for dense sand is $\psi=15°$, whereas loose sands have dilatancy angles of just a few degrees. For rocks the dilatancy angle ranges between 12° and 20°. It has been shown that the dilatancy angle of rocks decreases to 6° - 9° at confining pressures of about 200 MPa (Michelis, 1981). At high confining pressures, the dilatancy vanishes for soils, concrete, and rock.

The angle of internal friction ϕ as a strength parameter of the material is known for most soils, concrete, and rocks to be in the range of 15°-45°. In the analogue experiments of Lohrmann et al. (2003) the internal friction ϕ has been measured for different sands. For granular materials like sand, different angles of internal friction ϕ are obtained at peak strength and at stable strength (Figure 2.4, Lohrmann et al., 2003). Materials, such as sand, are characterized by a complex strain-dependent behavior, with strain-hardening prior to failure and subsequent strain-softening, until a dynamically constant shear load is reached (Figure 2.4). Whereas the internal angle of friction for sand at peak strength varies significantly mainly depending on grain size, the degree of homogeneity of grain size distribution and the filling method (sifted or poured) between different types of sand, the angle of internal friction at stable strength shows no systematic dependence on the mentioned parameters and is nearly the same for various types of sand (Lohrmann et al., 2003).
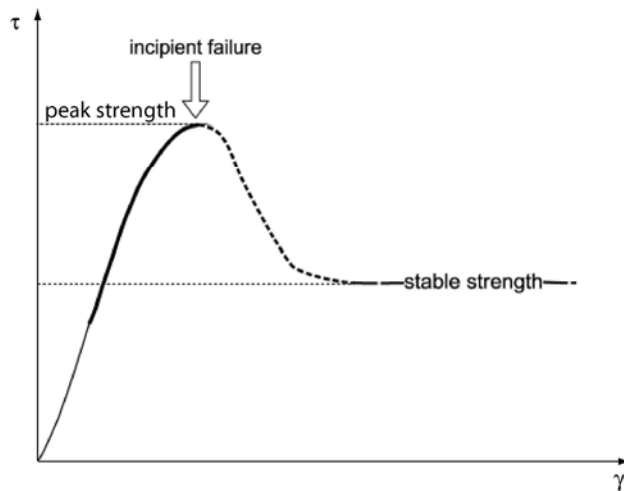
Figure 2.4: Relation of shear stress τ and angular shear γ for the material behavior of natural rocks (modified after Lohrmann et al., 2003)

In the numerical experiments, materials with internal angles of friction $\phi = 10°$ to $40°$ were used, which is an acceptable range for materials occurring in the crust. The dilatancy angle used in the models is ranging from $\psi = 0$ to $20°$. At high confining pressures of > 500 MPa, e.g. materials in 20 km depth, dilatancy vanishes (Vermeer & de Borst, 1984). Dilatation goes to zero after a few per cent of plastic strain, because rocks cannot increase in volume indefinitely, but can be subjected to high plastic deformation (Gerbault et al., 1998, Podladchikov, pers.comm.). Therefore, the majority of the numerical models were performed with $\psi = 0$. However, there are no systematic studies investigating how fast ψ decreases with depth or confining pressure, which could be applied to lower crustal structures like the ones investigated in this study. Thus, for simplicity, the numerical experiments of my study were performed with no volume change caused by brittle failure, i.e. $\psi = 0$. The parameters of the reference model are given in Table 5.1 (chapter 5.4).

2.2.3 Viscosity

It is well accepted that the behavior of rock materials can be described by a viscous rheology during long-duration tectonic processes (Turcotte & Schubert, 2002, Matsu'ura, 2004). The term "long", however, needs to be determined. Turcotte & Schubert (2002) describe a material which behaves elastically on short time scales and viscously on large time scales as a viscoelastic material (Figure 2.1c). The Maxwell strain rate model provides an equation for viscoelastic materials:

$$\dot{\varepsilon} = \frac{\sigma}{2\eta} + \frac{\dot{\sigma}}{G} \tag{2.15}$$

where η is the dynamic viscosity and G is the shear modulus, $G = E/(2+2v)$. The equation 2.15 has two parts: the viscous response $\sigma/2\eta$ and the elastic response $\dot{\sigma}/G$. The Maxwell time is defined as $\tau_{Maxwell} = \eta/G$. For $\tau < \tau_{Maxwell}$ elasticity dominates, and for $\tau > \tau_{Maxwell}$ viscous creep dominates.

The Maxwell times for the lithosphere and the mantle are vastly different, mainly ruled by the geothermal gradient. Typical viscosity values for a cold lithosphere above a subduction zone are about 10^{23}-10^{24} Pas (Braile, 2000). Values for the shear modulus G for sedimentary, metamorphic, or igneous rocks range from ~5 GPa to ~50 GPa (Turcotte & Schubert, 2002). Based on viscosity and shear modulus, the Maxwell time is ~10^{5} yr ($\eta = 10^{23} Pas$) to ~10^{6} yr ($\eta = 10^{24} Pas$). My numerical models are calculated for a time of 150000 yr. This model time is comparable with or smaller than the Maxwell time.

2.2.4   Reference rheological model

The above analysis of different rheological models leads me to the rheological structure of my reference model. In the following sections I compare several different rheological models, but the basis of my model of the fore-arc wedge will be an elasto-plastic rheology (equations 2.2 –2.5, 2.7). The rate of deformation is prescribed and only depends on a boundary condition (the rate of convergence between the two plates).

To compute the strain-stress relationship in elasto-plastic bodies I need to determine the plasticity consistency parameter λ (equation 2.11). I assume the elasto-plastic body is yielding and consider changes in stress and strain over small time increments. These changes in a Maxwell elasto-plastic body are:

$$d\varepsilon = d\varepsilon^{e} + d\varepsilon^{pl} \tag{2.16}$$

$$d\sigma = d\sigma^{e} = d\sigma^{pl} \tag{2.17}$$

Substitution of equations 2.3 and 2.11 into 2.16 yields:

$$d\varepsilon = D^{-1}d\sigma + \lambda \frac{\partial Q}{\partial \sigma} \tag{2.18}$$

and thus

$$d\sigma = D\left(d\varepsilon - \lambda\frac{\partial Q}{\partial\sigma}\right) \tag{2.19}$$

The yield condition 2.7 should be satisfied for the updated stresses:

$$F(\sigma + d\sigma) \approx F(\sigma) + \frac{\partial F}{\partial\sigma}d\sigma = \frac{\partial F}{\partial\sigma}d\sigma = 0 \tag{2.20}$$

Substituting 2.19 into 2.20 yields:

$$\frac{\partial F}{\partial\sigma}D\left(d\varepsilon - \lambda\frac{\partial Q}{\partial\sigma}\right) = 0 \tag{2.21}$$

And thus

$$\lambda = \frac{\partial F}{\partial\sigma}D\left(\frac{\partial F}{\partial\sigma}D\frac{\partial Q}{\partial\sigma}\right)^{-1}d\varepsilon \tag{2.22}$$

Note that in the above equation some terms in right hand side are tensors and cannot be simplified or re-ordered. Finally, the stress-strain relationship for an elasto-plastic body at yield is

$$d\sigma = \left[D - D\frac{\partial Q}{\partial\sigma}\frac{\partial F}{\partial\sigma}D\left(\frac{\partial F}{\partial\sigma}D\frac{\partial Q}{\partial\sigma}\right)^{-1}\right]d\varepsilon \tag{2.23}$$

The second term in the brackets turns to zero if the body is not at yield (*F<0*), or is unloading.

Uncertainties in (1) estimates of the rheological parameters and (2) the extrapolation of laboratory measurements to nature should be investigated carefully for specific applications. The laboratory experiments (to determine *E, ψ, φ*) discussed above were performed at high strain rates (10^{-5} - 10^{-4} s^{-1}), while characteristic strain-rates in the case I consider are approximately 10 orders of magnitude smaller.

The exact values of rheological properties that should be used in numerical experiments are not known. I have to vary the parameter sets and boundary conditions to find most appropriate values while being inside the wide range of acceptable parameters. In chapter 4 rheological parameters are extracted from available geophysical data. There are not many possibilities to get information about material parameters at some kilometers depth (e.g., borehole logging and core analysis). However, the limited depth and the small number of boreholes due to high drilling expenses preclude this method to give spacial information about the materials underground. Apart from laboratory experiments, which are limited in temperature and pressure due to apparatus limitations, numerical simulations are the only possibility to improve the understanding of the properties and rheologies of materials, as well as the processes at depth, which are not easily accessible.

2.3   Numerical approaches

Many complex scientific problems can only be solved as discrete problems numerically. The numerical methods are approximation methods, but are not approximate in the sense of being crude estimates. Many approaches were used to resolve earth-related problems. Among the most popular are the finite element method (FEM), the finite difference method (FDM) and the discrete element method (DEM). These numerical methods differ in the discretization method. Among the numerical approximation methods used for solving differential equations FEM and FDM are most frequently used and most universally applicable (Smith, 1986). Whereas FEM and FDM solve equations of continuous media, DEM solves equations for granular media (sometimes with the attempt to simulate continuous media). The main numerical method used in this study is the finite element method (FEM). The following chapters give a brief description of these three numerical methods and explain the choice of FEM for this study.

2.3.1   Discrete Element Method (DEM)

The discrete element method (DEM) is a family of numerical methods for computing the motion of a large number of particles like molecules or grains of sand. Applied to macroscopic problems, this method replaces a continuum with a set of finite size elements, the particles. The particles interact with each other through several types of forces: friction, when two particles touch each other; recoil, when two particles collide, and gravity (the force

of attraction between particles due to their mass), which is only relevant in astronomical simulations. A DEM simulation is started by putting all particles in a certain position and giving them an initial velocity. Then the forces which act on each particle are computed and added up to find the total force acting on each particle. An integration method is employed to compute the change in the position and the velocity of each particle during a certain time step from Newton's laws of motion. Then, the new positions are used to compute the forces during the next step, and this loop is repeated until the simulation ends.

DEM applications to geomodelling developed rapidly after Cundall proposed the distinct element method (e.g., Cundall & Strack, 1979). Recent applications include, for example, modelling the fracturing of rocks (Yoon & Jeon, 2004, Al-Busaidi et al., 2005), soil mechanics (García-Rojo et al. 2004), and geodynamics (e.g., Huhn, 2002, Vietor & Oncken, 2005).

Regarding the mechanical behaviour of soil or rock on different scales, microstructural behaviour such as localisation, fracturing and faulting can be modelled reasonably with DEM (Ehlers, 2006). While DEM has a big advantage in modelling large deformations because the particles can go far from the initial positions without numerical difficulties, it has also some disadvantages. The main disadvantage of DEM is the questionable relation between the laws of interaction between particles and the desired constitutive laws of continuous media. Another limitation of DEM is the limited number of particles, which interact through a set of contact laws. A large number of particles leads to huge numerical efforts and restrict the length of a simulation due to limited processor capacity. Especially 3D models are highly processor time consuming and thus not applicable to large scale models.

2.3.2 Finite Difference Method (FDM)

The finite difference method (FDM) was designed to solve (partial) differential equations (Marsal, 1989). The idea of the FDM is to transform the partial derivatives in difference equations over a small time and space interval. Differentiation,

$$\frac{\partial f}{\partial x} = \lim_{\Delta x \to 0} \frac{f(x + \Delta x) - f(x)}{\Delta x} \tag{2.24}$$

can be approximated by

$$\frac{\partial f}{\partial x} \approx \frac{f(x + \Delta x) - f(x)}{\Delta x} \tag{2.25}$$

if Δx is small. Thus, if the area of study is transformed on a mesh with the coordinates $x_1...x_N=\{x_i\}$, and the values of the function are discretised as $f(x)=f(\{x_i\})$, the derivative of the function f can be approximated by equation 2.25, assuming that $\Delta x_i=(x_{i+1}-x_i)$ is small. Thus, the partial derivative equations for function $f(x)$ can be replaced with the finite-difference equations to define $f(\{x_i\})$. The accuracy of FDM depends greatly on the density of the mesh $\{x_i\}$. The method is easily expandable to two- and three-dimensional problems.

In geomodelling FDM is used to solve problems of fluid flow and long-term evolution processes, considering a viscous behavior of the Earth materials (e.g., Gerya & Yuen, 2003).

The application of the FDM approach to the tasks of this study, however, is problematic. The most attractive feature of FDM is that it can be very easily implemented, but this method has significant limiting attributes. These attributes include the discretization by a stiff/non-deforming mesh due to the Eulearian approach and the restriction of the method in its basic form to only handle rectangular shapes and simple alterations. In my numerical experiments I want to resolve deformation with accuracy as high as possible and consequently the methods in which the grid follows deformation would be more suitable. Thus, the static grid of FDM rules out this method.

2.3.3   Finite Element Method (FEM)

The Finite Element Method (FEM) is the most popular method in numerical geodynamics. The FEM divides the study area into elements of variable geometry and size (Figure 2.5), assumes the distribution of the unknown functions inside elements, and requires that each element satisfies an integrated balance of stresses and boundary conditions. The method was successfully applied to problems of crustal deformation (e.g. Hampel & Pfiffner, 2006, Bird, 1996, Braun & Beaumont, 1995), mantle convection (Moresi et al., 2003, Phillips & Bunge, 2005, Bunge, 2005), thermal models (Springer, 1999, Peacock, 1996), and isostatic rebound (Wu, 2001, Kaufmann et al., 2000). The FEM combines a large amount of calculating techniques, briefly explained below. The calculations in this thesis are based on FEM and I provide more details on the FEM in the next section.
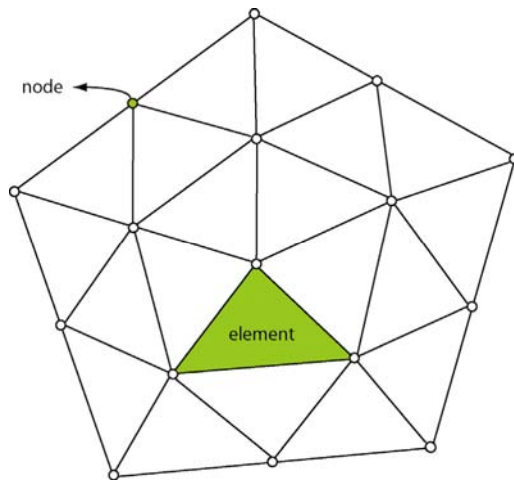
Figure 2.5: Discretized finite element model, finite number of elements are connected at so called nodal points

Concept of FEM

The method is based on the discretization of a domain into parts of arbitrary shape, these parts are called finite elements. The great advantage of FEM is the flexibility of the shapes of the elements. Tetrahedral and/or hexahedral elements can fill any complex shape of the problem domain. Discretization of irregularly shaped regions has traditionally been performed manually, from sketches. Today, state-of-the-art software packages automate the meshing process (ABAQUS User's Manual, 2004).

The concept of the FEM consists of the several numerical approaches (e.g., Kwon & Bang, 1997, Zienkiewicz & Taylor, 1998):

1. Shape functions define the value of functions inside the element via the values at the nodal points. Nodal points are usually located at the corners of the elements; however, there are element types in which nodal points are also located along the boundaries and/or inside the element. The unknown function assuming 1D, *F(x)*, is approximated inside each element by

$$F(x) = \sum_{i=1}^{n} H_i(x) F_i \tag{2.26}$$

where F_i are the values of *F* in the nodal points of the element, *n* is the number of the nodal points, and H_i are the shape functions. Shape functions have the following properties:

-   The shape function associated with node *i*, H_i, has a unit value at node *i* and vanishes at other nodes

- The sum of all shape functions is unity: $\displaystyle\sum_{i=1}^{n} H_i(x) = 1$

Equation 2.26 can be rewritten in the vector form:

$$F(x) = \bar{H}(x) \cdot \bar{F}' \tag{2.27}$$

where $\bar{H} = \{H_i\}$ and $\bar{F} = \{F_i\}$ are the vectors of the shape functions and nodal values of the function F with corresponding coordinates, and the prime indicates transposed vector.

2. The Galerkin method of discretization of the equations approximates the equations inside an element: All the governing equations are multiplied with the shape functions and integrated over the area of the element. This method requires the satisfaction of equations in the integrated sense. It can be better explained by an example. Consider the following equation to solve:

$$\frac{\partial^2 F}{\partial x^2} - F = 0 \tag{2.28}$$

This example is relevant to this study because the governing equations 2.1 in chapter 2.1 become second order derivative equations after substitution the rheological relations described in chapter 2.2. Application of the Galerkin method to equation 2.28 gives:

$$\int_{\Omega} \sum_{i=1}^{n} H_i(x) \left(\frac{\partial^2 F}{\partial x^2} - F \right) dx = 0 \tag{2.29}$$

where Ω is the area (volume) of the element. Substitution of 2.27 yields:

$$\int_{\Omega} \bar{H} \left(\frac{\partial^2 \left(\bar{H}(x) \cdot \bar{F}' \right)}{\partial x^2} - \bar{H}(x) \cdot \bar{F}' \right) dx = \int_{\Omega} \bar{H} \left(\frac{\partial^2 \bar{H}}{\partial x^2} \bar{F}' - \bar{H}(x) \cdot \bar{F}' \right) dx = 0 \tag{2.30}$$

3. The weak formulation allows simplifying the condition raised from 2.30, which requires that the shape functions should be smooth functions with a non-zero second derivative. To weaken this condition the 2.30 is integrated by parts:

$$\int_\Omega \bar{H}\left(\frac{\partial^2 \bar{H}}{\partial x^2}\bar{F}' - \bar{H}\cdot\bar{F}'\right)dx =$$

$$\int_\Omega \left(-\frac{\partial\bar{H}}{\partial x}\frac{\partial\bar{H}}{\partial x}\bar{F}' - \bar{H}\cdot\bar{H}\cdot\bar{F}'\right)dx + \int_\Gamma\left(\bar{H}\frac{\partial F}{\partial n}\right)d\Gamma = 0 \qquad (2.31)$$

The additional integral over the boundary of the element is related to the flux of the function F across the boundary Γ. Note that equation 2.31 does not require second order smoothness of the shape functions as they can be linear in this formulation. The use of linear shape functions results in simplicity of extrapolation inside the element and these functions are widely used. The results of this study are mainly obtained using linear shape functions.

4. Discrete equations are now possible to obtain. Note that the vector $\bar{F}$ does not depend on coordinates inside the element. Equation 2.31 can be rewritten:

$$K_e \cdot \bar{F}' = R_e \qquad (2.32)$$

where K_e is called a local (elemental) stiffness matrix and R_e is a boundary vector with its elements expressed by

$$K_e^{ij} = \int_\Omega\left(\frac{\partial\bar{H}_i}{\partial x}\frac{\partial\bar{H}_j}{\partial x} + \bar{H}_i\cdot\bar{H}_j\right)dx$$

$$R_e^i = \int_\Gamma\left(\bar{H}_i\frac{\partial F}{\partial n}\right)d\Gamma \qquad (2.32a)$$

with i and j varying from 1 to k, the number of nodes in the element. Note, that for all nodes which are not located on the boundary of the element, the right-hand side vanishes and the shape function associated with this node also vanishes on the boundary (see the first property of the shape functions).

The equation 2.32, however, cannot be solved separately from the other elements because the right-hand side of this equation is unknown. All the elements of the global domain should be combined into the global system of equations.

5. The global stiffness matrix can be obtained by putting all the elemental equations into the global system adding the equations for the nodes which are shared between different

elements. This procedure is not straight forward, because the nodes in one element can be shared between different elements and this procedure requires additional analysis of the connectivity between nodes and elements. After summation, the global system of equations becomes:

$$K_g \cdot \overline{F}_g{}' = R_g \qquad\qquad (2.33)$$

where $\overline{F}_g$ is the vector containing values of unknown function in all the nodes of the global domain, K_g is the global stiffness matrix and R_g is a boundary vector. R_g has non-zero values only in the nodes located on the border of the global domain, because if the node is shared between two (or more) elements, the sum of the boundary vectors R_e at this point is zero. If I consider equation 2.28 with non-zero right hand side (e.g., body forces) then R_g should be expanded accordingly.

6. Boundary conditions complete the system of equations of FEM. The problems of deformation usually require setting the boundary conditions on all boundaries of the modelled domain. Considering the example above, the boundary conditions have to be set too. Thus, all the nodes with non-zero values of R_g should be specified. The standard boundary conditions for boundary-value problems are:

- Dirichlet boundary conditions - setting the values for the unknown function along the boundaries. In this case, the entire equation for this node from equation 2.33 is replaced by simple equation $F_i=value.$
- Cauchy boundary conditions - setting the flux of the unknown function normal to the boundary. In this case, the value of the right-hand vector in this point can be easily calculated using equation 2.32a.

Equation 2.33 now can be solved to find the unknown function F in all the nodal points F_i of our model domain. Then, the entire field of the unknown functions can be reconstructed using equation 2.27.

This section presents only the essence of the FEM using a simplified example. The entire set of techniques used in the following calculations is based on the well developed theory of constructing, optimizing, and solving finite-element equations and would go beyond the scope of this thesis. For instance, the example considered above has only one degree of freedom (single equation), while the set of the governing equations for an elasto-plastic

material (equations 2.1) consists of three equations complicating the application of the FEM. Some specific details of the FEM used in this study are described in the following section.

Unlike the FDM, a grid point exchanges the information with all other grid points which share an element. The most attractive feature of the FEM is its ability to handle complex geometries and boundaries with relative ease. In FDM the solution does not exist outside the nodes, that is why the mathematical foundation of the finite element approximation is considered as more substantive. Depending on the problem, a FEM approximation is in many cases more accurate than in the corresponding FDM approach. Generally, the FEM is the method of choice in all types of analysis in structural mechanics especially for large scale 2D and 3D simulations. The FEM is a good choice for solving partial differential equations over complex domains or when the spatial discretization (degree of resolution) varies over the entire domain and the mesh is required to deform.

2.4   Implementation of FEM in ABAQUS and NISA

ABAQUS

ABAQUS is an advanced commercial software for finite element analysis. The software was initially created for the nuclear power and offshore engineering communities. More than 25 years of software development created a robust and reliable software, that is powerful and easy to use and now widely applied in different branches of industry, engineering, and science (e.g. automotive engineering, aerospace, defense, electronics, medicines, geosciences).

Over the last decade numerical modeling got more and more important for geodynamics. In the course of this development ABAQUS, as a powerful finite element tool, has been used to solve earth related problems. ABAQUS has been applied to simulate fluid migration (e.g. Kurz et al., 2003, Kurz et al. 2004), slab dynamics (e.g. Funiciello et al., 2003), shear zones (e.g. Regenauer-Lieb & Yuen, 2003), thrust wedge formation (e.g. Buiter et al., 2006), postglacial isostatic adjustment of the earth (e.g. Wu, 1999, Wu, 2001), and crustal deformation (e.g. Fischer, 2005).

The following features of ABAQUS make this software especially useful for this study. The software is able to model 3D problems. The Lagrangian approach, implemented in ABAQUS/Standard, is suitable for stress/displacement problems dealt within the framework of this study. It possesses an extensive library of elastic and inelastic material models, such as

linear elasticity, viscoelasticity, Drucker-Prager plasticity, and Mohr-Coulomb plasticity. It is possible to apply associated and non-associated plasticity. The element library contains 2D elements of triangular and quadrilateral shape as well as 3D elements of tetrahedron, wedge, and hexahedron shape including a wide range of special purpose element types, e.g. continuum elements, shell elements, beam elements, and spring elements. All elements can be modeled with linear or quadratic geometric order. ABAQUS/Standard provides a variety of methods to specify initial conditions (e.g. initial stress field due to gravity, buoyancy forces), boundary conditions (e.g. displacements, velocities), loads (e.g. gravity, pressure), and predefined fields for various analysis types. Several different types of constraints can be defined including multi-point constraints, kinematic coupling, and surface-based constraints. Particularly it provides contact modeling capabilities which include the contact between deformable bodies, between a deformable and a rigid body, or self-contact of a deformable body. A variety of interactions between surfaces can be modeled to suit the behavior required for different situations. These interactions include various friction models for tangential interactions, different types of normal interactions, fluid penetration between contacting surfaces, and debonding of initially bonded surfaces.

NISA

NISA is a family of finite element programs for structure analysis, fracture analysis, multi body mechanical system analysis, and many more. NISA II and DISPLAY III are two modules of this program family. NISA II is a program for linear and nonlinear static analysis, advanced dynamics, and many more applying the Lagrangian formulation. DISPLAY III is an interactive graphics program for geometry and finite element model building, analysis preparation and post-processing. Material models include Mises, Tresca, Mohr-Coulomb, and Drucker-Prager yield criterion. Associated plasticity is the only option in NISA II. Different kinds of loads can be applied e.g. conservative and non-conservative loading, thermal loading, and body forces. It is not possible to specify initial conditions. It provides simple 2D and 3D node to node contact elements and general surface to surface frictional contacts between bodies.

Comparison of ABAQUS and NISA – numerical benchmark test

GeoMod2004 (an international meeting on analogue and numerical modeling of geological processes, held in Switzerland in June 2004) suggested to calibrate and compare software packages for numerical modeling in geosciences. The benchmarking tests were performed using several numerical codes (ABAQUS, I2ELVIS, LAPEX-2D, Microfem, NISA, PFC2D, and Sopale) applied to the test problem (Figure 2.6). My personal contribution to this collaborative work (Buiter et al., 2006) was performing the test of the commercial software NISA.
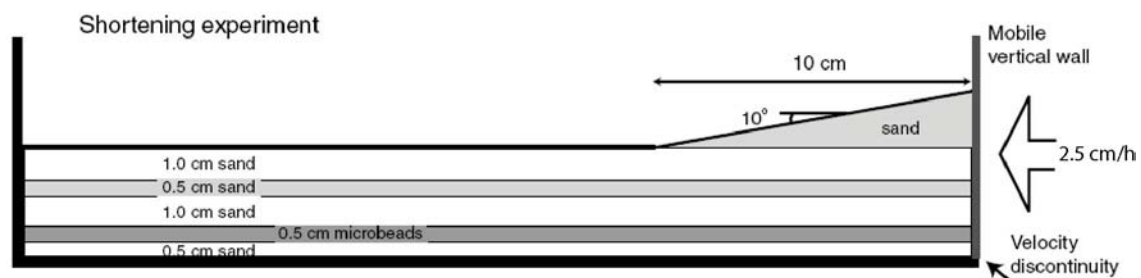

Figure 2.6: Set-up of the benchmarking shortening experiment (Buiter et al., 2006). Horizontal layers of sand (which have the same properties and differ in color only) with an embedded layer of weaker layer of microbeads are shortened by leftward move of a mobile wall on the right-hand side.

Among other numerical codes, two commercial software packages, ABAQUS and NISA, were used in the benchmark tests. Both commercial software packages failed to manage to reach the desired total shortening of 10 cm due to numerical distortions of elements. Even though the experiment performed with NISA reached a shortening by 2.3 cm, 0.5 cm larger than in the experiment performed with ABAQUS, the deformation in the latter experiment is much more localized and defined (Figure 2.7). The higher deformation phase reached by NISA is mainly due to the free-slip boundary condition at the base of the model. This is a significant simplification of the original requirement of the benchmark test (the coefficient of the basal friction supposed to be $\mu_b = 0.34$ in the experiments); however, NISA cannot handle contact surfaces with finite value of friction between them.
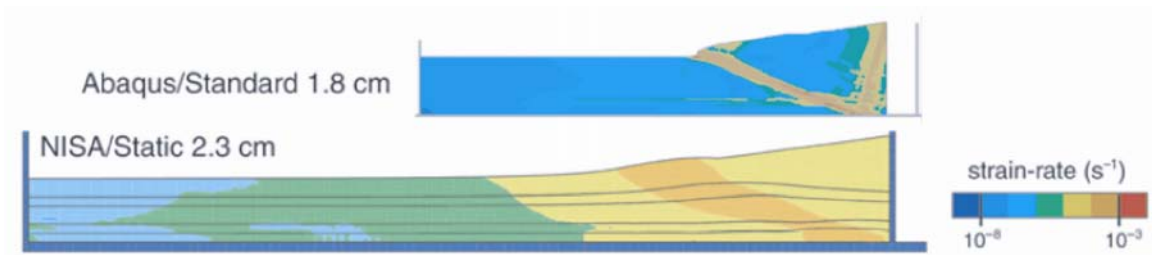
Figure 2.7: Results of the shortening experiment performed with ABAQUS and NISA. Shown are the strain-rates after 1.8 cm (ABAQUS) and 2.3 cm (NISA), respectively (Buiter et al., 2006).

The comparison of these two finite element software packages shows, that it is essential for localization of deformation to apply a non-associated plastic flow law, where the angle of dilatation is different to the angle of internal friction, and to implement strain softening for brittle material behavior; both features are possible with ABAQUS. The comparison of the two finite-element programs shows clearly the advantages of ABAQUS in the specification of material behavior. For more details on the entire benchmark test see the attached paper by Buiter et al., 2006 (Appendix A).

Three main arguments lead to the usage of the ABAQUS software package:

1) the possibility to model materials characterized by non-associated plasticity, which is the important constitutive property of materials in geosciences;
2) the option to apply a frictional contact between two surfaces, which is an important feature for modeling subduction zones;
3) specification of initial conditions

Another reason, based on a rather subjective opinion, is the user friendliness of ABAQUS.

3   Tectonic framework of the Andean fore-arc / arc system

The Andes are an outstanding example of an ocean-continent convergence zone resulting from subduction of the oceanic Nazca plate beneath the South American plate and generating a cordilleran-type mountain belt that stretches for more than 6000 km along the western rim of South America. This orogenic chain reaches a maximum width of about 800 km in its central part. The morphology of the central Andes is dominated by the high elevation of the Altiplano-Puna plateau (15°-28°S), which is the second largest continental plateau on Earth after the Tibetan plateau.

The Andean margin is notably marked by strong along-strike segmentation. This segmentation is characterized by along-strike variations in topography, morphological structure, tectonics, basin distribution (fore-arc, intra-arc, and back-arc basins), volcanism, subduction geometry, deep lithosphere structure, and geologic history (e.g. Jordan et al., 1983, Cahill & Isacks, 1992, Stern, 2004, Yañez & Cembrano, 2004, Tassara, 2005). First order Andean segments are the northern Andean segment (north of 15°S), the central Andean segment (between 15° to 34°S), the southern Andean segment (between 34°S to 47°S), and the austral Andean segment (south of 47°S) (Figure 1.1, Tassara, 2005). The Altiplano-Puna plateau, located in the central part of the Andes, has elevations higher than 3500 m and it is wider than 400 km along a symmetry axis which is parallel to the convergence direction (Gephart, 1994). The northern and central Andes are characterized by an enhanced orogenic topography with elevations of more than 2500 m and peaks of more than 6500 m. Compared to the northern and central Andes, the southern and austral Andes are characterized by a narrow (<150 km wide) mountain belt and lower elevation.

This section gives a short introduction to the first-order features of the central and southern Andean segments, the actual study objects of this work. The main focus will be given to the western margins of these segments, where the strain partitioning due to obliquity of convergence has the most pronounced morphological expression.

3.1   The north Chilean study area

Plate convergence was probably continuous in the central Andes from early Jurassic to the Holocene, although its parameters (e.g. convergence rate, convergence direction, and plate reorganization) have been subject to considerable variations (Scheuber et al., 1994).
The modern central Andean orogeny is the result of mountain building due to eastward subduction of the oceanic Nazca (Farallon) plate beneath the South American continental margin since late Oligocene / early Miocene times after many reorganizations of the oceanic plates in the eastern Pacific (e.g., Jordan & Alonso, 1987, Isacks, 1988, Sempere et al., 1990, Scheuber et al., 1994, Tebbens & Cande, 1997). The breakup of the oceanic Farallon plate into the Nazca and Cocos plates was one of the most outstanding plate boundary reorganization in late Oligocene / early Miocene in the Pacific with a tripling of the convergence rate up to 150 mm/yr at 25 – 20 Myr as a consequence thereof (Pardo-Casas & Molnar, 1987, Somoza, 1998, Lonsdale, 2005). The main phase of Andean orogeny is commonly attributed to the significant increase in plate convergence rate since around 25 Myr. Since early Miocene (<20 Myr) the convergence rate has decreased continuously to its current value of ~65 mm/yr at an azimuth of ~74° (Norabuena et al., 1999).

The orogen exhibits a characteristic tectonic subdivision into a fore-arc, a magmatic arc and a back-arc. Being exposed to continuous compression the fore-arc is further sub-divided into several morpho-structural units which show different amounts of uplift. These units are (from west to east): the extensional Costal Cordillera beginning offshore at the trench followed by the submarine slope and with average elevations onshore of about 1000 m and peaks up to 3000 m (Mt. Vicuña Mackenna with 3114 m), the extensional / transtensional Longitudinal Valley (the Pampa de Tamarugal; note that there is no Central Valley between Antofagasta and Santiago), a morphological depression present between 17°S and 27°S, the transpressional to compressional Precordillera, which reaches altitudes of 4300 m, and the Pre-Andine depression as a further fore-arc basin adjacent to the present magmatic arc (Figure 3.1, Hartley et al., 2000). Since the Paleozoic, the South American continent experienced an eastward shift of the magmatic arc in four stages: (1) a Jurassic- early Cretaceous arc in the Coastal Cordillera, (2) a mid-Cretaceous arc in the Longitudinal Valley, (3) a late Cretaceous-Paleogene arc in the Chilean Precordillera, and (4) the Miocene-Holocene arc in the Western Cordillera (Figure 3.1, Scheuber & Andriessen, 1990, Haschke et al., 2006).

The northern limit of the central Andean segment coincides with the northern boundaries of the Altiplano (~15°-23°S) and the central volcanic zone of the Andes (~15°-

28°S), whereas the southern limit of the central Andean segment coincides with the northern rim of the Central Valley (Valle Longitudinal, 34°-43°S) and the northern boundary of the southern volcanic zone of the Andes (~34°-45°S). These limits are also correlated with an abrupt N-S change from flat (less than 10° dip, 27° - 34°S) to normal (approximately 30° dip, south of 34°S) subduction in the depth range of 100 to 150 km, and with the intersection of the Nazca and Juan Fernández oceanic ridges with the continental margin (Yañez & Cembrano, 2004, Tassara, 2005). Based on along-strike variations of topography, volcanism, tectonic style, and subduction conditions, the central Andes can be divided into three second order segments, which are the Altiplano (15°-23°S), the Puna (23°-28°S), and the Frontal Cordillera (28°-34°S) (Jordan et al., 1983, Mpodozis & Ramos, 1989, Kley et al., 1999, Tassara, 2005). The active magmatic arc, with peaks of almost 7000 m altitude, is now situated in a distance of approximately 200 km from the trench and about 100 km above the Wadati-Benioff zone (Cahill & Isacks, 1992, ANCORP Working Group, 1999).

The fore-arc of the central Andean segment is characterized by a sediment-starved trench, due to a hyperarid climate and consequently the fore-arc is lacking an accretionary wedge (Scholl et al., 1970, von Huene & Ranero, 2003). The eastward migration (consumption of continental crust) of the trench-arc system since the Jurassic is a result of subduction erosion (e.g. Miller, 1970, Rutland, 1971, Stern, 1991, von Huene & Scholl, 1991). Features of tectonic erosion are material consumption, thinning of the fore-arc, trench retreat, and inland migration of the volcanic front (Miller, 1970, von Huene & Lallemand, 1990, von Huene & Scholl, 1991, Stern, 1989, Scheuber & Reutter, 1992, Scheuber, 1994, Kukowski & Oncken, 2006).

The modern Andean crust in the central segment is exceptionally thick, reaching up to 70 km beneath the Precordillera as deduced from seismic and gravimetric experiments (Wigger et al., 1994, Beck, 1996, ANCORP Working Group, 1999, Giese et al., 1999). The processes leading to this setting are not fully understood. Tectonic shortening of the crust due to increased westward drift of the South American plate is of great importance (Isacks, 1988, Kley & Monaldi, 1998, Silver et al., 1998, Oncken et al., 2006), but contributions from other processes like magmatic addition (Lamb & Hoke, 1997), underplating of material tectonically eroded from the fore-arc (Schmitz, 1994, Pelz, 2000, Victor, 2000), or hydration of the mantle wedge (Giese et al., 1999) may have contributed to the formation of the extremely thick crust and the high plateau. However, contraction is focused on the backarc regions, whereas the fore-arc was subjected to only minor shortening during the Neogene (Kley & Monaldi, 1998).
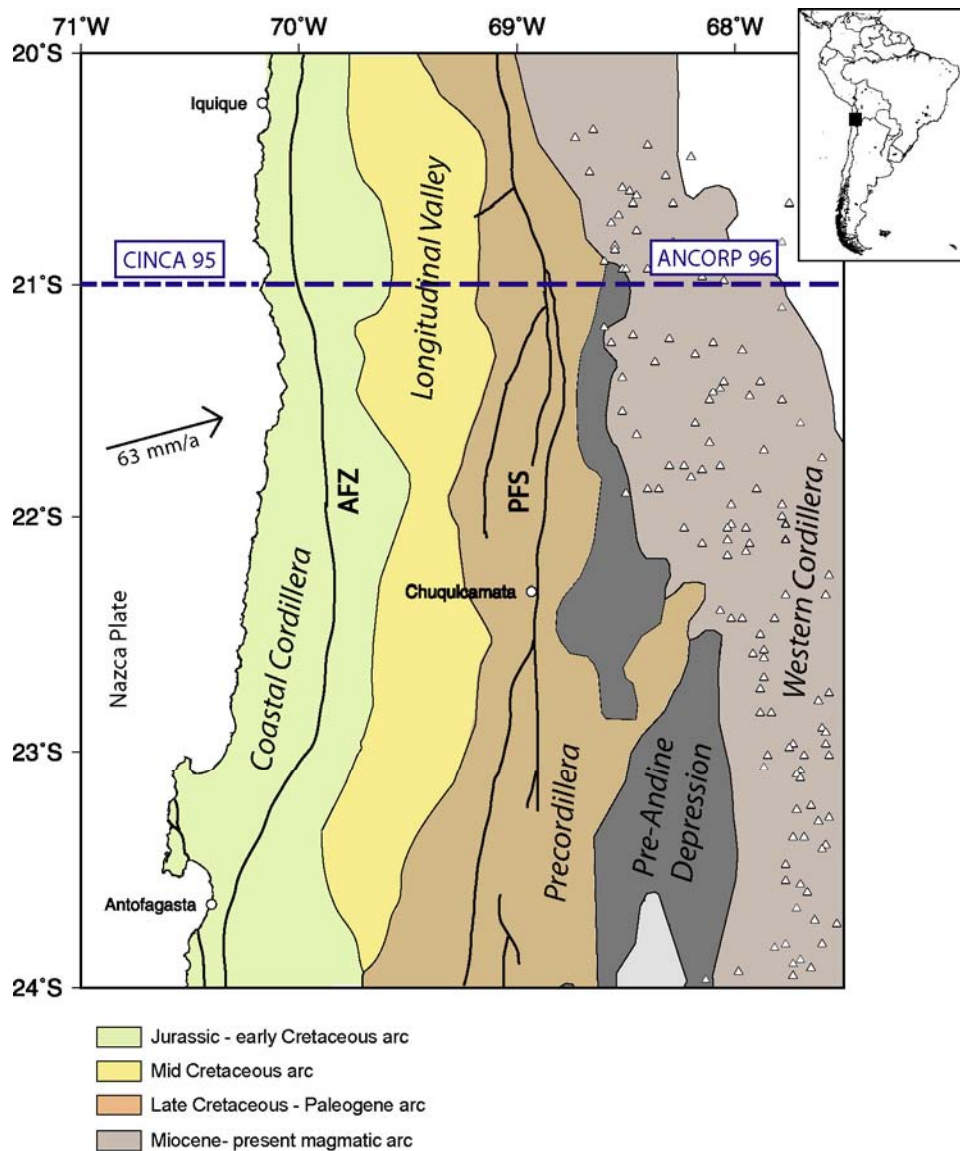
Figure 3.1: Geological map of the central Chilean segment (20° - 24°S) showing major morphostructural units, fault zones, recent volcanoes indicated by triangles, and dashed lines indicate positions of the CINCA '95 and ANCORP '96 seismic experiments (modified after Adam & Reuther, 2000 and Hoffmann-Rothe et al., 2002)

The parameters of plate convergence, such as obliquity, rate and dip of the subducting slab, varied throughout the Andean cycle (Pardo-Casas & Molnar, 1987, Somoza, 1998). This gave rise to different deformation phases and associated stress regimes within the continental margin. In particular, phases of pronounced oblique convergence can lead to the partitioning of deformation and varying trench normal and trench parallel components of slip (Beck, 1983, Beck Jr., 1991). This is believed to have caused the formation of two large trench parallel strike-slip fault systems of the fore-arc region, the Atacama Fault Zone (AFZ) in the Coastal Cordillera (Jurassic-early Cretaceous arc) and the Precordilleran Fault System (PFS) of the Precordillera (late Cretaceous-Paleogene arc) (Scheuber et al., 1994).

The more than 1000 km long AFZ developed in the late Jurassic as a sinistral strike-slip fault in the course of oblique subduction of the Aluk (Phoenix) oceanic plate in SE direction (Scheuber & Andriessen, 1990, Scheuber et al., 1995, Scheuber & Giese, 1999). The deformation was focused in the Jurassic – early Cretaceous magmatic arc, subjected to heating and fluid infiltration which reduced crustal strength (Scheuber et al., 1994). Strike-slip movements along the AFZ occurred mainly during the Neocomian, when the AFZ was an active structure of the magmatic arc. Later stages are characterised by only vertical movements (Hervé, 1987, Scheuber, 1987, Scheuber & Andriessen, 1990). According to the reorganisation of the subduction system, the sense of relative motion along the AFZ has changed to dextral in the late Cretaceous. Throughout the Neogene, the AFZ was reactivated several times with a lateral (strike-slip) component less significant than the (mostly eastward directed) dip-slip component. The sense of younger movements is not uniform along the AFZ as indications for both dextral and sinistral displacement can be found (Delouis et al., 1998, Pelz, 2000). Gonzáles et al. (2006) verify young activity on the AFZ. Based on surface exposure ages and fault scarp observations they calculate a 0.01 mm/yr minimum vertical fault slip rate.

The Precordilleran Fault system was initiated in the late Eocene within the Eocene-Oligocene magmatic arc (Reutter et al., 1996). The increase of the convergence rate in the Eocene lead to enhanced coupling between the two plates (Scheuber et al., 1994, Hoffmann-Rothe, 2002). In conjunction with high obliquity of convergence this caused the formation of a transpressive regime in the overriding plate. Active arc-normal shortening and arc-parallel dextral strike-slip along the forming PFS were the consequences of these changes. Mineral enrichment and alteration processes were structurally facilitated along the PFS and led to the formation of the economically important porphyry copper deposits of the Precordillera (e.g. Chuquicamata open pit copper mine).

The observations and reconstructions of geological features/settings are the starting point for my numerical calculations. The numerical model presented in this thesis focuses on the estimations of stresses and strains in the fore-arc wedge located along the western margin of the South American plate between the trench and the magmatic arc. The field observations presented above document that the two main strike slip zones were active in the past, but became rather inactive recently. Can we understand the recent pattern of deformation? Can we understand the reason for the termination of localized strike slip pattern at some point of the evolution of this segment?

3.2   The southern Andean study area

The southern Andean segment is limited along-strike by two major tectonic boundaries: the Juan Fernández Ridge (~33.5°S) to the north and the Chile Ridge (~46°S) to the south (Figure 1.1). Compared to the central Andean segment the mean elevation decreases to less than 2000 m south of 33°S. The mountain belt is about 300 km wide (E-W) and the crustal thickness below the magmatic arc is about 35-40 km in the southern Andean segment (Bohm et al., 2002, Lüth et al., 2003).

In the southern Andean segment, the continental lithosphere can be divided into three morphotectonic units: the fore-arc, the volcanic arc, and the backarc. The fore-arc consists of the Coastal Cordillera and the Longitudinal Valley. The Coastal Cordillera is a narrow mountain belt located between the coast and the Central Valley. It is ~10-100 km wide and ranges in elevation from 1500 m at Nahuelbuta (38°S) to only a few hundred meters in the Valdivia region (40°-41°S) (Figure 3.2). The Longitudinal Valley, an active extensional depocentre since the late Oligocene, is filled with sediments up to several kilometers thick (Jordan et al., 2001). It extends through the entire southern Andes with a discontinuity between 39°S and 40°S. The formation of the Central Valley basin started during a major phase of late Oligocene to middle Miocene extension (Muñoz et al., 2000, Jordan et al., 2001), synchronous to the start of major shortening in the central Andes at ~20°-24°S (Allmendinger, 1997).

The volcanic arc is a chain of basaltic Quaternary stratovolcanos with the basement consisting of Meso-Cenozoic intrusive rocks. South of 38°S, the active volcanic arc is superimposed on igneous rocks of the northern Patagonian batholith that are of Cretaceous to late Tertiary age. Together they form the Patagonian Cordillera (Tassara & Yañez, 2003).

The volcanic arc is aligned along the major trench-linked dextral Liquiñe-Ofqui Fault Zone (LOFZ) that cuts the upper plate for more than 1100 km between 38°S and 46.5°S (Figure 3.2, Jarrard, 1986, Hervé et al., 1994, Cembrano et al., 2000, Thomson, 2002, Glodny et al., 2006, Melnick et al., 2006). Activity along the LOFZ probably initiated in late Oligocene (Hervré, 1994), accommodating part of the convergence obliquity between the Nazca and South American plates since then (Rosenau et al., 2006). From kinematic modelling (Rosenau et al., 2006) mean Pliocene to recent shear rates of >10 mm/yr, increasing from north (38°S, ~13 mm/yr) to south (42°S, ~32 mm/yr), could be quantified. To the east the fore-arc region is bordered by the LOFZ. Most of the strain at the leading edge of the continental margin seems to be absorbed by the fore-arc and the LOFZ, which marks-off

the fore-arc to the east. Thus the development of a back-arc fold-and-thrust belt has been inhibited (Hervé et al., 1994). A similar situation might have existed in the late Jurassic to early Cretaceous evolution of the southern part of the central Andean segment, when the Atacama fault zone, as a major arc related fault zone, was active (Hervé et al., 1994).

North of 38°S the volcanic arc is part of the Principal Cordillera (Hildreth & Moorbath, 1988). A series of complex basins span the contemporaneous active continental margin, which itself is characterized by volcanic activity (Mpodozis & Ramos, 1989, Jordan et al., 2001). The volcanoes, situated approximately 270 km away from the trench and almost parallel to it, form a belt that is about 80 km wide (López-Escobar et al., 1995). The general NNE trending alignment of the volcanic arc corresponds spatially to the NNE trending lineaments of the LOFZ. The volcanic arc is probably also controlled by the LOFZ, where crustal fractures of the fault zone may serve as channel ways for the magma ascent (López-Escobar et al., 1995). Other observed NW-SE trending faults in this area are also related to the LOFZ. The Lanalhue and Bio-Bio-Aluminé Fault Zones are two major NW-SE trending fault zones, which constitute together with the LOFZ first order discontinuities (Rapela & Pankhurst, 1992, Bohm et al., 2002). These faults have an active character, as revealed by strike-slip movements in the volcanic arc (Bohm et al., 2002). Furthermore, active seismicity is observed along the LOFZ at ~42°S (Lange et al., 2007). Plutonic rocks, probably of Tertiary age, are in contact with the volcanic rocks along these faults (Cingolani et al., 1991).

The fore-arc of the southern Andean segment is characterized by the presence of an accretionary wedge due to high precipitation rates of ~2000 mm/yr and a resulting trench fill exceeding 2 km in thickness (Bangs & Cande, 1997). The accretionary wedge of the south Chilean fore-arc has built up since the Pliocene in front of an older accretionary complex of late Carboniferous to Triassic age (Bangs & Cande, 1997, Kukowski & Oncken, 2006). However, the temporal development of the south Chilean fore-arc shows a dominantly tectonically erosive mode due to a lack of accreted sediments of Mesozoic to Tertiary age (Glodny et al., 2006, Kukowski & Oncken, 2006).

Similar to the central Andean segment, the numerical models performed for this study aim to reconstruct the stress-strain pattern of the marginal wedge of the southern Andean segment. The central and the southern segments, however, behave differently: only the southern segment localizes deformation in form of active strike slip recently. Thus, in addition to the general task of reconstruction of the deformational pattern, I try to understand why the two segments behave differently.
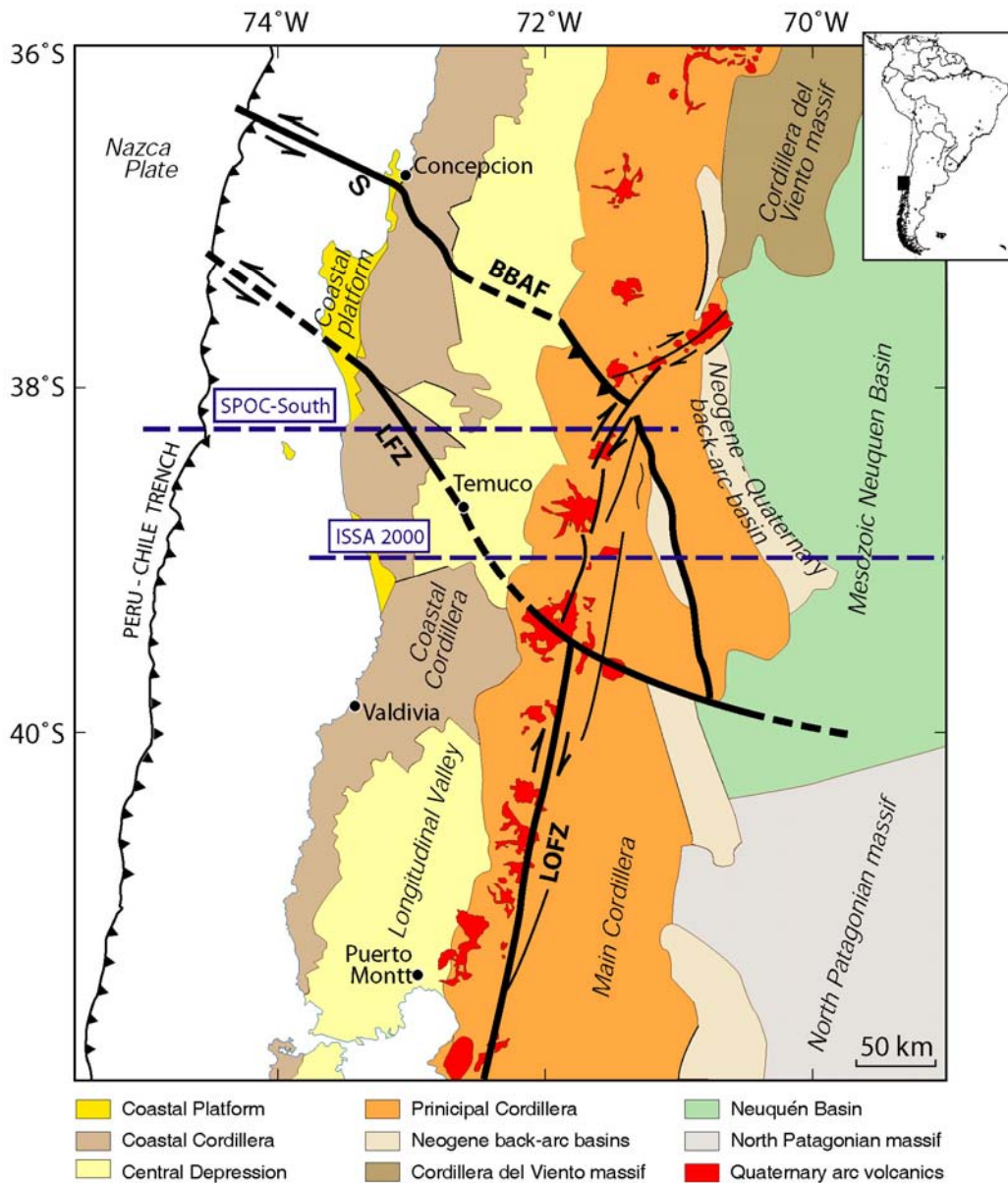
Figure 3.2: Geological map of the southern Chilean segment (36° - 42°S) showing major morphostructural units and fault zones. LOFZ - Liquiñe-Ofqui Fault Zone, LFZ – Lanalhue Fault Zone, BBAF – Bio–Bio-Aluminé Fault. Dashed lines indicate positions of the SPOC-South and ISSA 2000 seismic experiments. (after Melnick & Echtler, 2006)

3.3   Available data

The history of geological observations and data collection pertaining to the Andean orogeny goes back centuries. Alexander von Humboldt's research during his America expedition (1799-1804) covered different fields of science, including geology, mineralogy, and volcanology (Humboldt et al., 2004, 2006). The first Andes expedition of Charles Darwin, for example, took place in 1834 and aspects of mountain building were related with

all his three South America expeditions (Darwin, 1972). The data collection was boosted by the exploration of copper mines in the first half of the 19th century in the central Andes. The recent developments in the research technology (e.g., deep seismic, satellite images, and chronological techniques) brought the understanding of the Andean orogeny onto a new level.

Extensive research during the last several decades has led to the generation of a large geoscientific data base for the Andes (e.g. Rutland, 1971, Stauder, 1973, Jordan et al., 1983, Pardo-Casas & Molnar, 1987, Isacks, 1988, Stern, 1989, Tichelaar & Ruff, 1991, Dewey & Lamb, 1992).

Since 1992, considerable data and research on the Andes were generated by the "Collaborative Research Center 267" (SFB 267) entitled "Deformation Processes in the Andes". The data cover all disciplines of geoscience, including geology, geophysics, geodesy, and geochemistry for the areas of the central and southern Andes. These data are available on the SFB 267 website http://sfb267.geoinf.fu-berlin.de.

The main aim of the SFB 267 project was to investigate the interaction between different processes responsible for the evolution of subduction orogeny in the natural laboratory of the Andes. Research has greatly benefited from the multidisciplinarity of this joint initiative. The SFB 267 related studies were focused on the central and southern Andean segments. Comparison between these two parts of Andean orogeny is expected to lead to a better understanding of the factors controlling the evolution of the entire Andes.

The ongoing TIPTEQ project (from The Incoming Plate to mega-Thrust EarthQuake processes) as a successor of the SFB 267 aims to investigate the processes leading to mega-thrust earthquakes and their relation to processes in depth and at the surface at the southern Chilean subduction zone between 36° - 48°S. The research is focused on the seismogenic coupling zone, where earthquakes with magnitudes larger than 8 are generated. Data obtained within the TIPTEQ project complement the database established during the SFB 267 and cover all disciplines of geoscience.

Based upon these data, several conceptual models and syntheses on Andean deformation and its partitioning have been successfully launched (e.g., Fitch, 1972, Jarrard, 1986, Bevis et al., 1999, Hoffmann-Rothe, 2002, Khazaradze & Klotz, 2003). High resolution geophysical images provide insight in subsurface structures beneath the Andes (e.g. seismic interpretation by Yoon, 2005, gravity models by Tašárová, 2004 and Tassara, 2005). Numerical models aim at understanding how different parameters affect the Andean orogeny (Babeyko et al., 2006, Medvedev et al., 2006, Sobolev et al., 2006).

GPS Observations

The current rates of deformation can be evaluated by geodetical GPS measurements. Several GPS campaigns collected data along the western margin of South America. The data sets graphically illustrated below were compiled in Hoffmann-Rothe et al. (2006). Even though the recent achievements in GPS techniques bring confidence in the provided measurements, the direct comparison of the data below with geodynamic modelling should be made with care because the time scales of models (thousands of years) and geodetic data (years) differ significantly.

GPS sites mounted on the Nazca plate measure present day velocities of 6.36 cm/yr with respect to stable South America, which correspond to approximately 80% to the convergence rates predicted by the average 3 Myr NUVEL-1A model (DeMets et al., 1994, Angermann et al., 1999, Klotz et al., 1999, Norabuena et al., 1999). Results of several GPS campaigns performed in the northern Chilean study area suggest that the oblique Nazca– South America plate convergence is accommodated by oblique earthquake slip with no slip partitioning or trench parallel fore-arc sliver motion. Recent deformation due to ongoing Andean compression is concentrated in the thrust belt at the eastern margin of the Altiplano/Puna. GPS observations indicate a present day shortening rate of 3 – 4 mm/yr in the Sub-Andean (Klotz et al., 1999). These results are interpreted as a reflection of the interseismic strain accumulation above the Nazca-South America subduction zone due to the locked thrust zone extending down to about 50 km depth (Klotz et al., 1999).
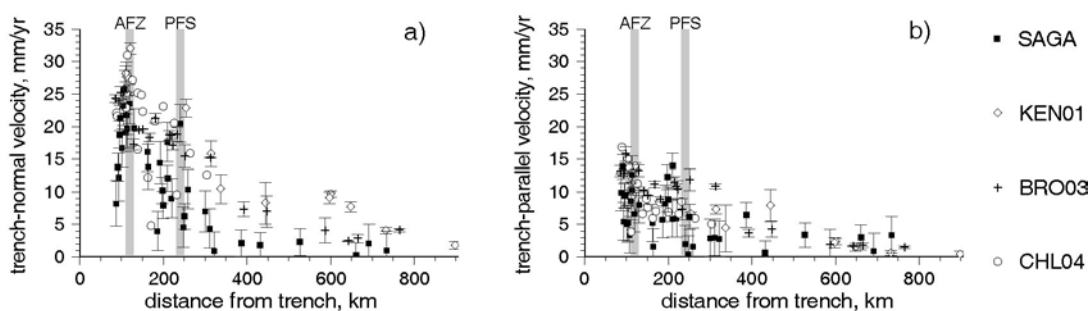

Figure 3.3: GPS data along the Chilean margin between 20° and 30°S shown in a margin-normal profile (modified after Hoffmann-Rothe et al., 2006): trench normal velocity component (a) and trench parallel velocity component (b). Included campaigns: SAGA – SAGA94–96 campaign excluding co – and post –seismic vectors of the 1995 M_W 8.0 Antofagasta earthquake (Klotz et al., 2001) and SAGA96-97 campaign (Khazaradze & Klotz, 2003); KEN01 – CAP and SNAPP networks north of 23°S (Kendrick et al., 2001; BRO03 – sites between 26° and 36°S (Brooks et al., 2003); CHL04 – sites between 18° and 24°S (Chlieh et al., 2004).

The velocity vectors point roughly parallel to the relative convergence direction of the Nazca and South America plates. The magnitude of velocity gradually decreases away from the trench (Figure 3.3).

Coastal GPS sites located in the southern Chilean study area show present day velocities of 40±10 mm/yr in the direction N80°-90°E. This velocity decreases to about 20-25 mm/yr towards the Andes (Ruegg et al., 2002). These results are interpreted as reflecting interseismic strain accumulation above the Nazca-South America subduction zone due to the locked thrust zone extending down to about 60 km depth (Ruegg et al., 2002). The velocity vectors point roughly parallel to the relative convergence direction of the Nazca plate and their magnitudes rapidly decrease away from the trench towards the Andes (Figure 3.4). Even though the data shown in Figure 3.4 supports the assumption of fore-arc sliver motion, additional data are needed to constrain fore-arc sliver motion more precisely. Compared to the northern Chilean study area the southern Chilean study area exhibits more pronounced partitioning of deformation along the LOFZ.
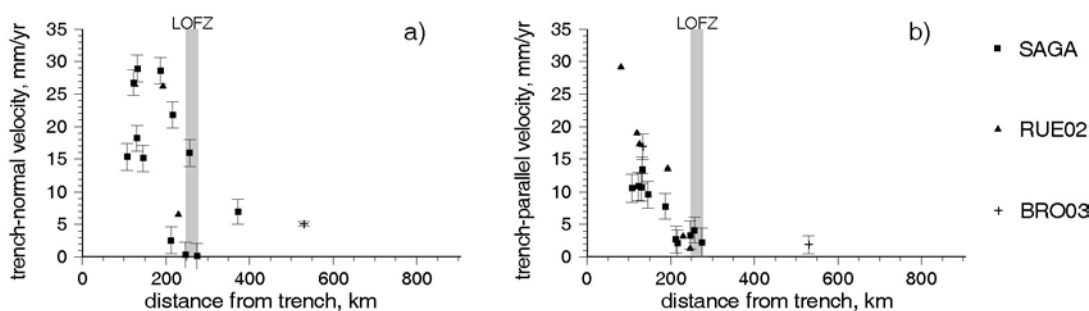

Figure 3.4: GPS data along the Chilean margin between 36° and 44°S shown in a margin-normal profile (modified after Hoffmann-Rothe et al., 2006): trench normal velocity component (a) and trench parallel velocity component (b). Included campaigns: SAGA – SAGA94–96 campaign excluding co – and post –seismic vectors of the 1995 M_W 8.0 Antofagasta earthquake (Klotz et al., 2001) and SAGA96-97 campaign (Khazaradze & Klotz, 2003); RUE02 – sites between 35° and 37°S (Ruegg et al., 2002); BRO03 – sites between 26° and 36°S (Brooks et al., 2003).

Seismic velocity models

The ANCORP'96 (Andean Continental Research Project 1996) experiment provides a seismic velocity model at a profile across the central Andes at 21°S (Figure 3.1, ANCORP Working Group, 2003). The ANCORP experiment observed the subduction of the Nazca plate under the South American continent along a 400 km long seismic reflection profile including integrated geophysical experiments. The onshore reflection and wide-angle ANCORP line continued the previously acquired offshore reflection data of the CINCA'95 project (Figure

3.1, Patzwahl et al., 1999, CINCA Working Group, 1997). Figure 3.5 shows that the v_P velocity in the fore-arc region (71°W – 69°W) down to 30 km depth varies between 3.6 km/s and 6.4 km/s, though the main part of the area is characterized by a velocity of about 6.0 km/s.
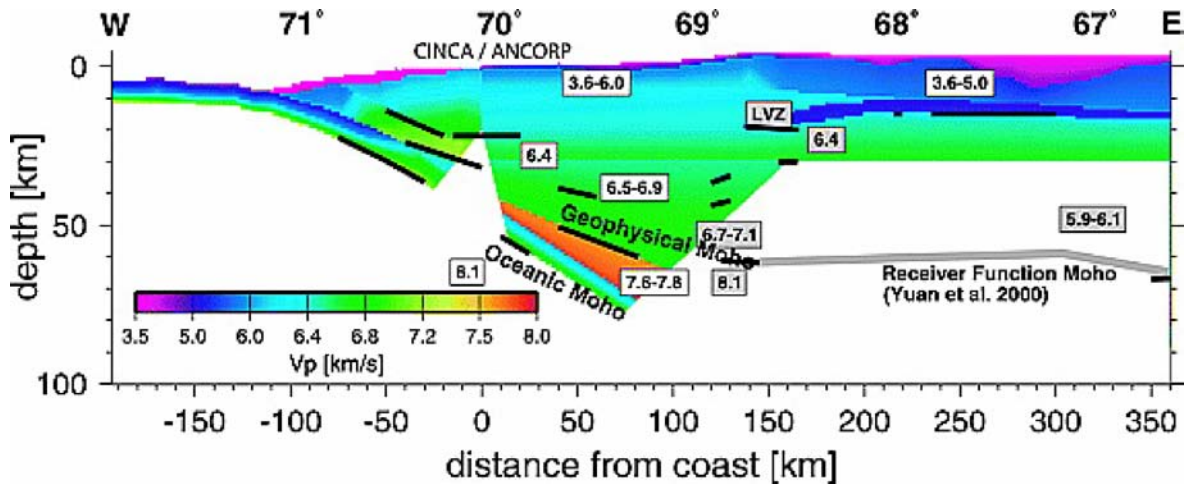

Figure 3.5: Velocity model along 21°S obtained by the ANCORP'96 onshore and CINCA'95 offshore experiments (ANCORP Working Group, 2003).

The ISSA 2000 (Integrated Seismological experiment in the Southern Andes) experiment provides a seismic velocity model across the southern Andes at 39°S (Figure 3.2, Lüth et al., 2003, Bohm et al., 2002). Figure 3.6 shows the v_P velocities in the fore-arc region (73.5°W – 72°W) at 39°S with average values of 6.2 km/s for the upper crust, and 6.6 km/s to 6.9 km/s for the lower crust.
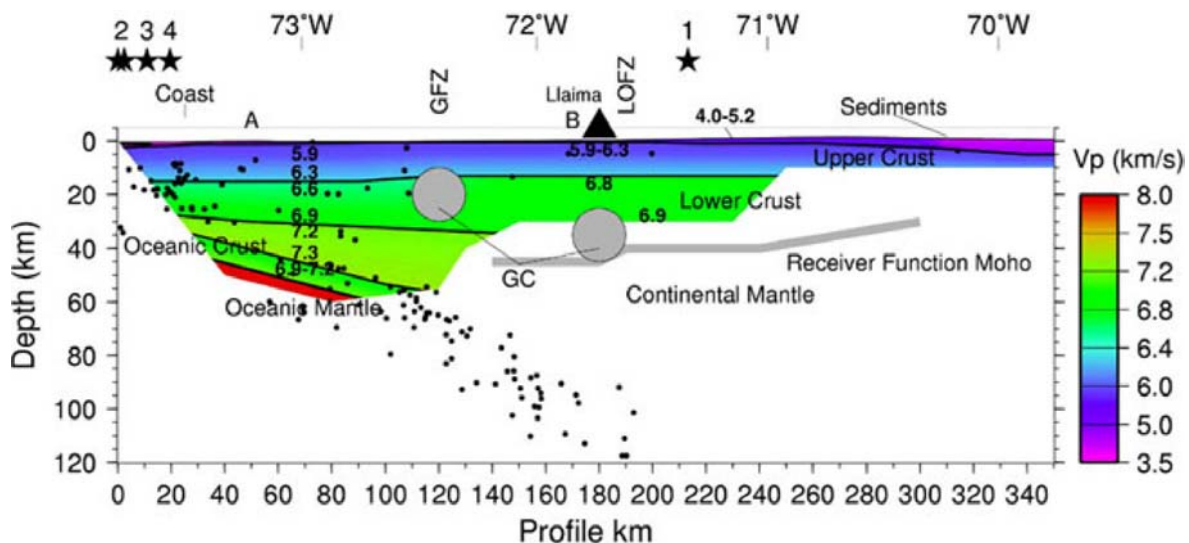

Figure 3.6: Velocity model at 39°S obtained by the ISSA 2000 experiment (Lüth et al., 2003). The gray circular patches indicate locations of good electrical (GC) conductors according to Brasse & Soyer (2001). Black dots indicate the earthquake hypocenters located from the ISSA 2000 passive seismological experiment (Bohm et al., 2002).

In the southern region a 2nd velocity model along the SPOC-south profile at 38.15°S is available. The SPOC (Subduction Processes Off Chile) experiment includes three seismic profiles between 36°S and 39°S, but only the SPOC-south profile has an offshore extension, where the part of the fore-arc beneath the sea level can be investigated (Krawczyk et al., 2003, Lüth et al., 2004). The SPOC experiments were focused on the investigation of the fore-arc and the seismogenic coupling zone. Figure 3.7 shows the profile at 38.15°S, where the v_P velocity in the fore-arc region (74.5°W – 73°W) down to 30 km depth varies between 3.5 km/s and 7.0 km/s.
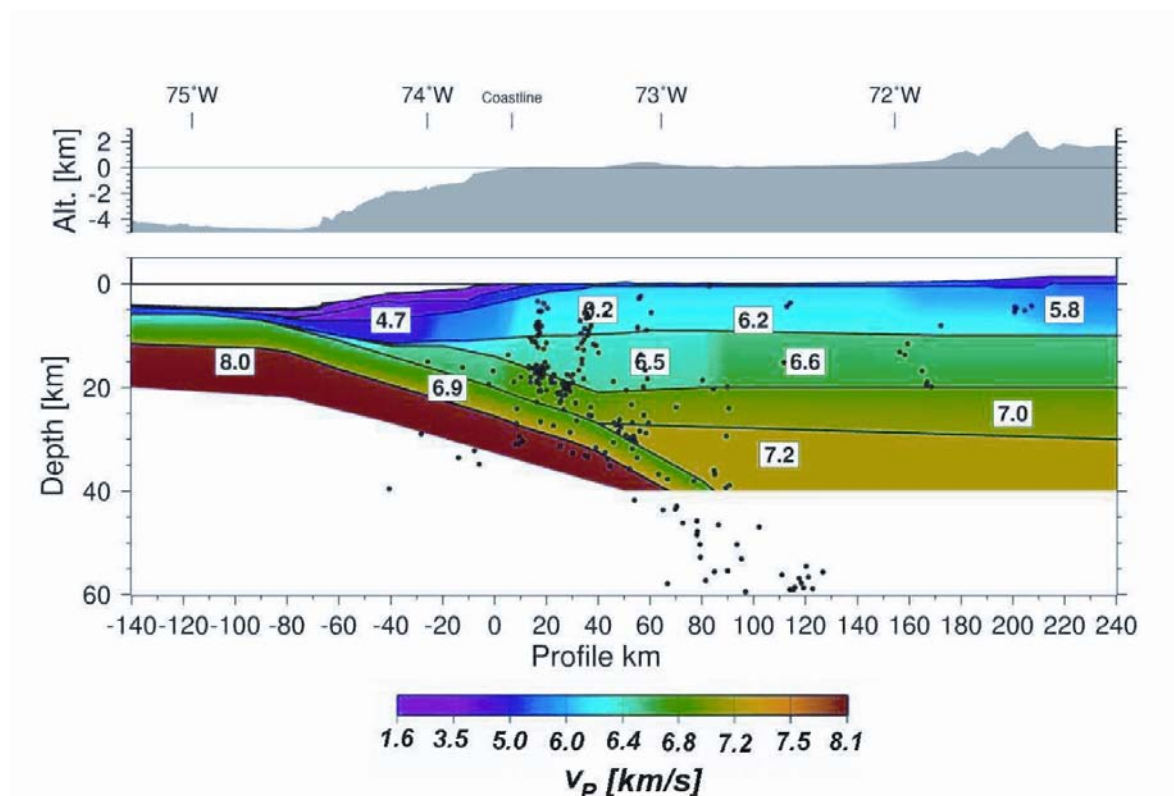

Figure 3.7: Velocity model at 38.15°S obtained by the SPOC experiment (Lüth et al., 2004). Black dots show earthquake hypocenters of seismicity recorded by the ISSA 2000 local network (Bohm et al., 2002).

Seismicity

About 90 % of the global earthquake activity occurs at convergent continental margins. And almost all earthquakes with magnitudes > 8 are strongly related to the subduction process. Most of the large subduction earthquakes are accommodated in the upper part of the plate interface between approximately 10 and 60 km depth. This upper part is also called the seismogenic zone and is characterized by a coupling between the subducting and overriding plate, which is assumed to be stronger than anywhere else along the plate interface.

The change in seismic behavior (the lower limit of the seismogenic zone) along the plate interface can be seen in Figure 3.8a, the depth distribution of the seismic activity shows a change in character at ~50 km depth from tightly clustered events to a more diffuse and sparse distribution below 50 km (Figure 3.8a, Patzig, 2000, Sobesiak, 2004).
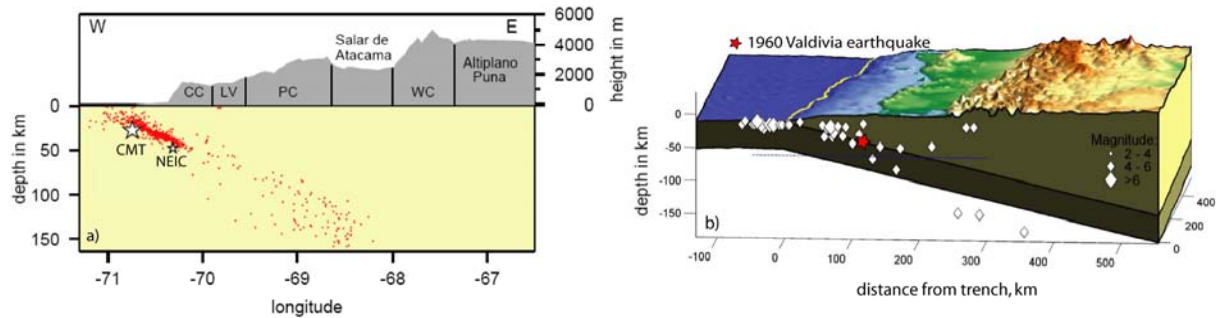

Figure 3.8. Depth and position of seismic events extracted for the northern (a) and southern (b) segments. (a) Seismic activity in the Antofagasta (~23.7°S) region, recorded in the framework of the CINCA '95 experiment; asterisks show locations of the hypocenters of the M_w=8.0 1995 Antofagasta earthquake (CMT – Harvard CMT Earthquake catalogue http://www.seismology.harvard.edu/CMTsearch.html, NEIC – USGS National Earthquake Information Center http://neic.usgs.gov/neis/epic/epic_rect.html); CC – Costal Cordillera, LV – Longitudinal Valley, PC – Precordillera, WC – Western Cordillera (modified after Sobesiak, 2004). (b) Seismic activity of the southern segment (37° - 42°S), data extracted from the Harvard CMT Earthquake catalogue. The red asterisk marks the location of the 1960 Valdivia earthquake suggested by Krawczyk et al., 2003.

The northern Chilean study area has a history of very large earthquakes. The Iquique event, believed to have magnitude of M_W=9.0 (Kelleher, 1972), happened in the area around Iquique in 1877. The assumed rupture plane reaches from 19°S to 23°S along the Chilean margin. Since the Iquique event in 1877 no very large earthquake has occurred in this region. Assuming a seismic cycle (reoccurrence time of very large earthquakes) of 100 to 120 years in this region (Comte et al., 1994), the Iquique fault plane area of 1877 can be defined as a seismic gap and therefore has a high hazard potential.

A recent major subduction zone earthquake in northern Chile, the M_W=8.0 Antofagasta event, occurred on the 30th of July, 1995. It covers a rupture plane, which stretches from 23°S, directly south of the 1877 Iquique rupture plane, to about 24.8°S along the Chilean margin. This earthquake is of particular importance, because it happened during the initial phase of the SFB 267 active field program, when several field campaigns including CINCA'95 were active. Immediately after the earthquake on the 30th of July 1995 the principle aim of the CINCA'95 project was changed from the investigation of the continental margin of northern Chile to the establishment of a temporary network to register the aftershock sequence of the 1995 Antofagasta earthquake. The CINCA'95 network recorded approximately 15000 events

with a daily average of 200 to 300 events (Patzig, 2000, Sobesiak, 2004). The aftershock sequence is shown in Figure 3.8a down to a depth of ~ 50 km.

In the southern Chilean study area the largest earthquake ever recorded with a moment magnitude of M_W=9.5 occurred in the area of Valdivia in 1960 (Figure 3.8b). The rupture plane has an estimated length of ~1000 km, starting at 38°S and extending to the south (Kelleher, 1972, Cifuentes, 1989). This devastating earthquake destroyed the city of Valdivia and caused damage from Conceptión to Puerto Montt.

One of the most destructive earthquakes ever occurred, the 1939 event in the area of the city Chillán, had an estimated magnitude of M_S=7.8 (Beck et al., 1998). The rupture plane starts directly at the northern border of the Valdivia rupture plane and extends ~ 250 km to the north. The event occurred at a depth of about 90 km and was an intraplate normal-faulting event (Campos & Kausel, 1990). There is an uncertainty in the mechanism of the 1939 Chillán event, however, the interpretation of an intraplate event rises the assumption of a seismic gap (for subduction zone earthquakes) north of the Vadivia rupture plane (Beck et al., 1998).

Density models

The density models have been created by C. Prezzi, A. Kirchner, and Z. Tašárová using the interactive modeling tool IGMAS (Interactive Gravity and Magnetics Application System), which provides a wide range of GIS (Geographical Information System) functions in a 3D space to integrate geophysical models, information, and data from both geophysics and geology (Schmidt 1996, Schmidt & Götze 1999). Even though the density models depend crucially on the initial configuration of bodies with certain densities, successful comparison of those models with observations gives confidence in a correct estimation of an average density. Density models created by C. Prezzi and A. Kirchner for the central Andes, and by Z. Tašárová for the southern Andes were used to constrain the numerical models (Prezzi et al., 2005, Kirchner 1997, Tašárová 2004).
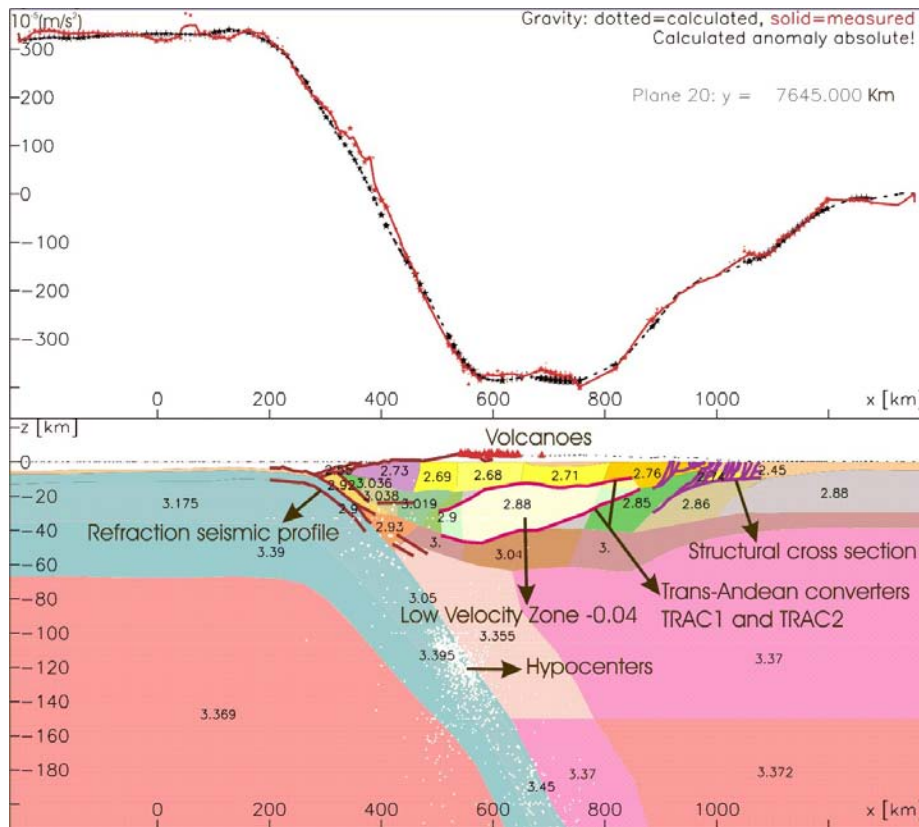
Figure 3.9: Model of Prezzi et al. (2005): density distribution along 21.3°S (bottom panel) and comparison between calculated and measured Bouguer anomaly (upper panel). Good correlation between two lines on the upper panel indicates reliability of the resolved density structure.

The density model of the continental crust along a profile at 21.3°S (Figure 3.9) is divided into many blocks of different densities varying from 2450 kg/m³ to 3040 kg/m³. The degree of accuracy of the density model is given by the fit of the calculated and measured Bouguer anomaly (Figure 3.9 top panel). Similar to the northern area, the crust of the southern area is divided into many density blocks. Figure 3.10 shows a density model designed to be representative for the entire southern study area (36° - 42°S). The density modeling of the southern area performed by Tašárová (2004) shows densities of the continental crust varying between 2650 kg/m³ and 3300 kg/m³. The area of the fore-arc is characterized by an average density of 2850 kg/m³.
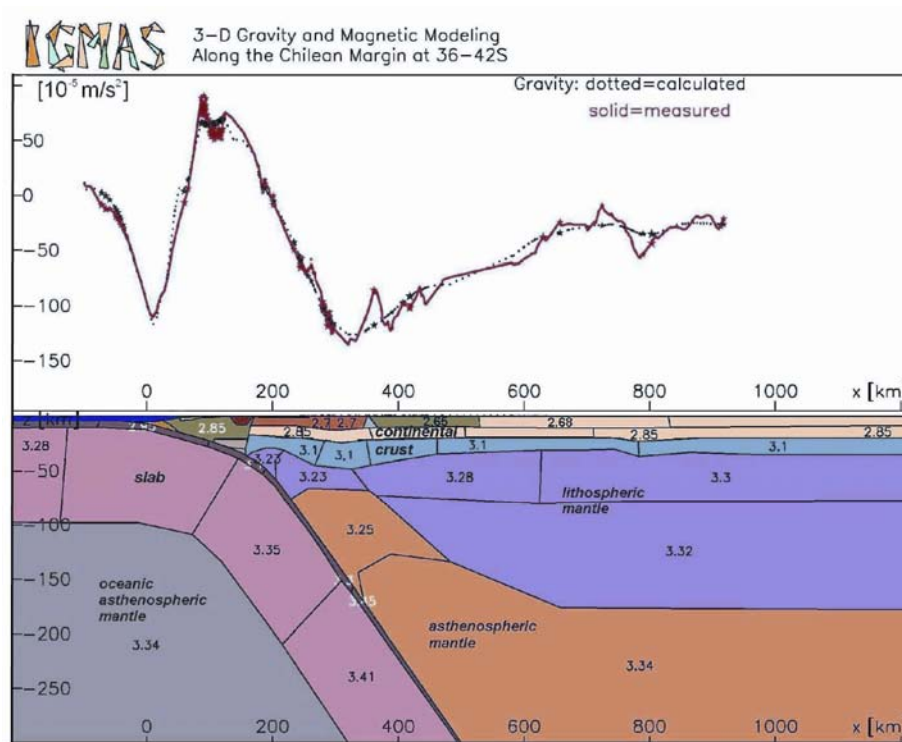
Figure 3.10: Representative gravity model for the southern Chilean margin at 36°S to 42°S (Tašárová, 2004): density distribution model (bottom panel) and comparison between measured (solid line) and calculated (dashed line) gravity anomalies (upper panel).

The density models presented above show that density of the fore-arc wedge material may vary; however, these variations are not critical and I do not expect that these variations may cause significant (first order) effects on the pattern of deformation. Only for very special conditions can density variation be relevant (e.g. to initiate the generation of cold plumes along the subducting slab as described by Gerya & Yuen, 2003). For the sake of simplicity, the numerical model of my study uses a simple one-layer wedge with a uniform density of 2800 kg/m³.

4 Analysis of the thermal structure of the Chilean subduction zone

The thermal structure of subduction zones plays an important role in understanding tectonic processes related to active subduction. To study these processes the thermal structure has to be taken into account, because the physical properties (e.g., density, thermal conductivity, specific heat, radiogenic heat generation, viscosity) are crucially depending on temperature. Several studies have shown that the updip (d_{up}) and downdip (d_{down}) limits of rupture in great subduction thrust earthquakes may be thermally controlled (e.g., Tichelaar & Ruff, 1991, Hyndman & Wang, 1993, Tichelaar & Ruff, 1993, Hyndman et al., 1997, Oleskevich et al., 1999, Moore & Saffer, 2001, Saffer & Marone, 2003). The updip and downdip limits enclose the coupled / seismogenic zone, whereas the areas above and below are characterized by stable sliding. The petrological definition of the coupled zone is based on the thermal structure along the plate interface. The updip limit is assumed to be associated with the temperature of 100° – 150°C, over which the transition of smectite to chlorite occurs (e.g., Hyndman et al., 1997). The downdip limit is assumed to be associated with a critical temperature of ~350°C, which marks the transition between stick slip and stable sliding for quartzo-feldspatic crustal rocks (e.g., Tse & Rice, 1986, Blanpied et al., 1991, 1995). A series of numerical experiments in this chapter investigating the thermal structure along the plate interface for both Chilean study areas were performed. The main aim of this series was to find the most realistic distribution of temperature along the interface between the plates. The thermal structure around the plate interface reveals the limits of coupling but also the type of transition (gradual or sharp) at the updip and downdip limits. The results of the thermal model series will help to constrain the spatial extent of the coupling zone (expressed by frictional contact) and the type of transition at the updip and downdip limit of the coupling zone (expressed by a gradual or sharp increase/decrease of friction).

4.1   The thermal model setup

Figure 4.1 presents a general view on the thermal model setup. The model assumes a thermal steady state. The dimensions of the models are 200 km depth by 940 km width for the northern geometry and 200 km depth by 840 km width for the southern geometry, respectively. The upper surface was set to have 0°C temperature.
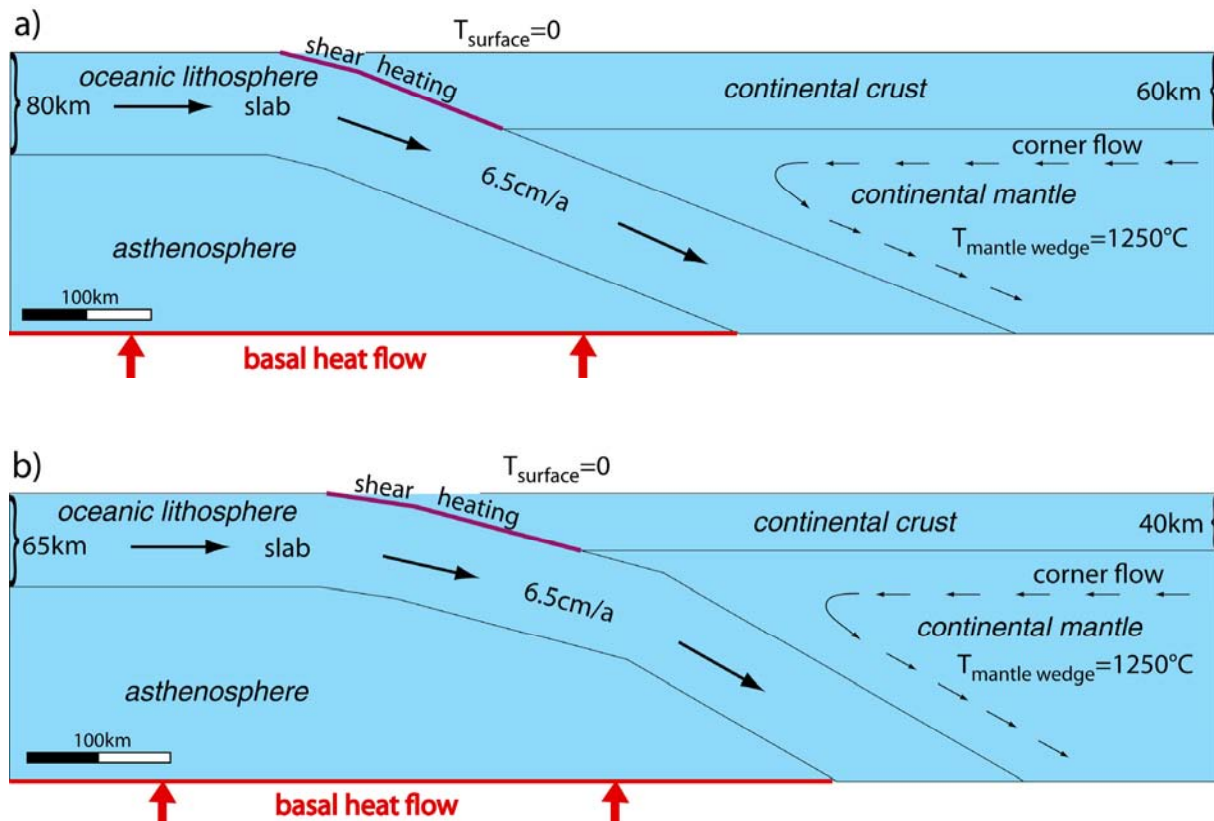

Figure 4.1: Geometry and boundary conditions for the thermal models for the northern (a) and southern (b) study area.

The boundary conditions of the model include zero heat fluxes along the lateral boundaries. The heat flow along the bottom of the model depends on the age of the incoming oceanic plate (Figure 4.3) and it is inversely proportional to the thickness of the oceanic lithosphere. The thickness of the oceanic lithosphere can be approximated by (Turcotte and Schubert, 2002):

$$y_L = 2.32\sqrt{\kappa t} \qquad\qquad (4.1)$$

where y_L is the thickness of the oceanic lithosphere in kilometers, t is the age of oceanic lithosphere, $\kappa = k/\rho c$ is the thermal diffusivity, c is the specific heat, ρ is the density, and k is the thermal conductivity. Figure 4.3 presents the age of oceanic lithosphere along the

western coast of South America. The basal heat flow decreases from 45 mW/m² on the left hand side of the model to 35 mW/m² next to the slab for the northern study area and from 50 mW/m² to 40 mW/m² for the southern study area. These basal heat flow values are somewhat lower than suggested by Stein & Stein (1994) and Stein (2003) (Figure 4.2) in order to get conservative estimations of the temperature distribution in the system.
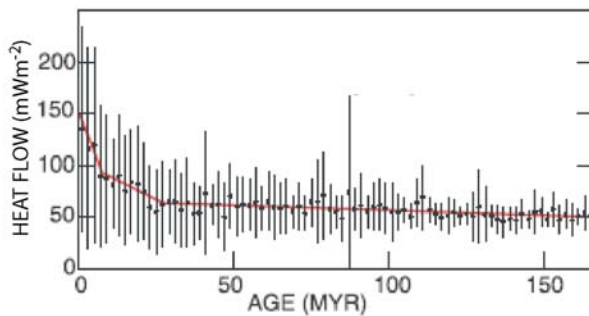

Figure 4.2: Measured heat flow means and standard deviations with oceanic crustal age; the red line represents the linear fit to the average heat flow from Stein & Stein (1994).

The thermal model accounts for mass flux in the system. That includes the motion of the subducting slab and the corner flow beneath the continental crust and above the subducting slab. The subducting slab goes down with a rate of 6.5 cm/yr, which corresponds to the convergence rate of the Nazca plate (e.g., Norabuena et al., 1998, Angermann et al., 1999, Klotz et al., 1999, Norabuena et al., 1999). The corner flow circulates counterclockwise with a rate of 3 cm/yr, an average velocity between the slab velocity and zero velocity in the center of the mantle wedge (Turcotte & Schubert, 2002). The mantle wedge enclosed by the corner flow was set to have a temperature of 1250°C. At that temperature asthenosphere becomes highly mobile and can not withstand high temperature gradients (e.g., Green et al., 2001).

Table 4.1: *Material parameters used in the thermal models for the five different units.*

	density [kg/m³]	conductivity [W/mK]	heat capacity [J/kgK]	heat generation [mW/m²]
cont. crust	2800	2.5	1000	$4.5e^{-z/3.5}$
cont. mantle	3200	5.0	1000	—
slab	3300	2.5	1000	—
asthenosphere	3300	f(T) 5…20	1000	—

Radiogenic heat generation *A* is applied to the continental crust using an exponential depth dependence (Turcotte & Schubert, 2002):

$$A(z) = 4.5e^{-z/3.5} \tag{4.2}$$

where *A(z)* is in mW/m² and *z* is depth in km.
In Table 4.1 all material parameters and reference values are listed which were used in the thermal models.
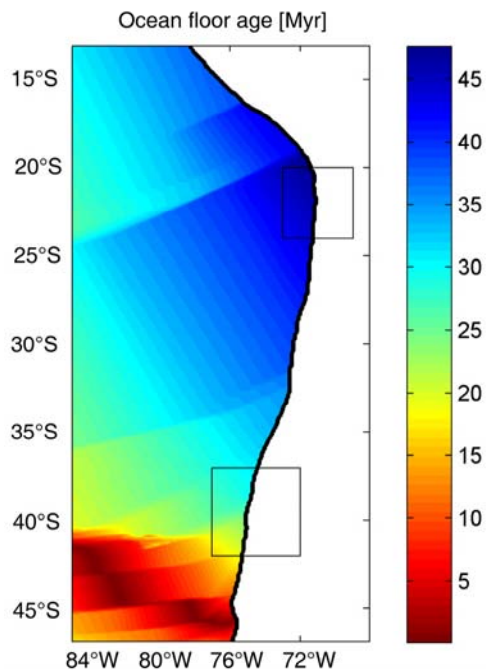

Figure 4.3: Age of ocean floor in Myr (Smith & Sandwell, 1997). Areas of interest, the northern and southern study area, are outlined by rectangles.

Fore-arc heat flow measurements are usually greater than predicted by simple conduction-advection models of subducting lithosphere requiring a contribution to surface heat flow from shear heating, radiogenic heat production, fluid advection, or the thermal effects of fore-arc deformation (Molnar & England, 1990, Tichelaar & Ruff, 1993, Peacock, 1996). The subduction of cool oceanic lithosphere exerts a primary control on the thermal structure of subduction zones by depressing the isotherms in the region of the subducting slab. Temperatures in a subduction shear zone reflect a trade-off between heating (from different possible sources mentioned above) and advective cooling from the subduction of cold oceanic lithosphere, which increase and decrease temperatures, respectively (Peacock, 1996). Considering the above mentioned different sources of heat production in the fore-arc of a subduction zone, the heat generated by shear heating plays an important role in the thermal structure (e.g., Dumitru, 1991). It is known that an essential amount of heating in a subduction zone is generated by shear heating (e.g. Molnar & England, 1990, Peacock, 1992, Tichelaar &

Ruff, 1993, Peacock, 1996, Scholz, 2002). The rate of shear heating Q_{sh} may be estimated (Turcotte & Schubert, 2002):

$$Q_{sh} = \tau v \qquad\qquad (4.3)$$

where τ is the shear stress and v is the convergence rate. For average shear stresses of ~ 20 MPa advective cooling and shear heating are approximately balanced for plate convergence rates of 10 – 100 mm/yr (Peacock, 1996). If shear stresses are < 20 MPa, then faster convergence rates lead to cooler subduction shear zone temperatures; if shear stresses are > 20 MPa, then faster convergence rates lead to warmer shear zone temperatures (Peacock, 1996). Based on heat flow measurements shear stresses in the range of 0 to 100 MPa (constant and depth dependent shear stresses) have been calculated (Molnar & England, 1990, Peacock, 1992, Tichelaar & Ruff, 1993, Peacock, 1996). Tichelaar & Ruff (1993) found shear stresses of 14 to 27 MPa for nine subduction zones using different radiogenic heat production models. Molnar & England (1990) calculated shear stresses of 55 to 84 MPa for two subduction zones, but did not take into account radiogenic heat production. Peacock (1992) used low temperatures recorded by blueschist-facies metamorphic rocks to calculate shear stresses of 0 to 100 MPa.

Using the knowledge about the depth extend (down to ~ 36 to 53 km) of the seismogenic zone due to recorded seismic events in the upper WBZ (Tichelaar & Ruff, 1993, Sobesiak, 2004) and the temperature constraint (the 350°C isotherm) for the lower limit of the seismogenic zone (Hyndman et al. 1997) numerical models were created to find appropriate values of shear stresses for the northern and southern study area. For the southern study area the depth extent of the seismogenic zone can be further constraint by the relocation of the 1960 Valdivia earthquake in the range of ~36 to 45 km (Krawczyk et al., 2003). The relocation of the 1960 Valdivia earthquake assumes a nucleation point at the downdip limit of the seismogenic zone (Krawczyk et al., 2003). In Table 4.2 the shear stresses together with the corresponding shear heating rates are listed. Constant shear stresses were assumed. The shear heating is applied along the plate interface from the trench down to the juncture slab - continental crust - mantle wedge (Figure 4.1).

The results of thermal models were obtained using ABAQUS (ABAQUS User's Manual, 2004). The finite-elements are linear quadrilateral elements with an average size of 3 by 3 km.

Table 4.2: *Rates of shear heating Q_{sh} applied to the thermal models for five different shear stresses τ and a constant convergence rate v=6.5 cm/yr.*

τ [MPa]	v [cm/yr]	Q_{sh} [mW/m²]
0	6.5	0
10	6.5	20.63
33	6.5	68.10
67	6.5	138.25
100	6.5	206.35

4.2 The thermal model results

The thermal models for the northern study area show that without shear heating (τ=0) the depth of the 350°C isotherm is far too deep (d_{down}~72 km) along the plate interface (Figure 4.4, Figure 4.6a). Even with shear heating rates for a corresponding shear stress of 33 MPa the 350°C isotherm cuts the plate interface at d_{down}~63 km (Figure 4.6a). To reach a depth of d_{down}~36 to 53 km for the 350°C isotherm along the plate interface corresponding shear stresses have to be $33 < \tau < 67$ MPa on average. The depths extend of ~36 to 53 km for the seismogenic zone corresponds to a coupling width W_f starting at the trench to 120 to 165 km along the plate interface (Figure 4.4).

Figure 4.4: Thermal model result for the northern study area without shear heating τ=0. The area of the potential seismogenic zone is zoomed (bottom panel), and in the area the coupling width W_f is plotted as red line, the transitional areas at the updip (100°C-150°C) and downdip (350°C-450°C) limit of the coupling zone are shown dashed.

The thermal models for the southern study area show different results compared to the north. The shallower corner flow causes that even the model without shear heating cuts the 350°C isotherm in the depth range between 36 and 45 km (Figure 4.5, Figure 4.6b). To fit the 350°C isotherm into the given depth range along the plate interface the shear stresses have to be $\tau < 67$ MPa on average (Figure 4.5, Figure 4.6b). The depths extend of ~36 to 45 km for the seismogenic zone corresponds to a coupling width W_f starting at the trench to 165 to 220 km along the plate interface.
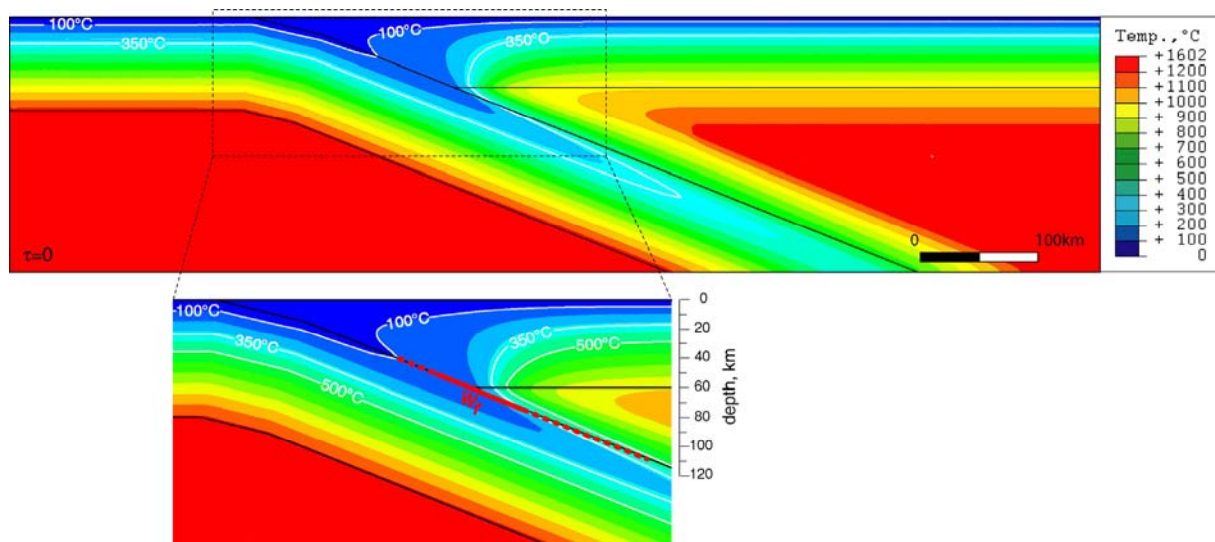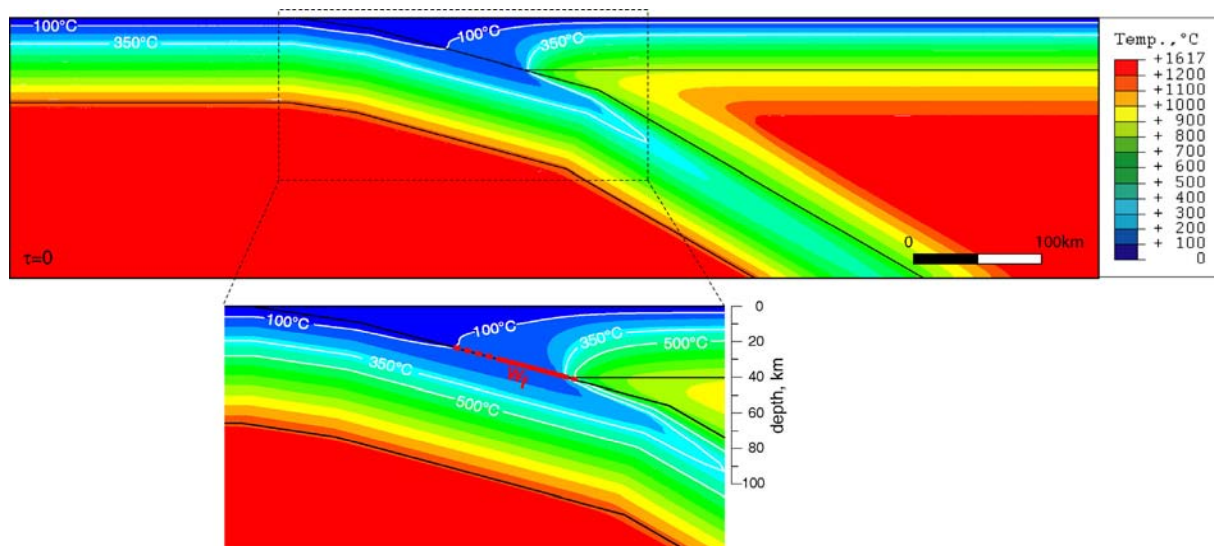

Figure 4.5: Thermal model result for the southern study area without shear heating $\tau = 0$. The area of the potential seismogenic zone is zoomed (bottom panel), and in the area the coupling width W_f is plotted as red line, the transitional areas at the updip (100°C-150°C) and downdip (350°C-450°C) limit of the coupling zone are shown dashed.

As discussed before, shear heating plays an important role in the thermal structure of a subduction zone (e.g. Molnar & England, 1990, Dumitru, 1991, Peacock, 1992, Hyndman & Wang, 1993, Tichelaar & Ruff, 1993, Peacock, 1996, Scholz, 2002). The results of the thermal models shown in Figure 4.4 and Figure 4.5, call for additional heating in order to adjust the depth extent of the seismogenic zone.

A series of thermal models with five different shear stresses applied at the plate interface has been calculated for the northern (Figure 4.6a) and the southern study area (Figure 4.6b). The results are presented as a temperature distribution along the plate interfaces. The results show that shear heating may dramatically change the thermal situation in the crust.
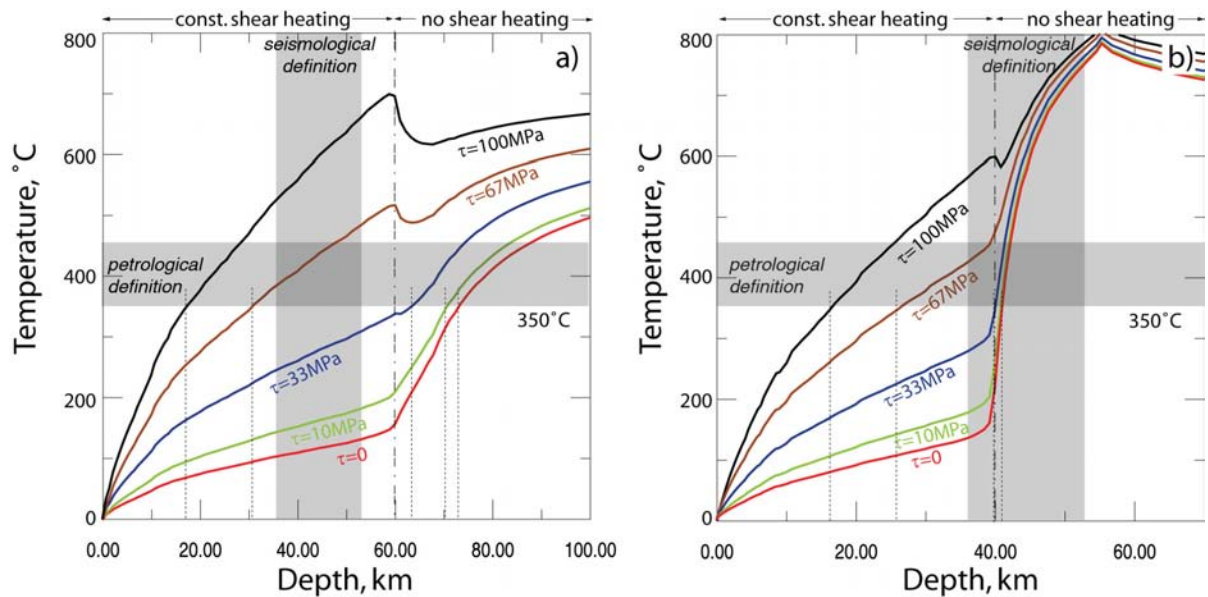
Figure 4.6: Thermal model results for the northern (a) and southern (b) study area. Temperature distribution along the boundary between the plates from the trench downwards. In both study areas five different shear stresses τ were applied. Dashed lines indicate where the 350°C isotherm cuts the plate interface. Vertical dash-dot line indicates the thickness of the continental crust. Grey shaded rectangles show the lower limits of the seismogenic zone for the petrological and seismological definitions, respectively; overlapping areas indicate realistic shear stresses τ needed to fit the supposed depth extent. The change in temperature at ~ 55 km depth in (b) is due to the change of slab geometry (slab dip, see Figure 4.5).

The turning point of these profiles for both, northern and southern regions is the point of triple junction of crust-slab-mantle (indicated by dash-dot line on Figure 4.6, at the depth of 60 and 40 km respectively). This point divides the profiles in shear heating dominating region (above) and mantle corner flow dominating regions (below). The high shear heating may result in temperatures at the base of the crust higher than at the top of lithospheric mantle beneath the Moho (see the local decrease in temperature at the vicinity of dash-dot lines for τ=100 MPa for both, northern and southern regions).

The differences between the two study areas are mainly due to different geometries. The thickness of the continental crust (60 km for the northern and 40 km for the southern study area) influences the thermal structure most, because the high temperature from the mantle wedge reaches a much shallower depth in the southern area compared to the northern area, which results in higher temperatures at shallower depths.

The results for both study areas show high thermal gradients in the vicinity of the triple point slab – continental crust – mantle wedge. This favours the assumption of a sharp transition between the downdip limit of the coupled zone and the interface below.

The thermal models for both study areas induce to query the thermally defined updip limit (~100 – 150°C, Hyndman et al., 1997) of the seismogenic zone. Taking into account reasonable shear stresses to match the downdip limit of the seismogenic zone, the 100 - 150°C isotherms cut the temperature path along the plate interface below 10 km depth Figure 4.6). Only with very high shear stresses shallower depths can be reached for these temperatures.

Hoffmann-Rothe et al. (2006) calculated the width W_f of the coupling zone using the analytical solution of Wang & He (1999). Starting at the depth of 10 km down to 50 km they calculated a coupling width W_f for the northern segment of 124 km and for the southern segment of 167 km. Considering a depth extend of the coupling zone of d_{down}~40 km these coupling widths W_f correspond to the lower limits of the coupling widths extracted from the thermal models of my study.

The shear stresses resulting from the thermal models allow estimating the coefficients of basal friction μ_b using the static friction law $\tau = C + \mu_b \sigma_n$, where τ is the shear stress, C is the cohesion, and σ_n is the normal stress. Assuming a constant shear stress along the plate interface of 67 MPa, which represents the upper bound of reasonable shear stresses, an average basal friction of $\mu_{b,north}$=0.10 for the northern study area and $\mu_{b,south}$=0.15 for the southern area is calculated. The thermal models assume a thermal steady state. The thermal relaxation time on crustal scale is supposed to be 15 to 30 Myr (Turcotte & Schubert, 2002).

4.3   Comparison with existing models

Here I compare my thermal model results with the model results of Oleskevich et al. (1999) and Springer (1999). Oleskevich et al. (1999) calculated 2D crossectional thermal models for five different profiles along the Chilean margin using the finite element technique. I choose two profiles presented in Oleskevich et al. (1999) to compare with results of my calculations: one profile from north Chile (along 21°S, Figure 4.7b) and one profile from south Chile (along 44°S, Figure 4.7e). The models include radiogenic heat generation in the continental crust, advective heat transport of the subducting oceanic plate, and the top and bottom boundaries are fixed at 0°C and 1400°C; frictional heating is applied at the shallow part of the interface with effective coefficients of friction less than 0.05; advection in the continental mantle (corner flow) is neglected (Oleskevich et al., 1999, Wang, pers.comm.).

Springer (1999) calculated three different finite element thermal models along a profile across the central Andes at about 21°S. For the comparison only the 2D subduction model covering the fore-arc region between the trench and the magmatic arc is of interest

(Figure 4.7c). The models include radiogenic heat generation in the continental crust, the oceanic crust, and the lithospheric mantle, advective heat transport of the subducting oceanic plate; the surface and base of the subducting slab are fixed at 0°C and 1250°C; below the continental crust a isothermal boundary condition of 1250°C is assumed; frictional heating is applied along the plate contact down to 125 km depth with a mean shear stress of 15 MPa; advection in the continental mantle (corner flow) is neglected (Springer, 1999).

The models of this study (Figure 4.7a,d) account for corner flow in the continental mantle, which is the main difference to the models of Oleskevich et al. (1999, Figure 4.7b,e) and Springer (1999, Figure 4.7c). The motion of the descending lithosphere (slab) induces mantle flow and drives a flow in the arc side corner (Turcotte & Schubert, 2002). This flow moves hot mantle material into the juncture slab–continental crust–mantle wedge and causes the depressed isotherms along the plate interface. In the models of Oleskevich et al. (1999) it is clearly visible, that without corner flow the temperatures above the plate interface are too low and are not as depressed as in the other models (Figure 4.7). Hence, the temperatures reached at 100 km depth along the plate interface are much too low (~300°C for north Chile and ~500°C for south Chile). The model of Springer (1999) prescribes a temperature of the continental mantle wedge of 1250°C, realised by an isothermal boundary condition at the bottom of the continental crust. With this constraint the thermal structure of the model is forced to result in depressed isotherms around the plate interface and temperatures at the plate interface in 100 km of 1250°C.

The Springer (1999) model also accounts for frictional heating at the plate interface, this explains the higher temperatures along the plate interface compared to the model in Figure 4.7a. However, considering the models of this study, which account for frictional heating at the plate interface shown in Figure 4.6, the Springer (1999) model fit into this model series. The comparison of the different thermal models exposes the importance of accounting for mantle wedge corner flow and confirms the reliability of my thermal models.
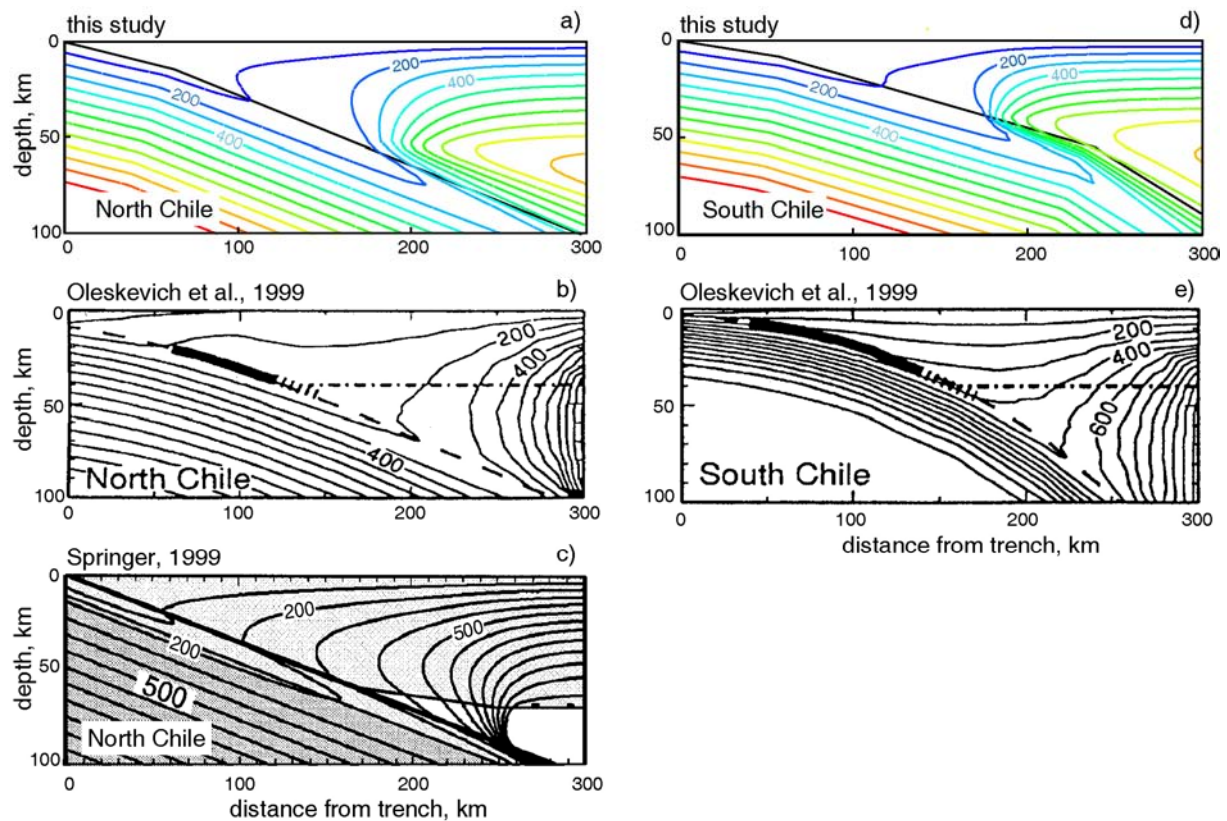
Figure 4.7: Cross sections showing isotherms (100°C intervals) for the 2D thermal models for north Chile (a,b,c) and south Chile (d,e). a) and d) are the results of this study (τ=0); black solid line indicates the plate interface. b) and e) are the results of Oleskevich et al. (1999); thick solid line marks the extent of inferred seismic behaviour; dashed line shows the plate interface; horizontal dash-dot line indicates the 40 km depth. c) is the result of Springer (1999) with a mean shear stress along the plate contact of 15 MPa.

5 Investigation of initial parameters of the model

The data presented in Section 3 is only a small portion of data regarding properties and evolution of the study areas (e.g., density, surface velocity, extent of the seismogenic zone, slab dip). Although the data is available in many different forms, putting the data into a numerical model requires additional analysis. A particular aim of this section is the choice of appropriate parameters representing the study areas out of sets of data points or profiles. This section converts the data available into the set of parameters which will be used to set up the 3D numerical experiments (Section 6). The parameters comprise topographic slope α, slab dip β, extent of coupling at the plate interface W_f, basal friction μ_b, and Young's modulus E. This section is especially important because subsequent numerical experiments are based on the simplified model. Thus, a limited number of parameters determined in this section will be used for the numerical experiments and should represent the study areas with the best possible accuracy, but still allow for efficient computing.
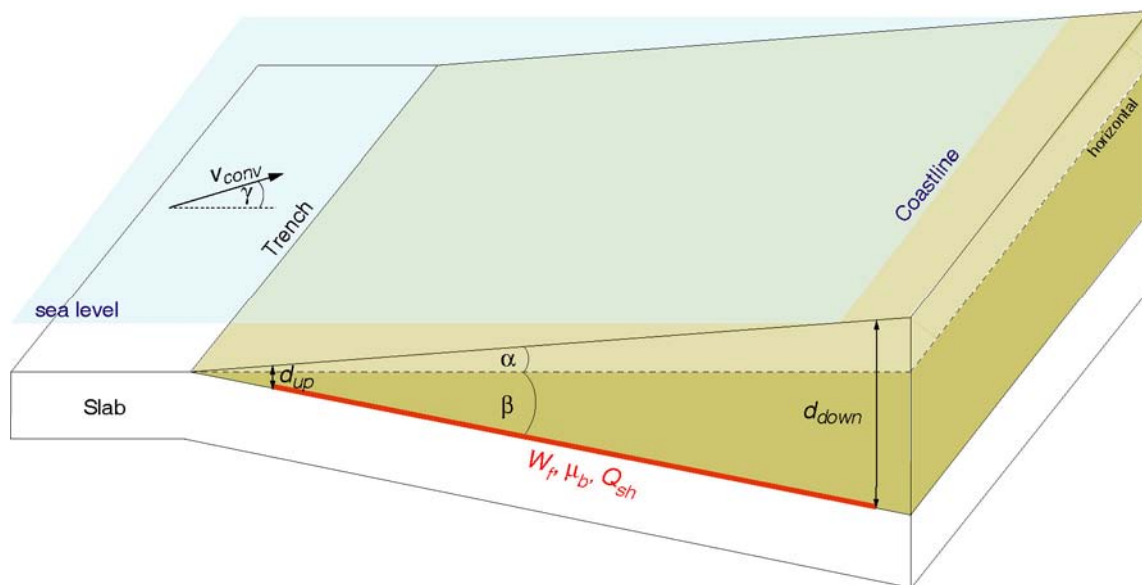
Figure 5.1: Schematic sketch of a subduction zone illustrating important parameters. α - average topographic slope, β - dip of the subducting slab, γ - obliquity of convergence, μ_b – coefficient of basal friction, d_{up} – updip depth of the frictionally coupled zone, d_{down} - downdip depth of the frictionally coupled zone, Q_{sh} – shear heating along the frictionally coupled zone, v_{conv} – convergence velocity of the subducting slab, W_f – width of the frictionally coupled zone

The parameters analysed in this chapter help to find appropriate values which reflect the properties of the Chilean fore-arc in terms of the geometry, the coupling between the two plates, and elastic material parameters. The topographic slope α and the slab dip β are analysed to constrain the numerical model geometrically (Figure 5.1). With respect to the coupling between the two plates the extent of coupling W_f and the frictional strength of coupling μ_b are investigated (Figure 5.1). The Young's modulus E as a rock specific material parameter is analysed to find characteristic values of E for the Chilean fore-arc.

5.1   Geometry of the fore-arc

The geometry of the fore-arc wedge plays an important role in the distribution of deformation. For the model I assume a simple wedge-type fore-arc that is defined using two parameters α and β that describe the average topographic slope and the slab dip, respectively.

The fore-arc topography of the northern study area is dominated onshore by the coastal cordillera with an average elevation of about 1000 m. In the southern study area the coastal cordillera has peaks with more than 1000 m height around 38°S near Nahuelbuta, but the average elevation of the coastal cordillera is only a few hundred meters. The depth of the trench differs between the two study areas by more than 3000 m. Figure 5.2 shows the average topography for both study areas and the model approximations. In the northern study area the topographic slope of the fore-arc wedge is assumed to be α =4° from the trench to 120 km east of it, further to the eastern boundary of the model the topographic slope is set to α =1° (Figure 5.2). In the southern study area a fore-arc slope of α =1° is assumed throughout the whole model.

The dip of the subducting slab varies significantly along strike and with depth (Isacks, 1988, Gutscher et al., 2000, Pardo et al., 2003, Yañez & Cembrano, 2004, Hoffmann-Rothe et al., 2006). The top of the downgoing plate can be imaged using depth solutions of subduction related seismicity and results of seismic experiments (seismic velocity models chapter 3.3). The vertical extend of the estimation of the slab dip β was focused on the depth extent of the seismogenic zone along the Chilean margin. The lower limit of the seismogenic zone coincides approximately with the 50 km contour line (Sobesiak, 2004). For simplification of the mechanical model I use only one slab dip β for the whole model, which represents the dip of the upper 50 km of the downgoing slab. Hoffmann-Rothe et al. (2006) compiled slab dips β for different depth extends along the Chilean margin. Based on this data an average slab dip

$\beta_{north}=18.4°$ for the northern study area and $\beta_{south}=13.4°$ for the southern study area was estimated.
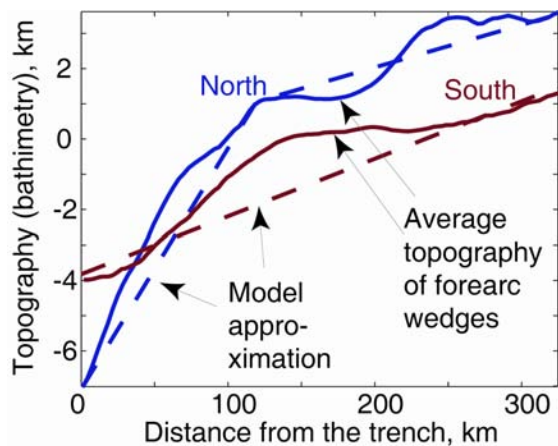

Figure 5.2: The solid lines indicate the average topography, blue – northern study area (20°-24°S), red – southern study area (37°-42°S) (topography/bathymetry from Smith & Sandwell, 1997). The dashed lines indicate the approximated topography for the 3D model for the northern (blue line) and southern (red line) study area.

5.2   Parameters controlling the extent of coupling zone

The coupling between the downgoing Nazca plate and the overriding South American plate plays a crucial role for the deformational pattern evolving at the surface of the continental fore-arc. The spatial extent of the coupled plate interface was identified differently in different studies:

1. The petrological definition of the coupling zone assumes that phase transitions of minerals control the updip and downdip limit of the coupling zone.

2. The seismological definition of the coupling zone assumes that the distribution of seismic events is controlled by strong coupling between the plates in the area of active subduction.

3. The geodetical definition of the coupling zone uses GPS data and elastic models to define areas of strong coupling.

The first definition is closely related to the thermal situation along the plate interface. The frictional strength reduces at certain depth due to thermally activated creep, when the material undergoes the brittle to ductile transition (Tichelaar & Ruff, 1991, Hyndman & Wang, 1993, Tichelaar & Ruff, 1993, Hyndman et al., 1997).

Hyndman et al. (1997) define the upper limit of strong coupling (and active seismicity) as controlled by the transition of smectite to illite and chlorite. This transition occurs between 100–150°C. However, this approach to define the updip limit is criticized in a series of studies (Moore & Saffer, 2001, Saffer & Marone, 2003, Schilling, personal communication). Clays,

such as smectite, usually represent a significant proportion of the incoming sediments that are accreted to subduction zone margins. However, the amount of smectite required to control the updip limit is not known (Hyndman et al. 1997). For sediment starved margins, like in the northern Chilean study area, the updip limit of the seismogenic zone can not be explained by this approach only (Moore & Saffer, 2001). Furthermore, in laboratory experiments illite shows velocity strengthening behaviour (stable sliding) under a wide range of conditions (Saffer & Marone, 2003). Mechanisms other than clay transformation may be more important in controlling the updip limit of the seismogenic zone, such as suggested by Saffer & Marone (2003): (1) shear localization and increased shear strain, (2) porosity reduction and increased consolidation state, (3) increasing effective stress due to increased total overburden and possibly variations in pore pressure, and (4) quartz cementation and pressure solution that may be associated with clay transformation.

For the downdip limit the critical transition is between velocity weakening (stick slip) to velocity strengthening (stable sliding) (Hyndman et al., 1997, Oleskevich et al., 1999, Scholz, 2002). Laboratory measurements on quartzo-feldspathic crustal rocks indicate for the transition of stick slip to stable sliding a critical temperature of ~350°C, for wet and dry conditions (Tse & Rice, 1986, Blanpied et al., 1991, 1995). This temperature corresponds well with that at the maximum depth of crustal earthquakes in continental areas globally (Brace & Byerlee, 1970, Chen & Molnar, 1983, Tse & Rice, 1986, Wong & Chapman, 1990, Hyndman & Wang, 1993, Hyndman et al., 1997, Oleskevich et al., 1999). The main factors that control the temperature at the plate interface are the thickness of insulating sediments on the incoming oceanic plate, the plate age and thus heat flow, age history, the convergence rate, and the plate/slab dip (Hyndman & Wang, 1993, Wang et al., 1995, Hyndman et al., 1997).

The second definition of the extent of the coupling between plates employs statistical analysis of seismic events to determine the strong coupling. Figure 3.8 (Section 3.3) presents seismic events plotted against depth and horizontal position. The events can be grouped in two main domains. The shallow tightly clustered events (10 – 60 km deep) are assumed to correspond to the strong coupling between plates (frictional instability), whereas deeper more diffuse and sparse distributed events are related to the Wadati-Benioff zone (WBZ), but can not be explained by any brittle or frictional processes due to the great pressure at these depths (Scholz, 2002).

The third definition of coupling is well illustrated by the work of Khazaradze and Klotz (2003). The authors put GPS data along the entire west margin of South America and

the geometry of the subducting slab into a 3D elastic dislocation model to find the distribution of two parameters, the area of total and partial coupling between plates. The best fit of the model to observations (GPS data) gives the width and depth extent of the coupling zone.

The three definitions of the coupling zone presented above use different approaches and result in different extents of the coupling zone. In order to choose the most realistic width and depth extent of the coupling zone for the 3D model (Section 6), the results of the numerical experiments of section 4 were used. The main question of this series was to find the distribution of temperature along the interface between plates. The thermal structure around the plate interface reveals the width of the coupling zone (using the petrological definition) but also the type of transition (gradual or sharp) at the updip and downdip limit of the coupling zone. The results of the thermal model series will be transferred to the 3D mechanical model in section 6 to constrain the spatial extent of the coupling zone (expressed by frictional contact) and the type of transition at the updip and downdip limit of the coupling zone (expressed by a gradual or sharp increase/decrease of friction).

The thermal models for the northern study area require the application of shear heating along the plate interface, otherwise the modelled depth of the 350°C isotherm as downdip limit is far too deep (d_{down}~72 km) compared to other observations. With shear stresses of $33 < \tau < 67$ MPa applied along the plate interface the downdip limit of the coupled zone reaches a depth extent of d_{down}~36 to 53 km for the 350°C isotherm. The depths extend of ~36 to 53 km for the seismogenic zone corresponds to a coupling width W_f starting at the trench to 120 to 165 km along the plate interface, which is in good agreement with the coupling width published by Hoffmann-Rothe et al. (2006).

The thermal models for the southern study area fit the 350°C isotherm into the depth range of ~36 to 45 km for shear stresses $\tau < 67$ MPa. The depths extend of ~36 to 45 km for the seismogenic zone corresponds to a coupling width W_f starting at the trench to 165 to 220 km along the plate interface, which corresponds to the results of Hoffmann-Rothe et al. (2006).

Constraints for 3D mechanical models from thermal models

The thermal models show:
  ▪ The petrological definition of the upper limit of the coupling between plates (corresponding to 100 – 150°C) is unlikely to be applied in the Nazca-South America

subduction zone. The coupling zone width defined this way is extremely small and does not correspond to seismological and geodetical data.

- All three definitions of the downdip limit for the coupled zone between the plates give similar results.
- The area of partial coupling presented in the geodetical study of Khazaradze and Klotz (2003) does not correlate with the petrological definition of the downdip end of the coupling.

The thermal study of this section results in the following reference models of coupling zones:

- In both, the northern and southern segment, the coupling zone begins at the trench.
- The length of the coupled zone is 124 km for the northern segment and 167 km for the southern segment.

5.3   Critical wedge model applied to western margin of South America

The strength of plate coupling is defined as the level of long-term/static shear stress along the plate interface, as if the subducting and overriding plate would slip continuously at the plate interface (Wang & Suyehiro, 1999, Wang, 2000). Subduction earthquakes cause stress drops, indicating an accumulation of stress before; however, based on a single event one cannot conclude whether the plates are strongly or weakly coupled along the interface. Strongly coupled plate interfaces, accumulating a high amount of stress, can result in greater compression of the overriding plate by overcoming the gravitational effect due to topography (Wang, 2000). The strength of the plate interface may be estimated from a static frictional law

$$\tau = C + \mu\sigma_n = C + \sigma_n \tan\phi \tag{5.1}$$

where τ and σ_n are shear and normal stress, C is the cohesion, μ is the coefficient of friction, and ϕ is the friction angle (Ranalli, 1995). The further study in this thesis defines the strength of coupling between plates as a value of μ along the boundary between the plates.

The local balance of stresses in equation 2.1, however, needs to be evaluated for the extent of coupling between the plates. That can be done based on the critical taper theory (Dahlen, 1984). If the shear stress caused by undergoing subducting plate is equilibrated by the gravitational force of the lithospheric wedge above the subduction, the wedge may stay stable exhibiting the critical taper geometry. The assumption of the steady state of the subduction wedge may be regarded as a too strong simplification. However, taking into

account the fast rate of subduction of the Nazca plate, the re-adjustment of the wedge should not take long if some forces are not balanced.

The critical taper theory assumes the wedge to be on the verge of Coulomb failure everywhere, and the critically tapered wedge is overlying a basal decollement (with frictional coefficient μ_b) along which frictional sliding is occurring. Analysis of stresses in the critical wedge links wedge geometry (topography α and slab dip β) with wedge rheology (angle of internal friction ϕ_{int}) and the property of basal decollement (frictional coefficient μ_b). The exact solution of the stresses (Dahlen, 1984) results in one stable regime and two unstable regimes, compressional and extensional, for the wedge. Wedges in both unstable regimes fail by thrusting, by normal faulting, or by a combination of thrusting and normal faulting (Dahlen, 1984). Figure 5.3 illustrates this solution on the examples of characteristic geometries for northern and southern study areas.
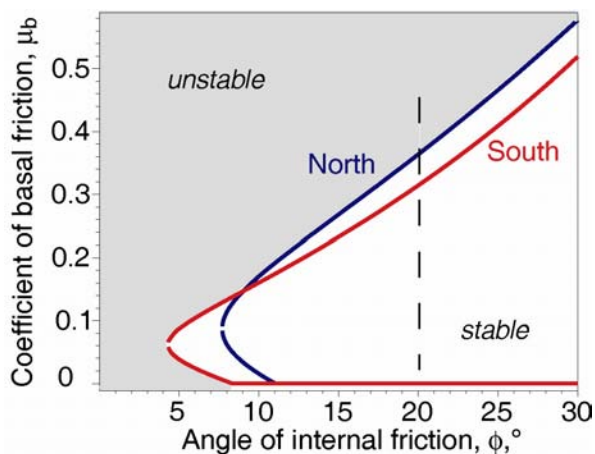

Figure 5.3: The critical taper theory divides the plot of coefficient of basal friction vs. angle of internal friction of the wedges into the areas of stable (inside the critical lines) and unstable regime. Calculations made for northern segment geometry outlined by blue line and for the southern segment by red line. Dashed line indicates internal friction of 20° used in the reference models.

The exact solution of Dahlen (1984) is based on the analysis of the orientation of principal stresses in the wedge. For small angles of topography and slab dip one can assume that the directions of principal stresses are horizontal and vertical. This assumption leads to an approximate, low angle, solution for a critical wedge:

$$\alpha + \beta = \left(\frac{1 - \sin \phi_{int}}{1 + \sin \phi_{int}} \right) \left(\beta + \mu_b \right) \tag{5.2}$$

where ϕ_{int} is the angle of internal friction of the material and μ_b the coefficient of basal friction. Figure 5.4 compares estimations of basal friction coefficient calculated assuming the western margin of South America in a critical state. Solutions obtained with the exact solution (Dahlen 1984) and the approximate solution (equation 5.2) are similar.
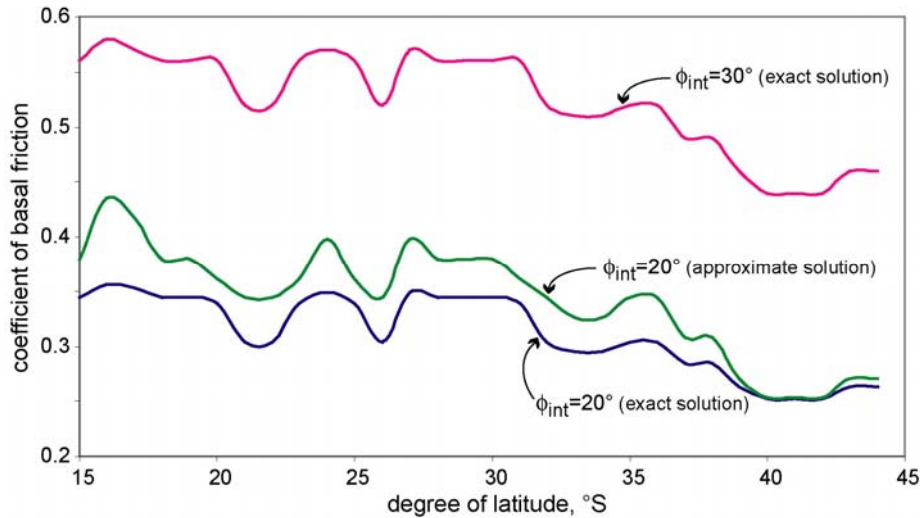
Figure 5.4: The critical taper theory assuming dry conditions applied to the western margin of the South America results in the distribution of critical coefficients of basal friction. Exact and approximate solutions for internal friction of $\phi_{int} = 20°$ give similar results.

Most of the earth-related materials exhibit an angle of internal friction of $\phi_{int} \sim 30°$. These properties are obtained in laboratory experiments for dry rocks. The effective properties of rocks can change in presence of water.

Considering wet conditions, the frictional law equation 5.1 changes to $\tau = C + \mu' \sigma_n$, where μ' is the effective coefficient of friction, defined as $\mu' = \mu(1-\lambda)$, where λ, the pore fluid factor, is defined as $\lambda = p_f / p_{litho}$ where p_f is the pore fluid pressure and p_{litho} the lithostatic pressure (Hubbert & Rubey, 1959, Sibson, 1990, Ranalli, 1995). λ varies between 0 and 1, in dry rock is $\lambda = 0$ and in water saturated rocks values $\lambda \geq 0.9$ can be reached. Under hydrostatic conditions, at shallow depths, where fractures are interconnected through to the surface $\lambda = p_f / p_{litho} \approx 0.4$, a typical value for wet crust (Sibson, 1990, Ranalli, 1995). Considering submarine conditions the pore fluid factor λ changes to $\lambda = (p_f - \rho_w g D)/(p_{litho} - \rho_w g D)$ where ρ_w is the water density, g the acceleration due to gravity, and D the water column above the solid surface (Davis et al., 1983, Dahlen, 1984, Hu & Wang, 2006). The presence of water, and consequently of fluid pressure results in weakening of the material and thus in further analysis I use an angle of internal friction 20° and calculate the effective basal friction based on the critical taper theory.

Figure 5.5 presents the parameters of the reference model, which uses the real geometry of the South American margin assuming the wedge is in a critical state. The angle of internal friction in the reference model, $\phi_{int} = 20°$, as well as resulting coefficient of basal

friction μ_b reflect weakening of earth material caused by pore fluid pressure. A general trend is observable: the decreasing coefficient of basal friction from north to south. The critical wedge theory allows approximating the basal friction for a given topographic slope, slab dip, and internal friction. An average value of 0.4 for the northern segment and 0.33 for the southern segment were chosen. These numbers serve as starting values for the numerical reference models.
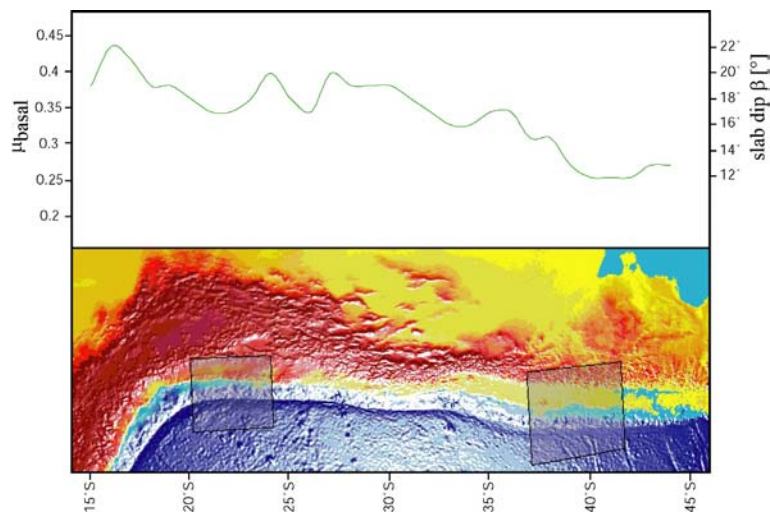

Figure 5.5: The critical taper theory applied to the western margin of the South America results in the distribution of critical coefficients of basal friction.

5.4 Analysis of gravity and seismic models to understand density and elastic properties

The analysis of velocity and density models lead to precise values of the Young's modulus, *E*. The choice of the density is based on the density models presented in chapter 3.3. These density models allow extracting average density values for the different lithological units. Average densities for the continental crust of ρ_{cont}=2800kg/m³ and for the slab of ρ_{slab}=3300kg/m³ were chosen for both, the northern and southern study area. For simplification reasons uniform densities are used.

Using the seismic velocity models of CINCA Working Group (1997), Patzwahl (1999), and ANCORP Working Group (2003) velocities v_p were extracted. The average velocity value of 6.0 km/s and the average density value of 2800 kg/m³ estimated from the velocity and density models respectively allow the calculation of *E* (equation 5.4, Figure 5.6).

Estimation of elastic parameters

The values of Young's modulus *E* and Poisson's ratio ν are the only specific material parameters governing elastic deformation. While the values for Poisson's ratio of most rocks are about 0.25 – 0.33, typical values of Young's modulus *E* vary significantly for different types of rock. Young's modulus varies from 10 to 90 GPa for sedimentary rocks, from 30 to 80 GPa for metamorphic rocks, and from 60 to 110 GPa for igneous rocks (Turcotte & Schubert, 2002).

Young's modulus can be determined by using the seismic v_P and v_S velocities together with the Poisson ratio ν and density ρ (Anderson, 1992).

$$E = f(v_P) = \frac{v_P^2 \rho \left(2\nu^2 + \nu - 1\right)}{\nu - 1}$$
$$E = f(v_S) = 2v_S^2 \rho(1+\nu) \tag{5.3}$$

Applying a Poisson ratio of $\nu = 0.25$ (which is commonly used in geosciences), the equations 5.3 can be simplified to:

$$E = f(v_P) = \frac{5}{6} v_P^2 \rho$$
$$E = f(v_S) = \frac{5}{2} v_S^2 \rho \tag{5.4}$$

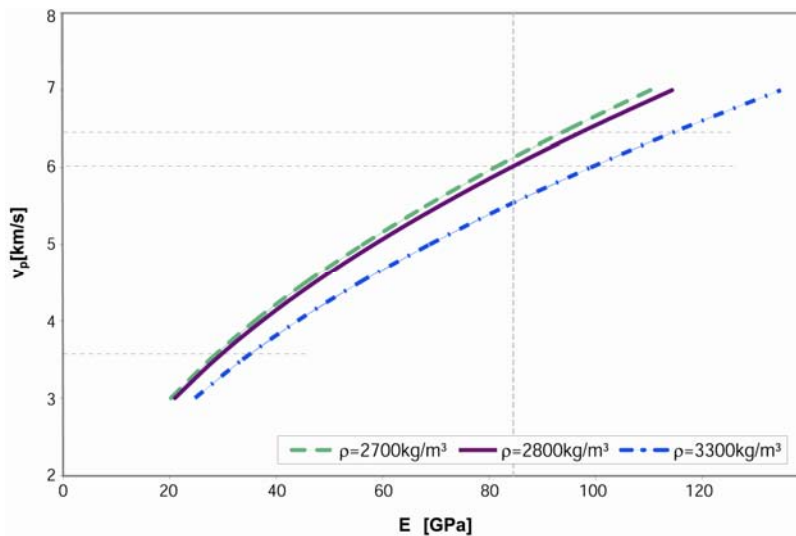**Figure 5.6**: Young's modulus *E* as a function of seismic velocity v_p for three different densities. Horizontal dashed lines indicate velocities of 3.6 km/s, 6.0 km/s and 6.4 km/s. Densities and velocities correspond to common values range observed at Chilean fore-arc regions (for more details see chapter 3). Vertical dashed line indicates *E*=85 GPa used in the numerical reference models.

Figure 5.6 shows variations of E for different values of seismic velocity v_P and density ρ. Thus, using equations 5.4, Figure 5.6, and field observations (e.g., interpretation of seismic data) one can compute characteristic values of the elastic modulus. Using densities and velocities extracted from the above mentioned models (CINCA Working Group, 1997, Kirchner, 1997, Patzwahl, 1999, ANCORP Working Group, 2003, Tašárová, 2004, Prezzi, 2005) a Young's modulus value of 85 GPa assuming a Poisson ratio of 0.25 was chosen as a representative value for both Chilean study areas. On Figure 5.6 the 85 GPa value for E is indicated by the vertical dashed line. This value was chosen as the initial value of E for wedge material.

In Table 5.1 all parameters are listed used in the numerical models for the northern and southern study area. These values correspond to the reference models performed for the two study areas.

Table 5.1: *Rheological/material parameters of the reference model*

Parameter	Reference values	
	North	**South**
Young's modulus, E	85 GPa	
Density, ρ	2800 kg/m³	
Poisson ratio, ν	0.25	
Angle of internal friction, ϕ_{int}	20°	
Dilatancy angle, ψ	0	
Slab dip, β	18.4°	13.4°
Width of coupling zone, w	124 km	167 km
Topography, α	4° - 1°	1°
Basal friction, μ	0.4	0.33

6   Numerical model of 3D deformation of the fore-arc wedge

This section presents the model set up and results for models of deformation of a fore-arc wedge at an obliquely convergent subduction zone. Two sets of models simulate the geometry and conditions derived from the northern Chilean (20°-24°S) and southern Chilean (37°-42°S) segments of this study.

The model is highly simplified in order to understand first-order features that control the difference in the styles of deformation between the two regions. The following assumptions can be considered as the most important:

- The simplified geometry of the models reflects first order features of the segments.
- The rheology of the wedges is assumed to be uniform. This assumption precludes understanding the influence of a (usually) highly rheologically stratified earth interior.
- The deformation of the subducting slab is ignored in the model. The slab (base of the model) moves only translationally along the boundary between the plates. This assumption precludes the analysis of the influence of additional horizontal tectonic forces.

These assumptions significantly simplify the models, but allow 3D modelling, catching the obliquity and the first-order features of deformations, and comparing the two segments.

The second part of this section presents the results of numerical calculations for the reference models and these results are then compared to the models with systematic parameter variation. For better comparison, each subsection presents results in which only one parameter is changed. This parameter study helps to find the preferred models for both, the northern and southern segments and thus to assess the possible causes of the differences in the styles of deformation between two segments.

The previous sections presented the approach to construct the two reference models (for the northern and southern segments, respectively). This section aims to check the applicability of the reference models.

For easier comparison, all the results are presented graphically using the same colour coding. The results are assessed by estimating the intensity of strike slip movements on the upper surface and by comparing the margin parallel and margin normal deformation rates achieved in the numerical model with the recent rates of deformations measured by GPS.

The results of the numerical calculations presented in this section should be compared to GPS data with caution. While the numerical calculations present an intermediate geological time scale (thousands to hundreds of thousands of years), the GPS data reflect only the recent state of movements (years to decades). Recent motion of the South American margin in the areas of the chosen segments is controlled by stick-slip motion (Khazaradze & Klotz, 2003) and thus results of GPS measurements should reflect higher coupling due to interseismic locking at the plate interface than the results of the numerical models reflecting hundreds of earthquake cycles.

6.1   Model setup

Figure 6.1 presents the simplified geometry of the models. The models consist of two main parts, the wedge itself and the subducting slab. The subducting slab, the base of the model, was modelled kinematically, as all the elements of the slab are assigned to the same displacement (or velocity V). This translational displacement is parallel to the slab dip and reflects the obliquity of subduction.

The geometry of the wedge is constrained by the dip of subducting slab and the topography (Figure 6.1c). The dip of the slab is assumed to be a constant for the two regions, and taken to 18.4° for the northern segment and 13.4° for the southern segment, respectively (Hoffmann-Rothe et al., 2006, Isacks, 1988, Yañez & Cembrano, 2004).

In the models, the topography of the wedges was simplified using averaged topography for the northern and southern segments (Figure 6.1). Figure 5.2 presents results of averaging based on topography/bathymetry data from Smith & Sandwell, 1997. The topography of the northern wedge was simplified into two segments approximately separated by the coastal line (α=4° west of coastal line, α=1° east of coastal line, Figure 6.1a). The southern wedge topography is simplified to be linear across the fore-arc (α=1°, Figure 6.1b).

The models have an extension of 900 km in the north-south direction. This large extend was chosen in order to minimise the boundary effects along the northern and southern boundaries of the model. The lithostatic pressure is set along the northern and southern boundaries; this condition is a great simplification because it does not account for variations of pressure due to additional stresses raised from the interaction between plates. Thus, the models show moderate (but local) effects along these boundaries. The central part of the wedge, however, is not affected by these perturbations, and the results presented below show only the central 450 km of the fore-arc wedge.
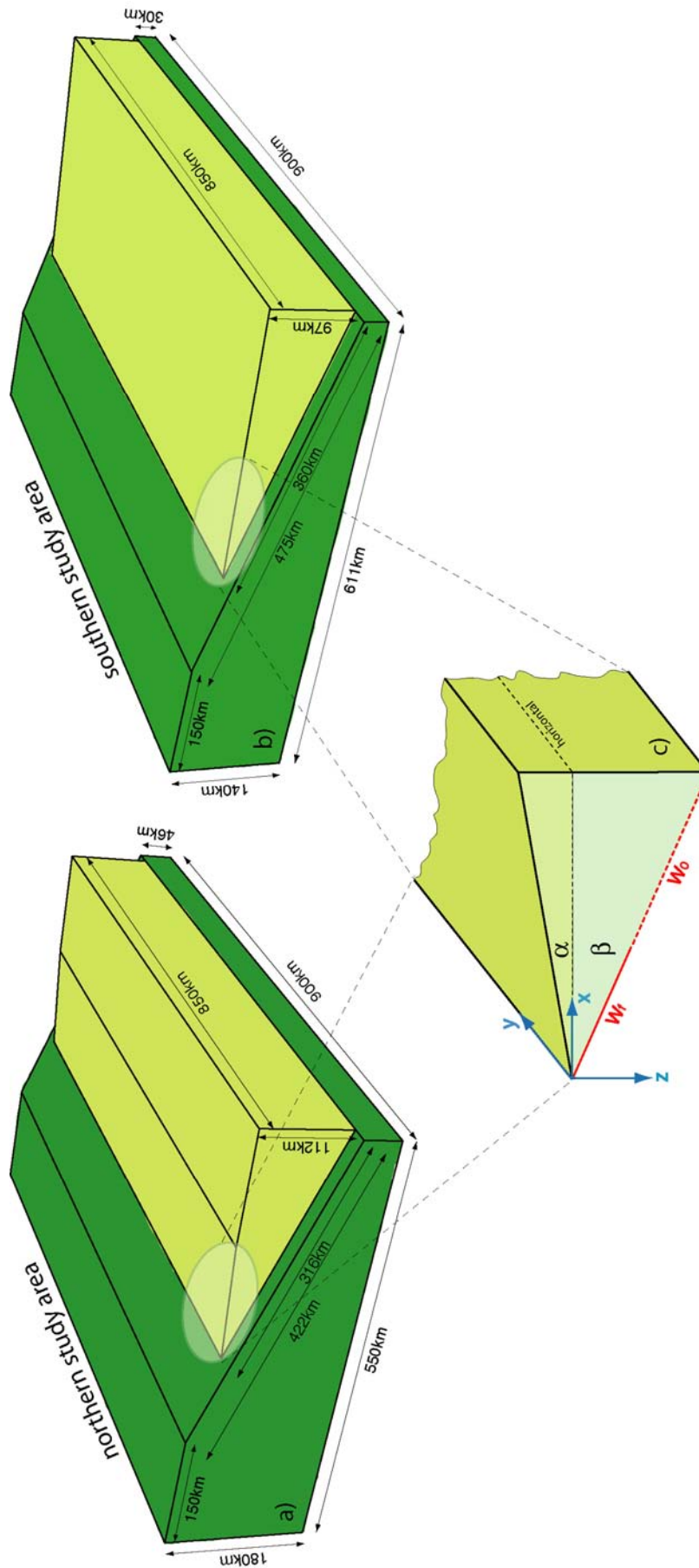
Figure 6.1: Geometry of the models: northern (a) and southern (b) study areas. Dark green basement represents the subducting Nazca plate. Light green wedge represents the western margin of South America. (c) Parameters used to describe the geometry of the wedge and its contact with the basement: α is the approximate dip of the topography, β is the dip of the bottom surface of the wedge (equals to the dip of subducting slab of the Nazca plate), W_f is the width of friction contact with the moving basement, and W_o is the width of frictionless contact. Note that these parameters are independent of the coordinate Y

The wedge extends 300-340 km in east-west direction. At the eastern boundary horizontal displacement is not allowed imitating strong coupling of the fore-arc wedge with main Andean orogeny. The backside of the wedge (eastern boundary), however, can move vertically allowing for possible uplift.

The upper surface of the fore-arc wedges is stress-free, whereas the bottom of the wedge is in dynamic contact with the subducting plate. The interface between fore-arc wedge and downgoing plate is modelled using a contact surface (Abaqus User's Manual, 2004). To simulate the coupled zone on the plate interface friction coefficients of 0.4 for the northern segment and 0.33 for the southern segment along W_f were used (Figure 6.1c). The friction changes abruptly to zero along W_0 (Figure 6.1c).
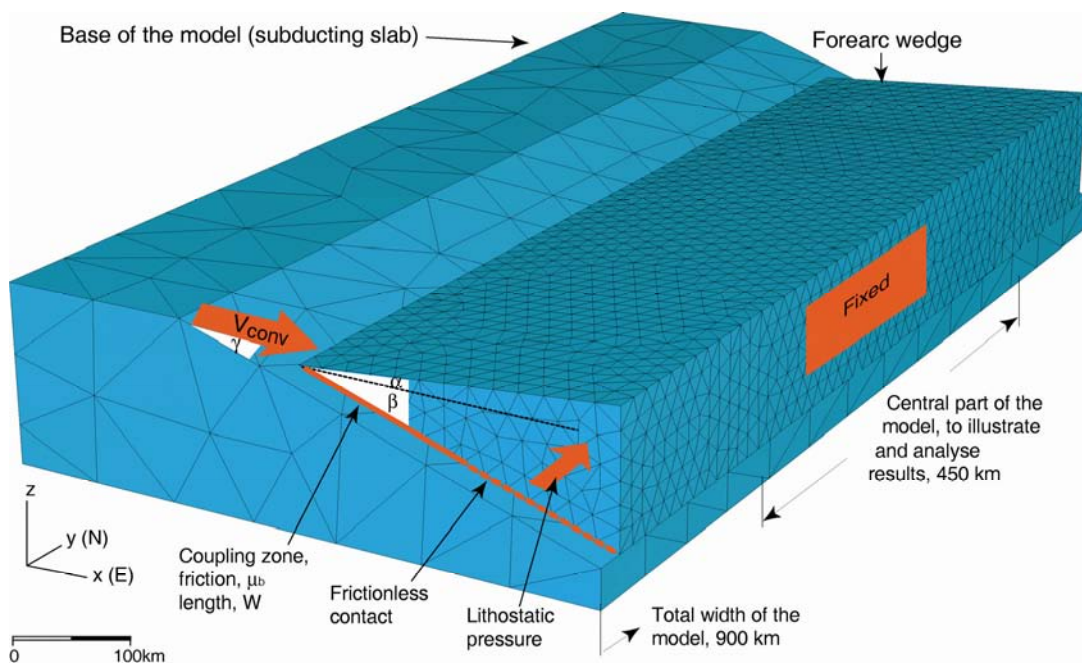

Figure 6.2: Perspective view on the model setup, boundary conditions and finite-element discretization. Note that the size of the elements of the base of the model is larger than the one of the fore-arc wedge.

The subducting plate and the fore-arc wedge are discretized by a mesh of approximately 75000 3D linear tetrahedral and wedge shaped elements (Figure 6.2). The kinematically prescribed motion of the subducting plate allows the use of coarse resolution, and thus elements of the plate have an average edge length of 80 km whereas elements of the wedge have an average edge length of 12 km. The ratio of the number of elements between plate and wedge is approximately 1:60, which allows a better resolution of the dynamically deformed wedge.

The deformation of the wedge was imposed by the motion of the basal part (subducting plate) along the boundary with the wedge with the rate of 6.5 cm/yr for a total displacement of 10 km in 150 thousand years.

The obliquity of the total displacement is referred to as γ, which is 20º in the reference model, but will be varied in other models. Because of the convergence obliquity, the total rate of convergence of 6.5 cm/yr is partitioned into a trench-normal velocity of 6.11 cm/yr and a trench-parallel velocity of 2.22 cm/yr. Projected onto the horizontal surface, these parts of the convergence rate are 5.80 and 2.22 cm/yr for the northern segment and 5.94 and 2.22 cm/yr for the southern segment. The corresponding horizontal displacement of the markers on the subducting slab are 8.91 and 3.42 km for the northern and 9.14 and 3.42 km for the southern segment (Table 6.1), respectively.

Table 6.1: *Displacement and velocity components applied to the subducting plate*

Slab dip	dx[km]	dy[km]	dz[km]	v_x[cm/yr]	v_y[cm/yr]	v_z[cm/yr]
α=18.4° (north)	8,917	3,420	-2,966	5,80	2,22	-1,93
α=13.4° (south)	9,141	3,420	-2,178	5,94	2,22	-1,42

A uniform material property (rheology and density) is assumed for the wedge material. The assumption of effective wedge rheology for (most probably) rheologically layered wedges may be a great simplification of the model. That, however, reduces the number of controlling parameters in the model and simplifies the search for answers to the main questions of this study. The rheological model for the wedge material was discussed in the sections 3 and 4. The values for specific rheological parameters will be discussed and tested in the following sections.

6.2   Reference models and models with a purely elastic wedge

North: Comparison between the reference model and the elastic model

Section 3 presented the elasto-plastic rheological model for the fore-arc wedge as the reference model. By the comparison of models with a plastic and a purely elastic rheology I want to estimate the importance of the plastic response of the rheology. Therefore I compare deformations in the reference model (elasto-plastic rheology) with deformations in a purely elastic wedge.
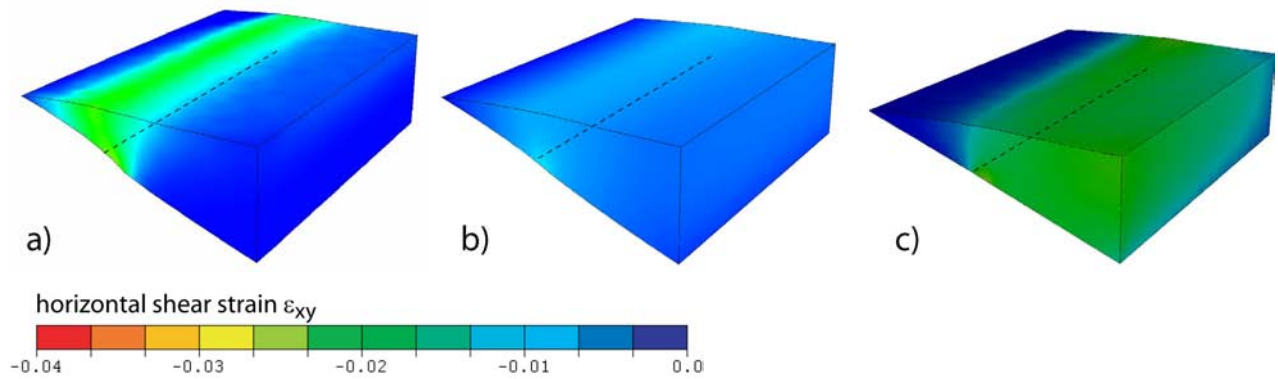
Figure 6.3: Comparison of the deformation in the reference elasto-plastic wedge (a) and in pure elastic wedges with E=85 GPa (b) and E=10 GPa (c) for the northern study area. Colours indicate shear strain in the model (note that the colour coding of the shear strain remains the same throughout this study). Only the central, 450 km, part of the models is shown (cf., Figure 6.2). The basal part (subducting slab, Figure 6.1) does not deform and is not shown. The dashed line shows boundary between friction and frictionless contact between wedge and subducting plate.

Technically, the purely elastic wedge can be modeled exactly in the same way as the reference model, but with an extremely high cohesion of the plastic part of rheology. High cohesion prevents yielding and thus the model behaves elastically during the experiment.

Figure 6.3a shows that the elasto-plastic wedge of the reference model exhibits active dextral motion. The shear strain is clearly correlated to the transition between the frictional and the frictionless contact between the wedge and subducting plate at the base of the wedge.

In contrast, the pure elastic model with the same elastic modulus, E=85 GPa (Figure 6.3b), is subjected to minor shear strain and this strain is distributed evenly across the wedge.

Figure 6.4: Comparison of surface velocity distribution resulting from the models with E=85 GPa (red line for reference elasto-plastic model, blue line for the elastic wedge model) with GPS measurements in the area of the central Chilean (northern) segment (symbols, see section 3 for details of GPS data; AVZ – Atacama Fault Zone, PFS – Precordilleran Fault System). Results and data are presented in (a) trench-normal direction and (b) trench-parallel direction.

To reach a rate of deformation comparable with the elasto-plastic model, the purely elastic model requires a reduction of the elastic modulus by almost an order of magnitude, down to 10 GPa (Figure 6.3c). This low elastic strength model results in well distributed deformations, but the value of the elastic modulus must be considered as too low.

South: The reference model and comparison with the northern segment

The comparison of the reference model with model with purely elastic rheology for the southern segment is identical to the models of the northern segment (Figure 6.5). The style of deformation of the elastic wedge does not correspond to observations because it does not result in concentrated deformation but in distributed deformation (see section 3). Thus this subsection is more concentrated on the comparison of the deformation of two reference models, the northern and southern.

The deformation of the reference models of the northern (Figure 6.3a) and southern (Figure 6.5a) are identical. The parameters of the reference models (Table 5.1) are chosen so that both models are in a state close to plastic failure. Thus, despite the two models have different geometries, the strain pattern of the two models is the same.

The natural examples, however, exhibit different styles of deformations. In the following part of this section I present parameters which can emulate the two models and approximate the natural examples.

horizontal shear strain ε_{xy}

-0.04   -0.03   -0.02   -0.01   0.0

Figure 6.5: Comparison of the deformation in the reference elasto-plastic wedge and in the pure elastic wedge for the southern study area. Colours indicate shear strain in the model (note that the colour coding of the shear strain remains the same throughout this study).
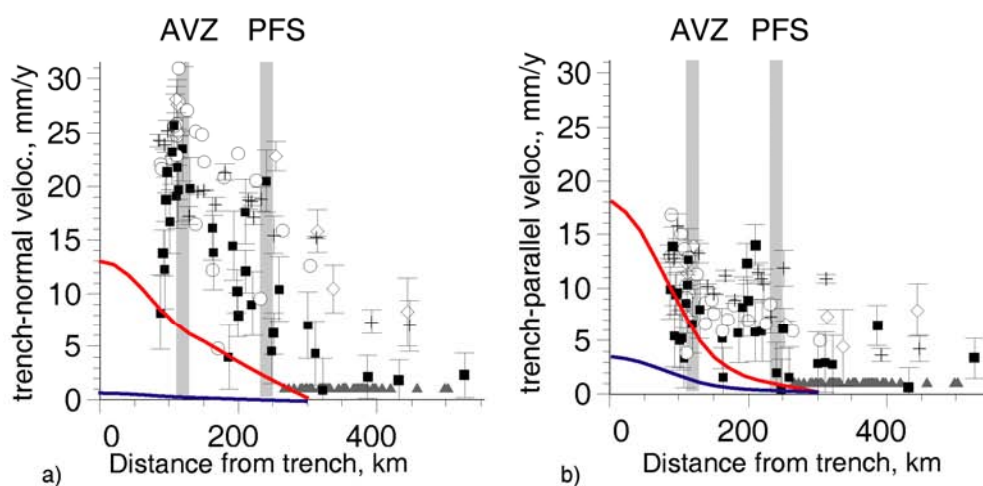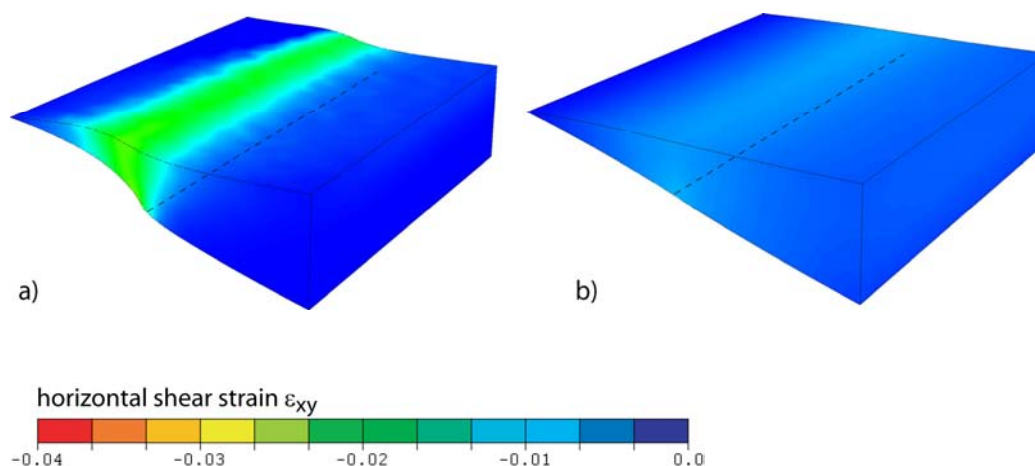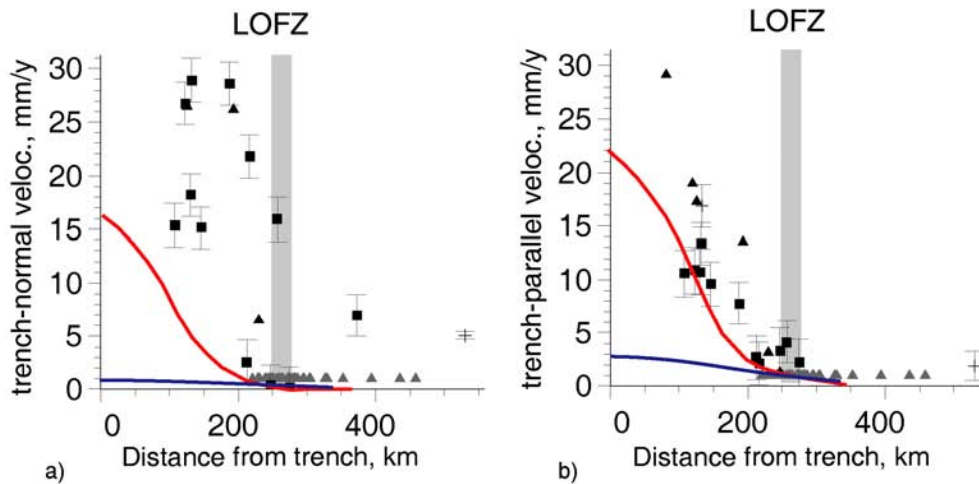
Figure 6.6: Comparison of surface velocity distribution resulting from the model (red line for reference model, blue line for the elastic wedge model) with GPS measurements in the area of the southern Chilean segment (symbols, see section 3 for details of GPS data; LOFZ - Liquiñe-Ofqui Fault Zone). Results and data are presented in (a) trench-normal direction and (b) trench-parallel direction.

6.3   Parameter study

6.3.1   Parameter: Basal friction

Section 3 constrained the coefficient of basal friction between Nazca plate and South America from the assumption that the geometry of the fore-arc wedges is governed by a critical taper. This approach provides an approximate value for the parameters of the wedge, however some variations of the coefficient of basal friction are possible.

This subsection presents the results of numerical modelling for different values of the coefficient of basal friction μ_b using the setup for the northern Chilean study area. Figure 6.7 presents the intensity of shear deformation for three different values of μ_b. A stronger coupling between the plates (higher coefficient of basal friction) leads to more intense shear.

However, the distribution of surface velocities (Figure 6.8) is not so obvious. The difference in velocities in the trench-normal direction (Figure 6.8a) is much higher than the difference in velocities in the trench-parallel direction (Figure 6.8b).

The high trench-normal velocity (and correspondingly high strain rate) observed in the model with $\mu_b = 0.5$ is resulting in fast thickening of the wedge and therefore its slope becomes steeper. This deformation will lead to a wedge characterized by a geometry corresponding to the critical taper. The two other models, in contrast, do not exhibit high trench-normal strain rates, and can maintain their actual geometry. Thus, the models with a

coefficient of basal friction higher than the one corresponding to the critical taper should be taken out of consideration.

Similar results were obtained for the southern segment. Figure 6.9 compares surface velocities for models with μ_b =0.3, 0.33 (reference), and 0.4. These smaller (cf. Figure 6.8) variations also result in an extreme high compression of the wedge for the case of the overcritical basal friction of 0.4.
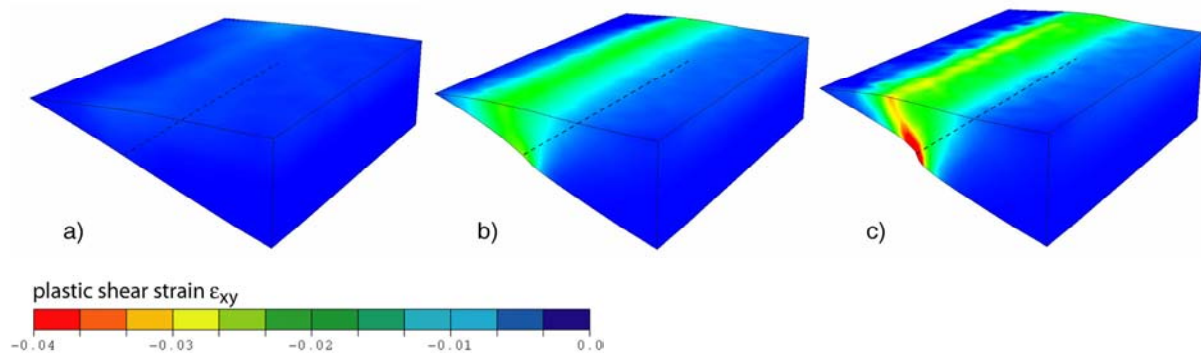
Figure 6.7: Comparison of deformation in models with different coefficient of basal friction, μ_b: 0.2 (a), 0.4 (b, reference model), and 0.5 (c). The intensity of deformation clearly correlates with the value of basal friction.

Figure 6.8: Comparison of GPS measurements in the area of the central Chilean (northern) segment (symbols, see section 3 for details of GPS data; AVZ – Atacama Fault Zone, PFS – Precordilleran Fault System) with surface velocity distribution resulting from the models with different coefficient of basal friction: 0.2 (green line), 0.4 (red line, reference model), and 0.5 (blue line). Results and data are presented in (a) trench-normal direction and (b) trench-parallel direction.

Figure 6.9: Comparison of GPS measurements in the area of the southern Chilean segment (symbols, see section 3 for details of GPS data; LOFZ - Liquiñe-Ofqui Fault Zone) with surface velocity distribution resulting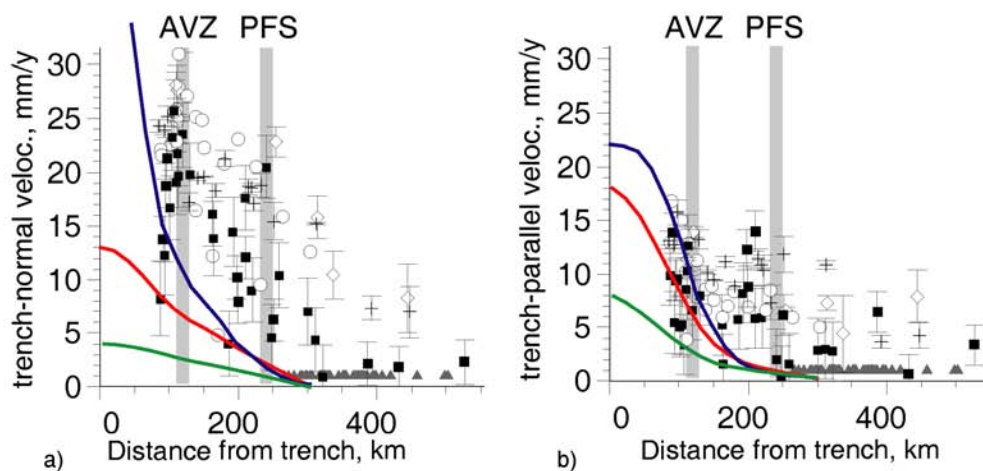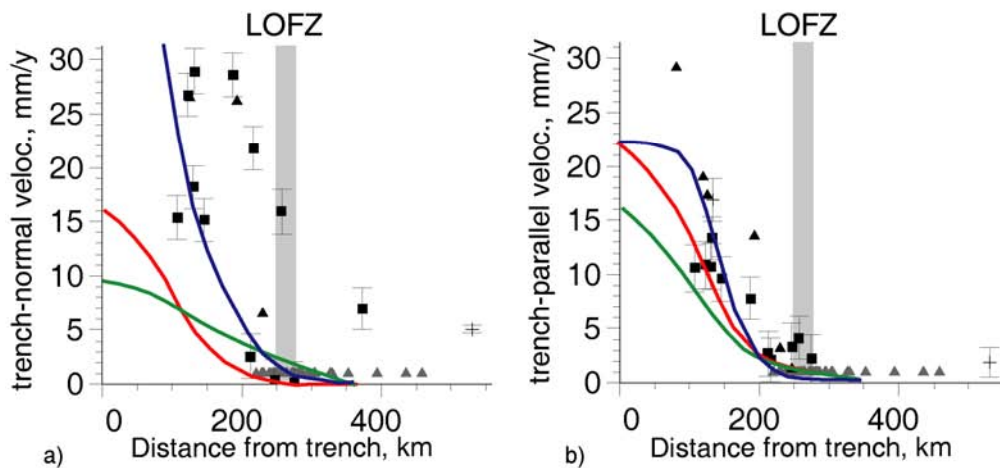 from the models with different coefficient of basal friction: 0.3 (green line), 0.33 (red line, reference model), and 0.4 (blue line). Results and data are presented in (a) trench-normal direction and (b) trench-parallel direction.

6.3.2   Parameter: Obliquity

The average angle of convergence, γ, between Nazca plate and South America is approximately 20º. This angle can change locally, however, because of the curvature of the South American margin (e.g., Hoffmann-Rothe et al., 2006). The most intense changes in the obliquity angle, north from 20º S, are related to the Bolivian orocline. The area of this study (south from 20º S) exhibits some variations in obliquity, although they are less pronounced than in the north of Chile. This subsection considers angles of obliquity (10º, 20°, and 30°) and compares the results with the reference model.

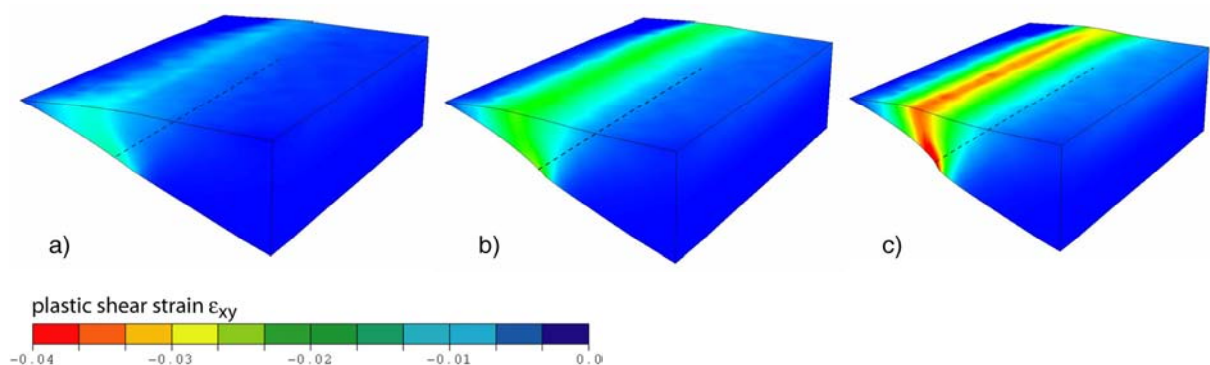**Figure 6.10**: Comparison of deformation in the models subjected to convergence with different obliquity angle, γ of 10º (a), 20º (b, reference model), and 30º (c). The intensity of deformation clearly increases with increase of obliquity.

Figure 6.10 shows that the intensity of deformation increases significantly with the increase of the obliquity angle. The deformation localizes significantly when γ is more than 20° and the wedge behaves plastically above the transition from a frictional to a frictionless contact between the plates. The corresponding weakening of the wedge in the area of plastic failure results in active deformation of the wedge in the trench-normal direction (blue line on Figure 6.11a).

Figure 6.11: Comparison of GPS measurements in the area of the northern Chilean (northern) segment (symbols, see section 3 for details of GPS data; AVZ – Atacama Fault Zone, PFS – Precordilleran Fault System) with surface velocity distribution resulting from the models with different angle of obliquity, γ: 10° (green line), 20° (red line, reference model), and 30° (blue line). Results and data are presented in (a) trench-normal direction and (b) trench-parallel direction.

A similar dependence of deformation on obliquity was obtained for the southern segment (Figure 6.12). The intensity of deformation increases significantly with the increase of the obliquity angle.
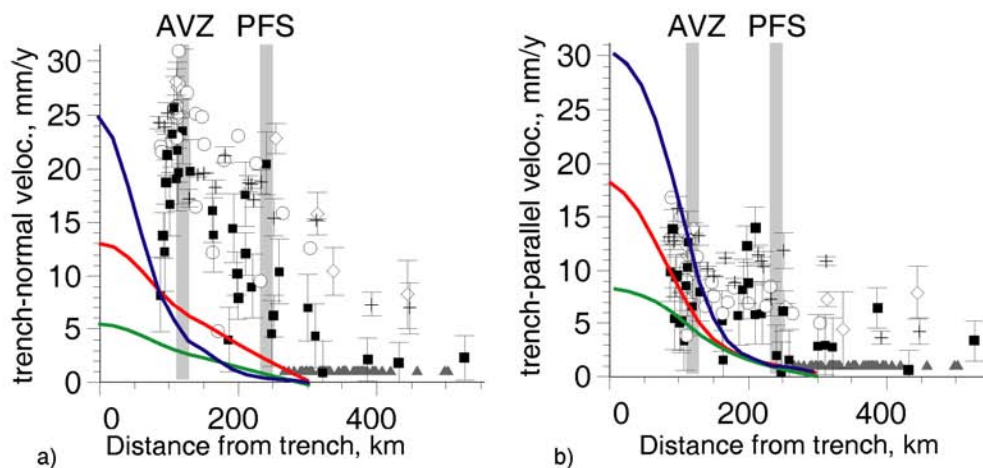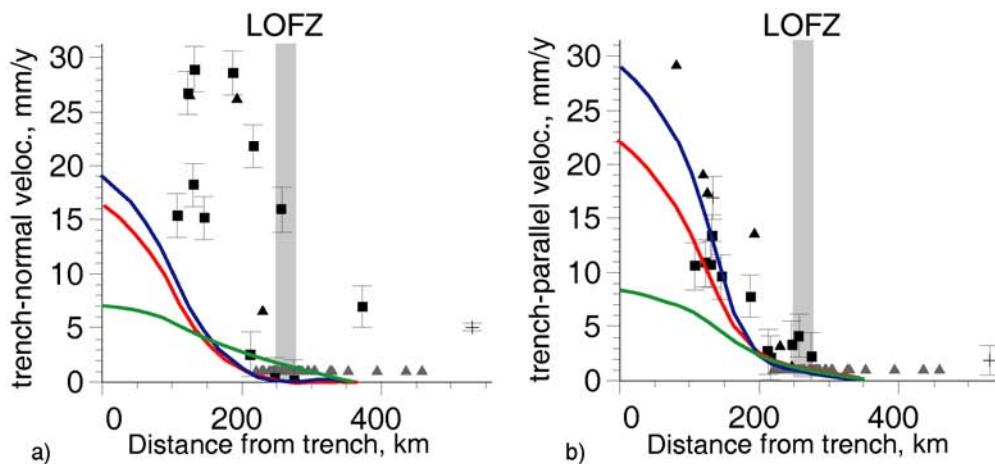
Figure 6.12: Comparison of GPS measurements in the area of the southern Chilean segment (symbols, see section 3 for details of GPS data; LOFZ - Liquiñe-Ofqui Fault Zone) with surface velocity distribution resulting from the models with different angle of obliquity, γ: 10º (green line), 20º (red line, reference model), and 30º (blue line). Results and data are presented in (a) trench-normal direction and (b) trench-parallel direction.

6.3.3   Parameter: Young's modulus

The uniform rheology throughout the fore-arc wedge is a considerable simplification of the model. The rheological parameters do not change, e.g., with depth, in the model even though the wedge is approximately 100 km deep. The rheological stratification of such deep structures should be significant. The use of an average rheology in the model is forced by numerical reasons because an introduction of rheological variations would result in a numerically unstable case.

To understand the influence of variations of an "average" rheology along the Chilean margin, the value of the elastic modulus E was varied in this subsection. Figure 6.13 presents results of numerical calculations for models with an elastic modulus smaller or equal to the elastic modulus in the reference model. The decreased elastic strength of the wedge can be attributed, for example, to weakening of the wedge due to long-term tectonic processes of deformation (especially around the northern segment, which is backstopped by highly deformed Central Andes). The results show that a decreasing elastic modulus results in widening and delocalization of deformation.

The velocity profiles (Figure 6.14b) show that the total trench-parallel displacement across the wedge remains the same for models with different elastic moduli. The profiles of the corresponding velocities, however, differ. Models with a higher elastic strength result in a higher local velocity gradient. This result can be understood considering the elasto-plastic rheology. A low Young's modulus model results in lower stresses for similar deformation as a

high Young's modulus. Thus, low Young's modulus models reach plastic yield later than strong models. Thus, localized plastic deformation is higher in models with a large Young's modulus for a given total displacement.
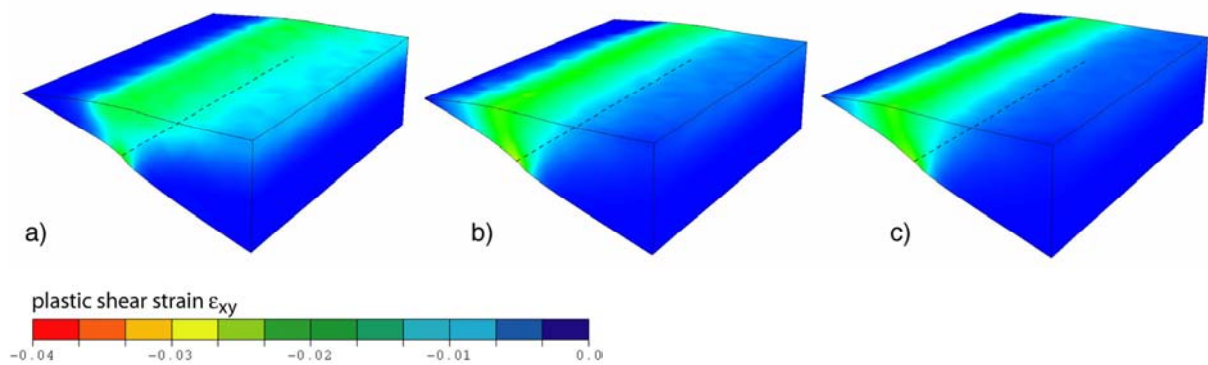
Figure 6.13: Comparison of deformation in the models with different elastic moduli, *E*: 30 GPa (a), 70 GPa (b), and 85 GPa (c, reference model). The concentration of deformation increases with increase of elastic strength.

The results for variations in Young's modus for the model of the southern segment show a similar dependence on the styles of deformation as observed for the northern segment (Figure 6.15).
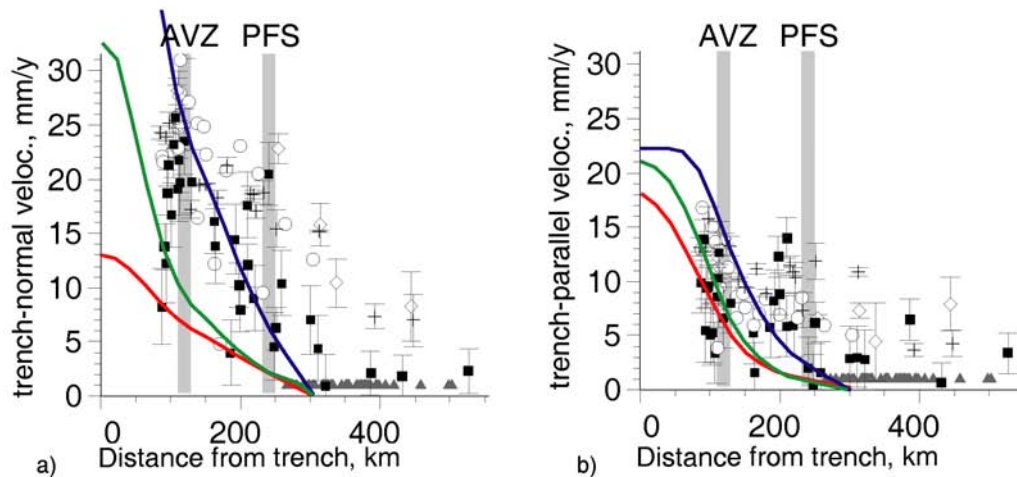
Figure 6.14: Comparison of GPS measurements in the area of the central Chilean (northern) segment (symbols, see section 3 for details of GPS data; AVZ – Atacama Fault Zone, PFS – Precordilleran Fault System) with surface velocity distribution resulting from the models with different elastic moduli, *E*: 30 GPa (blue line), 70 GPa (green line), and 85 GPa (red line, reference model). Results and data are presented in (a) trench-normal direction and (b) trench-parallel direction.
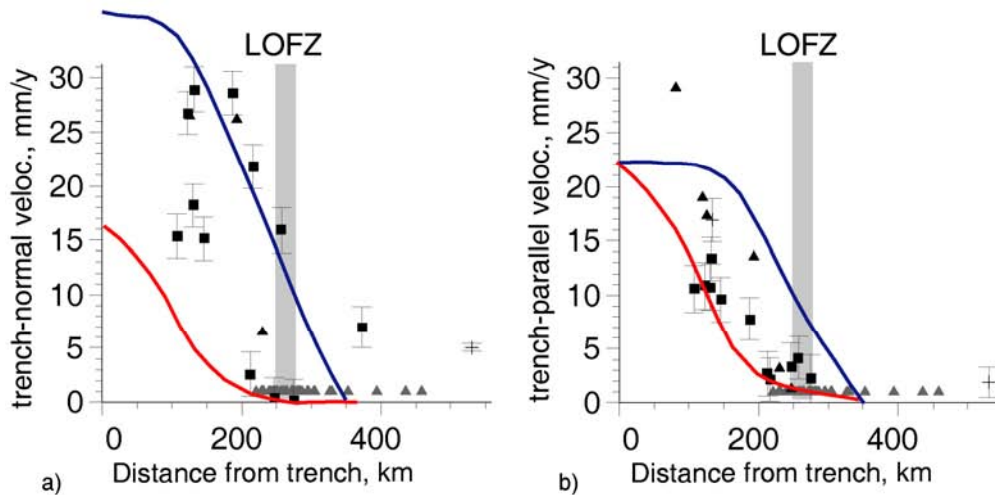
Figure 6.15: Comparison of GPS measurements in the area of the southern segment (symbols, see section 3 for details of GPS data; LOFZ - Liquiñe-Ofqui Fault Zone) with surface velocity distribution resulting from the models with different elastic moduli, *E*: 10 GPa (blue line), and 85 GPa (red line, reference model). Results and data are presented in (a) trench-normal direction and (b) trench-parallel direction.

6.3.4   Parameter: Slab dip

The models with different slab dips are compared to understand the influence of this parameter on the deformation of the fore-arc. All other parameters are kept constant as in the reference model.

Figure 6.16 shows that the smaller the slab dip, the easier it reaches plastic failure conditions. In terms of the critical taper theory, the thick slab with β=25° is in a stable regime whereas the wedge with β=13.4° is overcritical (the coefficient of basal friction is μ_b=0.4 for both cases). In this sense, the results with varying slab dip β and constant coefficient of basal friction μ_b are similar to set of models with varying coefficients of basal friction μ_b and constant slab dip β (Figures 6.7 – 6.9).

plastic shear strain ε_{xy}
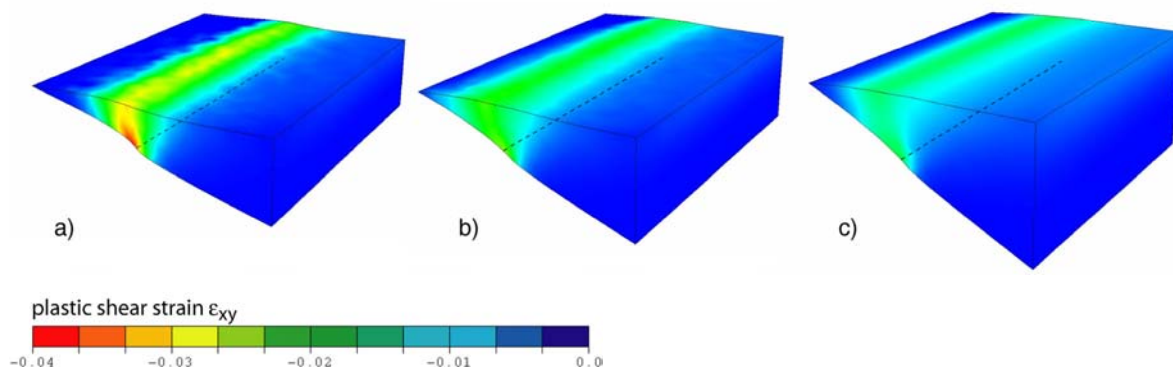
**Figure 6.16**: Comparison of deformation in the models with different dip of subducting slab, β: 13.4° (a), 18.4° (b, reference model), and 25° (c). The concentration of deformation increases with increase of elastic strength.

6.3.5   Long term evolution

The numerical experiments so far are calculated for a temporal evolution of 150 thousand years. To test the reliability of the results, in particular the favorable condition for the generation of strain partitioning, numerical experiments were performed with a time evolution of 1.5 Myr. The calculation of this long time period was only possible by the use of periodic boundary condition, applied to the northern and southern edge of the wedge. The periodic boundary condition is numerically more stable and allows considering longer evolution time for the numerical models. Periodic boundary conditions describe the relation between the displacement vectors u_i^α, u_i^β at two equivalent boundary points (α, β, Figure 6.17) and the average strain tensor can be expressed as

$$u_i^a - u_i^b = \overline{e}_{ij}\left(x_j^b - x_j^a\right) \tag{6.1}$$

where x_j denotes the position (ABAQUS User's Manual, 2004). This formulation requires a periodic mesh, i.e. the mesh of face A has to be an image of the mesh of face B, or vice versa (Figure 6.17).
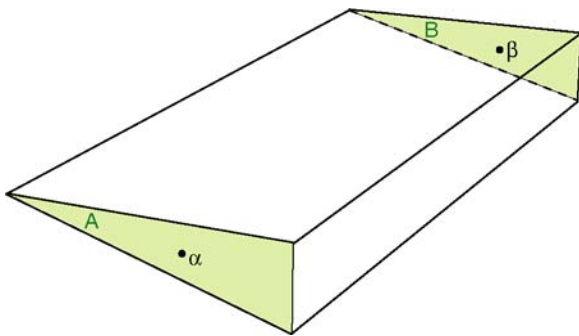
Figure 6.17: Sketch illustrates equivalent boundary points, α and β, of the periodic cell (enclosed by face A and B).

This boundary condition applied to the models of this section simply states that the northern and southern boundaries of the model wedges deform equally. The models were calculated with the following parameters favoring strain partitioning of the previous sections:

northern study area μ_b=0.4, E=70 GPa, γ=20°, β=18.4°

southern study area μ_b=0.33, E=85 GPa, γ=30°, β=13.4°

These results are presented in Figure 6.18.
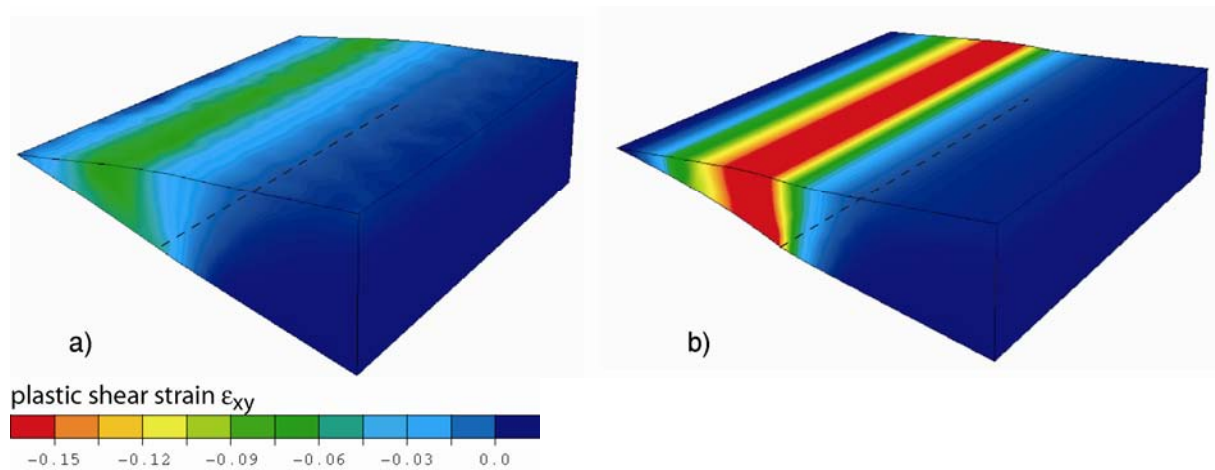
Figure 6.18: Results of numerical models with applied periodic boundary condition (a) northern study area and (b) southern study area. Plastic shear strain, ε_{xy}, is colour coded after 1.5 Myr.

The two sets of results presented on Figure 6.18 show that the tendency of the preferential models remains for longer time evolution. The southern segment develops in a more localized manner than the northern segment.

6.4 Preferred models for Chilean segments

The numerical experiments show favorable conditions for the generation of strain partitioning. An elasto-plastic behavior of rocks, sufficient obliquity of convergence ($\gamma > 20°$), strong coupling between the plates ($\mu_b > 0.3$), and a shallow slab dip favor the generation of strain partitioning in the fore-arc.

Controlling factors for the difference in the style of deformation between the northern and the southern Chilean segments may be an effectively weaker northern segment (related to the hot orogen to the east), a slightly higher obliquity in the southern segment, and the difference of the slab dip.

Table 6.2: *List of parameters used for the preferential models of the northern and southern study areas*

Parameter	northern study area	southern study area
slab dip, β	18.4°	13.4°
basal friction, μ_b	0.4	0.33
Young's modulus, E	30 GPa	85 GPa
obliquity, γ	20°	30°

The analysis of the parameters (section 6.3.1 to 6.3.4) allows setting up parameter combinations explaining the different styles of deformation in the two study areas. Model results, which fit first order observations, were achieved with the following parameters (correlated from north to south): a decreased slab dip, a decreased coefficient of basal friction, an increased Young's modulus, and an increased obliquity (Table 6.2). The northern segment shows distributed deformation, whereas the southern segment shows more localized deformation (Figures 6.19 and 6.20).
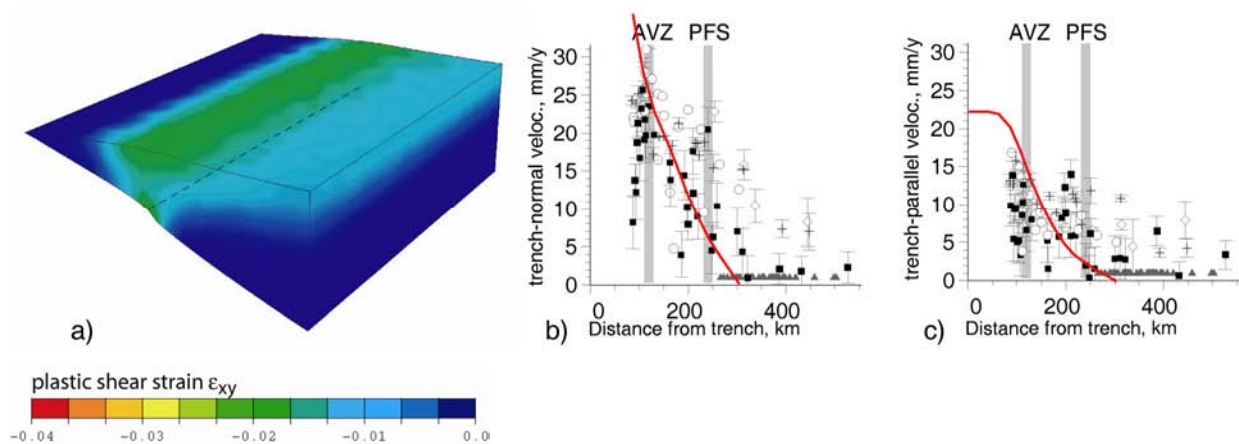
Figure 6.19: Preferential model for northern (central Chilean) study area. (a) illustrates the plastic shear strain, ε_{xy}, colour coded. (b) and (c) show the comparison of surface velocity distribution (trench-normal and trench-parallel) resulting from the model with GPS measurements (symbols, see section 3 for details of GPS data; AVZ – Atacama Fault Zone, PFS – Precordilleran Fault System).

The results of Section 6.3.1 suggest that the observed difference in styles of deformation between northern and southern segments may also be achieved by varying the coefficient of basal friction. Thus, application of higher coefficient of basal friction to the coupling between plates in the southern segment results in localized deformation. However, the recent observations and estimates (e.g., Hoffmann-Rothe et al., 2006; Lamb & Davis, 2003) point to the opposite condition in Nazca-South America collision, with strength of coupling decreasing southward. I, therefore, take into account a decreasing strength of coupling southward and select favorable models by this condition, even though this is the worst case scenario in terms of basal friction. This restriction is also compatible with my assumption of steady-state geometry of the fore-arc wedges (Section 5.3).
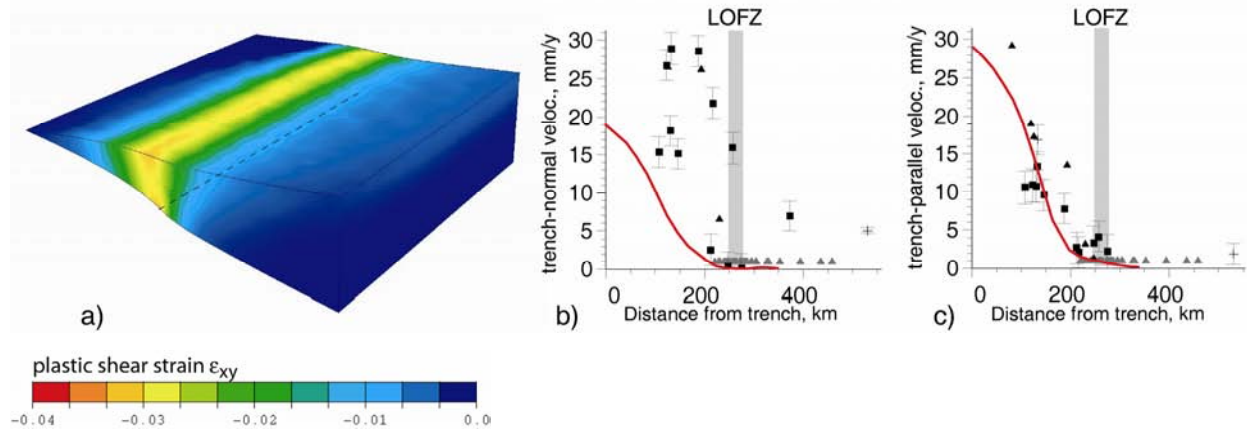
Figure 6.20: Preferential model for southern Chilean study area. (a) illustrates the plastic shear strain, ε_{xy}, colour coded. (b) and (c) show the comparison of surface velocity distribution (trench-normal and trench-parallel) resulting from the model with GPS measurements (symbols, see section 3 for details of GPS data; LOFZ - Liquiñe-Ofqui Fault Zone).

The results using periodic boundary conditions (section 6.3.5) give confidence in the models with shorter time evolution and strengthen the statement about the conditions responsible for the differences in style of deformation in the two Chilean study areas.

7   Discussion

In this section I compare the results of my numerical models as described in Section 6 with natural observations and with results of analogue and numerical experiments applied to similar problems. I discuss the influence of the strength and extent of coupling between the South American and the Nazca plate on surface deformation. Combining these studies helps to evaluate the results that I obtained from the numerical models of Section 6.

The main advantage of the model series presented in my work is that the approach used here combines several important features: (1) the use of three dimensions, (2) the implementation of contact surfaces for the description of the interface between the plates, and (3) the possibility to follow the evolution of the models in time. The parameter study presented in Section 6 shows that varying only a single parameter of the model, such as the coefficient of friction, the obliquity, or the Young's modulus, does not lead to satisfying results that compares well with observations. As a result of the modelling a set of parameters is suggested that is in good agreement with first order observations such as the displacement field.

The models of the northern study area with a Young's modulus of 30 GPa, an obliquity of the subducting Nazca plate of 20°, and a slab dip of 18.4° result in a distributed deformational pattern at the surface. The comparison of the model results for the last hundred thousand years with GPS measurements show that the displacement, calculated in the numerical models, in trench-parallel and trench-normal direction is correlating in trend and is comparable in amount. Whereas the trench-parallel velocity component acts sensitive to basal friction and obliquity (an increase of each parameter lead to an increase of the trench-parallel velocity), the trench-normal component acts sensitive to the Young's modulus (an increase of the parameter lead to a decrease of the trench-normal velocity. It should be noted, however, that the GPS measurements mirror short time (decades of years) deformation only. However, the tendency of the different deformational pattern in the northern and southern segment stays the same for longer time evolution models (1.5 Myr, section 6.3.5). On the geological time scale (100 thousands to millions of years), the deformational pattern at the surface has changed various times from distributed to localized deformation and vice versa (e.g., Hervé, 1987, Hervé et al., 1994, Scheuber et al., 1994). A slightly faster convergence rate

(> 15 cm/yr ~25Myr ago, Somoza, 1998) or higher friction at the plate interface (regular major earthquake events as a result of stick slip behaviour, Kelleher, 1972) change the style of deformation in the system to localization.

The models for the southern study area reach a localized deformation pattern at the surface with a Young's modulus of 85 GPa, an obliquity of the subducting Nazca plate of 30°, and a slab dip of 13.4°. Furthermore, the localization of deformation occurs above the sharp transition between frictional and frictionless coupling at the plate interface. The distance to the trench amounts ~170 km, which reflects approximately the distance of the LOFZ from the trench (Melnick & Echtler, 2006). Comparing these results with GPS measurements shows a good correlation in trend and amount of the displacement in trench-parallel direction, but the displacement in trench-normal direction is only correlating in trend and always smaller in amount. On the geological time scale, strain partitioning can be even more pronounced with faster convergence rate (Somoza, 1998) and higher friction at the plate interface (Kelleher, 1972, Beck et al., 1998).

The present modelling is focussed on differences in deformation along the Chilean margin in recent times. The change of the style of deformation during the long-term evolution of those areas is not investigated in this work, but can be a key question of further research.

7.1   Displacement pattern at the surface: comparison with other models

The models of Bevis & Martel (2001) are based on the two end member cases of oblique subduction (1) complete partitioning with the development of a fore-arc sliver and (2) distributed deformation within a mechanically coherent fore-arc. Similar to my model set up, Bevis & Martel (2001) also tried to build up the model as simple as possible, avoiding potential complexities associated with significant curvature of the subduction zone in map view or with rapid along strike variations in the obliquity of subduction. Figure 7.1 shows the horizontal surface velocity of the elastic half-space model of Bevis & Martel (2001). It is clearly visible that the surface velocity above the coupled zone is more oblique than the plate convergence vector. Immediately behind the coupled area, where frictionless contact starts, the surface velocity tends to the direction normal to the trench.

Klotz et al. (1999) considered interseismic accumulation of elastic strain due to subduction coupling. The displacements were modelled based on elastic half-space theory. Observations of present-day velocity were used to place constraints on the interseismic accumulation of elastic deformation.
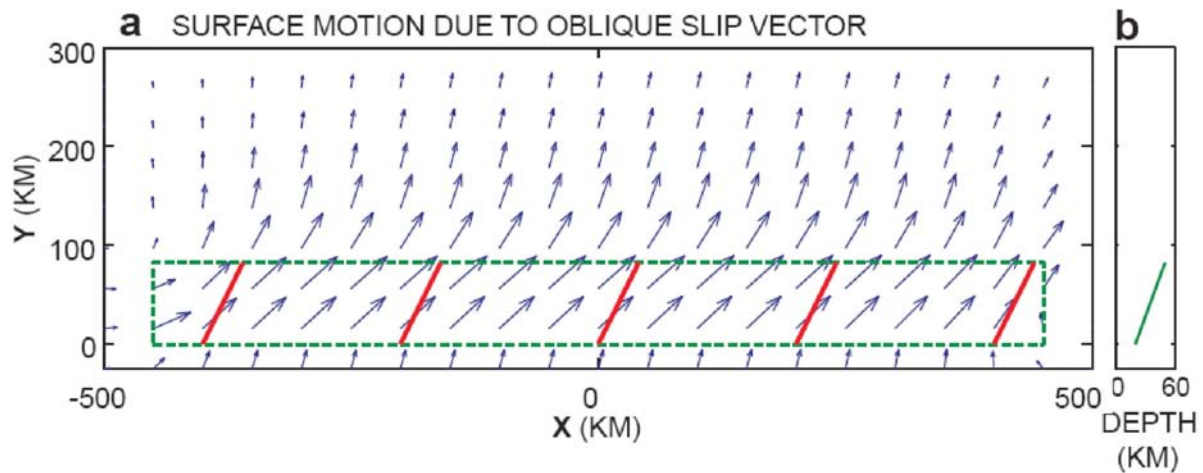
Figure 7.1: Elastic dislocation model by Bevis & Martel (2001): (a) the horizontal surface velocity of the overriding plate and (b) the depth extent of the coupled zone at the plate interface. Red lines indicate convergence direction; green dashed rectangle shows the projected coupled area at the plate interface.

Figure 7.2 shows the predicted horizontal interseismic displacements. The model assumes a locked plate interface down to 50 km depth with a transition zone of 50% coupling between 40 km and 50 km depth. Both phenomena, the higher obliqueness of the displacement vectors above the coupled zone and the decrease of the obliquity above the not coupled area, can be observed on Figure 7.2 as well. The comparison of the model results with the displacements of GPS sites reveals congruence of sites affected by the 1995 Antofagasta M_W=8.0 earthquake and discordance of sites which have not been affected by the earthquake (Klotz et al., 1995).

Figure 7.3 shows the horizontal surface displacement of the overriding plate of my 3D model representing the northern Chilean area. Similar to Bevis & Martel (2001) and Klotz et al. (1999) my results show displacement vectors above the coupled zone with a higher obliqueness than the convergence vector and the displacement vectors rotate to trench normal direction away from the coupled area.

In contrast to the pure elastic rheology used in the models of Bevis & Martel (2001) and Klotz et al. (1999) I used an elasto-plastic material behaviour (both, temporary and permanent deformations). The models also differ by the way the coupling was implemented at the plate interface. Bevis & Martel (2001) and Klotz et al. (1999) both fully locked a part of the seismogenic zone at the plate interface, whereas I use a constant coefficient of friction μ<0.4 along the assumed coupling zone.
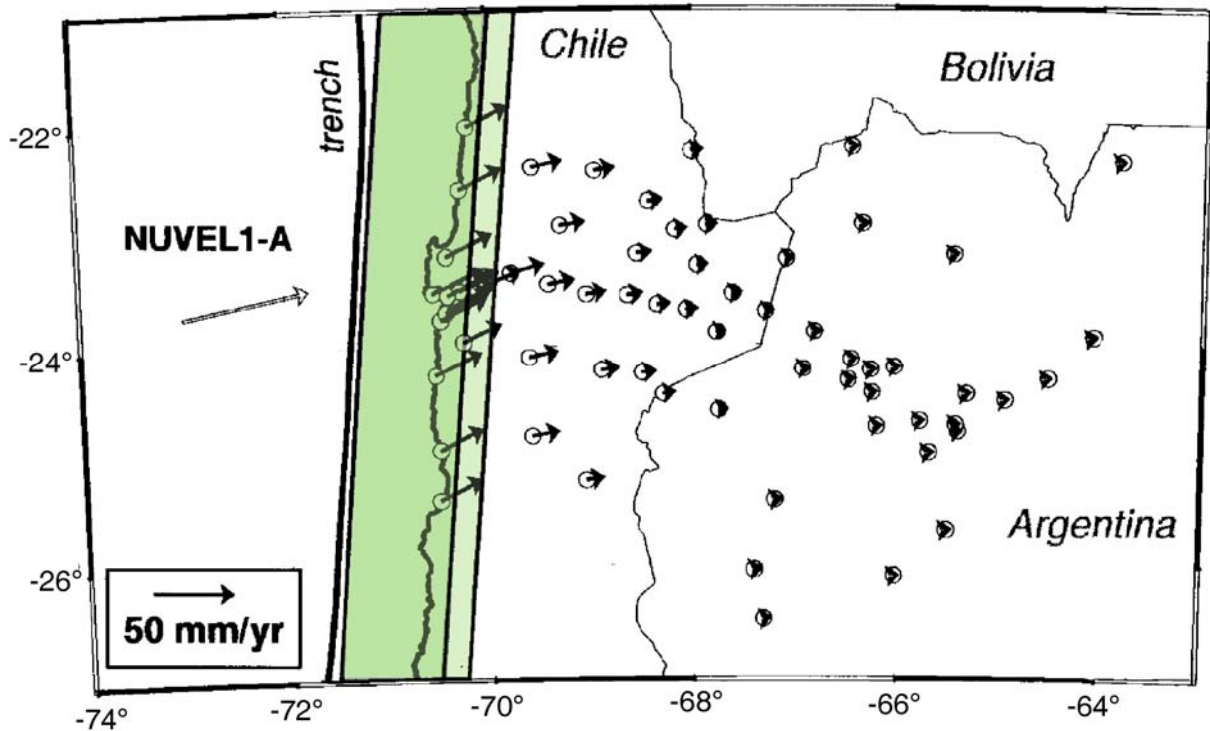
Figure 7.2: Elastic dislocation model modified after Klotz et al. (1999). Shown are the predicted horizontal interseismic displacements. The green shaded areas indicate the assumed locked plate interface (50% of coupling between 40 and 50 km depth denoted by the narrow rectangular).
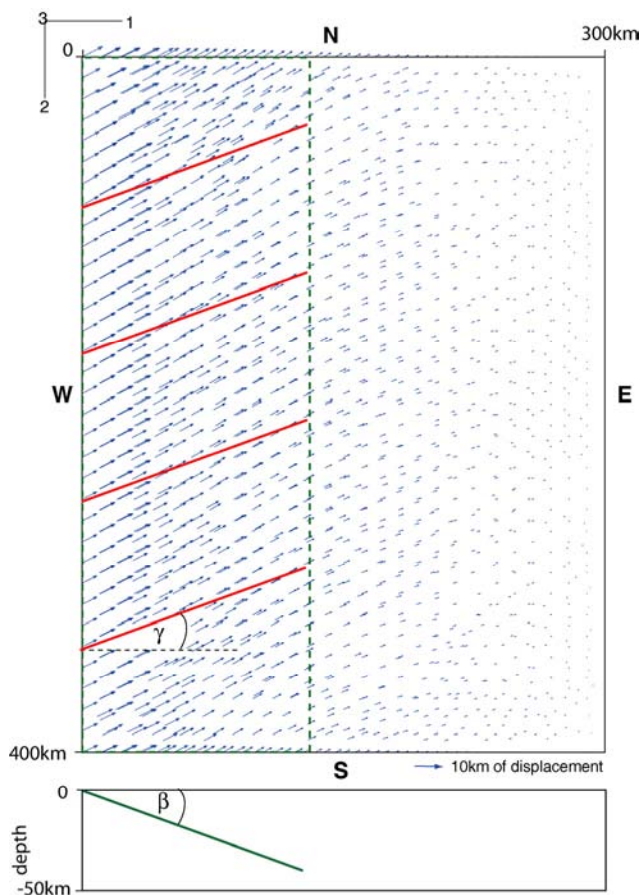
Figure 7.3: Model result of this study. Horizontal surface displacement of the overriding plate (reference model of the northern Chilean study area). Dashed green rectangle shows the frictional coupled area at the plate interface (μ_b=0.4). The red lines indicate the obliqueness of the subducting plate (γ =20°). Rectangle at the bottom shows the depth extend of the coupled area.

While all the models presented in this section are qualitatively comparable to GPS data, only model of Klotz et al. (1999) compares well quantitatively due to assumed constraints concerning surface velocity. Preferential models of this study display good comparison with trench-parallel velocities measured by GPS, but show partially smaller velocities in trench-normal direction for the southern Chilean study area (Figures 6.19 - 6.20).

To understand this discrepancy concerning the trench-normal velocities I present the example of results of modeling the 3D deformation pattern of Andes from Liu et al. (2002). The structure of this model varies compared to the models of this study mainly because of differences in boundary conditions applied to the western edge of Andean orogen. The model of Liu at al. (2002) does not consider subduction, but use an indenter type of Nazca – South America collision, and thus cannot be used to analyze fore-arc wedge deformation. However, the large difference between instantaneous and average rates of deformation in the study of Liu at al. (2002) presented in Figure 7.4 help understanding the difference between my results and GPS measurements.
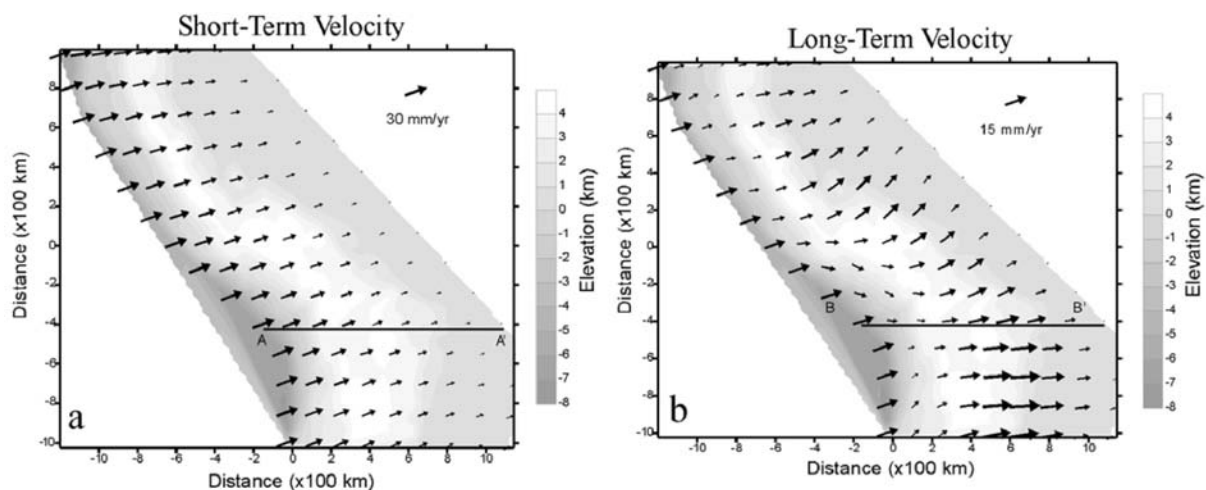
Figure 7.4: Model results of Liu et al. (2002) showing velocities across the northern central Andes. (a) Predicted surface velocities for short-term ($< 10^2$ yr) crustal deformation. (b) Predicted surface velocities for long-term ($> 10^6$ yr) crustal deformation.

The model of Liu at al. (2002) uses a stick-slip condition at the area of plate collision. During "stick" phase of deformation (Figure 7.4a) the South American plate is locked to the Nazca plate. When the stresses rise high, the system unlocks and gravitational spreading changes the deformation pattern, contributing to the average rates of deformation (Figure 7.4b).

The comparison presented in Figure 7.4 shows the importance analyzing which part of the instantaneous deformation during locking results in permanent deformation and which

part recovers during the slip phase of evolution. Applied to the models of the fore-arc wedge deformation, the trench-normal part of displacement acts to compress the wedge and it is most likely to recover almost completely (in the absence of significant thrusting in the study area). In contrast, the stress accumulated by the trench-parallel displacement of the subducting plate can be released by the plastic (non-recoverable) deformation in strike-slip zones. Thus, the model behavior over several stick-slip events should differ to the behavior during the locking event concerning the average accumulated displacement: whereas the trench-parallel rates may compare well, the trench-normal displacement of the model covering several stick-slip events should be smaller. This is well demonstrated in comparison between results of my preferential models for the southern study area with GPS data (Figure 6.20).

Thus, while the locked models of Klotz et al. (1999) and Bevis & Martel (2001) are designed to understand instantaneous rates of deformation (e.g., GPS data) and stresses, my models use average coupling along the interface designed for analysis of longer (geological time-scales) evolution. Different aims of the models give different results and the comparison of these models should be done with caution.

One more important observation can be drawn from the above consideration. Let me compare the wedge response (displacement) to the total displacement of the subducting plate. The ratio of the displacements of the wedge to displacement of the subducting plate may be much higher in the trench-parallel direction than the ratio in the trench-perpendicular direction. Thus, the coupling between plates may be considered as effectively anisotropic, higher in the trench-parallel direction.

7.2   Comparison with analogue experiments

Comparing the results of this study with analogue models highlights other aspects in the evaluation of the numerical models, such as the transition from frictional to frictionless contact and the strength of coupling, because of the 3D character of analogue experiments. To set up analogue experiments simulating oblique subduction is, however, complicated and thus there are not many studies in this field (Chemenda et al., 2000, McClay et al., 2004, Del Castello et al., 2005, Hoffmann-Rothe et al., 2004).

Analogue experiments support the setup of my model regarding the distribution of the friction along the boundary between plates. Only with an S-line (sharp transition from frictional to frictionless coupling), processes observed in nature such as strain partitioning can be reproduced (Chemenda et al., 2000, Hoffmann-Rothe et al., 2004).
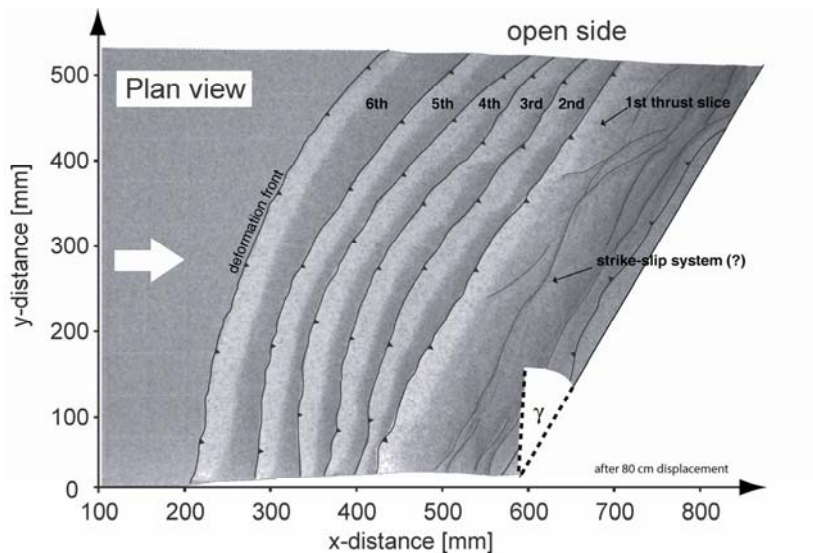
Figure 7.5: Analogue experiment modified after Hoffmann-Rothe et al. (2004)

Figure 7.5 shows the 3D analogue experiment of Hoffmann-Rothe et al. (2004). An obliquity of $\gamma=30°$ and a coefficient of friction between sand and the conveyor belt of $\mu_b\sim0.45$ are used. The experiment series done by Hoffmann-Rothe et al. (2004) exhibits cyclic behaviour of fore-arc thrusting in the accretionary system (Figure 7.6). The cyclic behaviour is characterized by a thrust-initiation phase, during which material is accreted and thrusts develop, and an underthrusting phase, during which material is transported underneath the accretionary complex. In terms of strain partitioning, in the thrust-initiation phase, the entire shortening is accommodated at the deformation front and a large lateral component of the incoming layer remains in the rearward fore-arc, and in the underthrusting phase the shortening reaches further into the fore-arc and thrusts and strike slip faults are forming locally (Figure 7.6).

Analogue models exhibit the initiation of strain partitioning only for very high obliquities. McClay et al. (2004) and Del Castello et al. (2005) investigated the formation of strike slip faults during oblique subduction testing various angles of obliquity. Their models show that the strike slip faulting is only possible if the angle of obliquity is larger than 60°. In the case of smaller angles (<60°) accretion and thrust faulting dominate. Furthermore their experiments show that wedges with strike slip faulting have steep slopes (Figure 7.7).
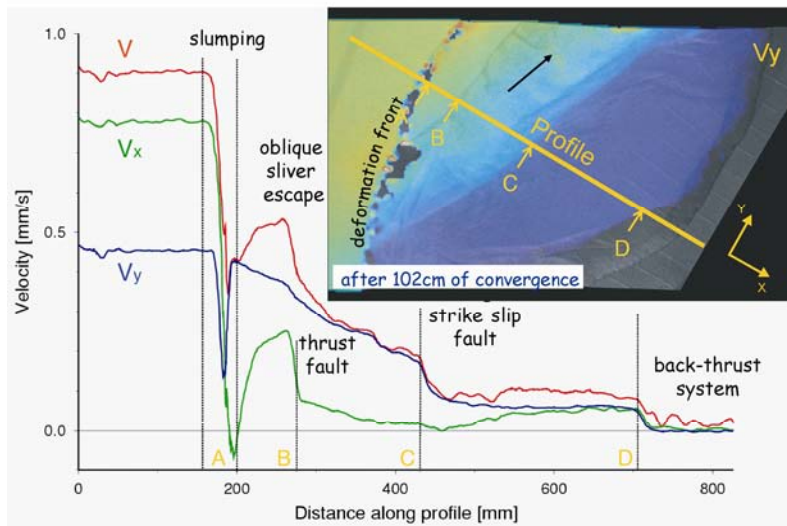
Figure 7.6: Horizontal velocities along a profile (displayed in the color coded picture of v_y) of the analogue experiment by Hoffmann-Rothe et al. (2004), displayed are the horizontal velocities after 102 cm of convergence.

Chemenda et al. (2000) analyzed the influence of basal friction and showed that the initiation of strain partitioning is possible only if friction along the plate interface is sufficiently high. So, partitioning is driven by the force resulting from the friction along the plate interface.
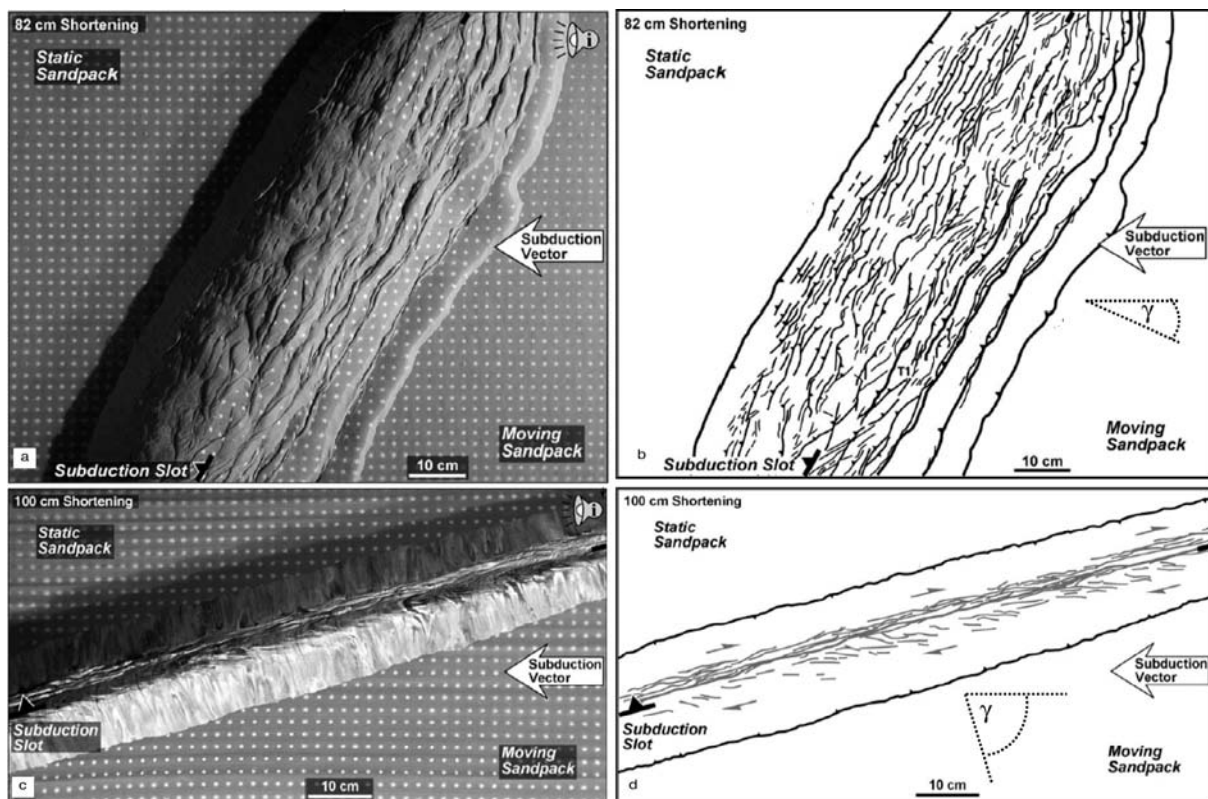
Figure 7.7: Analogue oblique convergence experiments modified after McClay et al. (2004); (a) photograph of the end of the model with 30° obliquity, (b) 30° obliquity model line interpretation; (c) photograph of the end of the model with 75° obliquity, (d) 75° obliquity model line interpretation.

The main difference between the analogue models and the numerical models of my thesis is in the interface between the overriding and subducting plate. The initiation of strain partitioning in the numerical models is controlled by the frictional sliding of the two plates. The evolution of the wedge and therefore the initiation of strain partitioning in the analogue models depends on the incoming layer of sand.

7.3   Variations of coupling between plates along the South American margin

The coupling along the plate boundary refers to a coupling force established at the plate interface. Shear stresses on the interface and the frictionally coupled area define the coupling force (Wang & He, 1999, Hoffmann-Rothe et al., 2006, Klotz et al., 2006).

Here I try to distinguish between two sets of possible explanations for the different styles of deformation in the northern and southern Chilean study areas. One set of plausible models refers to results presented in Section 6.3.1 (variations of basal friction). This set of experiments shows a general trend for the deformational pattern at the surface depending on basal friction. In the northern Chilean study area localized deformation cannot be expected for coefficients of basal friction lower than 0.3 (Figure 6.8). The same set of results (Figure 6.9) demonstrates localized deformation for the southern segment, if the coefficient of basal friction is higher than 0.4. Thus, these results explain the difference in the deformational pattern at the surface with the southward increase of the coefficient of basal friction. Furthermore, the estimates of basal friction from the thermal models favour a southward increase as well (section 4.2).

There are several studies, however, which predict an opposite trend, the southward decrease of the strength of coupling between the Nazca and the South American plate. Even though these studies use different approaches, they demonstrate similar results.

Observations at convergent margins show different modes of mass transfer, erosive and accretive. The amount of coupling is attributed to the mass transfer mode. Erosive margins are supposed to go along with higher strength of coupling, whereas accretive margins with lower coupling (Clift & Vannucchi, 2004, Kukowski & Oncken, 2006, Lamb & Davis, 2003). The supplied sediments in accretive margins lubricate the plate interface and cause lower coupling. Erosive margins are often characterized by rough structures (asperities) on the lower plate, which may lock the two plates. Thus, higher erosion of the western margin of the

Southern Andes should result in southward weakening of coupling between the plates (Clift & Vannucchi, 2004, Kukowski & Oncken, 2006, Lamb & Davis, 2003).

Lamb & Davis (2003) suggest a decreasing coupling at the plate interface from north to south resulting from the variations of shear stresses at the plate interface, which are needed support the high elevations and buoyancy contrasts in the Andes. Their explanation for a decreasing friction from north to south is the presence or absence of significant trench sediment fill.

Sobolev & Babeyko (2005) suggest a decreasing coupling at the plate interface from north to south resulting from thermomechanical numerical modelling, in which they relate the tectonic shortening of the South American plate with the frictional coupling at the plate interface. Only with a southward decrease of frictional coupling their models result in high crustal shortening for the central Andes and minor shortening for the southern Andes. Medvedev et al. (2006) obtained similar results based on thin-sheet numerical modelling of the recent state of deformation in the Nazca – South America collision. In both studies, the southward decrease of the amount of coupling is believed to control the development of the bending of the Andes (Bolivian orocline).

Yáñez & Cembrano (2004) suggest a decreasing coupling at the plate interface from north to south resulting from an empirical relationship between the strength of the plate interface (slip zone) and the age and convergence velocity of the oceanic plate, which they tested in numerical thermomechanical models. The age and convergence rate of the subducting plate directly affect the rheological behaviour at the plate interface: high slip layer (coupling) strength at shallow levels dominated by brittle behaviour (low temperatures, older oceanic plate), and lower slip layer (coupling) strength in high-temperature regimes dominated by viscous behaviour (younger oceanic plate). The decreasing age of the oceanic Nazca plate from north to south along the trench (Figure 4.3) is directly correlated with the decreasing slip layer strength.

Analysis by Wang & He (1999) would suggest a decreasing coupling at the plate interface from north to south resulting from the state of stress in the fore-arc, which depends on the topographic relief and the plate coupling force. The northern Chilean study area is characterized by as much as 300-350 km of crustal shortening (e.g., Isacks, 1988, Elger et al., 2005, Sobolev & Babeyko, 2005) indicating that the compressive plate coupling force exceeds the tensional gravitational force by far. Topography decreases southwards along the margin. Assuming a constant coupling force along the margin would result in increasing crustal shortening towards the south because of decreasing tensional gravitational force.

However, for the southern study area only minor (< 50 km) tectonic shortening has been reported (e.g., Allmendinger et al., 1997, Kley & Monaldi, 1998) implying a lower coupling force.

The model results in section 6.3.1 show that a southward increase in coupling would strengthen our observation of strain partitioning. However, the recent state of the art suggests opposite tendency. Thus, the preferential models use least favourable conditions in terms of the coefficient of basal friction. The preferential models of section 6.4 are in agreement with recent studies mentioned above describing a southward decrease of coupling. The different geometries of the two Chilean segments, in particular the slab dip β, provide the condition for the strain partitioning in the southern Chilean segment in cooperation with a decreasing coefficient of friction. For a smaller wedge taper (slab dip, β, + topography, α) less coupling is needed to generate strain partitioning.

7.4 Role of basal friction

The numerical experiments presented in this work show that the coefficient of basal friction is a crucial parameter governing the deformation. For the numerical models of the Chilean subduction zone the coefficient of basal friction is derived from the critical taper theory (Dahlen, 1984), using knowledge of the geometry and assumed or estimated material parameters of the study areas. This approach results in coefficients of basal friction of μ_b=0.4 for the northern study area and μ_b=0.33 for the southern study area. These values compare well with laboratory experiments on sand (Lohrmann et al., 2003). Several drill sites offshore the southern Chilean area show that the sediments are rich in clay minerals (Mix et al., 2003). Clay minerals reach lowest values for basal friction in laboratory experiments, $0.1 \leq \mu_b \leq 0.15$ (Kopf & Brown, 2003). But these drill cores alone do not allow making assumptions about the properties of sediments being subducted and transported into the subduction channel and the amount of sediments which is accreted at the toe of the fore-arc. Diaz-Naveas (1999) interpreted seismic reflection data between 34° to 42°S along the Chilean margin and showed that the materials mainly contributing to the accretionary wedge are turbidites with minor amounts of pelagic and hemipelagic sediments.

Subducting sediments and altered oceanic crust contain large amounts of fluids in pore spaces and hydrous minerals (Peacock & Hyndman, 1999). The mantle-slab interface is characterized by forming talc-rich minerals, which serve as a lubricant at the plate interface and thus decrease the coefficient of friction causing aseismic behaviour or stable sliding

(Peacock & Hyndman, 1999). This fluid controlled process of talc-rich mineral formation at the mantle-slab interface leads to the assumption of a transition of the frictional behaviour at the plate interface, which coincides with the downdip limit of the seismogenic zone. The downdip limit appears to be controlled by the temperature at the interface ~350°-450°C (Hyndman & Wang, 1993, Hyndman et al. 1997). The results of the thermal models presented in Section 4.2 show for the northern Chilean segment that without additional heating at the plate interface the 350°C isotherm would be far too deep, but for the southern Chilean segment the 350°C isotherm is in a reasonable depth even without applying additional heating. The most appropriate process to heat the plate interface is assumed to be shear heating along the plate interface in the subduction process. For the northern Chilean segment shear stress in the range of $33 < \tau < 67$ MPa is needed to shift the 350°C isotherm into a depth comparable with other observations. Scholz (2002) mentioned earthquake related stress drop values of $0.03 \leq \tau \leq 30$ MPa which is in good correlation with the results of the thermal models for the southern Chilean segment ($\tau < 67$ MPa). I may assume that the high shear stress needed in the northern Chilean segment is related to the exceptionally thick continental crust.

The numerical experiments (Section 6.3) show that values of basal friction higher than the values accepted in the reference models do not lead to acceptable results. The lower values of basal friction result in low rates of deformations. However, the term "low rates" should be treated with caution (see Section 6.1). The comparison with GPS data (<30 yr) should not be treated as the most important test for the models of long-term evolution (>100000 yr). The values of deformation rates obtained by GPS may represent current locking between the two plates, which cannot be the case while considering evolution during hundreds of thousands years, which involve many stages of locking and sliding.

Thus, disrespecting high rates of deformation recorded by GPS, I considered the models with low coefficients of friction. Figure 7.8 presents the results of numerical calculations based on the preferential model, but with a coefficient of friction of $0.15 \leq \mu_b \leq 0.2$. Even with this low friction coefficients a trend of deformation for both Chilean areas is sustained. The model of the northern Chilean area with a coefficient of friction of 0.2 exhibits a distributed deformational pattern (Figure 7.8a), whereas the southern Chilean area with a coefficient of friction of 0.15 has a more localized deformational pattern (Figure 7.8b). Both models are calculated for 1.8 Myr and all other parameters are adopted from the preferential models from Section 6.4. The results show that the used rheologies and material parameters are consistent on different time scales and for different intensity of interpolate coupling.

For the southern study area, Rosenau et al. (2006) describe mean Pliocene to recent shear rates of up to 32 mm/yr dextral movement along the Liquiñe-Ofqui Fault Zone. The models for the southern Chilean area result in shear rates of ~0.4 mm/yr. This implies that higher basal friction is needed in order to reach shear rates of a few centimetres per year. The results show that I can use higher coefficients of friction at the plate interface in order to adjust the observed shear rates and the boundary conditions to the numerical limitations.
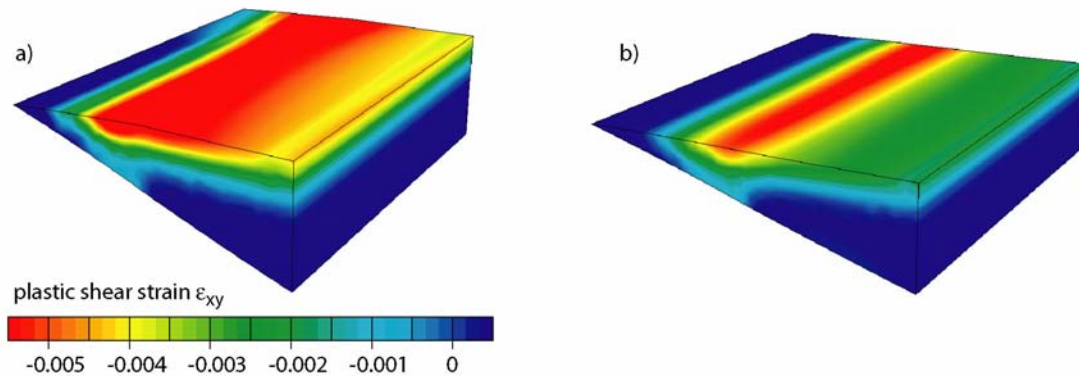
Figure 7.8: Results of numerical models using coefficients of basal friction twice smaller than in the preferential models, μ=0.2 for the northern Chilean area (a) and μ=0.15 for the southern Chilean area (b). Plastic shear strain ε_{xy} is colour coded after 1.8 Myr.

The coefficient of friction at the plate interface is a matter of discussion within the geosciences community. The 3D models of this work are supposed to clarify this discrepancy. The regular occurrence of major earthquakes along the Chilean margin is leading to the assumption of stick slip behaviour and high coefficients of friction at the plate interface before the nucleation of earthquakes. In contrast, there are examples where coefficients of effective friction in the range of $0.01 \leq \mu_b \leq 0.1$ are applied to large scale numerical models of tectonic evolution (e.g. Sobolev et al., 2006). Obviously, there is a difference between laboratory measurements and numerical models of more than one order of magnitude. Certainly, the laboratory measurements do not include processes controlled by temperature, such as fluid release or change of the rheology. Considering the brittle part of the lithosphere and an extension in three dimensions, the numerical models of this work and the related coefficients of friction $0.3 \leq \mu_b \leq 0.4$ at the plate interface are in good correlation with results of laboratory experiments. These relatively high coefficients of friction are necessary to produce models with distributed and localized deformational patterns in 3D.

Large scale numerical models of tectonic evolution of Andean orogeny (Yáñez & Cembrano, 2004; Sobolev et al., 2006; Medvedev et al., 2006) demonstrate that coupling

between the Nazca plate and South America is one of the most important parameters controlling the entire orogen. Even though these large scale models can not be compared directly to the models of this study because of longer time evolution, their cross-sectional (2D) approach, and lower resolution, they show the sensitivity of the models to the parameter of coupling. The significance of the coupling parameter has been also emphasised by the numerical models of this study.

The discrepancy in the values of basal friction, μ_b=0.4 (numerical models in this work) and μ_b≤0.1 (numerical models on entire Andean orogen, e.g., Sobolev & Babeyko, 2005, Medvedev et al., 2006), can be explained with the model set up, the different mechanical aspects addressed in the numerical models, the considered thermal constraints, and the consideration of fluid pressure in the models. The model of Sobolev et al. (2006) describes the subduction at the Chilean margin with slab pull of the oceanic Nazca plate and ridge push of the continental South American plate. This set up leads to higher normal stresses at the plate interface due to the two mechanical mechanisms contributing to the convergence. In the numerical models of my work only one mechanism, the kinematically described subducting Nazca plate, contributes to the subduction process.

Another aspect of the efficiency of coupling between plates was discussed above (in the conclusion of Section 7.1). The cyclic (stick-slip) style of deformation (discussed in Liu et al, 2002 and Wang & Hu, 2006) of the fore-arc wedge subjected to oblique basal traction may result in effectively anisotropic expression of the coupling. The plastic deformation in the strike-slip zones accumulates higher displacements in trench-parallel direction compared to the trench-normal displacements. The aim of this study was to analyze the strike-slip displacements, whereas numerical studies of the Andean orogen (e.g., Sobolev et al, 2006, Medvedev et al., 2006) are more concentrated in the trench-normal deformation.

7.5   Comparison with other subduction zones

Many subduction zones around the world show oblique convergence vectors. To check if the results of the models of my study can be generalized, six subduction zones (Aleutian, Cascadia, Ecuador-Colombia, Kuril, Sumatra, and Tonga-Kermadec, Figure 7.9) were chosen to study for similarities and differences compared to the Chilean areas. All these subduction zones are characterized by convergence oblique to the trench and strike slip faulting in the overriding plate. The strike slip faulting occurs in two different patterns: (1) parallel to the trench and 100 to 300 km inland from it (e.g., Fitch, 1972, Jarrard, 1986) and (2) inclined to

perpendicular to the trench (Jarrard, 1986a, Jarrad, 1986b). A brief description of each subduction zone is given in Appendix B and Table 7.1 lists the main parameters of these zones.
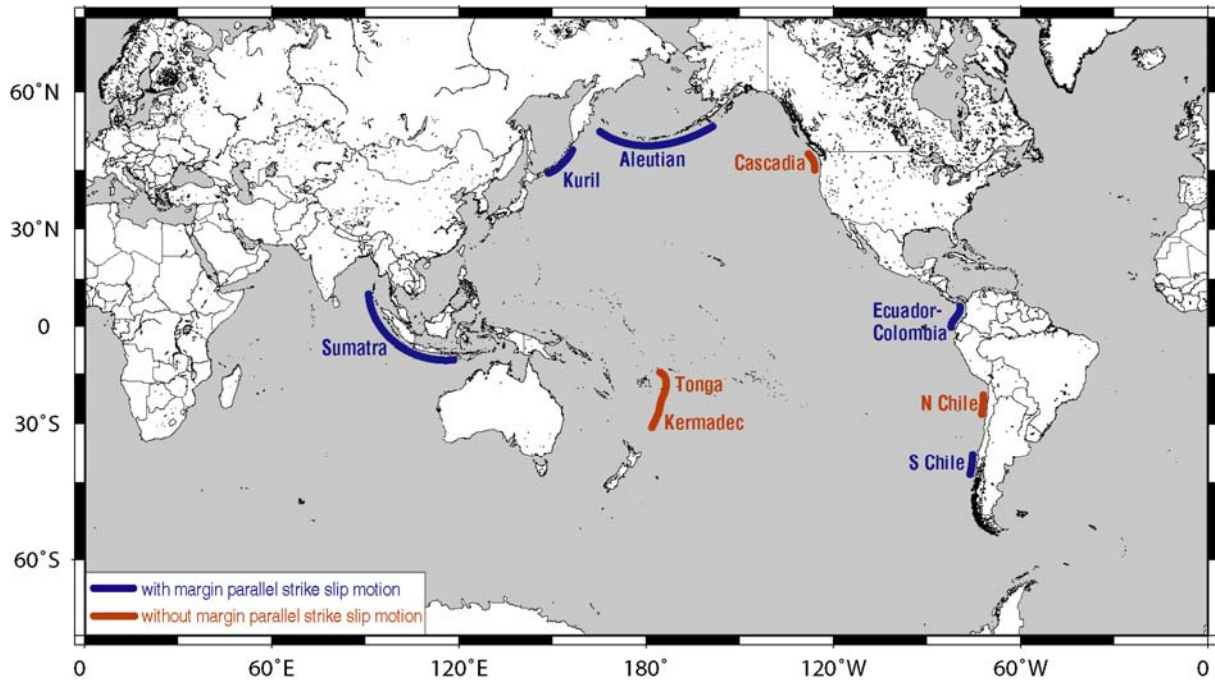
Figure 7.9: Subduction zones considered for the comparison, all characterized by convergence oblique to the trench.

The Aleutian subduction zone is characterized by the curvature of the Aleutian Island arc. This is a major difference compared to the two Chilean subduction zone segments considered here. Linked to the curvature, the change of the convergence vector is another major difference. The convergence rate is similar to the one observed in Chile.

The Cascadia subduction zone is marked by WNW trending left-lateral strike slip faults. Compared to the two segments of the Chilean subduction zone, small similarities can be found with the south Chilean area concerning the WNW trending Bio-Bio-Aluminé (BBAF) and Lanalhue (LFZ) strike slip faults. But a clear difference between the Cascadia subduction zone and Chile is the missing major strike slip fault in Cascadia.

The main feature of the Ecuador-Colombia subduction zone is the major trench parallel Romeral Fault Zone. The southern Chilean subduction zone shows clearly similarities regarding the major strike slip fault together with orientation and slip rate. Obliquity of the convergence vector and convergence rate are equal to the ones observed in the two Chilean subduction zones, essentially due to the fact of the same subducting oceanic Nazca plate.

The Kuril subduction is marked by the Kuril-Mid-Arc Fault, which acts as a major trench parallel strike slip fault. The southwestern part of Kuril can be compared to the south

Chilean zone regarding the presence of a major strike slip fault and the direction of motion along the fault. The obliquity of the convergence vector is similar to the one observed in the south Chilean subduction zone. Even though the convergence rate in south western Kuril is ~30% faster than in south Chile, the trench parallel motion accommodated in the strike slip fault is in the same range.

Table 7.1: *Listed are the different subduction zones with figure number, convergence rate, obliquity of the convergence vector, the arc parallel strike slip motion, and topographic variations (height difference: trench – orogenic belt).*

name	figure number	convergence rate	obliquity	arc parallel strike-slip motion	topographic variations
north Chile	1.1/1.2a	~65 mm/yr [1, 13,20,21]	~20°-30° [22,25]	<1 mm/yr [4,8,17,23,]	~ 10 km
south Chile	1.1/1.2b	~65 mm/yr [1,13,20,21]	~20°-30° [22,25]	>10 mm/yr [24]	~ 4 km
Aleutians	A2.1	~65-85 mm/yr [7,14]	~0-80° [5,7,14,31]	~20-40 mm/yr [7]	~ 6 km
Cascadia	A2.2	~40 mm/yr [5,19,29,30]	~25° [19]	0[*]	~ 7 km
Ecuad.-Col.	A2.3	~65 mm/yr [9,20,26,27]	~10°-40° [5,10]	~5-10 mm/yr [9,17]	~ 6 km
Kuril	A2.4	~90 mm/yr [5,11,12]	~10°-20° [10,12]	~6-11 mm/yr [6,17]	~ 4 km
Sumatra	A2.5	~60-70 mm/yr [15]	~35-50° [16,18]	~15-30 mm/yr [2,15,16,18]	~ 6 km
Tonga	A2.6	~160-240 mm/yr [3]	~10°-30° [3,28]	0[*]	~ 6 km
Kermadec	A2.6	~50 mm/yr [3]	~5° [3,28]	0[*]	~ 5 km

[*] no arc parallel strike slip fault

[1] Angermann et al., 1999, [2] Baroux et al., 1998, [3] Bevis et al., 1995, [4] Delouis et al., 1998, [5] DeMets et al., 1990, [6] DeMets, 1992, [7] Geist & Scholl, 1992, [8] Gonzáles et al., 2006, [9] Gutscher et al., 1999, [10] Jarrard, 1986b, [11] Kiruma, 1986, [12] Klaeschen et al., 1994, [13] Klotz et al., 1999, [14] Lallemant, 1996, [15] Malod & Kemal, 1996, [16] McCaffrey, 1992, [17] McCaffrey, 1996, [18] McCaffrey et al., 2000, [19] McCroy, 1996, [20] Norabuena et al., 1998, [21] Norabuena et al., 1999, [22] Pardo-Casas & Molnar, 1987, [23] Pelz, 2000, [24] Rosenau et al., 2006, [25] Somoza, 1998, [26] Taboada et al., 2000, [27] Trenkamp et al., 2002, [28] Wallace et al., 2005, [29] Wells et al., 2002, [30] Wilson, 2002, [31] Yu et al., 1993

The Sumatra subduction zone is subdivided by two major fault zones, the Mentawai fault and the Sumatra fault. The only similarity with the south Chilean area can be seen concerning the major strike slip fault. But the clear differences between the Sumatra subduction zone and Chile are the existence of two major strike slip faults, the degree of partitioning, and the convex curvature of the trench.

The Tonga-Kermadec subduction zone and the two Chilean segments are very different. Tonga-Kermadec is characterized by backarc spreading and the transform plate boundary, the Fiji Fracture Zone, marking-off Tonga to the north. These zones cannot be directly compared even though both are characterized by oblique convergence.

Some general statements can be revealed from the comparison of different subduction zones. Only the Sumatra subduction zone is marked by two major trench parallel strike slip faults of different natures and these faults accommodate the trench parallel convergence component by 100%. The northern Chilean segment is also characterized by two major margin parallel strike slip faults but both have the same nature; the Atacama Fault Zone originated in the Jurassic magmatic arc and the Precordilleran Fault System originated in the Eocene magmatic arc. In all other subduction zones with one active major trench parallel strike slip fault (south Chile, Ecuador-Colombia, and Kuril), only a part of the trench parallel convergence component is accommodated by these faults. The remaining part of the trench parallel component has to be accommodated by other mechanisms (e.g., block rotations).The Aleutian subduction zone (Geist & Scholl, 1992, Lallemant, 1996) and the Cascadia subduction zone (Appelgate et al., 1992, Goldfinger et al., 1992, McCaffrey et al., 2000, Wells & Simpson, 2001) exhibit block rotation. Both Chilean segments also indicate block rotation. The northern Chilean segment is characterized by counterclockwise rotation north of Arica and clockwise south of Arica (e.g., Somoza at al., 1996, Beck, 1998, Somoza et al. 1999, Prezzi & Alonso, 2002).The saw-tooth morphology of the coast line of southern Chilean segment suggests dextral rotations of these segments (Vietor et al., 2005).

The Kuril subduction zone is similar to both Chilean segments. Kuril is divided into two parts, the northern part without major trench parallel strike slip faulting and the southern part with a well developed trench parallel strike slip fault. The same pattern can be observed along the Chilean margin. The northern Chilean margin shows presently only minor active margin parallel strike slip motion (Gonzáles et al., 2006) and the southern Chilean margin shows trench parallel strike slip motion of ~1 cm/yr (Rosenau et al., 2006). The Kuril subduction zone would be a good example to compare in detail with the Chilean subduction zone because of the number of similarities.
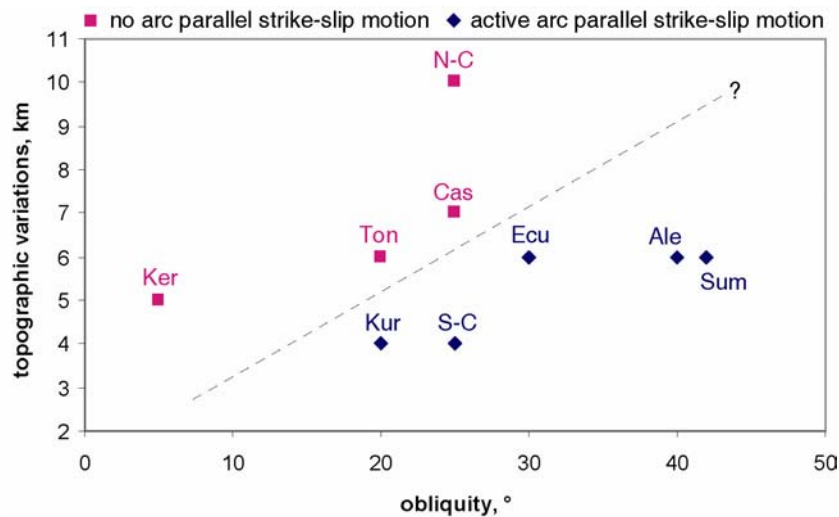
Figure 7.10: Plot shows relation between obliquity, topographic variations, and strike-slip motion of the different subduction zone. Ale – Aleutian, Cas – Cascadia, Ecu – Ecuador, Ker – Kermadec, Kur – Kuril, N-C – north Chile, S-C – south Chile, Sum – Sumatra, Ton – Tonga.

Although there are a number of similarities and dissimilarities in the subduction zones described above, I try to find first order parameters which can distinguish between subduction zones with and without strong partitioning of deformation due to active strike-slip trench-parallel faulting. Strike-slip deformation in the fore-arc wedge is impossible without oblique subduction, and thus, obliquity should be one of the measures that have to be taken into account. My numerical models and particularly the set of preferred models show another important characteristic that can separate localized and distributed deformation in the fore-arc wedge. The northern and southern Chilean segments differ by the strength of the wedge material. The source of that difference may be assessed to the maturity of the orogen created by the active subduction. The more developed northern segment of my study is reported to be hotter and thus weaker. As a simple first order measure of the maturity of orogens considered above I chose their topographic variations (Table 7.1). Figure 7.10 presents the behavior of the fore-arc wedges depending on the angle of obliquity and the perturbation of topography (difference in elevation between orogenic belt and trench). Higher obliquity and smaller topographic perturbations favor the trench parallel strike-slip faulting, whereas lower obliquity of subduction and higher topographic perturbations favor distributed deformation. Thus, the analysis of world-wide subduction zones supports the conclusions of my study.

8 Conclusions and future research

This thesis aimed to find reasons for the variations of styles of deformation observed along the western margin of South America. I examined the evolution of strain distribution in the fore-arc wedges subjected to oblique subduction using 3D numerical modeling. These models were constructed with the help of the analysis of field data and published models and augmented by additional numerical and analytical studies.

The models were applied to two representative areas of the South America margin (northern study area 20°-24°S and southern study area 37° - 42°S). In spite of the fact that both areas are subject to similar influence of the obliquely subducting Nazca plate, the surface expressions of deformation differ significantly (Sections 1 and 3). Although I used a simplified wedge-shape geometry to represent the fore-arc of both study areas, their main features were made similar to nature (Section 6.1). Through analyzing slab dip and surface topography of the two regions, I found that the wedge of the northern region is much thicker, but this condition alone is not enough to explain the difference in deformation styles.

The model uses an elasto-plastic rheology to describe wedge behavior (Section 2.2, see also Section 6.2 for comparison between elasto-plastic and pure elastic approaches). Equations, describing the system (Sections 2.1-2.3), were resolved using the commercial finite-element software package ABAQUS (Section 2.4).

Coupling between the Nazca and the South America plate is the important control of the deformation of the fore-arc wedge. Two main parameters of coupling: spatial distribution (extend of frictional contact between plates) and strength (expressed in the model by the coefficient of basal friction, μ_b), were studied extensively.

Thermal cross-sectional models (Section 5.2) were performed to analyze the depth extent of the frictionally coupled zone. Numerical simulations for both study areas have shown that the transition between frictional and frictionless coupling should be sharp because of high temperature gradients around the juncture slab - continental crust - mantle wedge. Furthermore the thermal models show the significance of shear heating applied to the plate interface. Reasonable results for the depth extent of the frictionally coupled zone can only be achieved by including shear heating along the plate interface. The calculated extent of frictional coupling compares well with results of other models.

The value of the coefficient of friction cannot be estimated directly and thus requires additional study. The reference models use coefficients of basal friction calculated from the Dahlen (1984) theory of critical tapers ($\mu_{b,north}$=0.4, $\mu_{b,south}$ =0.33). This theory does not account for the elastic part of the wedge in my models. Some other models (e.g., tectonic models by Sobolev et al, 2006; my thermal models from Section 4), however, point out that friction between the plates should be of a much smaller value. That uncertainty forced me to look for solutions with low dependence from the friction coefficient. Thus, the preferred models, based on high friction (Section 6.4), sustain their first order properties, such as significant difference in styles, even if the value of friction is reduced by a factor of two (Section 7.4).

Whereas a southward increase in coupling could explain the localized deformation in the southern study area, several independent observations (e.g., mode of mass transfer, tectonic shortening, age of incoming oceanic plate, state of stress in the fore-arc) give strong arguments that coupling should decrease to the south (Wang & He, 1999, Lamb & Davis, 2003, Clift & Vannucchi, 2004, Yañez & Cembrano, 2004, Sobolev & Babeyko, 2005, Kukowski & Oncken, 2006). Therefore other parameters must be responsible for the observed localized deformation. Consequently, I did not base my preferred models solely on the variations of the strength of coupling and checked the effect on the surface deformation of several parameters including obliquity, Young's modulus, and slab dip.

Most of the models exhibit preferential strike-slip strain with deformation localized in the vicinity of the transition from frictional to frictionless interaction between overriding and subducting plate (section 6.3). This behavior generally corresponds to the results of GPS studies.

The trench-normal velocities at the surface of the models are generally smaller than the ones obtained from GPS measurements. This may indicate that the interface of the two plates is currently locked and the contemporary rates of east-ward motion due to elastic shortening are higher than geologically averaged (section 7.1).

The parameter study exposes general trends with respect to a hierarchal order of the analyzed parameters. The larger the slab dip is, the bigger the wedge is, the more difficult it is to cause localized wedge deformation. The higher the obliquity is, the easier to partition the deformation of the wedge. The weaker the wedge material is, the easier to result in distributed wedge deformation. Obliquity of convergence and coupling between the plates are the factors that cause localization of deformation. Numerical experiments show that the increase of obliquity and interplate friction favors strain partitioning. Similarly, shallower slab dip and

stronger wedge material (higher Young's modulus) also lead to stronger localization of deformation.

Based on the parameters study (Sections 6.3), I constructed the preferred models for the northern and southern study areas (Section 6.4). The preferred models compare well to the different styles of deformations of corresponding natural areas and thus may explain the difference in styles. Two preferred models result in higher strain partitioning of southern segment due to following:

- a shallower subduction of the southern region: average slab dip is 18.4° in the northern segment compared to a smaller slab dip of 13.4° in the southern segment;

- a higher obliquity of the subducting plate in the southern segment: increase from 20° to 30° southward;

- an assumed weakening of the fore-arc wedge of the northern segment: Young's modulus decreases from 85 GPa in the southern segment down to 30 GPa in the northern segment.

The assumed weakening of the northern segment correlates with the warm thickened crust of the highly deformed Central Andes. I speculate that the contrast of the cold and low deformed southern segment with the northern segment represents the stages of evolution of the fore-arc in response to oblique subduction. Initially, a strong and brittle crust favors localized accommodation of oblique motion of the down going plate. That process activated recent motion of the Liquiñe-Ofqui Fault Zone and may be responsible for the active deformation of the Atacama Fault Zone and the Precordilleran Fault System in the northern segment on the earlier stages of development. As deformation continues, the wedge material becomes weaker and that the deformation pattern becomes more diffused.

The comparison of the two preferred models of this study with other areas subjected to oblique subduction (Section 7.5) supports my conclusions. Figure 7.10 shows that more developed zones (measured by topographic perturbations of subduction related orogenic system) tend to distributed deformation, whereas zones with lower topographic variations usually result in active strike-slip faulting.

The implementation of stick-slip behaviour would help to refine both thermal and mechanical model results. A continental lithosphere with a stratified and temperature sensitive rheology should be implemented. Coupled thermomechanical modelling enables us to derive stress and strain distribution dependent on the thermal state of the lithosphere. Apart from that, a dynamically modelled subducting and overriding plate will allow us to investigate the interaction between both plates.

References

ABAQUS User's Manual (2004), vol. 3, version 6.5, ABAQUS Inc., Providence, Rhode Island, USA

Adam, J. & Reuther, C.-D., 2000. Crustal dynamics and active fault mechanics during subduction erosion. Application of frictional wedge analysis on to the North Chilean Forearc, *Tectonophysics*, vol. 321, 297-325

Al-Busaidi, A., Hazzard, J.F. & Young, R.P. (2005). Distinct element modeling of hydraulically fractured Lac du Bonnet granite, *Journal of Geophysical Research*, vol. 110, B06302, doi:10.1029/2004JB003297

Allmendinger, R.W., Isacks, B.L., Jordan, T.E. & Kay, S.M. (1997). The evolution of the Altiplano-Puna plateau of the Central Andes, *Annual Reviews of Earth Science*, vol. 25, 139-174.

Altenbach, J. & Altenbach, H. (1994). *Einführung in die Kontinuumsmechanik*, Teubner, Stuttgart, 285 p.

ANCORP Working Group (1999). Seismic reflection image revealing offset of Andean subduction-zone earthquake locations into oceanic mantle, *Nature*, vol. 397, 341-344

ANCORP Working Group (2003). Seismic imaging of a convergent continental margin and plateau in the central Andes (Andean Continental Research Project 1996 (ANCORP'96)), *Journal of Geophysical Research*, vol. 108(B7), doi:10.1029/2002JB001771

Anderson, D.L. (1992). The earth's interior, In: Brown, G.C., Hawkesworth, C.J. & Wilson, R.C.L. (eds.), *Understanding the earth - a new synthesis*, Cambridge University Press, Cambridge, 44-66

Angermann, D., Klotz, J. & Reigber, C. (1999). Space-geodetic estimation of the Nazca-South America Euler vector, *Earth and Planetary Science Letters*, vol. 177, 329-334

Appelgate, B., Goldfinger, C., MacCay, M.E., Kulm, L.D., Fox, C.G., Embley, R.W. & Meis, P.J. (1992). A left-lateral strike-slip fault seaward of the Oregon convergent margin, *Tectonics*, vol. 11(3), 465-477

Babeyko, A.Y., Sobolev, S.V., Vietor, T., Oncken, O. & Trumbull, R. (2006). Weakening of the Upper Plate during Tectonic Shortening: Thermo-Mechanical Causes and Consequences, In: Oncken, O., Chong, G., Franz, G., Giese, P., Götze, H.-J., Ramos, V., Strecker, M. & Wigger, P. (eds.), *The Andes: Active Subduction Orogeny*, Frontiers in Earth Sciences, vol. 1, Springer

Bangs, N.L. & Cande, S.C. (1997). Episodic development of a convergent margin inferred from structures and processes along the southern Chile margin, *Tectonics*, vol. 16, 489-503

Bardet, J.P. (1990). Lode Dependences for Isotropic Pressure-Sensitive Elastoplastic Materials, *Journal of Applied Mechanics*, *ASME*, vol. 57, 498-506

Baroux, E., Avouac, J.-P., Bellier, O. & Sébrier, M. (1998). Slip-partitioning and fore-arc deformation at the Sunda Trench, Indonesia, *Terra Nova,* vol. 10(3), 139-144

Beaumont, C., Ellis, S. & Pfiffner, A. (1999). Dynamics of sediment subduction-accretion at convergent margins: Short-term modes, long-term deformation, and tectonic implications, *Journal of Geophysical Research*, vol. 104(B8), 17573-17601

Beck, M.E. (1983). On the mechanism of tectonic transport in zones of oblique subduction, *Tectonophysics*, vol. 93, 1-11

Beck Jr., M.E. (1991). Coastwise transport reconsidered: lateral displacement in oblique subduction zones, and tectonic consequences, *Physics of the Earth and Planetary Interiors*, vol. 68, 1-8

Beck Jr., M.E. (1998). On the mechanism of crustal block rotations in the central Andes, *Tectonophysics*, vol. 299, 75-92

Beck, S., Barrientos, S., Kausel, E. & Reyes, M. (1998). Source characteristics of historic earthquakes along the central Chile subduction zone, *Journal of South American Earth Sciences*, vol. 11(2), 115-129

Beck, S.L. (1996). Crustal-thickness variations in the central Andes, *Geology*, vol. 24(5), 407-410

Bevis, M., Taylor, F.W., Schutz, B.E., Recy, J., Isacks, B.L., Helu, S., Singh, R., Kendrick, E., Stowell, J., Taylor, B. & Calmant, S. (1995). Geodetic observations of very rapid convergence and back-arc extension at the Tonga arc, *Nature*, vol. 374, 249-251

Bevis, M., Smalley Jr., R., Herring, T., Godoy, J. & Galban, F. (1999). Crustal Motion North and South of the Arica Deflection: Comparing Recent Geodetic Results from the Central Andes, *Geochemistry, Geophysics, Geosystems G³*, vol. 1, 1999GC000011

Bevis, M. & Martel, S.J. (2001). Oblique plate convergence and interseismic strain accumulation, *Geochemistry, Geophysics, Geosystems G³*, vol. 2, doi:2000GC000125

Bird, P. (1996). Computer simulations of Alaskan neotectonics, *Tectonics*, vol. 15(2), 225-236

Blanpied, M.L., Lockner, D.A. & Byerlee, J.D. (1991). Fault stability inferred from granite sliding experiments at hydrothermal conditions, *Geophysical Research Letters*, vol.18, 609-612

Blanpied, M.L., Lockner, D.A. & Byerlee, J.D. (1995). Frictional slip of granite at hydrothermal conditions, *Journal of Geophysical Research*, vol. 100, 13045-13064

Bohm, M., Lüth, S., Echtler, H., Asch, G., Bataille, K., Bruhn, C., Rietbrock, A. & Wigger, P. (2002). The Southern Andes between 36° and 40°S latitude: seismicity and average seismic velocities, *Tectonophysics*, vol. 356, 275-289

Brace, W.F. & Byerlee, J.D. (1970). California earthquakes: Why only shallow focus?, *Science*, vol. 168, 1573-1575

Braile, L.W. (2000). Thermal Convection and Viscosity of a Fluid, www.eas.purdue.edu/~braile/edumod/convect/convect.doc

Brasse, H. & Soyer, W. (2001). A magnetotelluric study in the Southern Chilean Andes, *Geophysical Research Letters*, vol. 28(19), 3757-3760

Braun, J. & Beaumont, C. (1995). Three-dimensional numerical experiments of strain partitioning at oblique plate boundaries: Implications for contrasting tectonic styles in the southern Coast Ranges, California, and central South Island, New Zealand, *Journal of Geophysical Research*, vol. 100(B9), 18059-18074

Brooks, B.A., Bevis, M., Smalley, R., Kendrick, E., Manceda, R., Lauría, E., Maturana, R. & Araujo, M. (2003). Crustal motion in the Southern Andes (26°-36°S): Do the Andes behave like a microplate?, *Geochemistry, Geophysics, Geosystems G³*, vol. 4(10), doi:10.1029/2003GC000505

Buiter, S.J.H., Babeyko, A.Y., Ellis, S., Gerya, T.V., Kaus, B.J.P., Kellner, A., Schreurs, G. & Yamada, Y. (2006). The numerical sandbox; Comparison of model results for a shortening and an extension experiment, In: Buiter, S.J.H. & Schreurs, G. (eds), *Analogue and Numerical Modelling of Crustal-Scale Processes,* Geological Society, London, Special Publication, 253, 29-64

Bunge, H.-P. (2005). Low plume exess temperature and high core heat flux inferred from non-adiabatic geotherms in internally heated mantle circulation models, *Physics of the Earth and Planetary Interiors*, vol. 153, 3-10

Cahill, T. & Isacks, B. (1992). Seismicity and shape of the subducted Nazca plate, *Journal of Geophysical Research*, vol. 97, 17503-17529

Campos, J. & Kausel, E. (1990). The large 1939 intraplate earthquake of southern Chile, Seismological Research Letters, vol. 61(1), 43

Cembrano, J., Schermer, E., Lavenu, A. & Sanhueza, A. (2000). Contrasting nature of deformation along an intra-arc shear zone, the Liquiñe-Ofqui fault zone, southern Chilean Andes, *Tectonophysics*, vol. 319, 129-149

Chemenda, A., Lallemand, S. & Bokun, A. (2000). Strain partitioning and interplate friction in oblique subduction zones: Constraints provided by experimental modeling, *Journal of Geophysical Research*, vol. 105(B3), 55679-5581

Chen, W.P. & Molnar, P. (1983). Focal depths of intra-continental and intraplate earthquakes and their implications fort he thermal and mechanical properties of the lithosphere, *Journal of Geophysical Research*, vol. 88, 4183-4214

Chlieh, M., de Chabalier, J.B., Ruegg, J.C., Armijo, R., Dmowska, R., Campos, J. & Feigl, K.L. (2004). Crustal deformation and fault slip during the seismic cycle in the North Chile subdus´ction zone, from GPS and InSAR observations, *Geophysical Journal International*, vol. 158, doi:10.1111/j.1365-246X.2004.02326.x, 695-711

Cifuentes, I. (1989). The 1960 Chile earthquakes, *Journal of Geophysical Research*, vol. 94(B1), 665-680

CINCA Working Group (1997). Results of the marine geo-science survey SO-104/CINCA, paper presented at *VIII Congreso Geológico Chileno*, Uni. Católica del Norte, Antofagasta, Chile, 4-8 August

Cingolani, C., Dalla Salda, L., Hervé, F., Munizaga, F., Pankhurst, R.J., Parada, M.A. & Rapela, C.W. (1991). The magmatic evolution of northern Patagonia; New impressions of pre-Andean and Andean tectonic, *Geological Society of America*, Special Paper 265, 29-45

Clift, P. & Vannucchi, P. (2004). Controls on tectonic accretion versus erosion in subduction zones: Implications for the origin and recycling of the continental crust, *Review of Geophysics*, vol. 42, RG2001, doi:10.1029/2003RG000127

Cobbold, P.R. & Rosselo, E. (2003). Aptian to Recent compressional deformation, foothills of the Neuquen Basin, Argentina, *Marine and Petroleum Geology*, vol. 20(5), 429-443

Collot, J.-Y., Charvis, P., Gutscher, M.-A. & Operto, S. (2002). Exploring the Ecuador-Colombia active margin and inter-plate seismogenic zone, *EOS, Transactions*, American Geophysical Union, vol. 83(17), 189-190

Collot, J.-Y., Marcaillou, B., Sage, F., Michaud, F., Agudelo, W., Charvis, P., Graindorge, D., Gutscher, M.-A. & Spence, G. (2004). Are rupture zone limits of great subduction earthquakes controlled by upper plate structures? Evidence from multichannel seismic reflection data acquired across the northern Ecuador-southwest Colombia margin, *Journal of Geophysical Research*, vol. 109(B11103), doi:10.1029/2004JB003060

Comte, D., Pardo,M., Dorbath, L., Dorbath, C., Haessler, H., Rivera, L., Cisternas, A., Ponce, L. (1994). Determination of seismogenic interplate contact zone and crustal seismicity around Antofagasta, northern Chile using local data, *Geophysical Journal International*, vol. 116(3), 553-561

Conrad, C.P., Bilek, S. & Lithgow-Bertelloni, C. (2004). Great earthquakes and slab pull: interaction between seismic coupling and plate-slab coupling, *Earth and Planetary Science Letters*, vol. 218, 109-122

Cortés, M. & Angelier, J. (2005). Current states of stress in the northern Andes as indicated by focal mechanisms of earthquakes, *Tectonophysics*, vol. 403, 29-58

Cundall, P. A. & Strack, O.D.L. (1979). A distinct element model for granular assemblies, *Geotechnique*, vol. 29, 47–65

Dahlen, F.A. (1984). Noncohesive Critical Coulomb Wedges: An Exact Solution, *Journal of Geophysical Research*, vol. 89(B12), 10125-10133

Dahlen, F.A., Suppe, J. & Davis, D. (1984). Mechanics of Fold-and-Thrust Belts and Accretionary Wedges: Cohesive Coulomb Theory, *Journal of Geophysical Research*, vol. 89(B12), 10087-10101

Darwin, C. (1972). Geological Observations on the Volcanic Island and Parts of South America Visited During the Voyage of H M S Beagle, AMS Press, New York City, 648p.

Davis, D., Suppe, J. & Dahlen, F.A. (1983). Mechanics of Fold-and-Thrust Belts and Accretionary Wedges, *Journal of Geophysical Research*, vol. 88(B2), 1153-1172

Davis, R.O. & Selvadurai, A.P.S. (2002). *Plasticity and Geomechanics*, Cambridge University Press, Cambridge, 287 p

Del Castello, M., McClay, K.R. & Pini, G.A. (2005). Role of pre-existing topography and overburden on strain partitioning of oblique doubly vergent convergent wedges, *Tectonics*, vol. 24, doi:10.1029/2005TC001816

Delouis, B., Philip, H., Dorbath, L. & Cisternas, A. (1998). Recent crustal deformation in the Antofagasta region (northern Chile) and the subduction process, *Geophysical Journal International*, vol. 132(2), 302-338

DeMets, C., Gordon, R.G., Argus, D.F. & Stein, S. (1990). Current plate motions, *Geophysical Journal International*, vol. 101, 425-478

DeMets, C. (1992). Oblique Convergence and Deformation Along the Kuril and Japan Trenches, *Journal of Geophysical Research*, vol. 97(B12), 17615-17625

DeMets, C., Gordon, R.G., Argus, D.F. & Stein, S. (1994). Effect of recent revisions to the geomagnetic reversal time scale on estimates of current plate motions, *Geophysical Research Letters*, vol. 21, 2191-2194

Dewey, J.F. & Lamb, S.H. (1992). Active tectonics of the Andes, *Tectonophysics*, vol. 205, 79-95

Diaz-Naveas, J.L. (1999). *Sediment subduction and accretion at the Chilean convergent margin*, PhD thesis, CAU Kiel, 130 p.

Drucker, D.C. & Prager, W. (1952). Soil Mechanics and Plastic Analysis or Limit Design, *Quarterly of Applied Mathematics*, vol. 10(2), 157-165

Dumitru, T.A. (1991). Effects of Subduction Parameters on Geothermal Gradients in Forearcs, With an Application to Franciscan Subduction in California, *Journal of Geophysical Research*, vol. 96(B1), 621-641

Ehlers, W. (2006). Combining discrete and continuous media by homogenization techniques, 19th *Kongsberg Seminar,* Kongsberg (Norway), May 03-05, 17-18

Elger, K., Oncken, O. & Glodny, J. (2005). Plateau-style accumulation of deformation: Southern Altiplano, *Tectonics*, vol. 24(8), TC4020, doi:10.1029/2004TC001675

Ellis, S. & Stöckhert, B. (2004). Elevated stresses and creep rates beneath the brittle-ductile transition caused by seismic faulting in the upper crust, *Journal of Geophysical Research*, vol. 109, B05407, doi:10.1029/2003JB002744

Fischer, K.D. (2006). The influence of different rheological parameters on the surface deformation and stress field of the Aegean-Anatolian region, *International Journal of Earth Sciences*, DOI 10.1007/s00531-005-0031-0

Fitch, T.J. (1972). Plate Convergence, Transcurrent Faults, and Internal Deformation Adjacent to Southeast Asia and the Western Pacific, *Journal of Geophysical Research*, vol. 77(23), 4432-4460

Funiciello, F., Morra, G., Regenauer-Lieb, K. & Giardini, D. (2003). Dynamics of retreating slabs: 1. Insights from two-dimensional numerical experiments, *Journal of Geophysical Research*, vol. 108(B4), 2206, doi:10.1029/2001JB000898

García-Rojo, R., McNamara, S. & Herrmann, H.J. (2004). Discrete Element Methods for the Micro-Mechanical Investigation of Granular Ratcheting, In: Neittaanmäki, P., Rossi, T., Majava, K., Pironneau, O., Korotov, S., Oñate, E., Périaux, J. & Knörzer, D. (eds.), *European Congress on Computational Methods in Applied Sciences and Engineering – ECCOMAS 2004*, University of Jyväskylä, Department of Mathematical Information Technology

Geist, E.L. & Scholl, D.W. (1992). Application of Continuum Models to Deformation of the Aleutian Island Arc, *Journal of Geophysical Research*, vol. 97(B4), 4953-4967

Gephart, J.W. (1994). Topography and subduction geometry of the Central Andes: Clues to the mechanics of a non-collisional orogen, *Journal of Geophysical Research*, vol. 99(B6), 12279-12288

Gerbault, M., Poliakov, A.N.B. & Daignieres, M. (1998). Prediction of faulting from the theories of elasticity and plasticity: what ate the limits, *Journal of Structural Geology*, vol. 20(2/3), 301-320

Gerya, T.V. & Yuen, D.A. (2003). Rayleigh-Taylor instabilities from hydration and melting propel ,cold plumes' at subduction zones, *Earth and Planetary Science Letters*, vol. 212, 47-62

Giese, P., Scheuber, E., Schilling, F., Schmitz, M. & Wigger, P. (1999). Crustal thickening processes in the Central Andes and the different natures of the Moho-discontinuity, *Journal of South American Earth Sciences*, vol. 12, 201-220

Glodny, J., Echtler, H., Figueroa, O., Franz, G., Gräfe, K., Kemnitz, H., Kramer, W., Krawczyk, C., Lohrmann, J., Lucassen, F., Melnick, D., Rosenau, M. & Seifert, W. (2006). Long-Term Geological Evolution and Mass-Flow Balance of the South-Central Andes, In: Oncken, O., Chong, G., Franz, G., Giese, P., Götze, H.-J., Ramos, V., Strecker, M. & Wigger, P. (eds.), *The Andes: Active Subduction Orogeny*, Frontiers in Earth Sciences, vol. 1, Springer

Goldfinger, C., Kulm, L.D., Yeats, R.S., Appelgate, B., MacCay, M.E. & Moore, G.F. (1992), R´transverse structural trends along the Oregon convergent margin: Implications for Cascadia earthquake potential and crustal rotations, *Geology*, vol. 20, 141-144

Goldfinger, C., Kulm, L.D., Yeats, R.S, Appelgate, B., MacCay, M.E. & Cochrane, G.R. (1996). Active strike-slip faulting and folding of the Cascadia subduction-zone plate boundary and forearc in central and northern Oregon, In: Rogers, A.M., Walsh, T.J., Kockelman, W.J. & Priest, G. (eds.), *Assessing and reducing earthquake hazards in the Pacific Northwest*, Volume I, Professional Paper 1560, U.S. Geological Survey, 223-256

Goldfinger, C., Kulm, L.D., Yeats, R.S, Hummon, C., Huftile, G.J., Niem, A.R. & McNeill, L.C. (1996). Oblique Strike-Slip Faulting of the Cascadia Submarine Forearc: The Daisy Blank Fault Zone off Central Oregon, n: Bebout, G.E., Scholl, D.W., Kirby, S.H. & Platt, J.P. (eds.), *Subduction: Top to Bottom*, Geophysical Monograph 96, American Geophysical Union, Washington, D.C., 65-74

Gonzáles, G.L., Dunai, T., Carrizo, D. & Allmendinger, R. (2006). Young displacements on the Atacama Fault System, northern Chile from field observations and cosmogenic [21]Ne concentrations, *Tectonics*, vol. 25, TC3006, doi:10.1029/2005TC001846

Green, D.H., Falloon, T.J., Eggins, S.M. & Yaxley, G.M. (2001). Primary magmas and mantle temperatures, *European Journal of Mineralogy*, vol. 13, 437-451

Gutscher, M.-A., Malavieille, J., Lallemand, S. & Collot, J.-Y. (1999).Tectonic segmentation of the North Andean margin: impact of the Carnegie Ridge collision, *Earth and Planetary Science Letters*, vol. 168, 255-270

Gutscher, M.-A., Spakman, W., Bijwaard, H. & Engdahl, E. R. (2000). Geodynamics of flat subduction: Seismicity and tomographic constraints from the Andean margin, *Tectonics*, vol. 19(5), 814-833

Hackney, R., Echtler, H., Franz, G., Götze, H.-J., Lucassen, F., Marchenko, D., Melnick, D., Meyer, U., Schmidt, S., Tašárová, Z., Tassara, A. & Wienecke, S. (2006). The Segmented Overriding Plate and Coupling at the South-Central Chilean Margin (36°-42°S), In: Oncken, O., Chong, G., Franz, G., Giese, P., Götze, H.-J., Ramos, V., Strecker, M. & Wigger, P. (eds.), *The Andes: Active Subduction Orogeny*, Frontiers in Earth Sciences, vol. 1, Springer

Hampel, A. (2003). *Subduction of the Nazca Ridge at the Peruvian margin: Insights from geophysical data, analogue and numerical modelling*, PhD thesis, FU Berlin, 111p.

Hampel, A. & Pfiffner, A. (2006). Relative importance of trenchward upper plate motion and friction along the plate interface for the topographic evolution of subduction-related mountain belts, In: Buiter, S.J.H. & Schreurs, G. (eds), *Analogue and Numerical Modelling of Crustal-Scale Processes,* Geological Society, London, Special Publication, 253, 105-115

Hansen, B.C.E. (1958). Line ruptures regarded as narrow rupture zones – Basic equations based on kinematic considerations, *Proc. Brussels Conf. 58 on Earth Pressure Problems*, vol. 1, 39-48

Hartley, A.J., May, G., Chong, G., Turner, P., Kape, S.J. & Jolley, E.J. (2000). Development of a continental forearc: A Cenozoic example from the Central Andes, northern Chile, *Geology,* vol. 28(4), 331-334

Haschke, M., Günther, A., Melnick, D., Echtler, H., Reutter, K.-J., Scheuber, E. & Oncken, O. (2006). Andean tectonic evolution inferred from spatial and temporal variations in arc magmatism, In: Oncken, O., Chong, G., Franz, G., Giese, P., Götze, H.-J., Ramos, V., Strecker, M. & Wigger, P. (eds.), *The Andes: Active Subduction Orogeny*, Frontiers in Earth Sciences, vol. 1, Springer

Hervé, F. (1994). The Southern Andes between 39° and 44°S latitude: the geological signature of a transpressive tectonic regime related to a magmatic arc, In: Reutter, K.J., Scheuber, E. & Wigger, P.J. (eds), *Tectonics of the Southern Central Andes*, Springer, 243-248

Hervé, M.A. (1987). Movimiento sinistral en el Cretacico Inferior de la Zona de Falla Atacama al Norte de Paposo (24°S),Chile, *Revista Geológica de Chile*, num. 31, 37-42

Hetzel, R. & Hampel, A. (2005). Slip rate variations on normal faults during glacial-interglacial changes in surface loads, *Nature*, vol. 435, 81-84

Hildreth, W. & Moorbath, S. (1988). Crustal contributions to arc magmatism in the Andes of central Chile, *Contributions to Mineralogy and Petrology*, vol. 98, 455-489

Hoffmann-Rothe, A. (2002). *Combined structural and magnetotelluric investigation across the West Fault Zone in northern Chile*, Scientific Technical Report STR02/12 (GFZ), Universität Potsdam

Hoffmann-Rothe, A., Kukowski & Oncken, O. (2004). Phase dependent strain partitioning in obliquely convergent settings, *Bolletino de Geofisica Teorica ed Aplicata*, vol. 45(1), 93-97

Hoffmann-Rothe, A., Kukowski, N., Dresen, G., Echtler, H., Oncken, O., Klotz, J., Scheuber, E. & Kellner, A. (2006). Oblique convergence along the Chilean margin: Partitioning, margin-parallel faulting and force interaction at the plate interface, In: Oncken, O., Chong, G., Franz, G., Giese, P., Götze, H.-J., Ramos, V., Strecker, M. & Wigger, P. (eds.), *The Andes: Active Subduction Orogeny*, Frontiers in Earth Sciences, vol. 1, Springer

Homand, S. & Shao, J.F. (2000). Mechanical Behaviour of a Porous Chalk and Water/Chalk Interaction – Part II: Numerical Modelling, *Oil & Gas Science and Technology – Rev. IFP*, vol. 55(6), 599-609

Hu, Y. & Wang, K. (2006). Bending-like behavior of thin wedge-shaped elastic fault blocks, *Journal of Geophysical Research*, vol. 111(B06409), doi:10.1029/2005JB003987

Hubbert, M.K. & Rubey, W.W. (1959). Role of fluid pressure in mechanics of overthrust faulting, I. Mechanics of fluid filled porous solids and its application to overthrust faulting, *Bulletin of the Geological Society of America*, vol. 70, 167-206

Huhn, K. (2002). Analyse der Mechanik des Makran Akkretionskeils mit Hilfe der Finiten und der Diskreten Elemente Methode sowie analoger Sandexperimente, Scientific Technical Report STR02/02 (GFZ), Freie Universität Berlin

Humboldt von, A., Lubrich, O., Ette, O. & Kalscheuer, C. (2004). *Ansichten der Kordilleren und Monumente der eingeborenen Völker Amerikas*, Eichborn Verlag, 446 p.

Humboldt von, A., Ette, O. & Lubrich, O. (2006). *Kosmos. Entwurf einer physischen Weltbeschreibung*, Eichborn Verlag, 941 p.

Hyndman, R.D. & Wang, K. (1993). Thermal contraints on the zone of major thrust earthquake failure: The Cascadia subduction zone, *Journal of Geophysical Research*, vol. 98(B2), 2039-2060

Hyndman, R.D., Yamano, M. & Oleskevich, D.A. (1997). The seismogenic zone of subduction thrust faults, *The Island Arc*, vol. 6, 244-260

Isacks, B. (1988). Uplift of the central Andean plateau and bending of the Bolivian orocline, *Journal of Geophysical Research,* vol. 93, 3211-3231

Jarrard, R.D. (1986). Relations among subduction parameters, *Reviews of Geophysics*, vol. 24(2), 217-284

Jarrard, R.D. (1986b). Terrane motion by strike-slip faulting of forearc slivers, *Geology*, vol. 14(9), 780-783

Jordan, T.E., Isacks, B.L., Allmendinger, R., Brewer, J., Ramos, V.A. & Ando, C.J. (1983). Andean tectonics related to geometry of subducted Nazca plate, *Geological Society of America Bulletin*, vol. 94, 341-361

Jordan, T.E. & Alonso, R.N. (1987). Cenozoic stratigraphy and basin tectonics of the Andes mountains, 20-28° south latitude, *American Association of Petroleum Geologists Bulletin*, vol. 71, 49-64

Jordan, T.E., Schlunegger, F. & Cardozo, N. (2001). Unsteady and spatially variable evolution of the Neogene Andean Bermejo foreland basin, Argentina, *Journal of South American Earth Sciences*, vol. 14(7), 775-798

Kamesh Raju, K.A., Murty, G.P.S., Dileep Amarnath & Kumar, M.L.M. (2007). The west Andaman fault and its influence on the aftershock pattern of the recent megathrust earthquakes in the Andaman-Sumatra region, *Geophysical Research Letters*, vol. 34(2), L03305, doi:10.1029/2006GL028730

Kanamori, H. (1986). Rupture process of subduction-zon earthquakes, *Annual Reviews of Earth and Planetary Science Letters*, vol. 14, 293-322

Kaufmann, G., Wu, P. & Li, G. (2000). Glacial isostatic adjustment in Fennoscandia for a laterally heterogeneous earth, *Geophysical Journal International*, vol. 143(1), 262-273

Kelleher, J.A. (1972). Rupture zones of large South American earthquakes and some predictions, *Journal of Geophysical Research*, vol. 77(B11), 2087-2103

Kendrick, E., Bevis, M., Smalley, R.J. & Brooks, B.A. (2001). An integrated crustal velocity field for the central Andes, *Geochemistry, Geophysics, Geosystems G³*, vol. 2(11), doi:10.1029/2001GC000191

Khazaradze, G. & Klotz, J. (2003). Short- and long-term effects of GPS measured crustal deformation rates along the south-central Andes, *Journal of Geophysical Research*, vol. 108(B6), 2289, doi:10.1029/2002JB001879

Kimura, G. (1986). Oblique subduction and collision: Forearc tectonics of the Kuril arc, *Geology*, vol. 14, 404-407

Kirchner, A. (1997). *3D-Dichtemodellierung zur Anpassung des Schwere- und des Schwerepotentialfeldes der zentralen Anden*, PhD thesis, FU Berlin, 98 p.

Klaeschen, D., Belykh, I., Gnibidenko, H., Patrikeyev, S. & von Huene, R. (1994). Structure of the Kuril Trench from seismic reflection records, *Journal of Geophysical Research*, vol. 99(B12), 24173-24188

Kley, J. & Monaldi, C.R. (1998). Tectonic shortening and crustal thickness in the central Andes: How good is the correlation, *Geology*, vol. 26(8), 723-726

Kley, J., Monaldi, C.R. & Salfity, J.A. (1999). Along-strike segmentation of the Andean foreland: causes and consequences, *Tectonophysics*, vol. 301, 75-94

Klotz, J., Angermann, D., Michel, G.W., Porth, R., Reigber, C., Reinking, J., Viramonte, J., Perdomo, R., Rios, V.H., Barrientos, S., Barriga, R. & Cifuentes, O. (1999). GPS-derived Deformation of the Central Andes Including the 1995 Antofagasta M_w=8.0 Earthquake, *Pure and Applied Geophysics*, vol. 154, 709-730

Klotz, J., Khazaradze, G., Angermann, D., Reigber, C., Perdomo, R. & Cifuentes, O. (2001). Earthquake cycle dominates contemporary crustal deformation in Central and Southern Andes, *Earth and Planetary Science Letters*, vol. 193, 437-446

Klotz, J., Abolghasem, A., Khazaradze, G., Heinze, B., Vietor, T., Hackney, R., Bataille, K., Maturana, R., Viramonte, J. & Perdomo, R. (2006). Longterm deformation signals in the present-day deformation field and constraints on the viscosity, In: Oncken, O., Chong, G., Franz, G., Giese, P., Götze, H.-J., Ramos, V., Strecker, M. & Wigger, P. (eds.), *The Andes: Active Subduction Orogeny*, Frontiers in Earth Sciences, vol. 1, Springer

Kopf, A. & Brown, K.M. (2003). Friction experiments on saturated sediments and their implications for the stress state of Nankai and Barbados subduction thrusts, *Marine Geology*, vol. 202(3-4), 193-210

Krawczyk, C. & the SPOC Team (2003). Amphibious Seismic Survey Images Plate Interface at 1960 Chile Earthquake, *EOS, Transactions*, American Geophysical Union, vol. 84(32), 301-305

Kukowski, N. & Oncken, O. (2006). Subduction erosion – the „normal" mode of fore-arc material transfer along the Chilean margin?, In: Oncken, O., Chong, G., Franz, G., Giese, P., Götze, H.-J., Ramos, V., Strecker, M. & Wigger, P. (eds.), *The Andes: Active Subduction Orogeny*, Frontiers in Earth Sciences, vol. 1, Springer

Kurz, J.H., Jahr, T. & Jentzsch, G. (2003). Geodynamic modelling of the recent stress and strain field in the Vogtland swarm earthquake aera using the finite-element-method, *Journal of Geodynamics*, vol. 35, 247-258

Kurz, J.H., Jahr, T. & Jentzsch, G. (2004). Earthquake swarm examples and a look at the generation mechanism of the Vogtland/Western Bohemia earthquake swarms, *Physics of the Earth and Planetary Interios*, vol. 142, 75-88

Kwon, Y.W. & Bang, H. (1997). *The finite element method using MATLAB*, CRC Press, New York, 519 p.

Lallemant, H.G.A. (1996). Displacement partitioning and arc-parallel extension in the Aleutian volcanic arc, *Tectonophysics*, vol. 256, 279-293

Lamb, D.H. & Hoke, L. (1997). Origin of the high plateau on the Central Andes, Bolivia, South America, *Tectonics*, vol. 16, 623-649

Lamb, S. & Davis, P. (2003). Cenozoic climate change as a possible cause for the rise of the Andes, *Nature*, vol. 425, 792-797

Lange, D., Rietbrock, A., Haberland, C., Bataille, K., Dahm, T., Tilmann, F. & Flüh, E.R. (2007). Seismicity and geometry of the south Chilean subduction zone (41.5°S-43.5°S): Implications for controlling parameters, Geophysical Research Letters, vol. 34(6), doi:10.1029/2006GL029190

Liu, M., Yang, Y., Stein, S. & Klosko, E. (2002). Crustal Shortening and Extension in the Central Andes: Insights from a Viscoelastic Model, In: Stein, S. & Freymueller, J.T. (eds.), *Plate Boundary Zones*, Geodynamics eries 30, American Geophysical Union, Washington, D.C., 325-339

Lohrmann, J. (2002). *Identification of Parameters Controlling the Accretive and Tectonically Erosive Mass-Transfer Mode at the South-Central and North Chilean Forearc Using Scaled 2D Sandbox Experiments*, Scientific Technical Report STR02/10 (GFZ), Freie Universität Berlin, 233p.

Lohrmann, J., Kukowski, N., Adam, J. & Oncken, O. (2003). The impact of analogue material properties on the geometry, kinematics, and dynamics of convergent sand wedges, *Journal of Structural Geology*, vol. 25, 1691-1711

Lonsdale, P. (2005). Creation of the Cocos and Nazca plates by fission of the Farallon plate, *Tectonophysics*, vol. 404, 237-264

López-Escobar, L., Cembrano, J. & Moreno, H. (1995). Geochemistry and tectonics of the Chilean Southern Andes basaltic Quaternary volcanism (37-46°S), *Revista Geológica de Chile*, vol. 22(2), 219-234

Lüth, S., Wigger, P. & ISSA Working Group (2003). A crustal model along 39°S from seismic refraction profile-ISSA 2000, *Revista Geológica de Chile*, vol. 30(1), 83-101

Lüth, S., Wigger, P., Mechie, J., Stiller, M., Krawczyk, C., Bataille, K., Reichert, C., Flüh, E. & SPOC Research Group (2004). The crustal structure of the Chilean forearc between 36° and 40°S from combined offshore and onshore seismic wide-andle measurements – SPOC 2001, *Bolletino de Geofisica Teorica ed Aplicata*, Special Issue, GeoSur 2004

Malod, J.A. & Kemal, B.M. (1996). The Sumatra margin: oblique subduction and lateral displacement of the accretionary prism, In: Hall, R. & Blundell, D. (eds), *Tectonic Evolution of Southeast Asia,* Geological Society, London, Special Publication, 106, 19-28

Marsal, D. (1989). *Finite Differenzen und Elemente: numerische Lösung von Variations-problemen und partiellen Differentialgleichungen*, Springer Verlag, Berlin, Heidelberg, New York, London, Paris, Tokyo, 300 p.

Matsu'ura, M. (2004). Reproducing Core-Mantle Dynamics and Predicting Crustal Activities Through Advanced Computing, *Journal of the Earth Simulator*, vol. 1, 67-74

McCaffrey, R. (1992). Oblique Plate Convergence, Slip Vectors, and Forearc Deformation, *Journal of Geophysical Research*, vol. 97(B6), 8905-8915

McCaffrey, R. (1993). On the role of the upper plate in great subduction zone earthquakes, *Journal of Geophysical Research*, vol. 98(B7), 11953-11966

McCaffrey, R. (1996). Estimates of modern arc-parallel strain rates in fore arcs, *Geology*, vol. 24(1), 27-30

McCaffrey, R., Long, M.D., Goldfinger, C., Zwick, P.C., Nabelek, J.L., Johnson, C.K. & Smith, C. (2000). Rotation and plate locking at the southern Cascadia subduction zone, *Geophysical Research Letters*, vol. 27(19), 3117-3120

McCaffrey, R., Zwick, P.C., Bock, Y., Prawirodirdjo, L., Genrich, J.F., Stevens, C.W., Puntodewo, S.S.O. & Subarya, C. (2000). Strain partitioning during oblique plate convergence in northern Sumatra: Geodetic and seismologic constraints and numerical modelling, *Journal of Geophysical Research*, vol. 105(B12), 28363-28376

McClay, K.R., Whitehouse, P.S., Dooley, T. & Richards, M. (2004). 3D evolution of fold and thrust belts formed by oblique convergence, *Marine and Petroleum Geology*, vol. 21, 857-877

McCroy, P.A. (1996). Tectonic model explaining divergent contraction directions along the Cascadia subduction margin, Washington, *Geology*, vol. 24(10), 929-932

Medvedev, S., Podladchikov, Y., Handy, M.R. & Scheuber, E. (2006). Controls on the deformation of the central and southern Andes (10°-35°S): Insight from thin-sheet numerical modelling, In: Oncken, O., Chong, G., Franz, G., Giese, P., Götze, H.-J., Ramos, V., Strecker, M. & Wigger, P. (eds.), *The Andes: Active Subduction Orogeny*, Frontiers in Earth Sciences, vol. 1, Springer

Melnick, D., Rosenau, M., Folguera, A. & Echtler, H. (2006). Neogene tectonic evolution of the Neuquén Andes western flank (37-39°S), In: Kay, S.M. & Ramos, V.A. (eds.), *Evolution of an Andean margin: A tectonic and magmatic view from the Andes to the Neuquén Basin (35°-39°S),* Geological Society of America Special Paper 407, 73-95

Melnick, D. & Echtler, H. (2006). Morphotectonic and geologic digital map compilations of the south-central Andes (36°-42°S), In: Oncken, O., Chong, G., Franz, G., Giese, P., Götze, H.-J., Ramos, V., Strecker, M. & Wigger, P. (eds.), *The Andes: Active Subduction Orogeny*, Frontiers in Earth Sciences, vol. 1, Springer

Michelis, P.N. (1981). Work-softening and hardening behaviour of granular rocks, *Rock Mechanics*, vol. 14, 187-200

Millen, D.W. & Hamburger, M.W. (1998). Seismological evidence for tearing of the Pacific plate at the northern termination of the Tonga subduction zone, *Geology*, vol. 26(7), 659-662

Miller, H. (1970). Das Problem des hypothetischen 'pazifischen Kontinentes' gesehen von der chilenischen Pazifikküste, *Geologische Rundschau*, vol. 59(3), 927-938

Mix, A.C., Tiedemann, R., Blum, P., et al. (2003). *Proceedings of the Ocean Drilling Program (ODP),* Initial Reports vol. 202, College Station, TX (Ocean Drilling Program), doi:10.2973/odp.proc.ir.202.2003

Molnar, P. & England, P. (1990). Temperatures, Heat Flux, and Frictional Stress Near Major Thrust Faults, *Journal of Geophysical Research*, vol. 95(B4), 4833-4856

Moore, J.C. & Saffer, D. (2001). Updip limit of the seismogenic zone beneath the accretionary prism of southwest Japan: An effect of diagenetic to low-grade metamorphic processes and increasing effective stress, *Geology*, vol. 29(2), 183-186

Moresi, L., May, D., Freeman, J. & Appelbe, B. (2003). Mantle convection modelling with viscoelastic/brittle lithosphere: Numerical and computational methodology, http://vpac.org/vdt/snark/presentations/rd0201-paper-20030602-iccs03_aces03_lncs-mantle_convection_modelling.pdf

Mpodozis, C. & Ramos, V.A. (1989). The Andes of Chile and Argentina, In: Ericksen, G.E., Canas Pinochet, M.T. & Reinemund, J.A. (eds.), *Geology of the Andes and its relation to hydrocarbon and mineral resources*, Earth Science Series, Circum-Pacific Council of Energy and Mineral Resources, Houston, Texas, 59-90

Muñoz, J.B. & Stern, C.R. (1988). The Quaternari Volcanic Belt Of The Southern Continental Margin Of South America: Transverse Structural And Petrochemical Variations Across The Segment Between 38°S and 39°S. *Journal of South American Earth Science*, vol. 1(2), 147-161

Muñoz, J., Troncoso, R., Duhart, P., Cringnola, P., Farmer, L. & Stern, C.R. (2000). The relation of the mid-Tertiary coastal magmatic belt in south-central Chile to the late Oligocene increase in plate convergence rate, *Revista Geológica de Chile*, vol. 27(2), 177-203

Ncheuguim, E.K. (2006). Theoretical aspects of classical and Drucker-Prager cap models of elastoplasticity, http://www.aims.ac.za/resources/archive/2005/emma.pdf

Newman, J.B. (1979). Concrete under complex stress, In: Lyon, F.T. (ed.), *Developments in Concrete Technology*, Butterworth, London

Norabuena, E., Leffler-Griffin, L., Mao, A., Dixon, T., Stein, S., Sacks, S.I., Ocola, L. & Ellis, M. (1998). Space Geodetic Observations of Nazca-South America Convergence Across the Central Andes, *Science*, vol. 279, 358-362

Norabuena, E.O., Dixon, T.H., Stein, S. & Harrison, C.G.A. (1999). Decelerating Nazca-South America and Nazca-Pacific Plate Motions, *Geophysical Research Letters*, vol. 26(22), 3405-3408

Oleskevich, D.A., Hyndman, R.D. & Wang, K. (1999). The updip and downdip limit to great subduction earthquakes: Thermal and structural models of Cascadia, south Alaska, SW Japan, and Chile, *Journal of Geophysical Research*, vol. 104(B7), 14965-14991

Oncken, O., Hindle, D., Kley, J., Elger, K., Victor, P. & Schemmann, K. (2006). Deformation of the Central Andean upper plate system – facts, fiction, and contraints for plateau models, In: Oncken, O., Chong, G., Franz, G., Giese, P., Götze, H.-J., Ramos, V., Strecker, M. & Wigger, P. (eds.), *The Andes: Active Subduction Orogeny*, Frontiers in Earth Sciences, vol. 1, Springer

Oncken, O., Chong, G., Franz, G., Giese, P., Götze, H.-J., Ramos, V., Strecker, M. & Wigger, P. (2006), *The Andes: Active Subduction Orogeny*, Frontiers in Earth Sciences, vol. 1, Springer

Pacheco, J.F., Sykes, L.R. & Scholz, C. (1993). Nature of seismic coupling along simple plate boundaries of the subduction type, *Journal of Geophysical Research*, vol. 98(B8), 14133-14159

Papamichos, E., Brignoli, M. & Santarelli, F.J. (1997). An experimental and theoretical study of a partially saturated collapsible rock, *Mechanics of Cohesive-Frictional Materials*, vol. 2, 251-278

Pardo, M., Monfret, T., Vera, E., Eisenberg, A., Yañez, G. & Triep, E. (2003). Cambio en la subduccion de la de Nazca, de plana a inclinada, bajo Chile central y Argentina: Datos sismologicos preliminares, *X Congreso Geológico Chileno 2003*, Universidad de Concepción, Concepción, Chile, 6-10 October

Pardo-Casas, F. & Molnar, P. (1987). Relative motion of the Nazca (Farallon) and South American plates since late Cretaceous time, *Tectonics*, vol. 6, 233-248

Paterson, M.S. & Wong, T.-F. (2005). *Experimental Rock Deformation- The Brittle Field*, Springer-Verlag, Berlin, 348p.

Patzig, R. (2000). *Lokalbeben-Tomographie der Umgebung von Antofagasta (Nordchile) sowie Betrachtungen der Magnituden-Häufigkeits-Parameter in dieser Region*, Berliner Geowissenschaftliche Abhandlungen, Reihe B, Band 36, FU Berlin

Patzwahl, R., Mechie, J., Schulze, A. & Giese, P. (1999). Two-dimensional velocity models of the Nazca plate subduction zone between 19.5°S and 25°S from wide-angle seismic measurements during the CINCA'95 project, *Journal of Geophysical Research*, vol. 104(B4), 7293-7317

Peacock, S.M. (1992). Blueshist-facies metamorphism, shear heating, and P-T-t paths in subduction shear zones, *Journal of Geophysical Research*, vol. 97, 17693-17707

Peacock, S. M. (1996). Thermal and Petrologic Structure of Subduction Zones, In: Bebout, G.E., Scholl, D.W., Kirby, S.H. & Platt, J.P. (eds.), *Subduction: Top to Bottom*, Geophysical Monograph 96, American Geophysical Union, Washington, D.C., 119-133

Peacock, S. M. & Hyndman, R.D. (1996). Hydrous minerals in the mantle wedge and the maximum depth of subduction thrust earthquakes, *Geophysical Research Letters*, vol. 26(16), 2517-2520

Pelz, K. (2000). *Tektonische Erosion am zentralandinen Forearc (20°-24°S)*, Scientific Technical Report STR00/20, Freie Universität Berlin

Phillips, B. R. & Bunge, H.-P. (2005). Heterogenity and time dependence in 3D spherical mantle convection models with continental drift, *Earth and Planetary Science Letters*, vol. 233, 121-135

Prezzi, C.B. & Alonso, R.N. (2002). New paleomagnetic data from the northern Argentine Puna: Central Andes rotation pattern reanalyzed, *Journal of Geophysical Research*, vol. 107(B2), 2041, 10.1029/2001JB000225

Prezzi, C., Götze, H.-J. & Schmidt, S. (2005). Density structure of the Central Andes from 3D integrated gravity modelling, *6th International Symposium on Andean Geodynamics (ISAG),* Barcelona (Spain), September 12-14, 574-577

Ranalli, G. (1995). *Rheology of the Earth*, Chapman & Hall, London, 413 p.

Rapela, C.W. & Pankhurst, R.J. (1992). The granites of northern Patagonia and the Gastre Fault system in relation to the break-up of Gondwana, In: Storey, B.C., Alabaster, T. & Pankhurst, R.J. (eds), *Magmatism and the Causes of Continetal Break-Up,* Geological Society, London, Special Publication, 68, 209-220

Reutter, K.J., Scheuber, E. & Chong, G. (1996). The Precordilleran fault system of Chuquicamata, Northern Chile: evidence for revearsals along arc-parallel strike-slip faults, *Tectonophysics,* vol. 259, 213-228

Regenauer-Lieb, K. & Yuen D.A. (2003). Modeling shear zones in geological and planetary sciences: solid- and fluid-thermal-mechanical approaches, *Earth-Science Reviews*, vol. 63, 295-349

Roque, C.M.O.L. & Button, S.T. (2000). Application of the Finite Element Method I Cold Forging Processes, Journal of the Brazilian Society of Mechanical Sciences, vol. 22(2), 189-202

Rosenau, M., Melnick, D. & Echtler, H. (2006). Kinematic constraints on intra-arc shear and strain partitioning in the southern Andes between 38°S and 42°S latitude, *Tectonics*, vol. 25, TC4013, doi:10.1029/2005TC001943

Ruegg, J.C., Campos, J., Madariaga, R., Kausel, E., de Chabalier, J.B., Armijo, R., Dimitrov, D., Georgiev, I. & Barrientos, S. (2002). Interseismic strain accumulation in south central Chile from GPS measurements, 1996-1999, *Geophysical Research Letters*, vol. 29(11), 1517, doi:10.1029/2001GL013438

Ruff, L.J. (1989). Do trench sediments affect great earthquake occurrence in subduction zones?, *Pure and Applied Geophysics*, vol. 129, 263-282

Rutland, R.W.R. (1971). Andean Orogeny and Ocean Floor Spreading, *Nature*, vol. 233, 252-255

Saffer, D.M. & Marone, C. (2003). Comparison of smectide- and illite-rich gouge frictional properties: application to the updip limit of the seismogenic zone along subduction megathrusts, *Earth and Planetary Science Letters*, vol. 215, 219-235

Scheuber, E. (1987). *Geologie der nordchilenischen Küstenkordillere zwischen 24°30´ und 25°S – unter besonderer Berücksichtigung duktiler Scherzonen im Bereich des Atacama-Störungssystems*. PhD thesis, FU Berlin

Scheuber, E. & Andriessen, P.A.M. (1990). The kinematic and geodynamic significance of the Atacama fault zone, Northern Chile, *Journal of Structural Geology*, 12(2), 243-257

Scheuber, E. & Reutter, K.-J. (1992). Magmatic arc tectonics in the Central Andes between 21° and 25°S, *Tectonophysics*, vol. 205, 127-140

Scheuber, E. (1994). *Tektonische Entwicklung des nordchilenischen aktiven Kontinental-randes: Der Einfluß von Plattenkonvergenz und Rheologie*, 131p.

Scheuber, E., Bogdanic, T., Jensen, A. & Reutter, K.-J. (1994). Tectonic development of the North Chilean Andes in relation to plate convergence and magmatism since the Jurassic, In: Reutter, K.-J., Scheuber, E. & Wigger, P. (eds.), *Tectonics of the Southern Central Andes*, Springer, 121-139

Scheuber, E., Hammerschmidt, K. & Friedrichsen, H. (1995). ^{40}Ar/^{39}Ar and Rb-Sr analyses from ductile shear zones from the Atacama Fault Zone, northern Chile: the age of deformation, *Tectonophysics*, vol. 250, 61-87

Scheuber, E. & Giesse, P. (1999). Architecture of the Central Andes – a compilation of geoscientific data along a transect at 21°S, *Journal of South American Earth Sciences*, vol. 12, 103-107

Schmidt, S. (1996). 3D Modeling of Geoid and Gravity using GIS-Functions, *Österreichische Beiträge zu Meteorologie und Geophysik*, Heft 14, 137-144, Wien

Schmidt, S. & Götze, H.-J. (1998). Interactive Visualization and Modification of 3D Models using GIS-Functions, *Physics and Chemistry of the Earth*, vol. 23(3), 289-295

Schmitz, M. (1994). A balanced model of the southern Central Andes, *Tectonics*, vol. 13, 484-492

Scholl, D.W., Christensen, M.N., von Huene, R. & Marlow, M.S. (1970). Peru-Chile trench sediments and sea-floor spreading, *Geological Society of America Bulletin*, vol. 81, 1339-1360

Scholz, C.H. (1990). *The Mechanics of Earthquakes and Faulting*, Cambridge University Press, 439p.

Scholz, C.H. & Campos, J. (1995). On the mechanism of seismic decoupling and back arc spreading at subduction zones, *Journal of Geophysical Research*, vol. 100(B11), 22103-22115

Scholz, C.H. (2002). *The Mechanics of Earthquakes and Faulting*, Cambridge University Press, Cambridge, 471 p.

Sempere, T., Herail, G., Oller, J. & Bonhomme, M. (1990). Late Oligocene – early Miocene major tectonic crisis and related basins in Bolivia, *Geology*, vol. 18, 946-949

Sibson, R.H. (1990). Conditions for fault-valve behaviour, In: Knipe, R.J. & Rutter, E.H. (eds.), *Deformation Mechanisms, Rheology and Tectonics*, Geological Society, London, Special Publication, 54, 15-28

Silver, P.G., Russo, R.M. & Lithgow-Bertelloni, C. (1998). Coupling of South American and African Plate Motion and Plate Deformation, *Science*, vol. 279, 60-63

Smith, G.D. (1986). *Numerical Solution of Partial Differential Equations: Finite Difference Methods*, Oxford University Press, New York, 350 p.

Smith, W.H.F. & Sandwell, D.T. (1997). Global seafloor topography from satellite altimetry and ship depth soundings, *Science*, vol. 277, 1956-1962

Sobesiak, M. (2004). *Fault Plane Structure of the 1995 Antofagasta Earthquake (Chile) Derived From Local Seismological Parameters*, PhD thesis, University Potsdam, 137 p.

Sobolev, S.V. & Babeyko, A.Y. (2005). What drives orogeny in the Andes?, *Geology*, vol. 33(8), 617-620, doi:10.1130/G21557.1

Sobolev, S.V., Babeyko, A.Y., Koulakov, I., Oncken, O. & Vietor, T. (2006). Mechanism of the Andean orogeny: insight from numerical modelling, In: Oncken, O., Chong, G., Franz, G., Giese, P., Götze, H.-J., Ramos, V., Strecker, M. & Wigger, P. (eds.), *The Andes: Active Subduction Orogeny*, Frontiers in Earth Sciences, vol. 1, Springer

Somoza, R., Singer, S. & Coira, B. (1996). Paleomagnetism of upper Miocene ignimbrites at the Puna: An analysis of vertical-axis rotations in the Central Andes, *Journal of South American Earth Sciences*, vol. 11(3), 211-215 *Journal of Geophysical Research*, vol. 101(B5), 11387-11400

Somoza, R. (1998). Updated Nazca (Farallon) – South America relative motions during the last 40My: implications for the mountain building in the central Andean region, *Journal of South American Earth Sciences*, vol. 11(3), 211-215

Somoza, R., Singer, S. & Tomlinson, A. (1999). Paleomagnetic study of upper Miocene rocks from northern Chile: Implications for the origin of late Miocene-Recent tectonic rotations in the southern Central Andes, *Journal of Geophysical Research*, vol. 104(B10), 22923-22936

Song, T.A. & Simons, M. (2003). Large trench-parallel gravity variations predict seismogenic behaviour in subduction zones, *Science*, vol. 301, 630-633

Springer, M. (1999). Interpretation of heat-flow density in the Central Andes, *Tectonophysics*, vol. 306, 377-395

Stauder, W. (1973). Mechanism and spatial distribution of Chilean earthquakes with relation to subduction of the oceanic plate, *Journal of Geophysical Research*, vol. 78(23), 5033-5061

Stein, C.A. (2003). Heat flow and flexure at subduction zones, *Geophysical Research Letters*, vol. 30(23), 2197, doi:10.1029/2003GL018478

Stern, C. (1989). Pliocene to present migration of the volcanic front, Andean Southern Volcanic Front, *Revista Geológica de Chile*, vol. 16(2), 145-162

Stern, C. (1991). Role of subduction erosion in the generation of Andean magmas, *Geology*, vol. 19, 78-81

Stern, C.R. (2004). Active Andean volcanism: its geologic and tectonic setting, *Revista Geológica de Chile*, vol. 31(2), 161-206

Taboada, A., Rivera, L.A., Fuenzalida, A., Cisternas, A., Philip, H., Bijwaard, H., Olaya, J. & Rivera, C. (2000). Geodynamics of the northern Andes: Subductions and intracontinental deformation (Colombia), *Tectonics*, vol. 19(5), 787-813

Tašárová, Z. (2004). *Gravity data analysis and interdisciplinary 3D modelling of a convergent plate margin (Chile, 36° - 42°S)*, PhD thesis, FU Berlin, 169 p.

Tassara, A. & Yañez, G. (2003). Relación entre el espesor elástico de la litosfera y la segmentación tectónica del margen andino (15-47< degrees >S), *Revista Geológica de Chile*, vol. 30(2), 159-186

Tassara, A. (2005). *Structure of the Andean continental margin and causes of its segmentation*, PhD thesis, FU Berlin, 165 p.

Tebbens, S.F. & Cande, S.C. (1997). Southeast Pacific tectonic evolution from early Oligocene to present, *Journal of Geophysical Research*, vol. 102(B6), 12061-12084

Thomson, S.N. (2002). Late Cenozoic geomorphic and tectonic evolution of th ePatagonian Andes between latitudes 42°S and 46°S: An appraisal based on fisson-track results from the transpressional intra-arc Liquiñe-Ofqui fault zone, *Geological Society of America Bulletin*, vol. 114(9), 1159-1173

Tichelaar, B.W. & Ruff, L.J. (1991). Seismic coupling along the Chilean subduction zone, *Journal of Geophysical Research*, vol. 96, 11997-12022

Tichelaar, B.W. & Ruff, L.J. (1993). Depth of Seismic Coupling Along Subduction Zones, *Journal of Geophysical Research*, vol. 98(B2), 2017-2037

Trenkamp, R., Kellogg, J.N., Freymueller, J.T. & Mora, H.P. (2002). Wide plate margin deformation, southern Central America and northwestern South America, CASA GPS observations, *Journal of South American Earth Sciences*, vol. 15(2), 157-171

Tse, S.T. & Rice, J.R. (1986). Crustal earthquake instability in relation to the depth variation of frictional slip properties, *Journal of Geophysical Research*, vol. 91, 9452-9472

Turcotte, D.L. & Schubert, G. (2002). *Geodynamics*, Cambridge University Press, Cambridge, 456 p.

Turner, S. & Hawkesworth, C. (1997). Contraints on flux rates and mantle dynamics beneath island arcs from Tonga-Kermadec lava geochemistry, *Nature*, vol. 389, 568-573

Vermeer, P.A. & de Borst, R. (1984). Non-associated plasticity for soil, concrete and rock, *HERON*, vol. 29(3), 1-64

Victor, P. (2000). *Die Entwicklung der Altiplano Westflanke und ihre Bedeutung für die Plateaubildung und Krustenverdickung in N-Chile (20°-21°S)*, Scientific Technical Report STR00/13 (GFZ), Freie Universität Berlin

Vietor, T., Echtler. H., Müller, H., Nowaczyk, N. & Oncken, O. (2005). Neogene block rotations in the south central Chilean forearc (36°S-39°S): New constraints from paleomagnetic data, *Terra Nostra*, vol. 2005/1, 19th Colloquium on Latin American Geosciences–Potsdam, Germany, April 18–20, 2005, 133-134

Vietor, T. & Oncken, O. (2005). Controls on the shape and kinematics of the Central Andean plateau flanks: Insights from numerical modeling, *Earth and Planetary Science Letters*, vol. 236, 814-827

von Huene, R. & Lallemand, S.E. (1990). Tectonic erosion along the Japan and Peru convergent margins, *Geological Society of America Bulletin*, vol. 102(6), 704-720

von Huene, R. & Scholl, D.W. (1991). Observations at convergent magins concerning sediment subduction, subduction erosion, and the growth of continental crust, *Reviews of Geophysics*, vol. 29(3), 279-316

von Huene, R. & Ranero, C.R. (2003). Subduction erosion and basal friction along the sediment-starved convergent margin off Antofagasta, Chile, *Journal of Geophysical Research*, vol. 108(B2), 2079, doi:10.1029/2001JB001569

von Humboldt, A., Lubrich, O., Ette, O. & Kalscheuer, C. (2004). *Ansichten der Kordilleren und Monumente der eingeborenen Völker Amerikas*, Eichborn Verlag, 446p.

von Humboldt, A., Lubrich, O. & Ette, O. (2006). *Kosmos. Entwurf einer physischen Weltbeschreibung*, Eichborn Verlag, 941p.

Wallace, L.M, McCaffrey, R., Beavan, J. & Ellis, S. (2005). Rapid microplate rotations and backarc rifting at the transition between collision and subduction, *Geology*, vol. 33(11), 857-860

Wang, K., Hyndman, R.D. & Yamano, M. (1995). Thermal regime of the southwest Japan subduction zone: Effect of age history of the subducting plate, *Tectonophysics*, vol. 248, 53-69

Wang, K. & He, J. (1999). Mechanics of low-stress forearcs: Nankai and Cascadia, *Journal of Geophysical Research*, vol. 104(B7), 15191-15205

Wang, K. & Suyehiro, K. (1999). How does plate coupling affect crustal stresses in Northeast and Southwest Japan?, *Geophysical Research Letters*, vol. 26(15), 2307-2310

Wang, K. (2000). Stress-strain 'paradox', plate coupling, and forearc seismicity at the Cascadia and Nankai subduction zones, *Tectonophysics*, vol. 319, 321-338

Wang, K. & Hu, Y. (2006). Accretionary prisms in subduction earthquake cycles: The theory of dynamic Coulomb wedge, *Journal of Geophysical Research*, vol. 111(B6), doi:10.1029/2005JB004094

Wells, R.E. & Simpson, R.W. (2001). Northward migration of the Cascadia forearc in the northwestern U.S. and implications for subduction deformation, *Earth Planets Space*, vol. 53, 275-283

Wells, R.E., Blakely, R.J. & Weaver, C.S. (2002). Cascadia microplate models and within-slab earthquakes, In: Kirby, S.H., Wang, K. & Dunlop, S.G. (eds.), *The Cascadia Subduction Zone and arc volcanism*, U.S. Geological Survey Open-File Report 02-328, Geological Survey of Canada Open File 4350, 17-23

Wells, R.E., Blakely, R.J., Sugiyama, Y., Scholl, D.W. & Dinterman, P.A. (2003). Basin-centered asperities in great subduction zone earthquakes: A link between slip, subsidence, and subduction erosion, *Journal of Geophysical Research*, vol. 108(B10), 2507, doi:10.1029/2002JB002072

Wigger, P.J., Schmitz, M., Araneda, M., Asch, G., Baldzuhn, S., Giese, P., Heinsohn, W.-D., Martinez, E., Ricaldi, E., Röwer, P. & Viramonte, J. (1994). Variation in the Crustal Structure of the Southern Central Andes Deduced from Seismic Refraction Investigations, In: Reutter, K.-J., Scheuber, E. & Wigger, P. (eds.), *Tectonics of the Southern Central Andes*, Springer, 23-48

Wilson, D.S. (2002). The Juan de Fuca plate and slab: Isochron structure and Cenozoic plate motions, In: Kirby, S.H., Wang, K. & Dunlop, S.G. (eds.), *The Cascadia Subduction Zone and arc volcanism*, U.S. Geological Survey Open-File Report 02-328, Geological Survey of Canada Open File 4350, 9-12

Wong, I.G. & Chapman, D.S. (1990). Deep intraplate earthquakes in the western United States and their relationship to lithospheric temperatures, *Seismological Society of America Bulletin*, vol. 80, 589-599

Wright, D.J., Bloomer, S.H., MacLeod, C.J., Taylor, B. & Goodlife, A.M. (2000). Bathymetry of the Tonga Trench and Forearc: a map series, *Marine Geophysical Researches*, vol. 21, 489-511

Wu, P. (1999). Modelling postglacial sea levels with power-law rheology and a realistic ice model in the absence of ambient tectonic stress, *Geophysical Journal International*, vol. 139, 691-702

Wu, P. (2001). Postglacial induced surface motion and gravity in Laurentia for uniform mantle with power-law rheology and ambient tectonic stress, *Earth and Planetary Science Letters*, vol. 186, 427-435

Yáñez, G. & Cembrano, J. (2004). Role of viscous plate coupling in the late Tertiary Andean tectonics, *Journal of Geophysical Research*, vol. 109, B02407, doi:10.1029/2003JB002494

Yoon, J. & Jeon, S. (2004). Experimental verification of a pts mode II test for rock, *International Journal of Rock Mechanics and Mining Sciences,* vol. 41, 8-13

Yu, G., Wesnousky, S.G. & Ekström, G. (1993). Slip Partitioning along Major Convergent Plate Boundaries, *Pure and Applied Geophysics*, vol. 140(2), 183-210

Yuan, X., Sobolev, S.V., Kind, R., Oncken, O. & Andes Seismology Group (2000). New constraints on subduction and collision processes in the central Andes from comprehensive observations of P to S converted seismic phases, *Nature*, vol. 408, 958-961

Zienkiewicz, O.C. (1972). *Introductory Lectures on the Finite Element Method*, Springer Verlag, Wien, New York, 99p.

Zienkiewicz, O.C. & Taylor, R.L. (1998). *The Finite Element Method*, Fourth Edition, vol. 2, McGraw-Hill Book Company, London, 807p.

Appendices

Appendix A

The numerical sandbox: Comparison of model results for a shortening and an extension experiment

Susanne J.H. Buiter, Andrey Yu. Babeyko, Susan Ellis, Taras V. Gerya, Boris J.P. Kaus, Antje Kellner, Guido Schreurs & Yasuhiro Yamada

The numerical sandbox: comparison of model results for a shortening and an extension experiment

SUSANNE J. H. BUITER[1], ANDREY YU. BABEYKO[2,8], SUSAN ELLIS[3],
TARAS V. GERYA[4], BORIS J. P. KAUS[5], ANTJE KELLNER[2],
GUIDO SCHREURS[6] & YASUHIRO YAMADA[7]

[1]*Centre for Geodynamics, Geological Survey of Norway, 7491 Trondheim,
Norway (e-mail: susanne.buiter@ngu.no)*
[2]*GeoForschungsZentrum Potsdam, Telegrafenberg, 14473 Potsdam, Germany*
[3]*Institute of Geological and Nuclear Sciences, P.O. Box 30368, Lower Hutt, New Zealand*
[4]*Swiss Federal Institute of Technology, Sonneggstrasse 5, 8092 Zürich, Switzerland*
[5]*Department of Earth Sciences, University of Southern California, Los Angeles, USA*
[6]*Institute of Geological Sciences, University of Bern, Baltzerstrasse 1-3,
3012 Bern, Switzerland*
[7]*Department of Civil and Earth Resources Engineering, Kyoto University,
Kyoto 606-5801, Japan*
[8]*Now at Institut für Meteorologie und Geophysik,
J.W. Goethe Universität Frankfurt, Germany*

Abstract: We report results of a study comparing numerical models of sandbox-type experiments. Two experimental designs were examined: (1) A brittle shortening experiment in which a thrust wedge is built in material of alternating frictional strength; and (2) an extension experiment in which a weak, basal viscous layer affects normal fault localization and propagation in overlying brittle materials. Eight different numerical codes, both commercial and academic, were tested against each other. Our results show that: (1) The overall evolution of all numerical codes is broadly similar. (2) Shortening is accommodated by in-sequence forward propagation of thrusts. The surface slope of the thrust wedge is within the stable field predicted by critical taper theory. (3) Details of thrust spacing, dip angle and number of thrusts vary between different codes for the shortening experiment. (4) Shear zones initiate at the velocity discontinuity in the extension experiment. The asymmetric evolution of the models is similar for all numerical codes. (5) Resolution affects strain localization and the number of shear zones that develop in strain-softening brittle material. (6) The variability between numerical codes is greater for the shortening than the extension experiment.

Comparison to equivalent analogue experiments shows that the overall dynamic evolution of the numerical and analogue models is similar, in spite of the difficulty of achieving an exact representation of the analogue conditions with a numerical model. We find that the degree of variability between individual numerical results is about the same as between individual analogue models. Differences among and between numerical and analogue results are found in predictions of location, spacing and dip angle of shear zones. Our results show that numerical models using different solution techniques can to first order successfully reproduce structures observed in analogue sandbox experiments. The comparisons serve to highlight robust features in tectonic modelling of thrust wedges and brittle-viscous extension.

Numerical and analogue modelling methods represent two different techniques with which the evolution of geological structures, such as fold-and-thrust belts and sedimentary basins, can be investigated. The underlying assumption with both methods is that their results approximate the development of structures in the real Earth in a reasonable manner. We may then expect that the results of analogue and numerical models look similar when applied to the same

set-up. This expectation motivated us to directly compare results of numerical models obtained with different codes and results of analogue experiments from different laboratories. The aims of our study are (1) to compare results from different numerical codes and (2) to test the similarity of numerical and analogue models, in order to help establish robust features of tectonic models on the scale of the upper crust.

The companion paper (Schreurs *et al.* 2006) presents the results of an analogue comparison study with ten participating modelling laboratories. Two experimental set-ups were tested: (1) a brittle convergent thrust wedge experiment and (2) a brittle-viscous extension experiment. The reproducibility of modelling results between the laboratories was found to be fairly high as shown by the same general trends in the results. Differences between the analogue models were found in, for example, number of faults, fault spacing and dip, and surface slopes. The study highlights the importance of (1) a careful determination of properties of the granular material and (2) the effect of lateral side boundaries on resulting structures due to friction between model materials and sidewalls. A sandbox needs to be wide enough, therefore, to avoid such boundary effects, and structures should if possible be studied in sections well away from the sidewalls.

We present numerical equivalents of the two analogue experiments of Schreurs *et al.* (2006). The conditions of the analogue modelling apparatus and the analogue material properties are approached as closely as possible. We compare the numerical results to each other through determination of their qualitative (visual) and quantitative (measurements of, for example, surface slope and shear zone dip) similarities and differences. Our study is not a numerical benchmark in its strictest sense as this would require the use of the exact same initial setup, material properties, boundary conditions, mesh size and time step size (see for example the numerical convection benchmarks of Blanckenbach *et al.* 1989; van Keken *et al.* 1997). Instead, we show the variability in results obtained by using different solution methods (finite element method, finite difference method and distinct element method) and allowing variations in mesh and time step size and boundary conditions (e.g., implementation of boundary friction). With our approach, we test the code-independence of tectonic structures predicted by numerical models and our findings are, therefore, of direct relevance for studies in which numerical experiments are used to investigate geological processes. Eight numerical codes were used in

our comparison: Abaqus/Standard, LAPEX-2D, I2ELVIS, Microfem, NISA/Static, PFC^{2D}, SloMo and Sopale. A description of these codes is given in the next section.

The combination of our study with the accompanying paper results in a series of numerical and analogue model experiments, which are compared in a qualitative and quantitative manner with each other. Our results can be used to evaluate how closely various numerical solution methods can reproduce analogue model conditions. Issues that should be considered carefully in the 'numerical sandbox' include the suitability of continuum methods (e.g., finite element method) in simulating the behaviour of discontinuous grains, the importance of dilation and compaction in granular materials, and the representation of velocity discontinuities. Numerical modelling of sandbox experiments poses significant computational challenges requiring that numerical codes are able to (1) calculate large deformations, (2) represent complex boundary conditions, including frictional boundaries and free surfaces, and (3) include a complex rheology involving both viscous and frictional/plastic materials. These challenges reflect directly the state-of-the-art requirements for numerical modelling of large-scale tectonic processes.

The two experimental set-ups were designed to reflect set-ups commonly used in the study of upper-crustal tectonic processes. Convergent thrust wedges have been studied with analytical techniques (Davis *et al.* 1983; Dahlen 1984), analogue experiments (e.g., Mulugeta 1988; Gutscher *et al.* 1998*a*; Storti *et al.* 2000) and numerical models (e.g., Strayer *et al.* 2001; Burbridge & Braun 2002). Similarly, brittle-viscous extension has been investigated with analogue (e.g., Michon & Merle 2000; Bahroudi *et al.* 2003) and numerical (e.g., Behn *et al.* 2002; Wijns *et al.* 2003) methods. A few previous studies have combined numerical and analogue modelling methods for studying a tectonic process on the scale of the crust. Sassi *et al.* (1993) investigated the reactivation of pre-existing faults in a compressive regime and showed how the visualization of the stress field in the numerical results (obtained with a distinct element method) could help in the interpretation of the observed reactivation of some low angle faults. The models calculated with the distinct element method by Saltzer & Pollard (1992) of structures in sedimentary layers overlying basement normal faults show a high resemblance to deformation patterns typically observed in sandbox models. A high level of agreement between analogue and numerical models of

brittle and brittle-viscous thrust wedges was obtained by Ellis *et al.* (2004). Their results indicate that the continuum approximation of the finite element method does not necessarily need to be a strong limitation in modelling granular materials. An encouraging agreement between results from finite element and analogue models is also shown by Panien *et al.* (2006); Cruden *et al.* (2006) and Le Pourhiet *et al.* (2006).

Numerical and analogue modelling techniques share the advantages and disadvantages of trying to capture aspects of a geological process in a model. Both methods allow the evolution of structures to be observed, which can be helpful in generating ideas on the origin and development of structures observed in the field. With numerical and analogue models it is possible to vary model parameters easily and determine their relevance for the process under consideration. However, models are also only an approximation of the natural situation and their restrictions should be taken into account when interpreting their results. Advantages of the numerical method are the easy quantification of model results, including the possibility of tracking stresses, strain and strain-rates during the evolution of the model, and the relatively large freedom in choice of material properties (including a relatively easy implementation of temperature-dependent rheologies), boundary conditions and geometries. Some approaches lose accuracy when dealing with large deformation situations (due to remeshing, for example) or large viscosity contrasts. The resolution of 3D models is in general still quite low. Analogue models on the other hand are very suitable for studying the 3D evolution of structures with time. This makes it possible to evaluate the effects of,

for example, lateral changes in material properties or oblique extension. The technique is limited in the application of temperature dependent rheologies, phase changes and variations in geometries. Numerical and analogue techniques are partly complementary and the combination of both methods may help establish the robustness of model results (see also Smart & Couzens-Schultz 2001).

Modelling methods

Material properties

The models contain three materials, which have properties resembling those of quartz sand, glass microbeads and polydimethylsiloxane (PDMS). In the analogue comparison, every laboratory used its own granular materials, which typically differ in frictional properties and density (see Schreurs *et al.* (2006) and Table 1). In the numerical experiments fixed values are used to allow the comparison of the numerical results to each other (Table 1). The material behaviour of the numeric brittle materials is characterised by a Coulomb failure-frictional criterion:

$$\sigma_t = \sigma_n \tan(\phi) + C \qquad (1)$$

where σ_t denotes shear stress, σ_n normal stress, ϕ the angle of internal friction and C cohesion. Measurements of the properties of analogue granular materials show that deformation initially occurs through a combination of elastic and frictional strain-hardening behaviour until failure at peak strength (ϕ_{peak}), followed by a strain-softening phase until a stable strength

Table 1. *Material properties*

Material	Values in numerical models					Measured analogue properties*←				
	Density (kg m^{-3})	C (Pa)	$\phi_{peak}^{\dagger}$	$\phi_{stable}^{\ddagger}$	η (Pa s)	Density (kg m^{-3})	C (Pa)	$\phi_{peak}^{\dagger}$	$\phi_{stable}^{\ddagger}$	η (Pa s)
Sand	1560	10	36°	31°		1350–1740	3–150	33°–45°	28.2°–39°	
Microbeads	1480	10	22°	20°		1400–1600	−25–50	21°–29.2°	20°–26.2°	
PDMS	965				5e4	965				5e4
Side friction		0	19°	19°				20°§	16°–17°§	

*Values from Schreurs *et al.* (2006) for the materials used in the laboratories of University of Bern, IFP Rueil-Malmaison, University of Parma, University of Pavia and University of Toronto. Sand is sieved from 20 cm height with an approximate filling rate of 250 grams/minute. PDMS from Weijermans (1986).
†Angle of internal friction at peak strength.
‡Angle of internal friction at stable strength.
§GFZ sand measured by J. Lohrmann shows an angle of internal friction of 20° softening to 16° (fine-grained sand, 20–200 μm) or 17° (coarser sand, 20–650 μm).

32   S. J. H. BUITER *ET AL.*

(ϕ_{stable}) is reached (Lohrmann *et al.* 2003; Panien 2004; see also Jaeger & Cook 1979). Five of the eight numeric codes used in our study include elastic material behaviour. For sand, the elastic component is probably relatively small (J. Adam pers. comm.). Most of the numerical models (six of eight) have been run without dilation and (de)compaction of the materials is, therefore, not automatically taken into account. The strengthening of material in the initial strain-hardening phase seen in analogue models (Adam *et al.* 2005) is in these cases not included. Strain-softening from peak strength to stable strength is assumed to be caused by dilatation of sand at yield and is explicitly prescribed in the numeric models that do not include dilatation. The softening is simulated by a linear decrease in the angle of internal friction over a finite strain interval of 0.5 to 1.0 (finite strain is total accumulated effective strain as measured by the square root of the second invariant of the strain tensor). The cohesion values of the analogue materials were determined using different measuring apparatus (see Schreurs *et al.* 2006) and show a large variation. Cohesion is obtained by extrapolation of the shear stress versus normal stress curve and is, therefore, likely to be an overestimate at low stress values where the stress curve is no longer a straight line, but has a convex-outward shape (Ranalli 1987; Schellart 2000). The boundary friction between sand and the sidewalls and base of the model (which are covered with an 'Alkor' foil in the analogue experiments) is approximately 20°, softening to 16°/17° (for fine sand with grain size 20–200 μm and coarse sand with grain size 20–650 μm, J. Lohrmann, pers. comm.) and a constant value of 19° has been used in the numerical experiments.

PDMS is a Newtonian material with a viscosity of 5×10^4 Pa s (at room temperature and strain rates below 3×10^{-3} s^{-1}, Weijermars 1986) and low Maxwell times. It is modelled as a linear viscous material: $\tau = 2\eta\dot{\varepsilon}$, for deviatoric stress τ, viscosity η, and strain-rate $\dot{\varepsilon}$.

Scaling

Some of the models are scaled up from the analogue sandbox-scale (cm) to upper-crustal scale (km). This scaling requires that dynamic similarity is observed (Hubbert 1937; see also Ellis *et al.* 2004). Dynamic similarity is maintained when force ratios and length ratios are constant. The models in this study can be scaled completely through the following three relationships: (1) geometric similarity:

$$\frac{l_n}{l_a} = \text{constant} \qquad (2)$$

where l_n and l_a are the lengths in the numerical and analogue model, respectively; (2) constant ratio of gravitational force to viscous force between the numerical and the analogue model:

$$\frac{\rho g l^2}{\eta v} = \text{constant} \qquad (3)$$

where ρ density, g gravitational acceleration, η viscosity and v velocity; and (3) constant ratio of frictional strength (σ_y) to lithostatic pressure:

$$\frac{\sigma_y}{\rho g l} = \text{constant} \qquad (4)$$

The values for ρ, ϕ and g in the numerical models are within the ranges of the analogue values (Table 1).

Description of the numerical codes

In the following, only a brief description of the main features of the numerical codes is given and the reader is referred to the references provided for more detailed information. Specific assumptions concerning the boundary conditions for the experiments are discussed with the description of the model set-up for each experiment.

Abaqus/Standard. Results obtained with Abaqus/Standard are shown for both experiments and were provided by Susan Ellis. Abaqus is a Lagrangian Finite Element code with implicit time integration (Abaqus/Standard User's Manual 2003). Material behaviour is visco-elasto-plastic and materials deform elastically until plastic or viscous yield is reached, after which deformation continues on yield. Tests for the shortening experiment show that material quickly reaches plastic yield once it enters the deforming region. Plastic yielding is modelled using a non-associative plastic flow law with dilation chosen as zero (to facilitate comparison with the other experiments). Strain softening is included. Boundary friction is implemented through an elastic-stick contact surface formulation. The experiments are scaled such that 1 cm equals 1 km in the numerical model.

I2ELVIS. Taras Gerya provided results from his I2ELVIS code (the successor of I2VIS, Gerya & Yuen 2003) for both experiments. I2ELVIS solves the Stokes equation for creeping

flows using the finite difference method on a Eulerian staggered grid combined with a marker-in-cell technique. Material behaviour is visco-elasto-plastic and incompressible (with, therefore, zero dilation). Elasto-plastic deformation dominates for sand-like material due to the high background viscosity of 10^{12} Pa s, which results in a large visco-elastic relaxation time (10^6 s). In contrast viscous deformation dominates for PDMS-like material due to the low viscosity of 5×10^4 Pa s, which gives small visco-elastic relaxation times (0.05 s). Strain softening is included. Boundary friction is incorporated through frictional contact layers (4 elements wide at the sides and 2.5 elements high at the base). Free surface behaviour is obtained through a low viscosity 'air' layer on top of the model ($\eta = 1$ Pa s and $\rho = 1$ kg m^{-3}). The experiments are not scaled.

LAPEX-2D. Model results for LAPEX-2D were provided by Andrey Babeyko for both experiments. LAPEX-2D solves for balances of mass, momentum and energy through an explicit Lagrangian Finite Difference technique (FLAC-type) (Cundall & Board 1988; Poliakov *et al.* 1993; Babeyko *et al.* 2002). Material and history properties including full stress and strain tensors are tracked and updated by using particles. The material behaviour is visco-elastic with plastic yielding. Dilatation is zero. Strain softening is included. Boundary friction is implemented through explicitly added frictional forces at the boundary nodes (newly added feature for these experiments). The experiments are scaled whereby 1 cm equals 10 km in the numerical model.

Microfem. Susan Ellis also provided model results calculated with Microfem (Fullsack 1995) for both experiments. Microfem is a plane-strain arbitrary Lagrangian Eulerian finite element code. The Stokes equation for incompressible creeping flows is solved on a Eulerian grid on which material properties are tracked using a Lagrangian material grid. A free surface is achieved through vertical stretch or shortening of the Eulerian grid. Material behaviour is either viscous or plastic and incompressible (zero dilatation). Strain softening is included. The version used here is modified from the original code from the Dalhousie Geodynamics group. Frictional contacts are incorporated in a simple manner by allowing nodes to move unconstrained tangential to the boundary once frictional yield is exceeded (Ellis *et al.* 2004). The experiments are scaled

such that 1 cm equals 1 km in the numerical models.

NISA II/Static 12.0. Results for the shortening experiment were provided by Antje Kellner. NISA/Static is a Lagrangian Finite Element code (NISA II User Manual 1997). It solves the equations of mechanical equilibrium for visco-elasto-plastic materials, but was used in an elasto-plastic mode for this study. Associated Mohr-Coulomb plasticity is used with a dilatation angle equal to the angle of internal friction. Strain softening is not included. Boundary friction is implemented through the contact element tool: For each frictional boundary two contact surfaces are defined. A contact element combines two contact surfaces facing each other. The experiment is not scaled.

PFC^{2D}. Results for the shortening experiment using the Distinct Element Method PFC^{2D} (PFC^{2D} User's Guide 1999) were provided by Yasuhiro Yamada. The model domain consists of discrete circular elements where only neighbours interact. Linear elasticity (force-displacement law; Cundall & Strack 1979) is incorporated through normal and shear forces at element contacts. The force in the normal direction and a pre-defined friction coefficient determine the inter-element friction in the shear direction. During deformation the size of each element is preserved and only the arrangement in the particle assembly is distorted. Dilatation is incorporated as a change in the inter-element porosity. Strain softening is not included. Boundary friction is incorporated in a similar manner as the inter-element friction. The experiments are scaled whereby 1 cm equals 300 m in the numerical model.

SloMo. Results for the extension experiment were provided by Boris Kaus. SloMo is a plane-strain finite element code (Kaus 2005) which solves the Stokes equations for incompressible materials. The rheology is visco-elasto-plastic with Mohr-Coulomb plasticity. A mixed formulation is employed, with linear, discontinuous, shape-functions for pressure and quadratic shape functions for velocity to avoid spurious pressures (Pelletier *et al.* 1989). Uzawa-type iterations are used to satisfy the incompressibility constraint (Cuvelier *et al.* 1986). In this work, the code has been used in a Lagrangian fashion, with regular remeshing to deal with large deformations (see also Poliakov & Podladchikov 1992). Iterations are performed for plasticity, to ensure that both the force balance and the plastic yield functions

34 S. J. H. BUITER *ET AL.*

are satisfied simultaneously. The interface between sharply varying material properties is tracked by marker-chains, whereas other material properties are stored on the integration points. Strain softening is included. Dilatation is zero. The experiment is not scaled.

Sopale. Model results for Sopale are shown for both experiments and were provided by Susanne Buiter. Sopale is a plane-strain arbitrary Lagrangian Eulerian finite element code (Fullsack 1995) and is the successor of Microfem. A more efficient tracking of material properties (whereby the Lagrangian particles are no longer only constrained to a regular grid and particle injection maintains a high particle density) allows a higher resolution. This version has been modified from the original code to allow horizontal stretch or shortening of the Eulerian grid (in addition to the vertical Eulerian grid modification for free surface behaviour). Strain softening is included. Boundary friction is implemented through the use of frictional contact layers (4 elements wide at the sides and 4 elements high at the base). The experiments are scaled such that 1 cm scales up to 1 km in the numerical model.

Shortening experiment

Model set-up

The shortening experiment follows a more or less classic set-up used to study fold-and-thrust belt evolution with analogue models. Shortening is achieved by moving the right-hand wall inward while the left wall and base are held fixed. The model consists of 'sand' layers with an embedded 0.5 cm thick layer of weaker 'microbeads' (Fig. 1a). Total height is 3.5 cm. The length of the models is variable (Table 2), but since deformation did not reach the left wall in any of the models, all were considered long enough. At the right side an initial wedge 10 cm long with 10° surface slope overlies the model. This wedge slope is in the stable field for a sand wedge (as calculated for this set-up from Dahlen 1984; Zhao *et al.* 1986). The two main problems with representing the analogue set-up numerically lie with the boundary conditions. First, different solutions were applied to simulate boundary friction (contact boundary friction or frictional boundary layers). Second, the mobile wall moving over the base of the sandbox represents a velocity discontinuity, which may lead to high pressures in this corner.
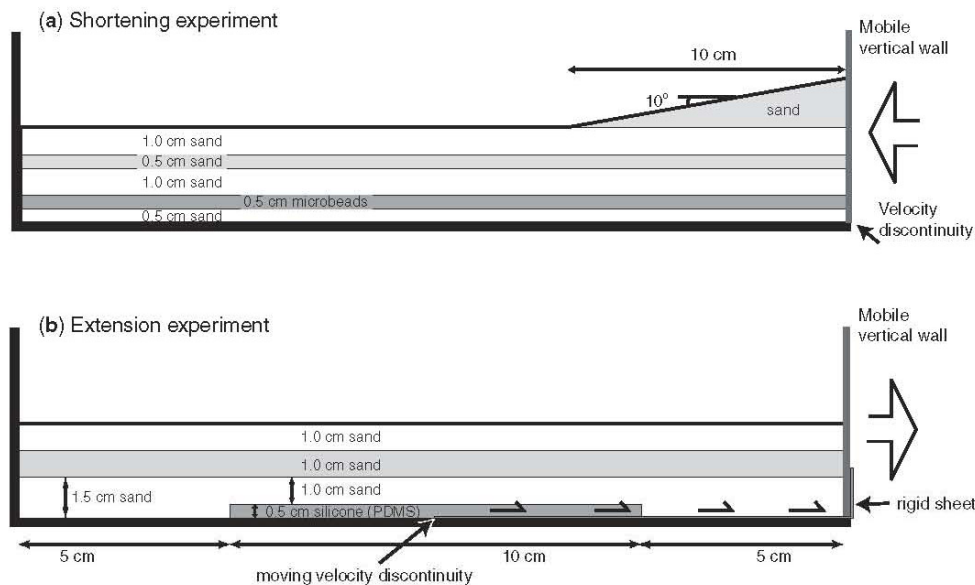

Fig. 1. (**a**) Set-up of the shortening experiment. Horizontal layers of 'sand' (which have the same properties and differ in colour only) with an embedded layer of weaker 'microbeads' are shortened through a mobile wall on the right-hand side which is pushed leftwards. (**b**) Set-up of the extension experiment. A viscous layer (PDMS, 10 × 0.5 cm) lies in the central part of the model on the base. The rest of the model consists of three 'sand' layers (only differing in colour). Extension is achieved by moving the right wall with the attached 10 cm long sheet outwards to the right.

THE NUMERICAL SANDBOX 35

Table 2. *Shortening experiments*

Code	Method*←	Nodes[†]	Track points	Domain length[‡]	Norm. elem. size[§]	$E^{\|}$← (MPa)	ν^1	η^2 (Pa s)
Abaqus/Standard	FEM	301×36	n.a.	30 km/30 cm	0.1	0.5	0.25	5e6
I2ELVIS	FDM + MIC	900×75	393750	45 cm	0.05	3	0.50	1e12
LAPEX-2D	FDM + MIC	351×71	400000	400 km/40 cm	0.075	0.1	0.125	4.5e10
Microfem	ALE	201×36	7236	28 km/28 cm	0.17	n.a.	n.a.	4e13[3]
NISA/Static	FEM	$201 \times 14/18$	n.a.	50 cm	0.25	0.5–1.0[¶]	0.25	n.a.
PFC^{2D}/Kyoto	DEM	$\sim$18000	n.a.	12 km/40 cm	0.06	n.a.	n.a.	n.a.
Sopale	ALE	401×71	253411	40 km/40 cm	0.08	n.a	n.a.	4.6e13

*FEM = Finite Element Method, FDM = Finite Difference Method, ALE = Arbitrary Lagrangian Eulerian, DEM = Distinct Element Method, MIC = Marker-in-Cell.
[†]Nodes in horizontal × vertical direction, or total number of nodes.
[‡]First value is for the numerical model, second value is its equivalent scaled down to the sandbox scale. Height is 3.5 (left-hand side) to 5.26 cm (top of wedge at right-hand side).
[§]Normalized element size is measured as the square root of element area, scaled to sandbox scale (cm).
[‖]Young's modulus, scaled to sandbox scale.
[¶] 0.5 MPa for microbeads, 1.0 MPa for sand.
[1]Poisson ratio.
[2]Background viscosity, scaled to sandbox scale.
[3]Equivalent linear viscosity; a non-linear viscosity was used in the calculations.

The shortening experiment was run with seven numerical codes (Abaqus/Standard, I2ELVIS, LAPEX-2D, Microfem, NISA/Static, PFC^{2D} and Sopale). Five experiments have zero dilatation, while NISA/Static and PFC^{2D} are dilatational. Details of the set-up for each code are given in Table 2. The initial geometry for all numerical models is shown in Figure 2a. The following code-specific assumptions and explanations apply:

Abaqus/Standard. Because Abaqus/Standard uses a Lagrangian formulation and remeshing was not employed, the code cannot handle large deformations and fails to converge at an early step.

I2ELVIS. The rigid mobile wall (with a background viscosity of 10^{14} Pa s and a shear modulus of 10^2–10^4 MPa) is moving inside the computational domain and is, therefore, not simulated through an external boundary condition. The right-hand side frictional boundary layer is limited in vertical extent. During shortening, part of the weak 'air' layer at the top of the model moves spontaneously to behind the mobile wall.

LAPEX-2D. Diffusive erosion (diffusion coefficient of the order 10^{-6} m^2 s^{-1}) is applied at the surface to avoid steep slope angles not supported by the current meshing technique.

Microfem. A small amount of surface smoothing is applied. Tests have shown that this does not significantly affect the dynamic evolution.

NISA II/Static. Because NISA/Static uses a Lagrangian approach without remeshing, the code cannot handle large deformations and fails to converge at an early step.

PFC^{2D}. The density of all materials is 1600 kg m^{-3} and, therefore, differs slightly from the values used in the other experiments (Table 1). The radii size is randomized within 12–24 m (sand) and 5–10 m (microbeads). Shearing tests suggest a shear angle in bulk behaviour of 35° for sand and 25° for microbeads. The basal boundary condition has the same friction angle as sand and is, therefore, higher than the value used in the other experiments.

Sopale. To avoid numerical instabilities associated with an abrupt velocity change the mobile wall velocity is smoothed by extrapolating the applied velocity to 0 over the lowermost 200 m (equals 0.2 cm) of 'sand' (excluding the basal frictional layer). A minimal amount of diffusive erosion (diffusion coefficient 10^{-9} m^2 s^{-1}) is applied at the surface.

Model results

The structural evolution of all models is shown in Figure 2 with plots of geometry and strain-rates after 2, 6, 10 and 14 cm of shortening (unless specified otherwise). Shear zones can readily be identified on the geometry plots, while the strain-rate plots visualize their propagation, moment of initiation and later abandonment.
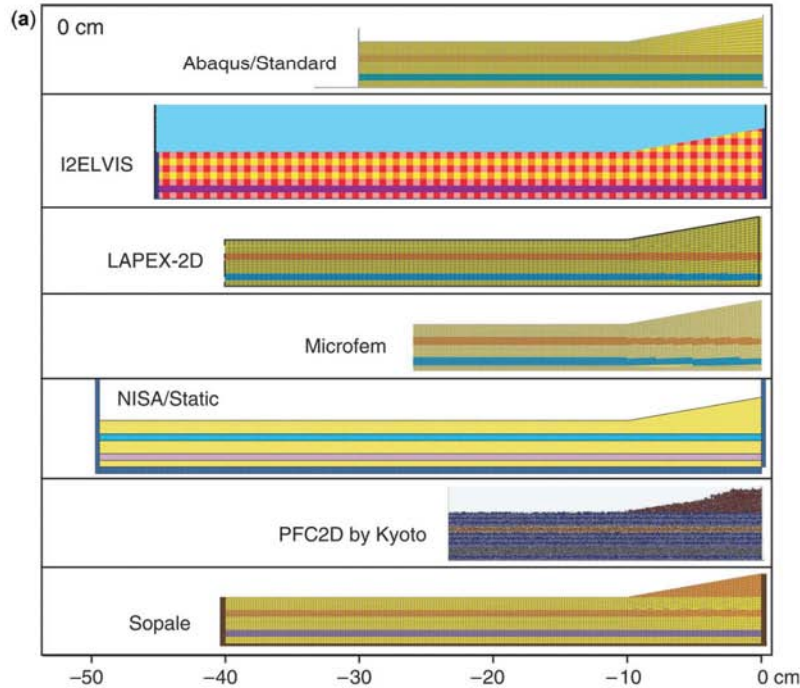
36   S. J. H. BUITER *ET AL.*

Fig. 2. Results for the shortening experiment. All quantities (including strain-rates) are scaled down to the sandbox scale. (**a**) Initial geometries. The grid of Abaqus/Standard is the calculation grid, while for LAPEX-2D, Microfem and Sopale the shown grid is (a subset of) the tracking grid. (**b**) Geometries after 2 cm. Note that Abaqus/Standard and Microfem are shown after 1.8 cm and NISA/Static after 2.3 cm. (**c**) Strain-rates after 2 cm (Abaqus/Standard and Microfem after 1.8 cm, NISA/Static after 2.3 cm). (**d**) Geometries after 6 cm. (**e**) Strain-rates after 6 cm. (**f**) Geometries after 10 cm. (**g**) Strain-rates after 10 cm. (**h**) Geometries after 14 cm. (**i**) Strain-rates after 14 cm.

WebColor

The strain-rate plots also show when the weak embedded layer is utilized and whether shear zones propagate forward along the weak layer or along the base of the model. In continuum numerical models shear displacement is not accommodated along discrete fault planes, but rather along more distributed shear zones. For ease of comparison with the analogue models, we will, however, sometimes refer to 'faults' when describing numerical results.

In order to allow a comparison of all model results in a more quantitative manner we measured the following properties (Table 3, Figs 3 and 4): amount of displacement at which forward thrusts form, their dip angle, the spacing between thrusts, the amount of fault-controlled shortening, surface slope, when the embedded weak layer is activated, and the length of the detachment in this layer. We found, however, that our measurements were influenced by the measurer and subject to small differences in interpretation. The values reported

here were, therefore, completely measured by two people, in the same manner, and subsequently averaged. A fault was considered to be initiated when deformation had clearly localized along it as shown by strain-rate maxima and small finite displacement of the deforming material. Dip angles were measured on the finite deformation plots and represent a dip angle for the whole shear zone (not differentiating between upper and lower dip angles). The variation in dip angle values between the two measurers was on average 2° (ranging between 0°–5°). Measurements of surface slope are rather inaccurate in the initial stages of shortening when only one thrust has formed (Fig. 4b), but improve substantially as soon as a second thrust has formed (Fig. 4c). From then on the difference between the values measured by the two measurers did not exceed 3°. Oscillations in surface slope angles occur just before or after the formation of a new thrust, depending on the degree to which a new thrust is

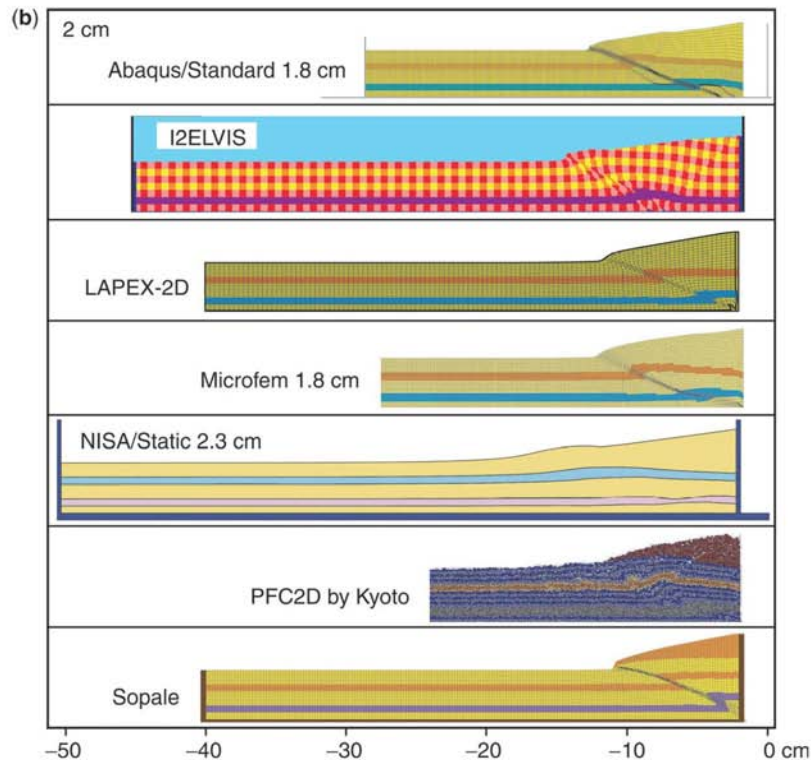THE NUMERICAL SANDBOX   37
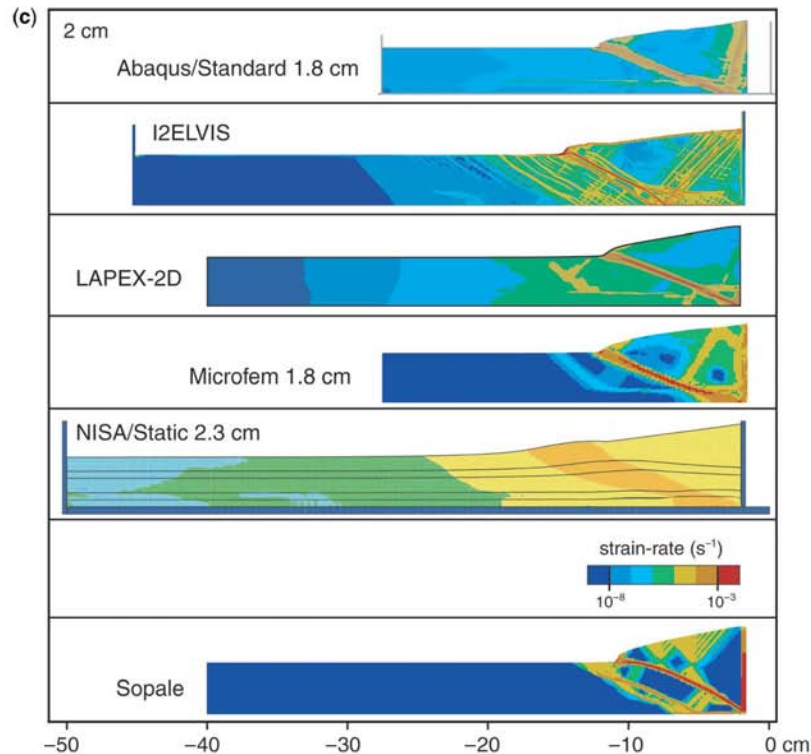

Fig. 2. *Continued.*

WebColor

incorporated into the wedge. To determine the amount of shortening accommodated by faults, we measured the offset of layers at a fault by using the cut-off points of the layers and the fault. Folding of layers towards a fault zone was classified as folding-controlled shortening. Fault-controlled shortening was in a number of cases difficult to determine accurately as the cut-off points of layers with faults were smeared out. The ranges in Table 3 reflect the differences between the two measurers.

The numerical models share many similarities: (1) Shortening is accommodated by in-sequence forward propagation of thrusts (Figs 2 and 3a). (2) The first-formed forward thrust roots at the base of the mobile wall in most of the experiments (Figs 2b and c). (3) By 2 cm of displacement an active forward thrust has formed in all models (Fig. 2b). (4) The location where the first-formed forward thrust reaches the surface is influenced by the surface wedge in almost all of the experiments (except maybe NISA/Static) (Fig. 2b). (5) The embedded weak layer accommodates shear displacement in almost all experiments when sufficient shortening has occurred to increase the surface wedge (Table 3) (the strain-rate plots for I2ELVIS show activity of the weak layer, but no finite strain accumulates here). (6) The surface slope remains in the stable field for critical taper theory (calculated from Dahlen (1984) and Zhao *et al.* (1986) for homogeneous sand) (Fig. 4). Activation of the embedded weak layer has no discernable effect on surface slope (Table 3 and Fig. 4). The stable taper field for a cohesive wedge building in 2.5 cm thick material above the weak layer is almost the same as the stable field shown in Figure 4.

Although the manner in which the models accommodate shortening leads to a similar style of deformation, it is also clear from Figures 2, 3 and 4, and Table 3 that variations exist among the models. Differences between the model results are: (1) The number of thrusts that have formed at a specified amount of displacement is variable (maximum two thrusts difference in the displacement range examined here) (Figs 2 and 3a). (2) The dip angle of the

38   S. J. H. BUITER *ET AL.*

Fig. 2. *Continued.*

forward thrusts shows variations of up to 14°. The dip angle of the first thrusts is most likely influenced by the initial surface wedge. Later thrusts have dip angles between 45° (non-dilatant Roscoe angle) and 45° − $\phi/2$ (Coulomb angle) (Vermeer 1990). (3) The distance between a newly formed thrust and the previously formed thrust is highly variable (Fig. 3c). (4) The embedded weak layer is first activated at different amounts of shortening (Table 3). (5) The amount of fault controlled shortening differs highly (Table 3).

Sensitivity analyses

An important advantage of numerical models is the ease with which the sensitivity to model parameters can be investigated. We tested the variability of the numerical results to assumptions regarding the model set-up (mesh resolution and elasticity) and values of material properties (cohesion and basal friction). We found that the evolution of thrusts is influenced by the resolution of the calculation domain, which may

provide a partial explanation of differences found between the numerical results. Figures 5a and b show the difference after 10 cm displacement for I2ELVIS caused by increasing the normalized element size (Table 2) from 0.05 to 0.1, thus reducing the resolution. A higher resolution tends to increase the number of shear zones, while the individual shear zones become more focussed. A similar trend can be seen when comparing the result from the two ALE-type codes Microfem (lower resolution) and Sopale (higher resolution). Studies using analogue sandbox experiments found that thrust spacing depends on layer thickness, basal friction and surface slope (Mulugeta 1988; Mulugeta & Koyi 1992; Gutscher *et al.* 1998b). However, as pointed out by Mulugeta (1988) changes in material layering may perturb a systematic thrust spacing and it may be, therefore, that the embedded weak ('microbeads') layer in our set-up partly contributes to the observed irregularity in thrust spacing. The sensitivity of shear zone width and spacing is discussed further with the results of the extension
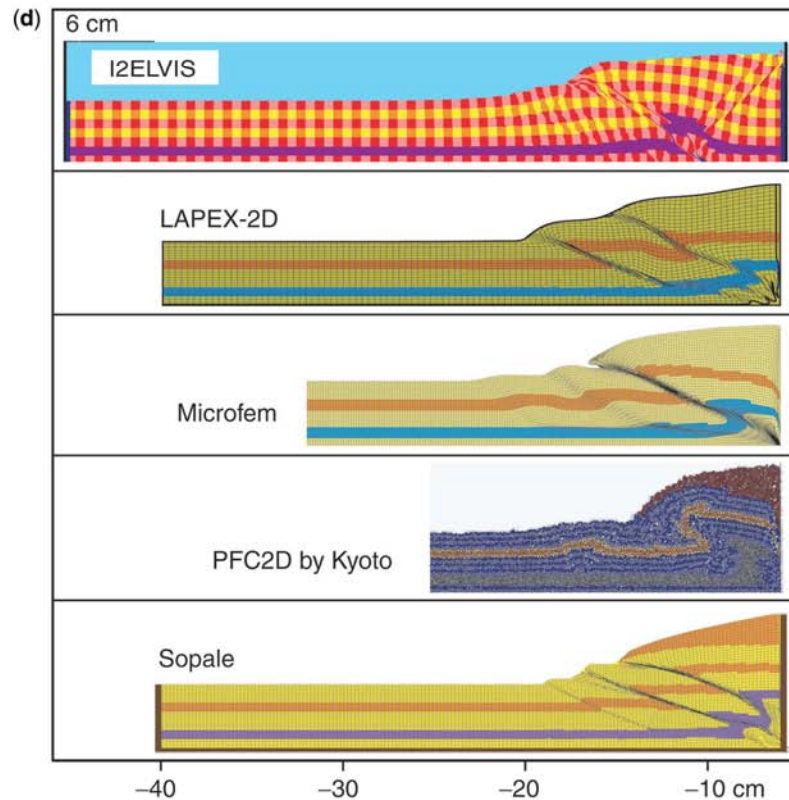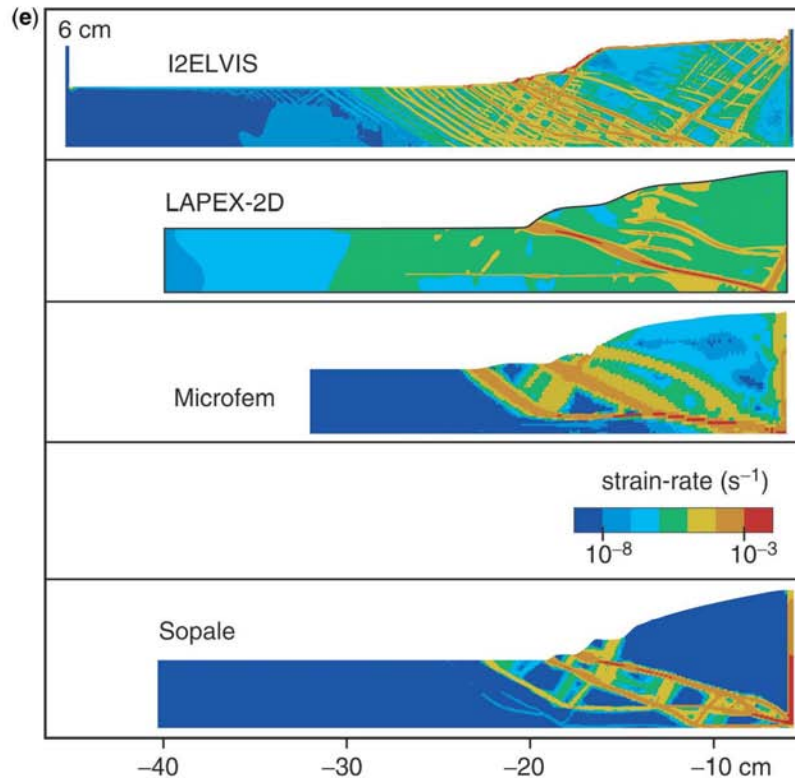
Fig. 2. *Continued.*

experiment (section on *Localization of shear deformation*).

We have assumed that in sandbox-type experiments the amount of finite strain that can be accommodated by elastic material behaviour is small. Abaqus/Standard, I2ELVIS, NISA/-Static and LAPEX-2D include elastic behaviour and their deformation is essentially elasto-plastic in the shortening experiment, while Microfem and Sopale behave essentially rigid-plastic. A general comparison of the large-deformation results shows that the elastic component in material behaviour may lead to slightly more distributed deformation (as strain can also be accommodated between shear zones), but that overall the effect of elasticity is small for our set-up and material properties. In LAPEX-2D, effective elastic strain remains below approximately 2%.

Critical taper theory predicts that the strength of the frictional materials directly influences the taper angle that can be supported. With higher cohesion values the range of stable taper angles increases (from Zhao *et al.* 1986). Ellis *et al.* (2004) found in their thrust wedge experiments that surface slope increases with increasing cohesion, whereby the increase in surface slope mainly occurs at the toe of the material which has been thrust up. Tests with Sopale show that variations in the slope angle of the enveloping surface for cohesion variations from 0 to 100 Pa are limited (2° for displacements of 10 cm or more) without a clear trend towards higher slopes for higher cohesion. Higher cohesion material can support steeper edges of thrust sheets (Figs 5c, d and e). As the higher cohesion value was assigned to 'sand' and 'microbeads' alike, the strength contrast across the 'microbeads' layer is reduced and less shear displacement is consequently accommodated along it.

From Sopale experiments we find that a decrease in the basal friction angle (from 19° to 10°) reduces the surface slope (with around 8°

40   S. J. H. BUITER *ET AL.*

Fig. 2. *Continued.*

for the later shortening stages). This trend is in accordance with critical taper theory, which predicts lower critical taper angles for lower basal friction (Davis *et al.* 1983), and has also been found in other thrust wedge studies (Gutscher *et al.* 1998a; Vanbrabant *et al.* 1999). For low basal friction forward propagation of thrusts occurs faster.

Implications of the numerical experiments

The numerical results for the thrust wedge experiment show similar deformation styles in which shortening is accommodated in a mainly rigid-plastic manner by in-sequence forward propagation of thrusts. Thrust wedge formation and propagation is, therefore, a robust feature of the seven models. However, despite the use of similar initial set-ups, material properties and boundary conditions, variability in structural evolution arises. These differences highlight the possible ranges in structural evolution and measurable quantities (e.g., surface slope) due to

the application of different numerical codes, variable resolution and different implementation of boundary conditions. A fascinating unexpected result is the role of measurer bias in determining quantities such as dip and thrust spacing. Our results indicate that thrust spacing and the number of thrusts versus displacement should be considered carefully when evaluating results from numerical simulations and applying these (in a general manner) to natural systems. This implies that although numerical models may be used 'qualitatively' to interpret the mechanics of thrust wedges, limitations exist to the extent to which quantifiable measures such as thrust fault sequences may be compared at the present time. Future code comparisons may be helpful in reducing the differences between the numerical model results. Test experiments should preferably have a simplified set-up (avoiding abrupt changes in velocity boundary conditions which may require numerical smoothing), the same grid resolution, and material properties as similar as possible.

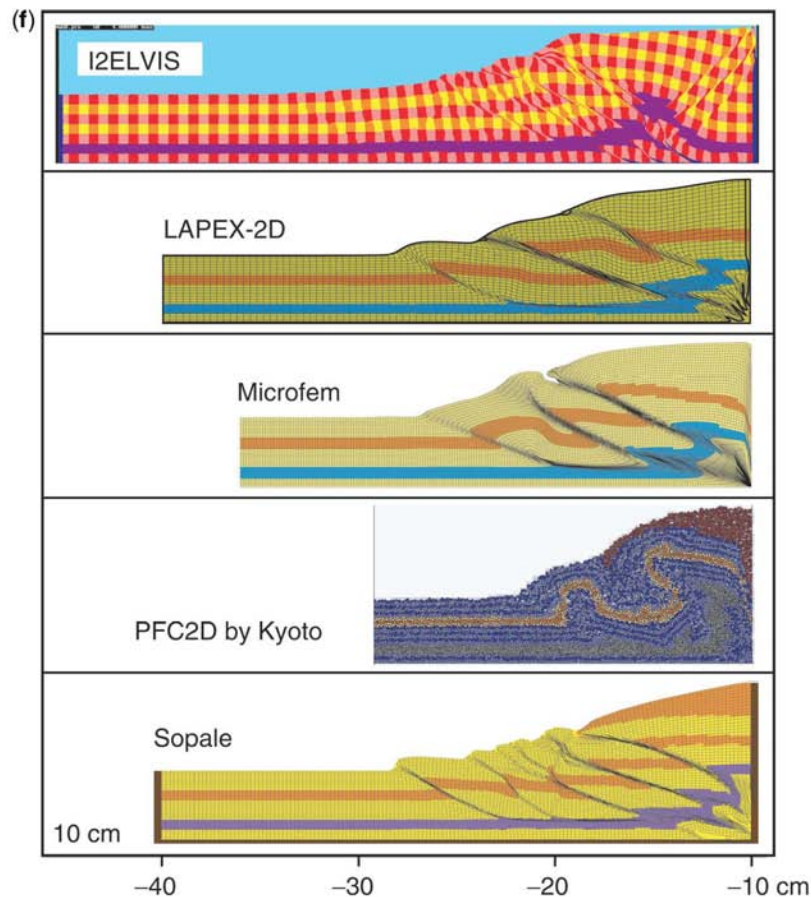THE NUMERICAL SANDBOX   41

Fig. 2. *Continued.*

Comparison to analogue results

Figure 6 compares the numerical model geometries at 2 and 14 cm of displacement to results at equivalent stages from the analogue experiments of the laboratories of Bern, IFP, Parma, Pavia and Toronto (Schreurs *et al.* 2006). We have selected those analogue experiments that have the same set-up as our numerical experiments (i.e., no conveyor belt type experiments) and for which cross-sectional information was recorded. The properties of the granular materials used in the five analogue experiments are variable (e.g., sand: ϕ_{peak} between 33.2° and 45°, ϕ_{stable} 29.2°–39°; microbeads: ϕ_{peak} 22.3°–26.4°, ϕ_{stable} 20.6°–26.2°; the exact values can be found in Schreurs *et al.* (2006)) and this probably affected the analogue results.

As the analogue granular materials are dilatant, they compact upon shortening. The strain-hardening effect this causes has not been included in most of the numerical experiments. Three analogue experiments were monitored through glass sidewalls (Parma, Pavia, Toronto) while two recorded internal deformation with X-ray CT tomography (Bern, IFP). In the accompanying paper (Schreurs *et al.* 2006) it is shown that edge effects may influence the deformational structures close to the lateral (observation) sidewalls. The extent of edge effects may be evaluated by surface monitoring and cutting of sections after the final stage of the experiment. The quantification of parameters in all analogue and numerical experiments was as much as possible done in the same manner. Ranges of parameters that were measured in the analogue
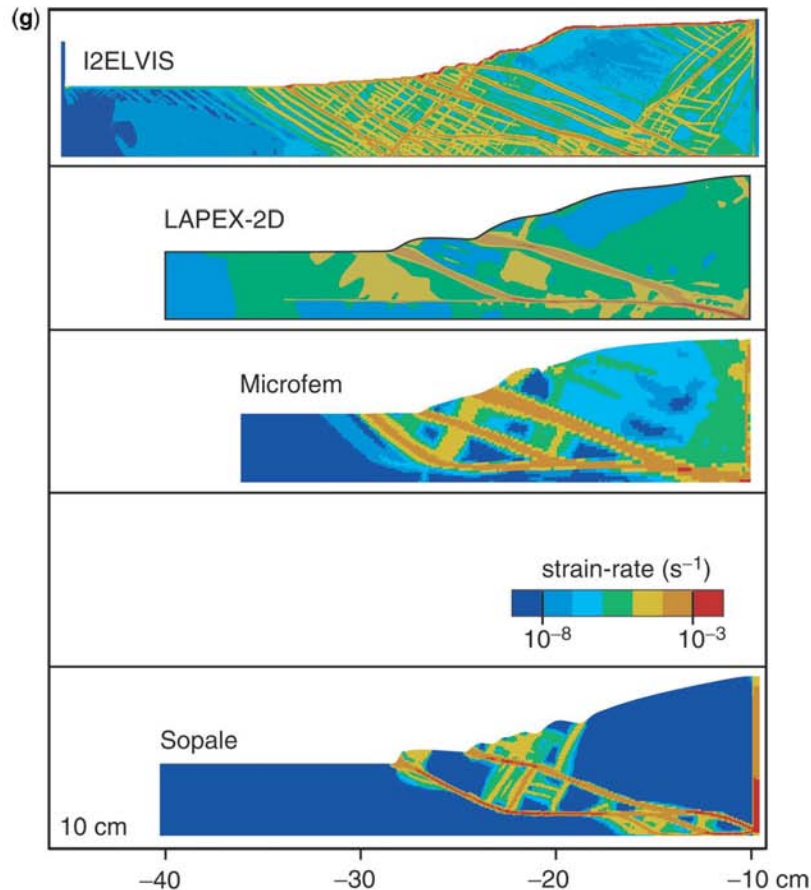
Fig. 2. *Continued.*

experiments (number of thrusts, dip angle, thrust spacing, fault-controlled shortening, microbeads layer activation and surface slope) are indicated in the figures and table which report the numerical values (Figs 3 and 4 and Table 3).

The comparison of our numerical results to the analogue models leads to the following observations: (1) The variability between numerical codes is about the same as the degree of variability between different analogue models. (2) The numerical codes produce the same overall structure and sense of forward-propagation seen in the analogue models. (3) Most of the analogue models show the forward thrust (at 2 cm displacement, Fig. 6a) propagating from a basal point located to the left of the lower right-hand corner, whereas most of the numerical models show the forward thrust propagating from this corner. This may reflect a difficulty in the

numerical models of representing the velocity discontinuity at the corner. Panien *et al.* (2006) show that thrust localization near the mobile wall is sensitive to the exact implementation and smoothing of the applied velocity near the basal corner. Alternatively, the actual velocity discontinuity in the analogue models may not be so sharply defined as implied by the set-up (Fig. 1) and just a small exit slot may smooth the impact of the velocity discontinuity.

(4) Most of the analogue models show a distinct backthrust at 2 cm displacement which is poorly represented in most of the numerical models (except in the results of I2ELVIS, in which the mobile wall is part of the computational domain and has a 0.05 cm high exit slot at the base) (Fig. 6a). The absence of the backthrust in the numerical models may link to the strong preference for the first forward thrust
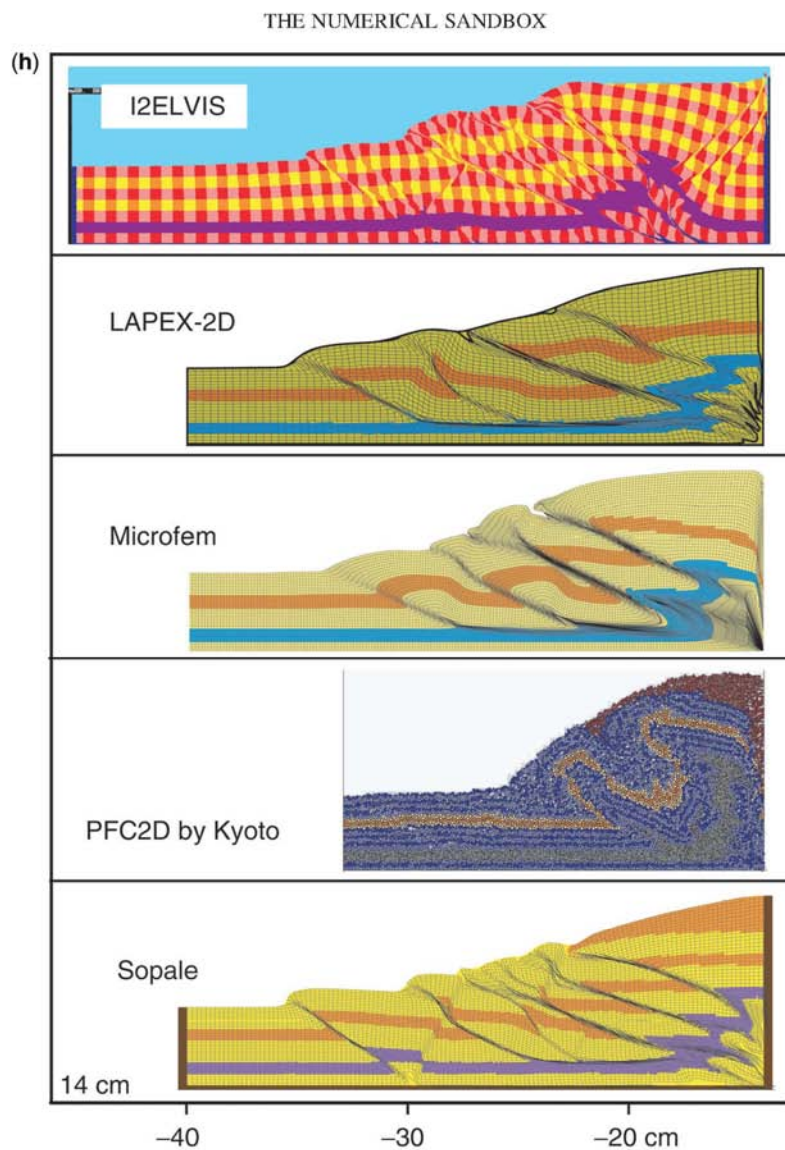
(h)

I2ELVIS

LAPEX-2D

Microfem

PFC2D by Kyoto

Sopale

14 cm

−40   −30   −20 cm

Fig. 2. *Continued.*   **WebColor**

to initiate at the basal right-hand corner, as this configuration does not allow for a backthrust propagating up from the base. Interestingly, in the thrust wedge models of Ellis *et al.* (2004) (which were run with Microfem) a backthrust is visible and the first forward thrust roots to the left of the mobile wall. The exit slot below the mobile wall in these simulations may smooth the corner discontinuity, which suppresses the tendency for the thrust to localize in the basal corner and then allows a backthrust to form. Alternatively, the backthrust in these experiments could be due to the high angle of friction for the backstop. (5) The analogue models show the first thrust intersecting the surface to the left of the imposed wedge, as do the numerical models (Fig. 6a).

(6) Localization of deformation in shear zones in the initial stages of shortening occurs slightly earlier in the numerical models than in the

44   S. J. H. BUITER *ET AL.*
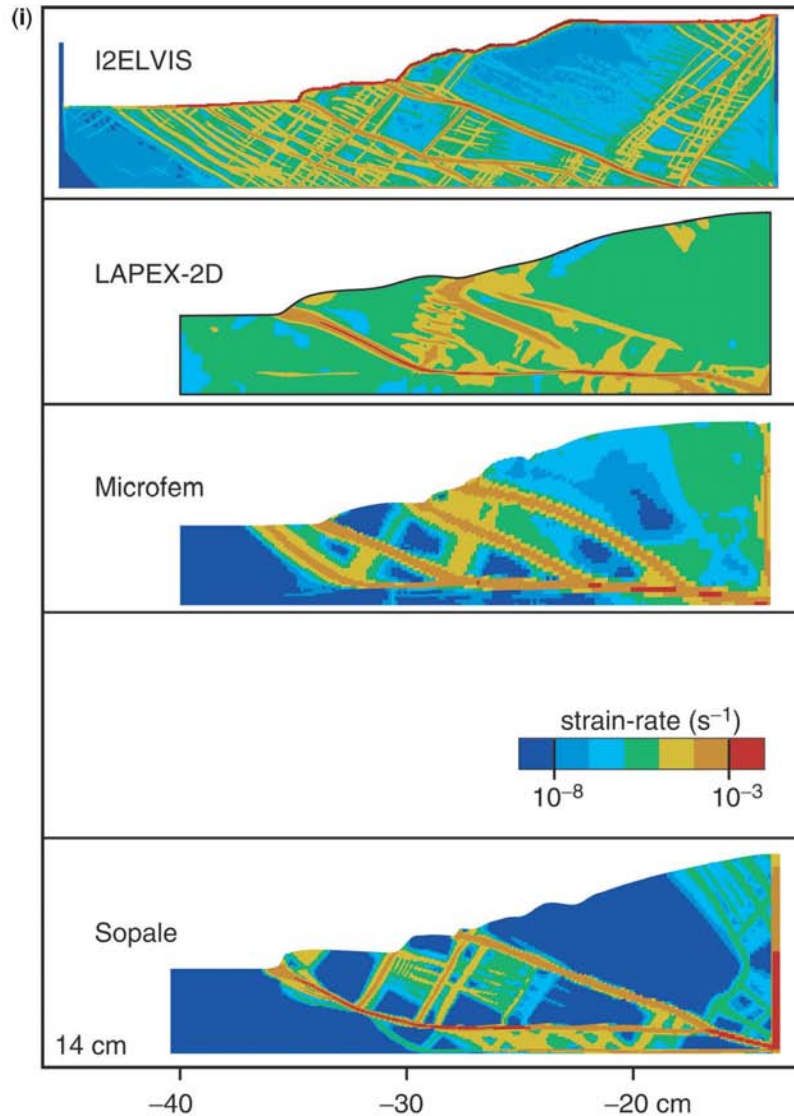
Fig. 2. *Continued.*

analogue models. The analogue models accommodate up to 0.5 cm of shortening through lateral compaction before visible faults form. (7) The variation in the number of thrusts between different numerical codes is approximately the same as the variation between equivalent analogue models (Fig. 3a). (8) The spacing of thrusts is less variable between the numerical codes than between the analogue experiments (Fig. 3c). (9) The dip angles of the forward thrusts are generally slightly lower in the analogue experiments (between 19° and 33°) than in the numerical experiments (between 20° and 39°) (Fig. 3b). The analogue experiments follow the theoretical values for Coulomb dip angles (Vermeer 1990) quite closely, which for the frictional properties of these five analogue experiments range between approximately 23° and 29°. The predicted values for the numeric dip angles lie between 27° (Coulomb dip angle)

Table 3. *Quantification of shortening experiments**←

Code	Fault short.† at 4 cm	'Microbeads' layer	
		Activated at	Detachm. length
Abaqus/ Standard	n.a.	n.a.	
I2ELVIS	2.5–2.6	never	
LAPEX-2D	1.9–2.8	3	7.4
Microfem	1.5–2.3	4	6.2
NISA/Static	n.a.	n.a.	
PFC²ᴰ/Kyoto	1.5–1.8	6	8.0
Sopale	2.0–2.8	4	5.0
Analogue ranges‡	1.9–2.9	5.0–never	2.2–9.3

*All values referred to sandbox scale in cm. Output stages typically available at 0, 0.5, 1, 2 and then every 2 cm of shortening.
†Fault-controlled horizontal shortening determined by cut-off points between layers and the faults.
‡Analogue values from experiments of University of Bern, University of Parma, University of Pavia, IFP Rueil-Malmaison and University of Toronto (Schreurs *et al.* 2006).

and 45° (non-dilatant Roscoe dip angle). The first thrusts may be influenced by the surface wedge, leading to lower values for their dip angles. (10) The surface slopes measured for the numerical models plot around the lower ranges of the analogue surface slopes (Fig. 4). This is probably caused by the generally lower strength of the numerical materials in comparison with many of the analogue materials (Table 1).

Most of the differences between the numerical and analogue models may be attributed to the difficulty in representing the exact set-up of the analogue model and to differences in material properties. Despite these differences, the numerical models still produce a similar taper geometry and evolutionary style to the analogue models.

Extension experiment

Model set-up

The extension experiment examines the influence of a weak, basal viscous layer on normal fault localization and propagation in overlying brittle materials. The model is 20 cm wide and 3.5 cm high (Fig. 1b). It consists of three 'sand' layers (only coloured differently) and a 10 cm wide and 0.5 cm high layer of viscous PDMS, which overlies the central basal part of the model. A thin rigid sheet covering the base of the model extends from the middle to the right lateral wall and is attached to it. Extension is achieved by moving the right wall outward to
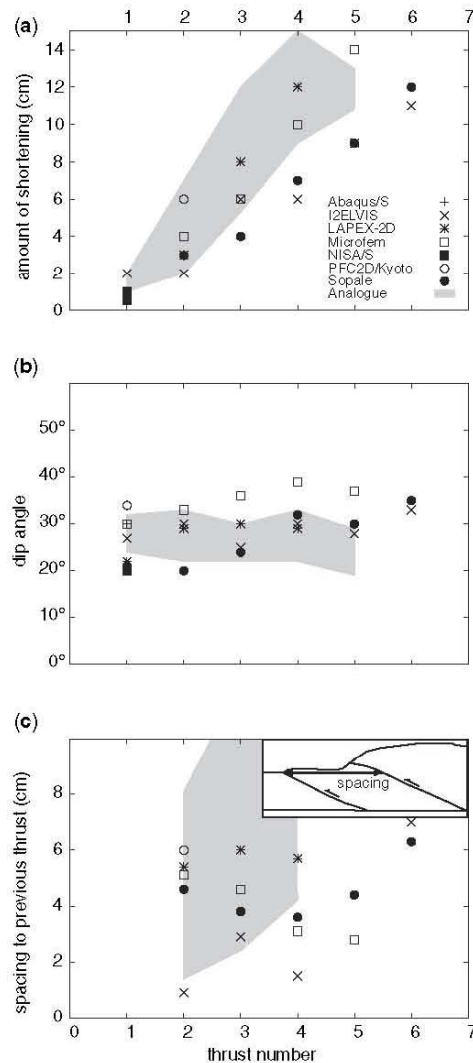

Fig. 3. (a) The amount of displacement at which a forward thrust forms shows that all experiments have forward propagation of thrust formation. (b) Dip angle of forward thrusts at the moment of their initiation. A dip angle of approximately 19° is expected for the first thrust if its location was entirely controlled by the initial wedge. (c) Spacing to the previous forward thrust measured at the moment of initiation of the new forward thrust. Inset shows how thrust spacing is measured. The quantities in (b) and (c) have been measured at the same stages of shortening as depicted in (a). The grey bands denote the range of values measured for the analogue experiments of University of Bern, IFP Rueil-Malmaison, University of Parma, University of Pavia and University of Toronto (see also Fig. 6 and Schreurs *et al.* 2006).
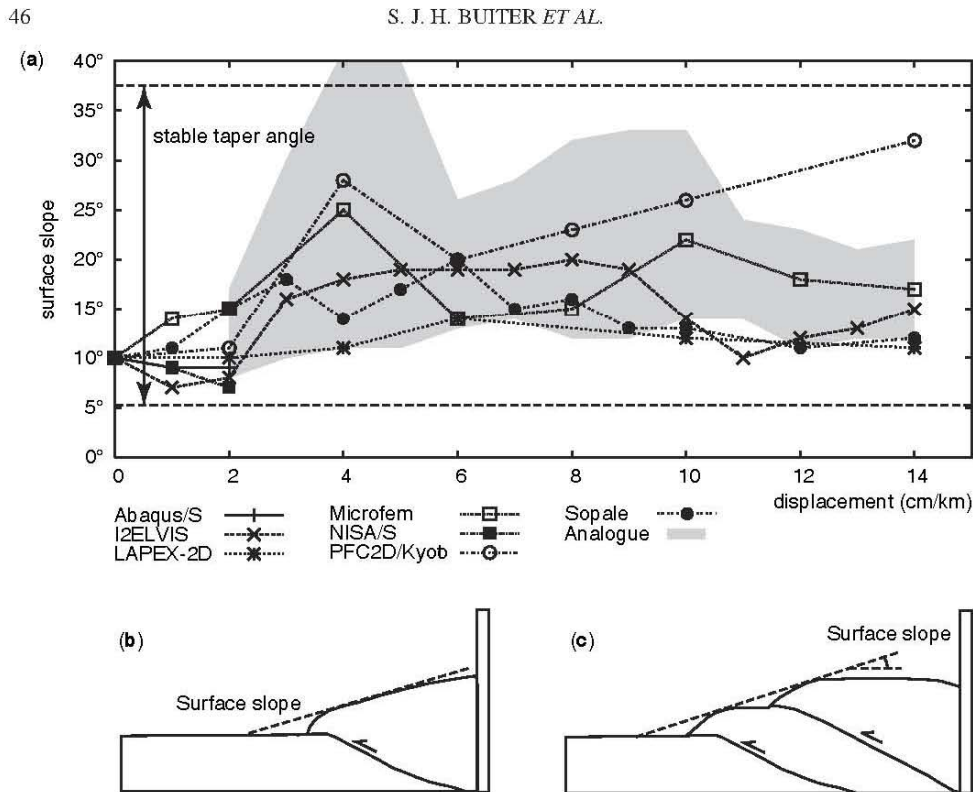
46   S. J. H. BUITER *ET AL.*

Fig. 4. (**a**) Surface slope versus amount of displacement. Surface slopes as measured in the analogue experiments of University of Bern, IFP Rueil-Malmaison, University of Parma, University of Pavia and University of Toronto (Schreurs *et al.* 2006) are shown as a grey band. (**b**) Schematic figure showing how surface slope has been determined for the early stages of shortening. It is clear that the initial surface slope angles are difficult to determine. (**c**) For two or more thrusts, the surface slope has been determined by drawing the enveloping surface.

the right at a rate of 2.5 cm/hr. This velocity is also transmitted to the right basal half of the model through the basal sheet. The tip of the basal sheet forms a migrating velocity disconti-nuity. The base of the model, the basal sheet and the sidewalls are again covered with Alkor foil (prescribed boundary friction is 19°). The boundary condition of silicone overlying this foil was treated differently in the models. The extension experiment was run with six nume-rical codes (Abaqus/Standard, I2ELVIS, LAPEX-2D, Microfem, SloMo and Sopale; Table 4), which were all non-dilatational for this experiment. The initial geometries are shown in Figure 7a. The following code-specific assumptions apply:

Abaqus/Standard. Basal friction is applied along the entire bottom boundary. The change in velocity at the basal velocity discontinuity is accommo-dated over 4 elements (0.4 km scaling to 0.4 cm). The model diverged after 1.5 cm of displacement.

I2ELVIS. Basal friction is applied along the whole bottom boundary. The rigid mobile wall and a 0.5 mm thin rigid plate (with a back-ground viscosity of 10^{14} Pa s and a shear modulus of 10^2-10^4 MPa) are included into the computational domain. During extension, part of the weak 'air' layer at the top of the model is spontaneously displaced from behind the mobile wall.

LAPEX-2D. Basal points above the moving sheet are assigned the velocity of the sheet, whereas basal points to the left of the moving sheet are held fixed. The change in velocity at the basal velocity discontinuity is accommodated over 4 elements (2.7 km scaling to 0.27 cm).

Microfem. Basal friction is applied along the entire bottom boundary. The change in velocity at the basal velocity discontinuity is smoothed over 3 nodes (0.25 km scaling to 0.25 cm). The domain width is 25 km (25 cm).
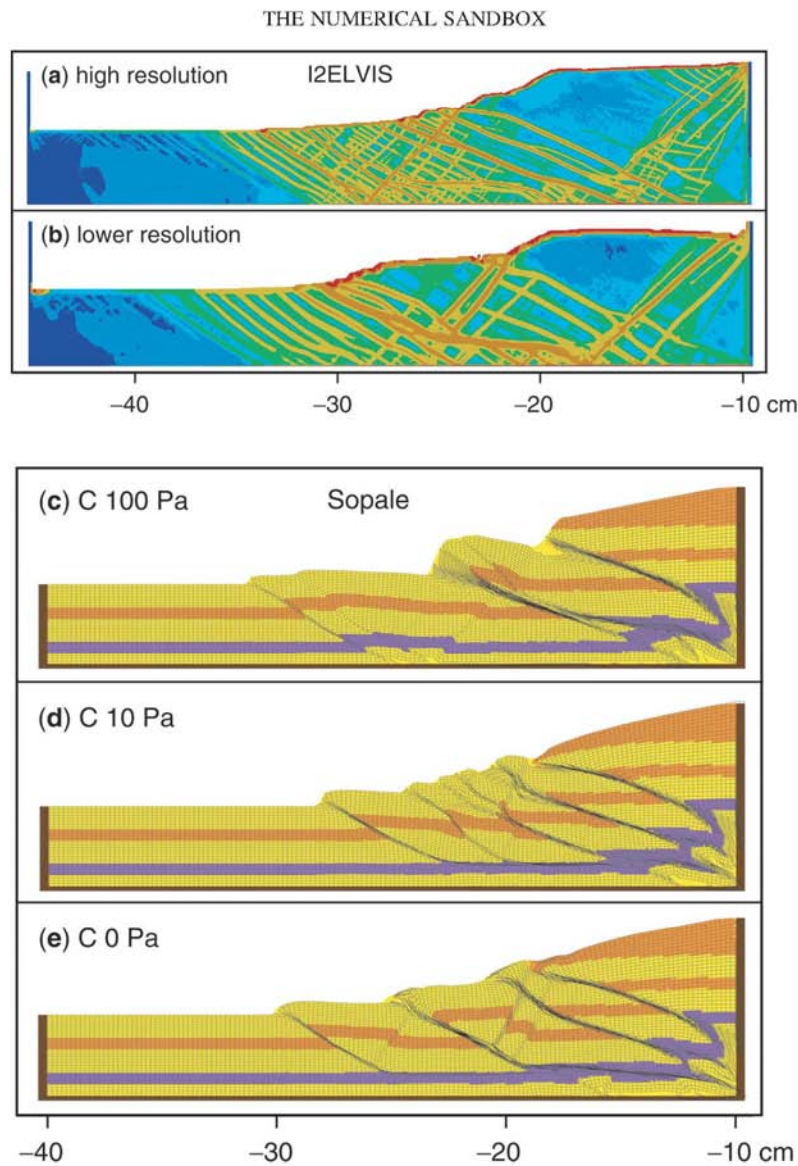
THE NUMERICAL SANDBOX   47

Fig. 5. Sensitivity tests for the shortening experiment. I2ELVIS results after 10 cm of displacement for (**a**) high resolution (normalized element size 0.05 as in Fig. 2) and (**b**) lower resolution (normalized element size 0.1). Sopale results after 10 cm of displacement for (**c**) a cohesion of 100 Pa (sandbox scale), (**d**) a cohesion of 10 Pa (as in Fig. 2), and (**e**) a cohesion of 0 Pa.

WebColor

SloMo. Basal points above the moving sheet are assigned the velocity of the sheet, whereas points to the left are held fixed. The basal velocity discontinuity is accommodated by a linear decrease in velocity over 0.5 cm (10 elements).

Sopale. Basal points above the moving sheet are assigned the velocity of the sheet, whereas basal points to the left of the moving sheet are held fixed. The change in velocity at the basal velocity discontinuity is accommodated over 4 elements (0.2 km scaling to 0.2 cm). The vertical sides are held fixed (however, this boundary condition has no effect as deformation does not propagate to the lateral ends of the model).
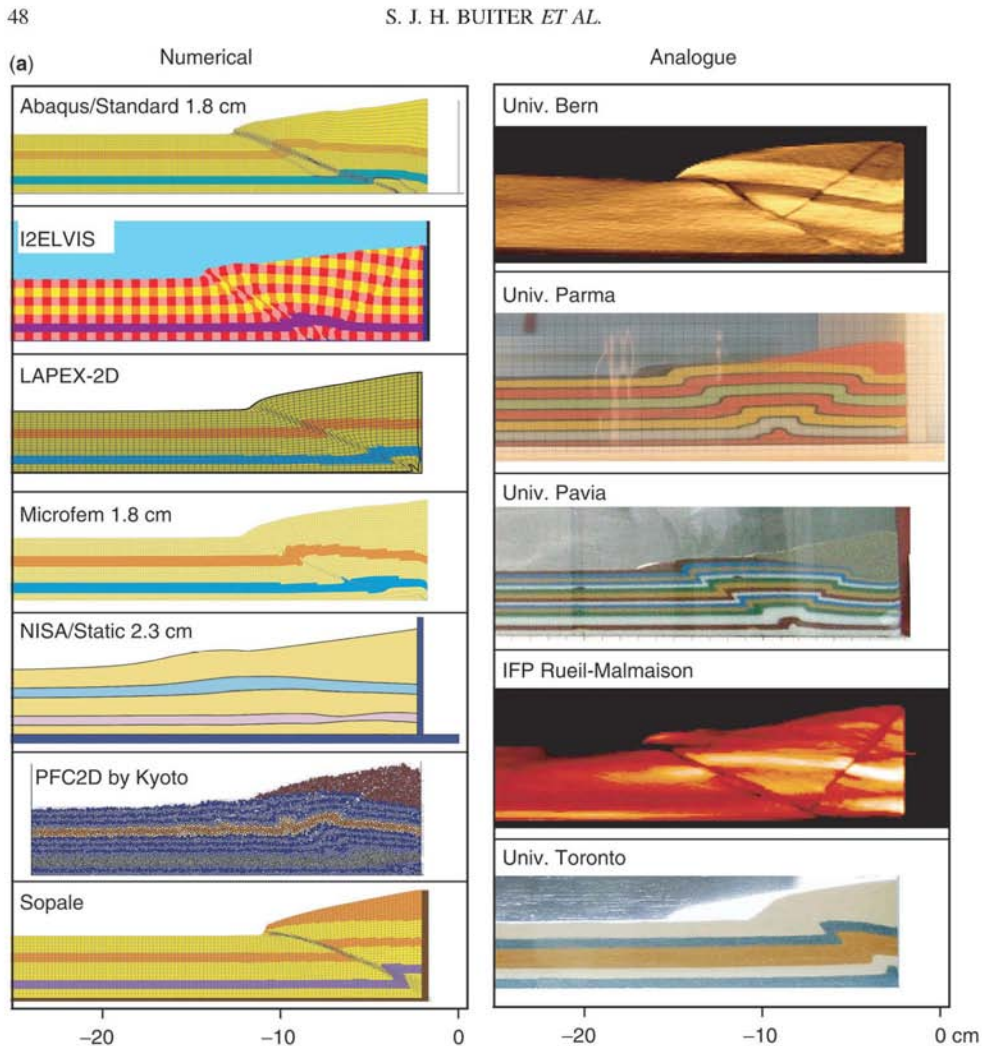
48   S. J. H. BUITER *ET AL.*

Fig. 6. Comparison of numerical and analogue results for the shortening experiment. (**a**) 2 cm of shortening (note that the model domain has been cropped on the left-hand side). (**b**) 14 cm of shortening.   **WebColor**

Model results

The evolution of the six numerical models is shown in Figure 7 with plots of geometry and strain-rate (after 1, 2 and 5 cm of extension) and pressure (after 1 and 5 cm). Measurements of fault dip, location of fault initiation, fault-controlled extension and fault migration are shown in Table 5 and Figure 8. The measurement procedure was the same as for the shortening experiment. The initial set-up of the experiment is symmetric and the very first deformation

structures should, therefore, be symmetric. The symmetry is disrupted as the basal sheet is pulled out from underneath the model.

Analysis of the numerical results allows the following observations (Figs 7 and 8, Table 5): (1) Extension first leads to the formation of two conjugate shear zones centred at the basal velocity discontinuity (the tip of the basal sheet) with a dip angle of 45° to 55° (Fig. 7b, Table 5). The dip angles are within the values expected for dynamic pressure-dependent non-dilatant Mohr-Coulomb shear zones, where predictions
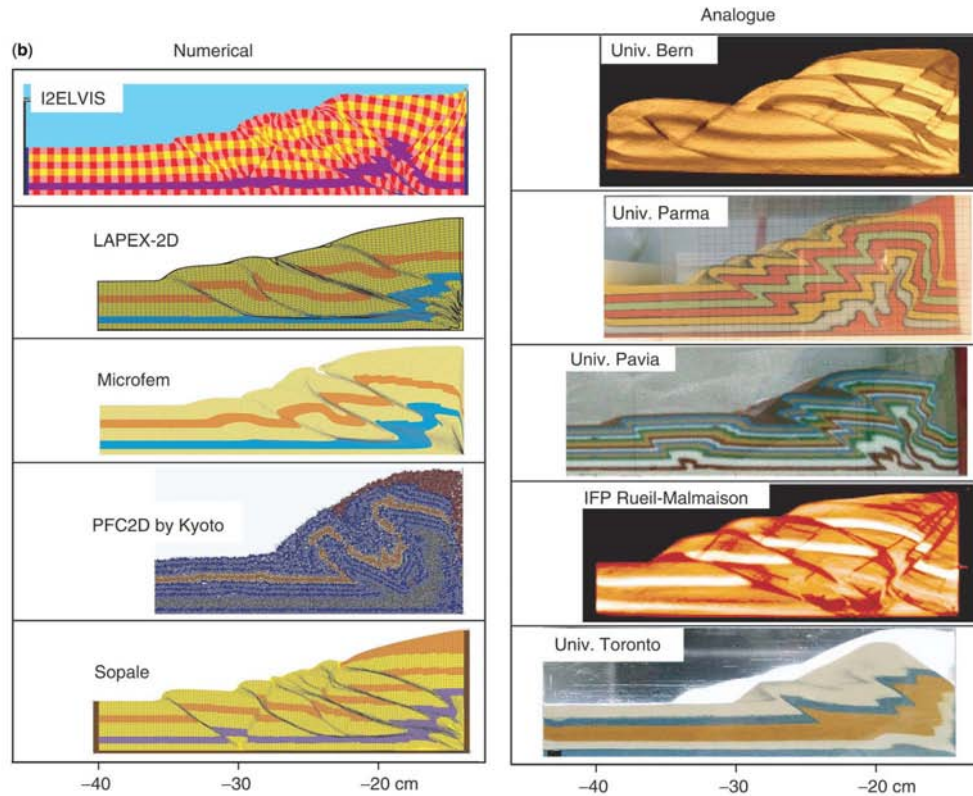
Fig. 6. *Continued.*

WebColor

Table 4. *Extension experiments*

Code	Method[*←]	Nodes[†]	Track points	Norm. elem. size[‡]	E[§] (MPa)	ν[‖←]	η[¶] (Pa s)	Δt[1]	Veloc.[2]
Abaqus/ Standard	FEM	201×36	n.a.	0.1	0.5	0.25	5e6	varies	2.2 cm/yr
I2ELVIS	FDM + MIC	400×75	175000	0.05	3	0.50	1e12	/0.008 h	2.5 cm/hr
LAPEX-2D	FDM + MIC	301×71	340000	0.0577	0.1	0.125	4.5e10	1 yr/1.4e-3s	1 cm/yr
Microfem	ALE	201×61	12261	0.1	n.a.	n.a.	4e13[3]	700 yr/22.2s	2.2 cm/yr
SloMo	FEM	401×71	94500	0.05	0.005	0.50	1e9	/5s	2.5 cm/hr
Sopale	ALE	401×71	253411	0.05	n.a.	n.a.	4.6e13	1000yr/7.2s	0.5 cm/yr

[*]FEM = Finite Element Method, FDM = Finite Difference Method, ALE = Arbitrary Lagrangian Eulerian, MIC = Marker-in-Cell.
[†]Nodes in horizontal × vertical direction.
[‡]Normalized element size is measured as the square root of element area, scaled to sandbox scale (cm).
[§]Young's modulus, scaled to sandbox scale.
[‖]Poisson ratio.
[¶]Background viscosity (for sand), scaled to sandbox scale. The numerical value for the viscosity of the silicone for the scaled experiments can be derived from the analogue viscosity value (5e4 Pa s), the numerical velocity and the scaling relationships (Equation 3).
[1]Time step used in the calculations. First value is for the numerical model, second value is its equivalent, scaled to the sandbox scale.
[2]Velocity on sandbox scale is 2.5 cm/hr for all experiments.
[3]Equivalent linear viscosity; a non-linear viscosity was used in the calculations.
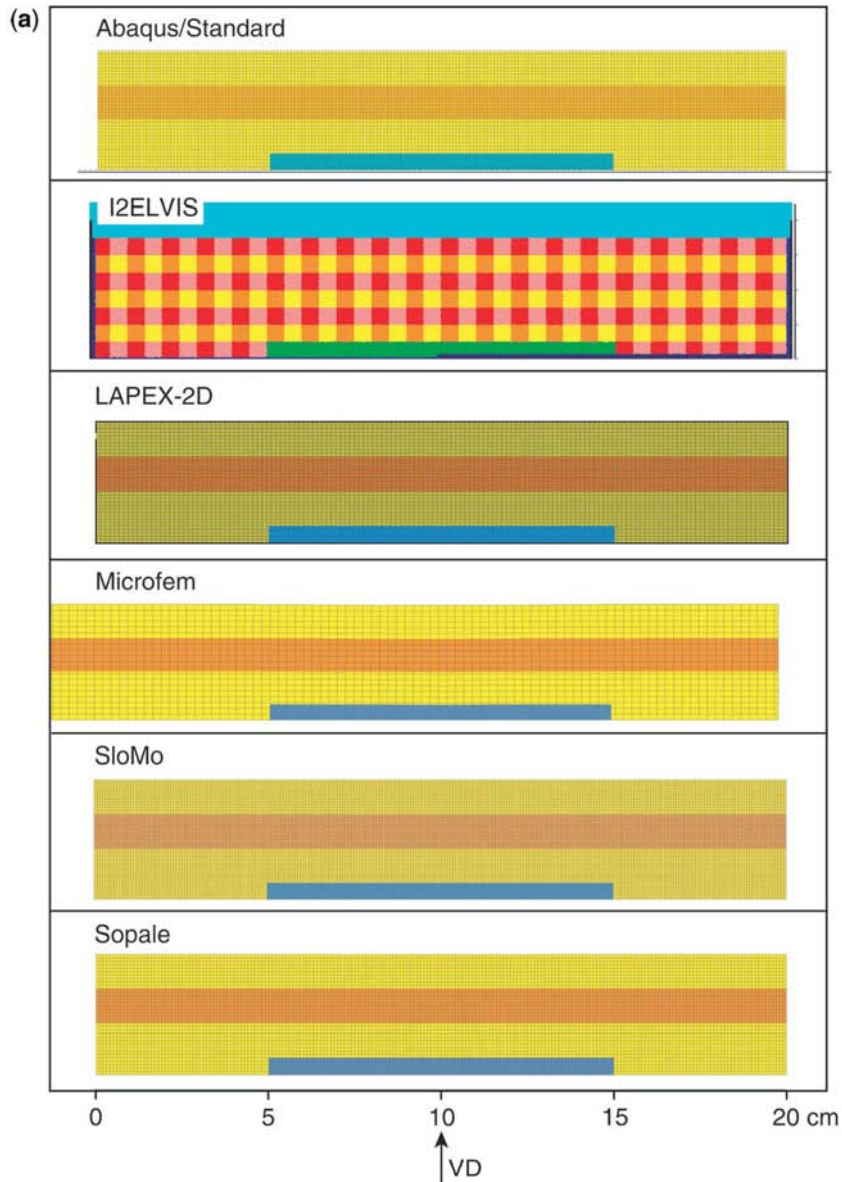
50   S. J. H. BUITER *ET AL.*

Fig. 7. Results for the extension experiment. All quantities (including strain-rates and pressures) are scaled down to the sandbox scale. (**a**) Initial geometries. The grid of Abaqus/Standard is the calculation grid, while for LAPEX-2D, Microfem, SloMo and Sopale the shown grid is (a subset of) the Lagrangian tracking grid. (**b**) Geometries after 1 cm, including analogue examples of University of Bern and IFP Rueil-Malmaison. VD = velocity discontinuity. (**c**) Strain-rates after 1 cm. (**d**) Dynamic pressures after 1 cm. (**e**) Geometries after 2 cm. (**f**) Strain-rates after 2 cm. (**g**) Geometries after 5 cm, including analogue examples of University of Bern and IFP Rueil-Malmaison. (**h**) Strain-rates after 5 cm. (**i**) Dynamic pressures after 5 cm.
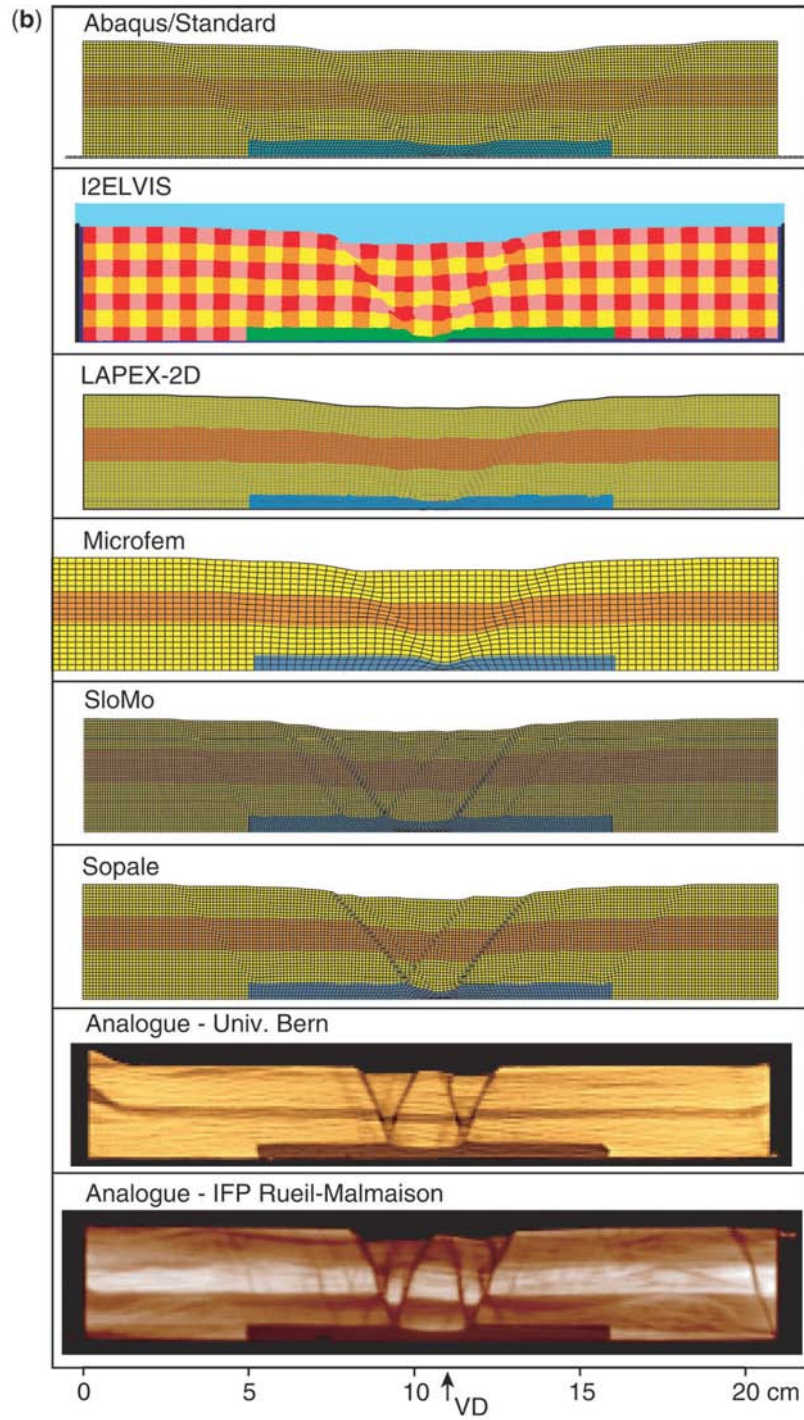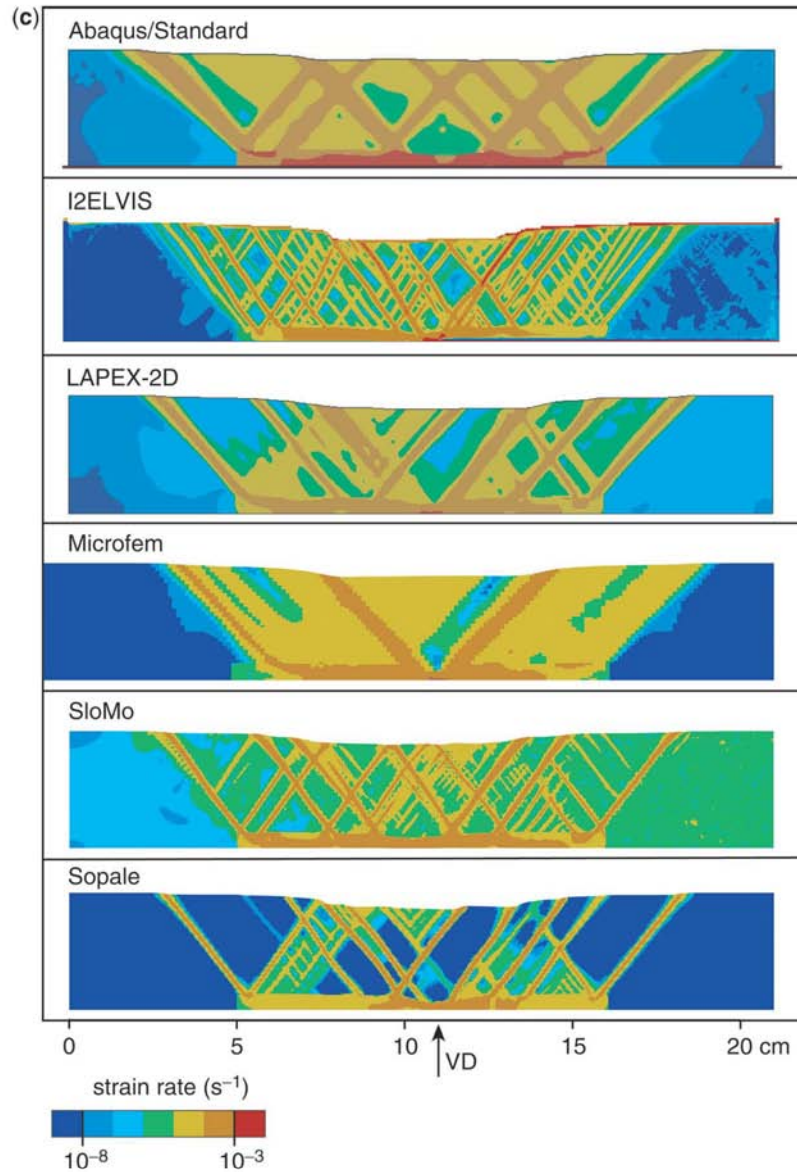
WebColor

THE NUMERICAL SANDBOX   51

(b)

Abaqus/Standard

I2ELVIS

LAPEX-2D

Microfem

SloMo

Sopale

Analogue - Univ. Bern

Analogue - IFP Rueil-Malmaison

0   5   10 ↑VD   15   20 cm

Fig. 7. *Continued.*

WebColor

52   S. J. H. BUITER *ET AL.*

Fig. 7. *Continued.*

for fault inclination range between 45° (Roscoe angle) and 45° + $\phi/2$ (Coulomb angle) (Vermeer 1990). The agreement in fault dip angles among the models is reflected in the similarity in dynamic pressures at 1 (and also 5 cm) of extension (Figs 7d and i). (2) The viscous layer distributes deformation quickly and at 1 cm of extension distributed shear zones are visible in all models (Fig. 7c). The left and right side edges of the viscous layer are found quickly (Table 5).

(3) With continued extension, the shear zones migrate to the right, the silicone layer thins and the surface depression becomes wider and asymmetric in shape (Figs 7d–g). The structural evolution of all the large-deformation models is very similar, especially in light of the differences in basal boundary condition. This suggests that

THE NUMERICAL SANDBOX   53
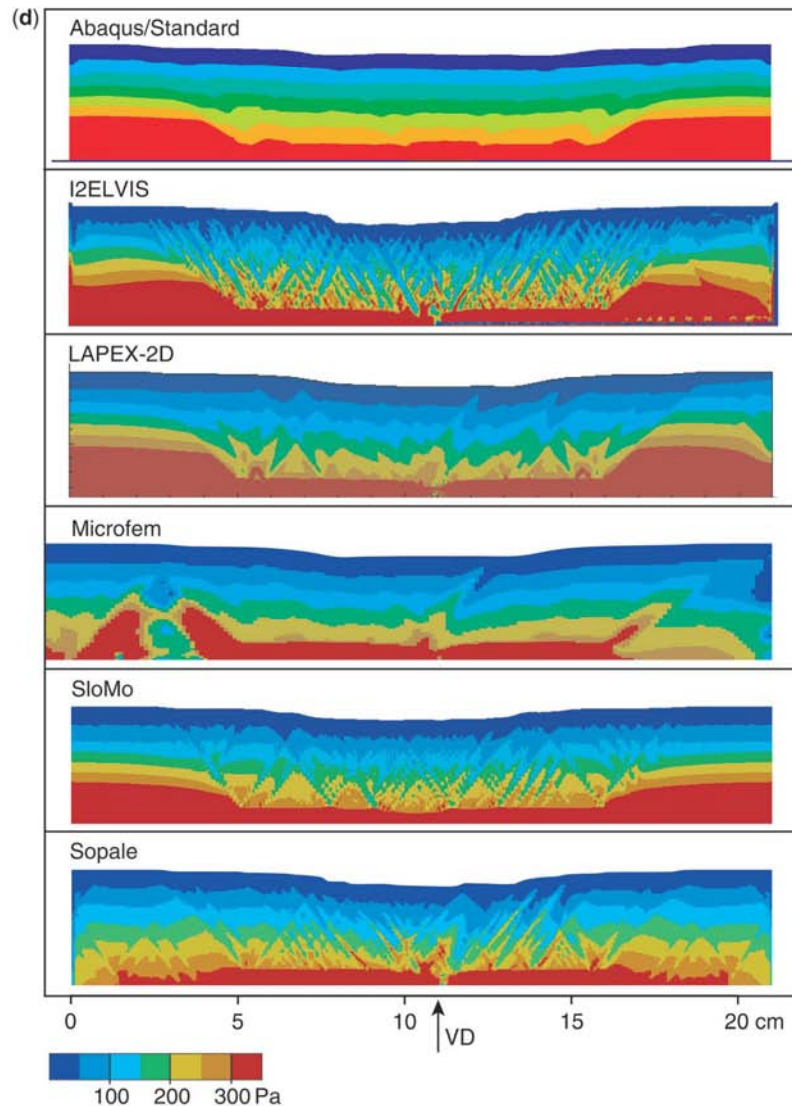
Fig. 7. *Continued.*

the basal contact is not as important as the interaction between the moving velocity discontinuity and the viscous layer. (4) The evolution in dip angle of the first formed shear zone to the right of the velocity discontinuity is fairly similar for the different models (Fig. 8a). For larger amounts of extension (>5 cm), we find that block rotation becomes more pronounced and fault dip decreases.

(5) The first formed shear zone moves to the right as the basal sheet is pulled out (Fig. 8b). A general trend is that fault migration is slower than the velocity with which the basal sheet is pulled because deformation is taken up by the block to the right of the first formed shear zone (e.g., through the formation of new shear zones). The differences between the numerical models are small and the effect on the resulting geometries is small as well. (6) The amount of fault-controlled extension is again highly variable (Table 5), as was observed for the shortening experiment.

(7) The dynamic pressure field (Figs 7d and i) is more heterogeneous than the strain-rate field

54   S. J. H. BUITER *ET AL.*
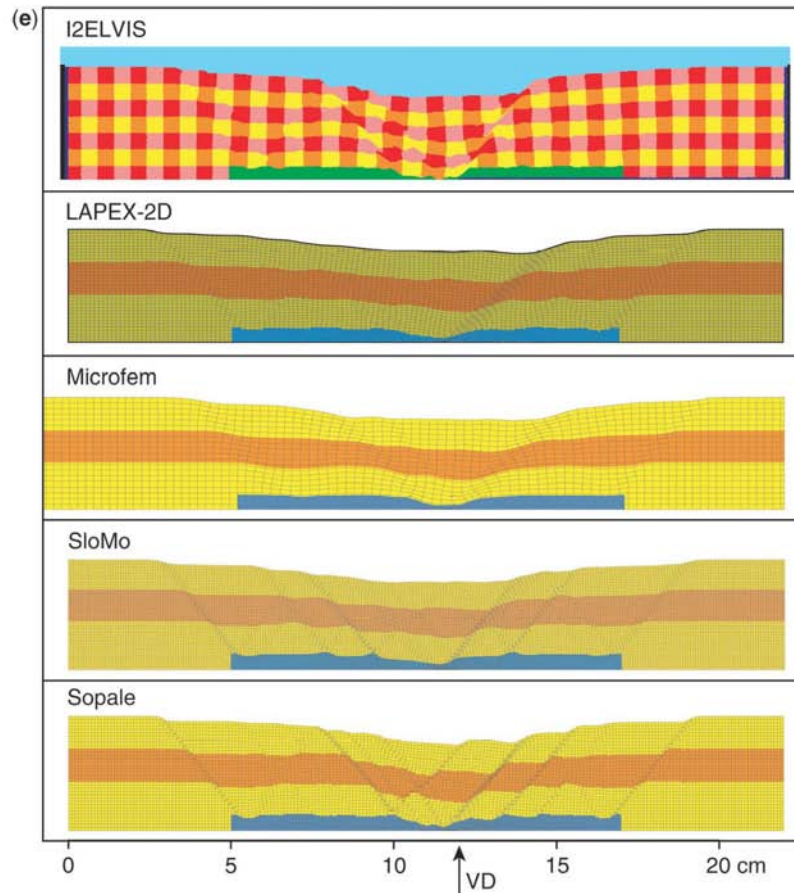
Fig. 7. *Continued.*

(Figs 7c and h) and visualizes both existing shear zones (currently or previously active) and potential shear zones (which are not necessarily activated). A comparison of the pressure fields for LAPEX-2D and Sopale shows that the seemingly rigid footwall blocks at the sides of the model behave in a different way in the two models. In Sopale the footwalls are at yield, whereas in LAPEX-2D they show an infinitesimal amount of elastic deformation (10^{-5} approximately) and are not at yield. In a purely viscous-plastic code (such as Sopale) any amount of deformation in a high-viscosity limit brings the stresses immediately on yield. This is not the case for a visco-elasto-plastic code where the material has an additional freedom to deform elastically. The dynamic pressure for Abaqus/Standard is less well resolved due to the relatively low resolution of the model, which may perhaps also incorporate a certain degree of pressure smoothing. The pressure plots for Microfem show the effects of the stick-slip friction basal boundary condition. This creates a region of enhanced dynamic pressure in the left footwall block, which is not seen in the results for the other codes. However, the enhanced pressures do not have a large influence on deformation since the average strain-rates in this region are low.

Localization of shear deformation

Comparison of the six experiments shows that the degree of focussing of deformation on shear zones may vary significantly (Table 5, Fig. 7). Results from I2ELVIS and Sopale demonstrate
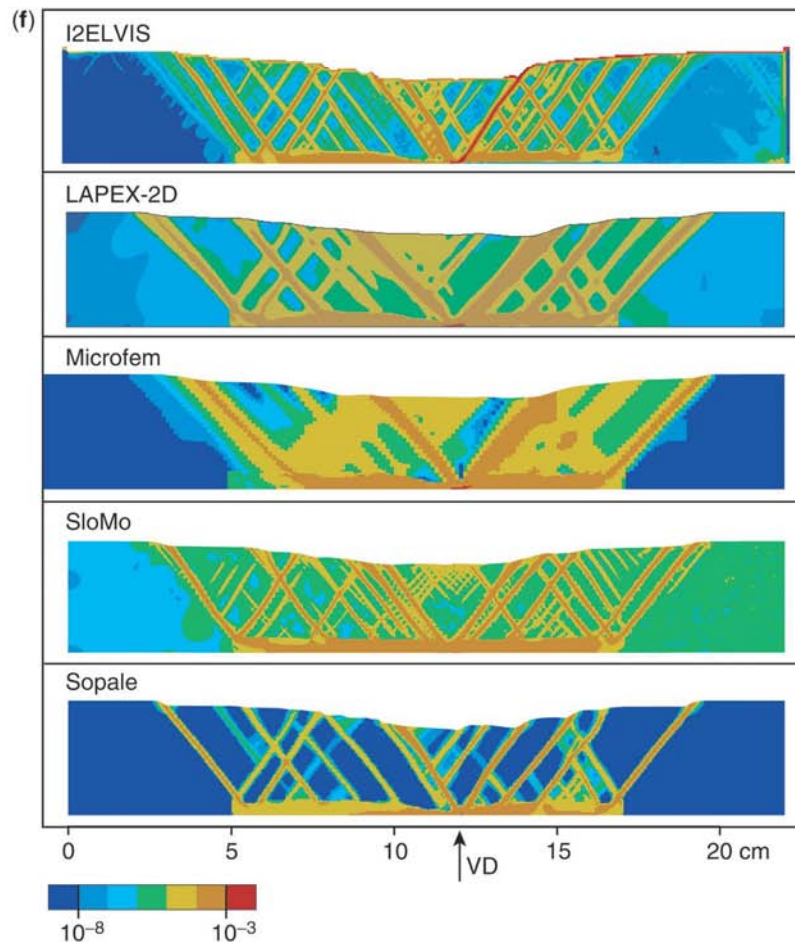
THE NUMERICAL SANDBOX   55

(f) I2ELVIS

LAPEX-2D

Microfem

SloMo

Sopale

10^{-8} 10^{-3}

Fig. 7. *Continued.*

WebColor

that both the degree of localization and the number of shear zones that form strongly increases with increasing resolution of the numerical grid. This can also be seen from a comparison of the results from Microfem (lower resolution ALE code) and Sopale (higher resolution ALE code) (Fig. 7). According to Cundall (1990), the ratio of elastic bulk modulus to lithostatic pressure is an important parameter for fault spacing, whereby an increase in this ratio decreases fault spacing. In nature, the value of this dimensionless ratio is expected to vary over orders of magnitude (for example, between 17 and 4432, using an elastic modulus of $10^{10}-10^{11}$ Pa, ρ 2300–3000 kg m^{-3} and height 1–20 km) and the variation in this ratio for the four numerical experiments that include

elastic material behaviour is of the same order (between 3 and 1867 using the elastic *shear* modulus, ρ 1560 kg m^{-3}, height 3.5 km). However, in the set-up of our experiment, the viscous layer and the velocity discontinuity control the initial location of shear zones and this set-up is, therefore, not suitable for a systematic study of shear zone spacing.

The use of dynamic pressure in Mohr-Coulomb plasticity significantly increases the localization of deformation in shear zones (tests with I2ELVIS and Sopale, Fig. 9). A Von Mises model (no pressure dependence) with an equivalent strength and softening to the Mohr-Coulomb models shows a considerably lower degree of localization (Figs 9a and d). With a depth-dependent pressure (Fig. 9b) localization
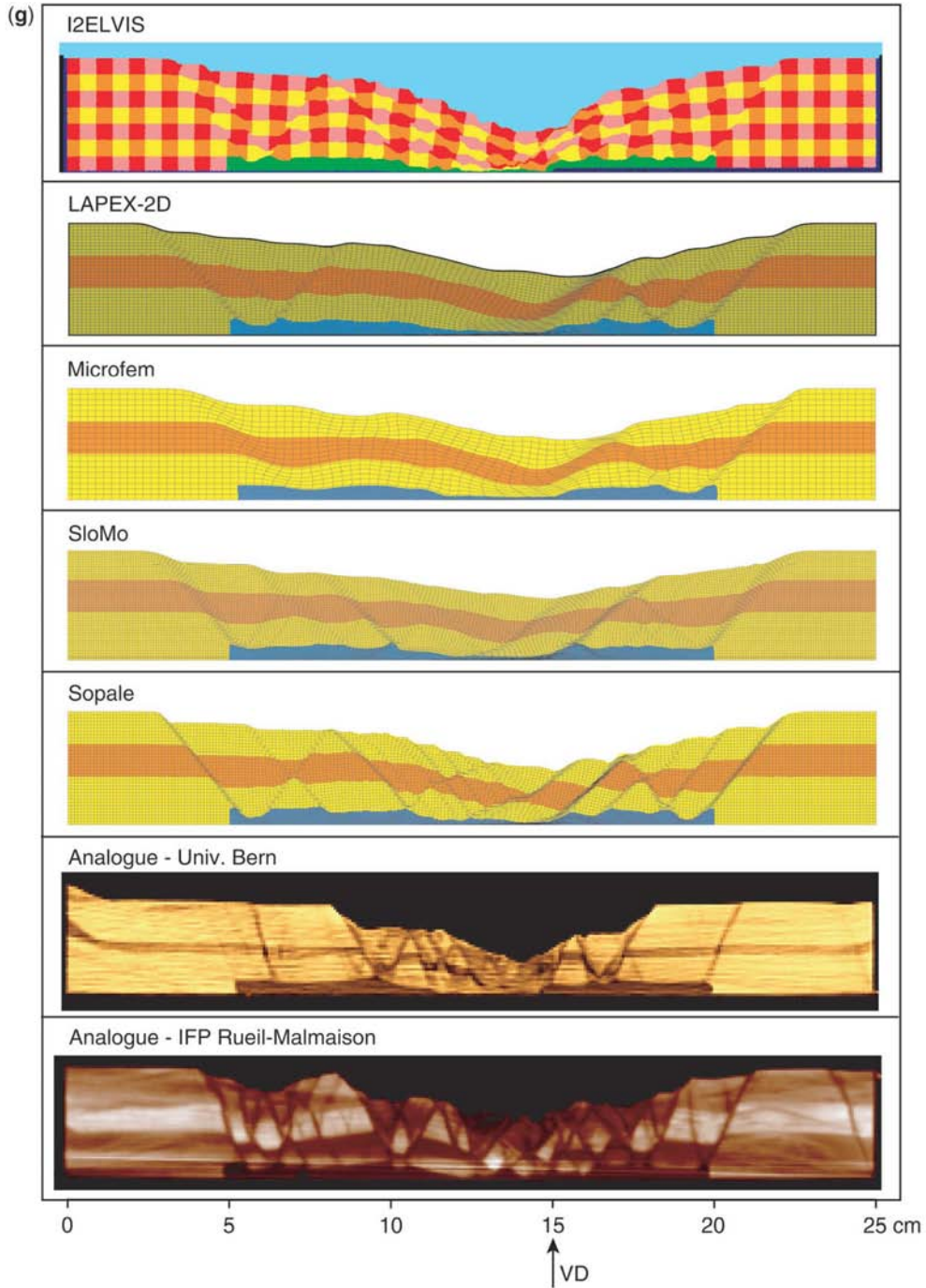
56   S. J. H. BUITER *ET AL.*

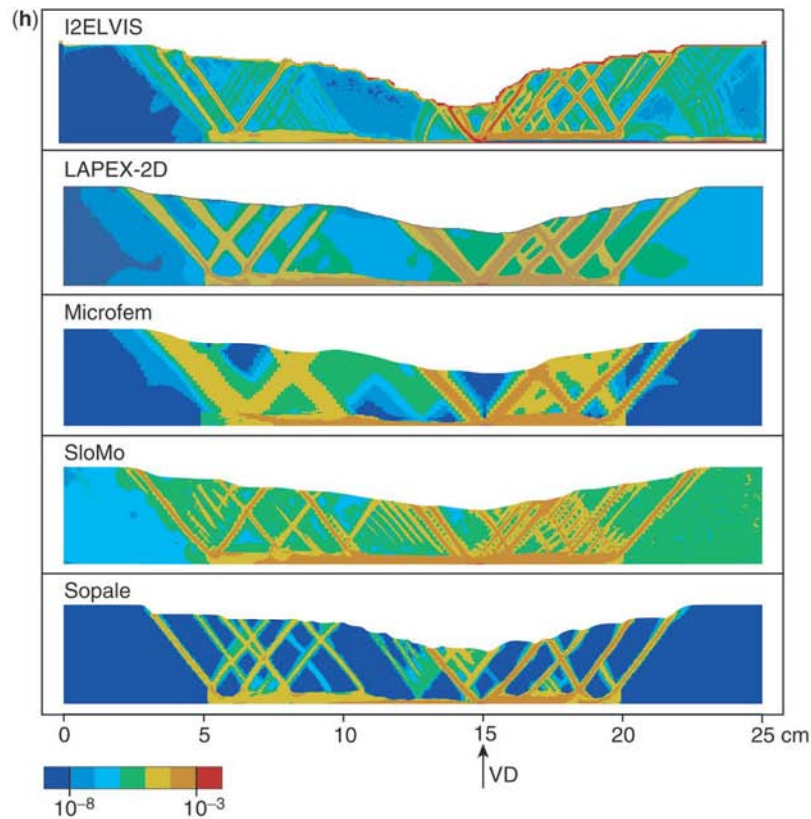**Fig. 7.** *Continued.*

WebColor

Fig. 7. *Continued.*

WebColor

is still less than in the dynamic pressure case (Figs 9c and e). To be noted here is that the dynamic pressure is calculated differently in the two codes compared in Figure 9 (see also Figs 7d and i). Sopale (and also Microfem) calculate dynamic pressure through a penalty formulation with a high but finite penalty ratio (Fullsack 1995) which leads to quasi-incompressibility (or a slight compressibility). In I2ELVIS the purely incompressible continuity equation is solved. Our test calculations with I2ELVIS have also shown that for a marker-in-cell technique, the numerical width of shear zones depends strongly on the interpolation schemes which are used for strain rate, stress and viscosity: numerical diffusion due to the interpolation between nodes of the grid and the markers can cause strong (two- to fivefold) widening of shear zones leading to a decrease in strain-rate contrast. Finite element and finite difference codes have a tendency to reduce shear zone width with decreasing element size,

implying that numerical shear zone width is mesh-dependent. Very fine meshes probably underestimate the width of localized shear zones in comparison with observed shear band widths in granular media (see also de Borst & Sluys 1991; Zervos *et al.* 2001).

Sensitivity analyses

In the extensional models presented here, two different boundary conditions were applied at the base. In Abaqus/Standard, I2ELVIS and Microfem, boundary friction was applied along the whole bottom boundary, including along the viscous material. In LAPEX-2D, SloMo and Sopale, grid points on the basal sheet were assigned the velocity with which the sheet was pulled and points to the left of the sheet were held fixed. The high level of agreement between the modelling results of the six experiments shows that any effect of this variation in basal boundary condition is small. The tip of
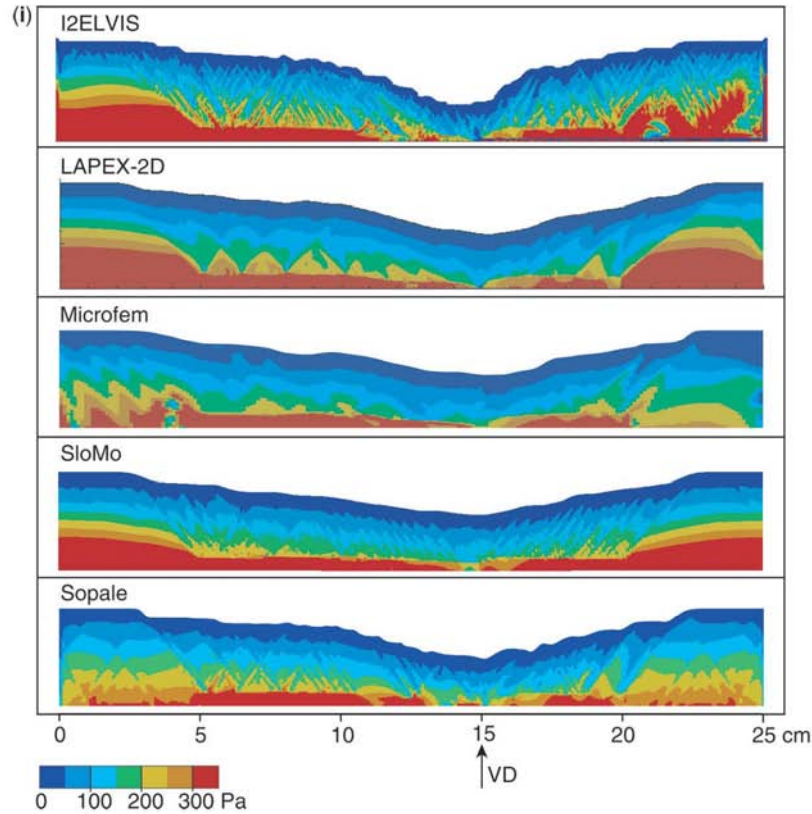
58   S. J. H. BUITER *ET AL.*

Fig. 7. *Continued.*

the basal sheet serves to initially localize deformation in a symmetric manner in the centre of the model. An experiment with a free slip base without basal sheet (run with Sopale) shows that in this case shear zones first form at the edges of the viscous layer and soon after in the centre of the model.

Experiments with I2ELVIS and Sopale show that a lower extensional velocity (which is equivalent to a lower viscosity for the viscous layer)

Table 5. *Quantification of extension experiments*[*][←]

Code	Fault ext.[†] at 2 cm	Fault initiation at ends of PDMS		Fault on left side of VD		Fault on right side of VD	
		Left	Right	dip	when	dip	when
Abaqus/Standard	–	0.5	0.5	45°	0	45°	0
I2ELVIS	0.9–1.2	never	2	51°	1	52°	1
LAPEX-2D	0.7–0.9	0.5	0.5	51°	0.5	53°	0.5
Microfem	0.5–1.2	never	1.5	46°	0.5	48°	0.5
SloMo	0.7–0.8	2	2	53°	1	55°	1
Sopale	1.1–1.3	0.5	0.5	50°	0.5	52°	0.5
Analogue ranges[‡]	0.9–1.0	never	2–4.5	65°–69°	0.5	60°–65°	0.5

[*]All values referred to sandbox scale in cm. Output stages typically available at 0, 0.5, 1 and then every cm of extension.
[†]Fault-controlled horizontal extension determined by cut-off points between layers and the faults.
[‡]Analogue values from experiments of University of Bern and IFP Rueil-Malmaison (Schreurs *et al.* 2006).
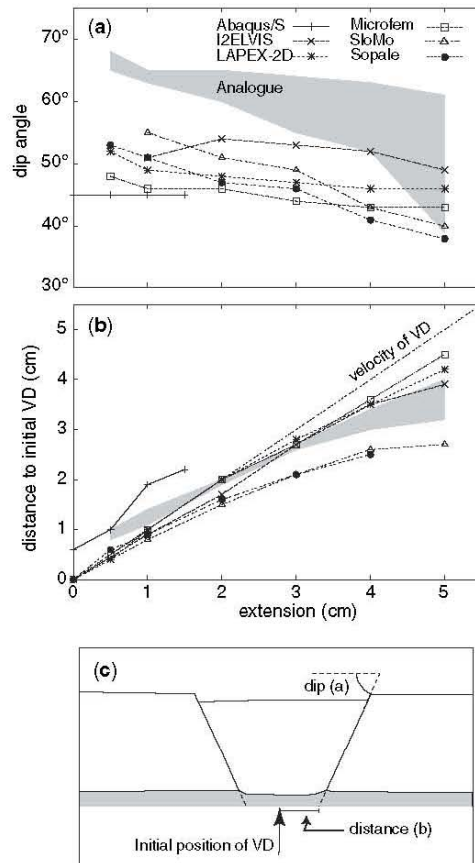
Fig. 8. (a) Dip angle of the first-formed normal fault on the right-hand side of the velocity discontinuity (the tip of the basal sheet) versus extension. (b) Migration of the same fault. The migration is measured relative to the initial position of the tip of the basal sheet. (c) Schematic drawing showing how the quantities in (a) and (b) were measured. The grey bands denote the range of values measured for the analogue experiments of University of Bern and IFP Rueil-Malmaison (see also Fig. 7 and Schreurs *et al.* 2006).

size) leads to the development of more shear zones which are better focussed, as discussed above. This can also be seen from a comparison of Microfem (lower resolution) to Sopale (higher resolution) results and is again similar to our observation for the shortening experiment.

Implications of the numerical experiments

Comparison between the different numerical codes for the extension experiment shows a high level of agreement. All predict the same location of maximum thinning and show the same general evolution and stepping out of shear zones. High-resolution numerical codes (e.g., Sopale) predict rotation of shear zones with larger finite deformation. The extensional results show much less variation compared to the shortening experiment. Ellis *et al.* (2004) suggest that experiments involving weak viscous layers reduce the influence of boundary conditions on both analogue and numerical results, and instead pass control to rheological strength contrasts within the model domain. In our set-up, the weak viscous basal layer serves to reduce the effect of stress discontinuities due to the basal velocity discontinuity.

Although the overall dynamics and evolution of the different numerical codes are similar, differences in the number of shear zones that develop, the timing at which the ends of the viscous layer are activated and the shear zone dip can be seen. These differences partly appear to reflect differences in mesh resolution. As for the shortening experiment, we find that caution is required in interpretations from numerical results involving number of shear zones and shear zone spacing.

Our numerical experiments may also have important implications for the understanding of pressure distributions in large-scale tectonic processes involving the development of shear zones. As follows from our results, the dynamic pressure field (Figs 7d and i) in a medium subjected to brittle/plastic deformation deviates strongly from the lithostatic distribution often assumed in geosciences. These results are in line with other theoretical studies (e.g., Mancktelow 1995; Petrini & Podladchikov 2001; Burg & Gerya 2005) which predict significant underpressure and overpressure effects in orogenic processes. This, in turn, may have strong consequences for the pressure-temperature evolution of deformed rocks complexes composing the Earth's crust and lithospheric mantle.
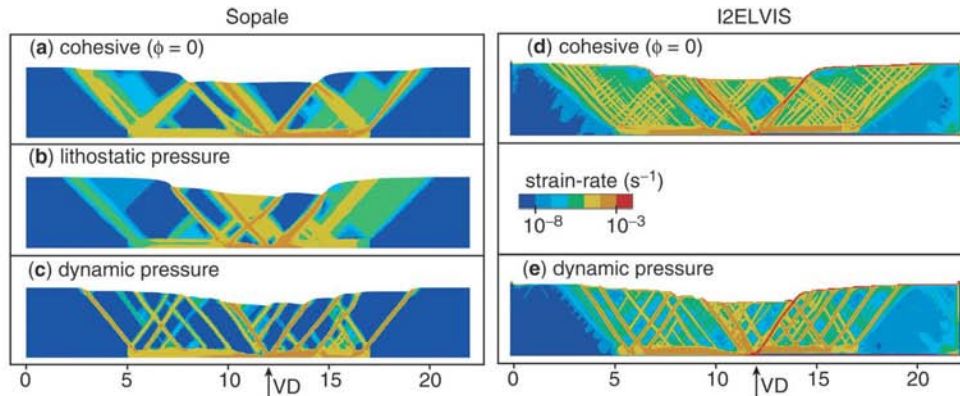
Q2.1

favours a more efficient outward propagation of shear zone development. The surface depression is less deep. A higher cohesion of the 'sand' material leads to locally steeper surface slopes, similar to our observations for the shortening experiment. We found that a reduction or increase in the strain softening range does not affect the results significantly. Tests with I2ELVIS and Sopale also showed that a higher resolution calculation grid (smaller element

60   S. J. H. BUITER *ET AL.*

Fig. 9. A comparison of strain-rates for I2ELVIS and Sopale after 2 cm of extension shows the influence of the plasticity description. (**a**) and (**d**) Angle of internal friction $\phi = 0$. Cohesion softens from 170 Pa to 140 Pa (sandbox scale). These values mimic the same strength and strength reduction as for the frictional extension models. (**b**) Sopale for Mohr–Coulomb plasticity with depth-dependent pressure. (**c**) and (**e**) Mohr–Coulomb plasticity with dynamic pressure (standard case).   **WebColor**

Comparison to analogue results

Only two analogue experiments documented cross-sectional information at different extension stages and could be used to compare the numerical results against. The analogue results of the University of Bern and IFP Rueil-Malmaison show an overall similar evolution, but differ in the velocity with which normal faults are distributed outwards (Schreurs *et al.* 2006). The geometries of the numerical and analogue experiments after 1 and 5 cm of extension are shown in Figures 7b and g. The dip angle and migration of the first formed shear zone to the right of the velocity discontinuity are compared in Figure 8. In the numerical experiments reported here the mobile wall velocity is directly applied to the right-hand side of the models. However, in the analogue sandbox the role of the mobile wall is likely only to prevent the sand from collapsing and does not provide a driving force. The extension is passed to the model by the moving basal sheet. Because there is a sufficient distance between the right-hand wall and the velocity discontinuity this is, however, not likely to affect the analogue–numerical comparison.

Comparison of the numerical results to the two analogue experiments shows that: (1) The numerical experiments predict the overall dynamics and evolution of the analogue system reasonably well. (2) In both analogue and numerical results, shear zones initiate at the basal velocity discontinuity and with increasing extension new shear zones develop outwards. (3) Both numerical and analogue results show a rotation of shear zones with shallowing dip

angles for increasing extension. (4) The velocity with which the first formed normal fault to the right of the velocity discontinuity moves to the right is very similar between the two analogue results and the numerical models (Fig. 8b). (5) The main difference between the analogue and numerical results is the dip angle of the shear zones (Figs 7 and 8a). The dip angles in the analogue experiments are much steeper (between 60° and 69° initially) and follow Coulomb behaviour, with dip angles predicted by $45° + \phi/2$ (63°–68° for the material properties of the two analogue experiments). All numerical extension models assume zero dilation and for dynamic pressure-dependent Mohr–Coulomb behaviour dip angles between 45° (Roscoe) and $45° + \phi/2$ (Coulomb) are then to be expected (Vermeer 1990) (45°–63° for our material properties). The observed initial dip angles (45°–55°) are in the lower range of the theoretical values. Assigning a non-zero dilatation angle, ψ, to 'sand' will increase the theoretical minimum dip angle value to $45° + \psi/2$. Tests with I2ELVIS show that a non-zero dilatation angle indeed results in higher dip angles for the shear zones.

The numerical sandbox

Our study presents a direct qualitative and quantitative comparison of numerical and analogue model results for two experimental set-ups aimed at simulating upper-crustal tectonic processes. Results from seven numerical codes are compared to results from five analogue

laboratories for a brittle thrust wedge experiment, while results from six numerical codes are compared to results from two analogue laboratories for a brittle-viscous extension experiment. The accompanying paper (Schreurs *et al.* 2006) shows additional analogue shortening and extension results, which could not be used in our comparison as either cross-sectional information was not recorded during the experiment or a different material (clay) was used.

A comparison of analogue experiments from different laboratories has to take into account that differences may occur in material properties (whereby properties may even slightly change due to storage conditions or small vibrations), modelling apparatus, model set-up (width and length) and in the set-up technique of individual experimenters. The effects of some variations can be tested by determining the reproducibility of each experiment in the same laboratory, but it is clearly of importance to determine the inter-laboratory reproducibility of analogue model results as well. The accompanying paper (Schreurs *et al.* 2006) shows an encouraging first order agreement of model results of different analogue laboratories, despite variability in model widths and in material properties.

In comparison, numerical experiments have the potential to be much more reproducible, since material properties, model set-up and boundary conditions can be specified exactly. However, set-ups between different experimenters may also vary in subtle ways depending on assumptions used, and even slightly different ways of interpreting and prescribing the initial set-up. The eight numerical codes used in our comparison differ with each other for the following properties and assumptions: (1) resolution, imposed element aspect ratios, and type of element; (2) time step (extension experiment); (3) smoothing of velocity discontinuities; (4) implementation of frictional boundaries; (5) material properties (dilatation and elasticity); (6) scaling; (7) calculation of dynamic pressure; and (8) surface smoothing (shortening experiment). Our results indicate that grid resolution, representation of boundary conditions (boundary friction and velocity discontinuities), calculation of dynamic pressure and dilatation require careful attention in sandbox-type experiments. In contrast, elastic material behaviour, scaling of the experiment and small amounts of surface smoothing appear to play only a minor role.

Our results highlight that different numerical solution methods (finite difference method, finite element method, distinct element method) can successfully be used to reproduce structures seen in analogue sandbox models. The numerical codes can do reasonably well in qualitatively predicting the dynamic evolution of the system in shortening and extension, shear zone (fault) formation, and taper geometry (shortening experiment). The level of variability between the numerical results is about the same as the degree of variability between the analogue results. Numerical codes show differences with each other, and the analogue experiments, for detailed location, dip and spacing of shear zones. As the initial set-up and material properties of analogue models can be relatively well constrained, their results can form a useful test for numerical models. Numerical models may, therefore, benefit from future studies focusing on the differences between analogue and numerical modelling results. Our results indicate that future experiments should preferably choose a simplified set-up that reduces the effects of boundary conditions and especially abrupt changes in boundary velocities, prescribe resolution and time step size, use material behaviour which is as similar as possible and, if possible, quantify results in an unambiguous manner.

Our results emphasize the importance of the following issues for numerical sandbox-type studies: (1) the ability to model large deformation structures; (2) the ability to represent boundary friction, velocity discontinuities and a free surface; (3) the representation of a composite (elasto)-visco-plastic rheology; (4) calculation with a relatively high resolution (important for shear zone evolution, for example); (5) minimization of numerical diffusion; and (6) consensus on the procedure for quantification of the results. These are important for studies in which numerical and analogue models are used in combination, but reflect at the same time the requirement to study Earth tectonic processes.

Conclusions

Two experimental set-ups inspired by settings from structural geology were used to compare eight numerical codes to each other. Despite differences in set-up and material behaviour between the individual experiments, the results are useful in showing that: (1) Numerical codes at the present time are capable of modelling the dynamic evolution of compressional and extensional settings, including shear-zone development, forward propagation of thrust wedges, and taper geometry of convergent wedges. The qualitative behaviour of the different codes is similar. (2) A quantitative analysis of the results of these codes shows a higher degree of variability, particularly in number of shear

62　　　　　　　　　　　　　S. J. H. BUITER *ET AL.*

zones that develop and their spacing and dip angle. (3) A comparison between the results of the numerical codes and equivalent analogue experiments shows agreement in the overall evolution of the system and in the localization of deformation onto faults/shear zones. The variability among the numerical results is of the same order as the variations among the analogue results. Differences with the analogue results are also apparent, for example, in dip angles of extensional shear zones, degree of localization, and the development of backthrusts in the shortening experiment. Reducing these differences represents an interesting challenge for numerical modellers.

We hope that the comparisons shown here are a useful guide to the structural geology community, in highlighting the degree to which numerical codes may be used to reproduce experiments in the sandbox and/or processes at the scale of the upper crust.

References

Q2.2 ABAQUS/STANDARD USER'S MANUAL 2003. Vol. 1 & 2, version 6.4. Abaqus Inc, Pawtucket, Rhode Island, USA.

ADAM, J. & URAI, J. L. *ET AL.* 2005. Shear localization and strain distribution during tectonic faulting – new insights from granular-flow experiments and high-resolution optical image correlation techniques. *Journal of Structural Geology*, **27**, 283–301.

BABEYKO, A. YU., SOBOLEV, S. V., TRUMBULL, R. B., ONCKEN, O. & LAVIER, L. L. 2002. Numerical models of crustal scale convection and partial melting beneath the Altiplano-Puna Plateau. *Earth and Planetary Science Letters*, **199**, 373–388.

BAHROUDI, A., KOYI, H. A. & TALBOT, C. J. 2003. Effect of ductile and frictional décollements on style of extension. *Journal of Structural Geology*, **25**, 1401–1423.

BEHN, M. D., LIN, J. & ZUBER, M. T. 2002. A continuum mechanics model for normal faulting using a strain-rate softening rheology: implications for thermal and rheological controls on continental and oceanic rifting. *Earth and Planetary Science Letters*, **202**, 725–740.

BLANKENBACH, B. & BUSSE, F. *ET AL.* 1989. A benchmark comparison for mantle convection codes. *Geophysical Journal International*, **98**, 23–38.

BURBIDGE, D. R. & BRAUN, J. 2002. Numerical models of the evolution of accretionary wedges and fold-and-thrust belts using the distinct-element method. *Geophysical Journal International*, **148**, 542–561.

BURG, J.-P. & GERYA, T. V. 2005. Viscous heating and thermal doming in orogenic metamorphism: numerical modelling and geological implications. *Journal of Metamorphic Geology*, **23**, 75–95.

CRUDEN, A. R., NASSERI, M. B. & PYSKLYWEC, R. 2006. Surface topography and internal strain variation in wide hot orogens from three-dimensional analogue and two-dimensional numerical vise models. *In*: BUITER, S. J. H. & SCHREURS, G. (eds) *Analogue and Numerical Modelling of Crustal-Scale Processes*. Geological Society, London, Special Publications, **253**, xx–yy.

CUNDALL, P. A. 1990. Numerical modelling of jointed and faulted rock. *In*: ROSSMANITH, A. (ed.) *Mechanics of Jointed and Faulted rocks*. Balkema, Rotterdam, 11–18.

CUNDALL, P. A. & BOARD, M. 1988. A microcomputer program for modelling large-strain plasticity problems. *In*: SWOBODA, G. (ed.) *6th International Conference in Numerical Methods in Geomechanics*. A. A. Balkema, Brookfield, VT, 2101–2108.

CUNDALL, P. A. & STRACK, D. L. 1979. A discrete numerical model for granular assemblies. *Geotechnique*, **29**, 47–65.

CUVELIER, C., SEGAL, A. & VAN STEENHOVEN, A. A. 1986. *Finite Element Methods and Navier-Stokes Equations*. Reidel Publishing Company, Dordrecht, 483pp.

DAHLEN, F. A. 1984. Noncohesive critical Coulomb wedges: an exact solution. *Journal of Geophysical Research*, **89**, 10, 125-10, 133.

DAVIS, D., SUPPE, J. & DAHLEN, A. 1983. Mechanics of fold-and-thrust belts and accretionary wedges. *Journal of Geophysical Research*, **88**, 1153–1172.

DE BORST, R. & SLUYS, L. J. 1991. Localization in a Cosserat continuum under static and dynamic loading conditions. *Computer Methods in Applied Mechanics and Engineering*, **90**, 805–827.

ELLIS, S., SCHREURS, G. & PANIEN, M. 2004. Comparisons between analogue and numerical models of thrust wedge development. *Journal of Structural Geology*, **26**, 1659–1675.

THE NUMERICAL SANDBOX   63

FULLSACK, P. 1995. An arbitrary Lagrangian-Eulerian formulation for creeping flows and its application in tectonic models. *Geophysical Journal International*, **120**, 1–23.

GERYA, T. V. & YUEN, D. A. 2003. Characteristics-based marker-in-cell method with conservative finite-difference schemes for modelling geological flows with strongly variable transport properties. *Physics of the Earth and Planetary Interiors*, **140**, 293–318.

GUTSCHER, M.-A., KUKOWSKI, N., MALAVIEILLE, J. & LALLEMAND, S. 1998a. Material transer in accretionary wedges from analysis of a systematic series of analog experiments. *Journal of Structural Geology*, **20**, 407–416.

GUTSCHER, M.-A., KUKOWSKI, N., MALAVIEILLE, J. & LALLEMAND, S. 1998b. Episodic imbricate thrusting and underthrusting: Analog experiments and mechanical analysis applied to the Alaskan Accretionary Wedge. *Journal of Geophysical Research*, **103**, 10, 161-10, 176.

HUBBERT, M. K. 1937. Theory of scale models as applied to the study of geologic structures. *Bulletin of the Geological Society of America*, **48**, 1459–1520.

JAEGER, J. C. & COOK, N. G. W. 1979. *Fundamentals of Rock Mechanics*. John Wiley and Sons, New York, 585pp.

KAUS, B. J. P. 2005. *Modelling approaches to geodynamic processes*. PhD thesis, ETH Zürich.

LE POURHIET, L., MATTIONI, L. & MORETTI, I. 2006 3D modelling of rifting through a pre-existing stack of nappes in the Gulf of Corinth (Greece): a mixed analogue/numerical approach. *In*: BUITER, S. J. H. & SCHREURS, G. (eds) *Analogue and Numerical Modelling of Crustal-Scale Processes*. Geological Society, London, Special Publications, **253**, xx–yy.

LOHRMANN, J., KUKOWSKI, N., ADAM, J. & ONCKEN, O. 2003. The impact of analogue material properties on the geometry, kinematics, and dynamics of convergent sand wedges. *Journal of Structural Geology*, **25**, 1691–1771.

MANCKTELOW, N. S. 1995. Nonlithostatic pressure during sediment subduction and the development and exhumation of high pressure metamorphic rocks. *Journal of Geophysical Research*, **100**, 571–583.

MICHON, L. & MERLE, O. 2000. Crustal structures of the Rhine graben and the Massif Central grabens: An experimental approach. *Tectonics*, **19(5)**, 896–904.

MULUGETA, G. 1988. Modelling the geometry of Coulomb thrust wedges. *Journal of Structural Geology*, **10**, 847–859.

MULUGETA, G. & KOYI, H. 1992. Episodic accretion and strain partitioning in a model sand wedge. *Tectonophysics*, **202**, 319–333.

NISA II™ USER'S MANUAL VERSION 7.0, 1997. Engineering Mechanics Research Corporation, Troy, Michigan, USA.

PANIEN, M. 2004. *Analogue modelling experiments of basin inversion using well-characterized granular materials and comparisons with numerical models*. Ph.D. thesis. University of Bern, Switzerland.

PANIEN, M., BUITER, S. J. H., SCHREURS, G. & PFIFFNER, O. A. 2006. Inversion of a symmetric basin: Insights from a comparison between analogue and numerical experiments. *In*: BUITER, S. J. H. & SCHREURS, G. (eds) *Analogue and Numerical Modelling of Crustal-Scale Processes*. Geological Society, London, Special Publications, **253**, xx–yy.

PELLETIER, D., FORTIN, A. & CAMARERO, R. 1989. Are FEM solutions of incompressible flows really incompressible? (Or how simple flows can cause headaches!) *International Journal of Numerical Methods in Fluids*, **9**, 99–112.

PETRINI, K. & PODLADCHIKOV, Y. 2000. Lithospheric pressure-depth relationship in compressive regions of thickened crust. *Journal of Metamorphic Geology*, **18**, 67–77. **Q2.1**

PFC²ᴰ USER'S GUIDE 1999. Version 3.0. Itasca Consulting Group, Inc. **Q2.2**

POLIAKOV, A. N. & PODLADCHIKOV, Y. Y. 1992. Diapirism and topography. *Geophysical Journal International*, **109**, 553–564.

POLIAKOV, A. N., CUNDALL, P. A., PODLADCHIKOV, Y. Y. & LYAKHOVSKY, V. A. 1993. An explicit inertial method for the simulation of the visco-elastic flow: an evaluation of elastic effects on diapiric flow in two- and three-layers models. *In*: STONE, D. B. & RUNCORN, S. K. (eds) *Flow and Creep in the Solar System: Observations, Modelling and Theory*. Kluwer Academic Publishers, 175–195.

RANALLI, G. 1987. *Rheology of the Earth: deformation and flow processes in geophysics and geodynamics*. Allen & Unwin Inc., Winchester, USA, 366pp.

SALTZER, S. D. & POLLARD, D. D. 1992. Distinct element modelling of structures formed in sedimentary overburden by extensional reactivation of basement normal faults. *Tectonics*, **11(1)**, 165–174.

SASSI, W., COLLETTA, B., BALÉ, P. & PAQUEREAU, T. 1993. Modelling of structural complexity in sedimentary basins: the role of pre-existing faults in thrust tectonics. *Tectonophysics*, **226**, 97–112.

SCHELLART, W. P. 2000. Shear test results for cohesion and friction coefficients for different granular materials: scaling implications for their usage in analogue modelling. *Tectonophysics*, **324**, 1–16.

SCHREURS, G. & BUITER, S. J. H. ET AL. 2006. Analogue benchmarks of shortening and extension experiments. *In*: BUITER, S. J. H. & SCHREURS, G. (eds) *Analogue and Numerical Modelling of Crustal-Scale Processes*. Geological Society, London, Special Publications, **253**, xx–yy.

SMART, K. J. & COUZENS-SCHULZ, B. A. 2001. Mechanics of blind thrusting: Comparison of numerical and physical modelling. *The Journal of Geology*, **109**, 771–779.

STORTI, F., SALVINI, F. & MCCLAY, K. 2000. Synchronous and velocity-partitioned thrusting and thrust polarity reversal in experimentally produced, doubly-vergent thrust wedges: Implications for natural orogens. *Tectonics*, **19(2)**, 378–396.

64   S. J. H. BUITER *ET AL.*

STRAYER, L. M., HUDLESTON, P. J. & LORIG, L. J. 2001. A numerical model of deformation and fluid-flow in an evolving thrust wedge. *Tectonophysics*, **335**, 121–145.

VANBRABANT, Y., JONGMANS, D., HASSANI, R. & BELLINO, D. 1999. An application of two-dimensional finite-element modelling for studying the deformation of the Variscan fold-and-thrust belt (Belgium). *Tectonophysics*, **309**, 141–159.

VAN KEKEN, P. E., KING, S. D., SCHMELING, H., CHRISTENSEN, U. R., NEUMEISTER, D. & DOIN, M.-P. 1997. A comparison of methods for the modelling of thermochemical convection. *Journal of Geophysical Research*, **102**, 22, 477-22, 495.

VERMEER, P. A. 1990. The orientation of shear bands in biaxial tests. *Geotechnique*, **40**, 223–236.

WEIJERMARS, R. 1986. Flow behaviour and physical chemistry of bouncing putties and related polymers in view of tectonic laboratory applications. *Tectonophysics*, **124**, 325–358.

WIJNS, C., BOSCHETTI, F. & MORESI, L. 2003. Inverse modelling in geology by interactive evolutionary computation. *Journal of Structural Geology*, **25**, 1615–1621.

ZERVOS, A., PAPANASTASIOU, P. & VARDOULAKIS, I. 2001. A finite element displacement formulation for gradient plasticity. *International Journal for Numerical Methods in Engineering*, **50**, 1369–1388.

ZHAO, W.-L., DAVIS, D. M., DAHLEN, F. A. & SUPPE, J. 1986. Origin of convex accretionary wedges: evidence from Barbados. *Journal of Geophysical Research*, **91**, 10246–10258.

Appendix B

A brief description of six subduction zones: Aleutian, Cascadia, Ecuador-Colombia, Kuril, Sumatra, and Tonga-Kermadec

Aleutian

The Aleutian volcanic island arc marks the boundary between the Pacific plate and the Bering Sea region, which is part of the North American plate (Figure A2.1). The relative convergence velocity increases from ~66 mm/yr in the east to ~86 mm/yr in the west (Geist & Scholl, 1992, Lallemant, 1996). The convergence vector changes from almost perpendicular to the trench in the east to almost parallel to the trench in the west (e.g., DeMets et al., 1990, Geist & Scholl, 1992, Yu et al., 1993, Lallemant, 1996). The modern phase (5 Myr to present) of the evolution of the Aleutian Island arc is characterized by complex strike slip faulting, normal faulting, and block rotations (Geist & Scholl, 1992, Lallemant, 1996). No major margin parallel strike slip fault has been evolved. The deformation in the overriding plate can be considered as distributed, because the deformation is not concentrated within one localized shear zone but within many faults and fractures distributed over the entire overriding plate (Geist & Scholl, 1992).
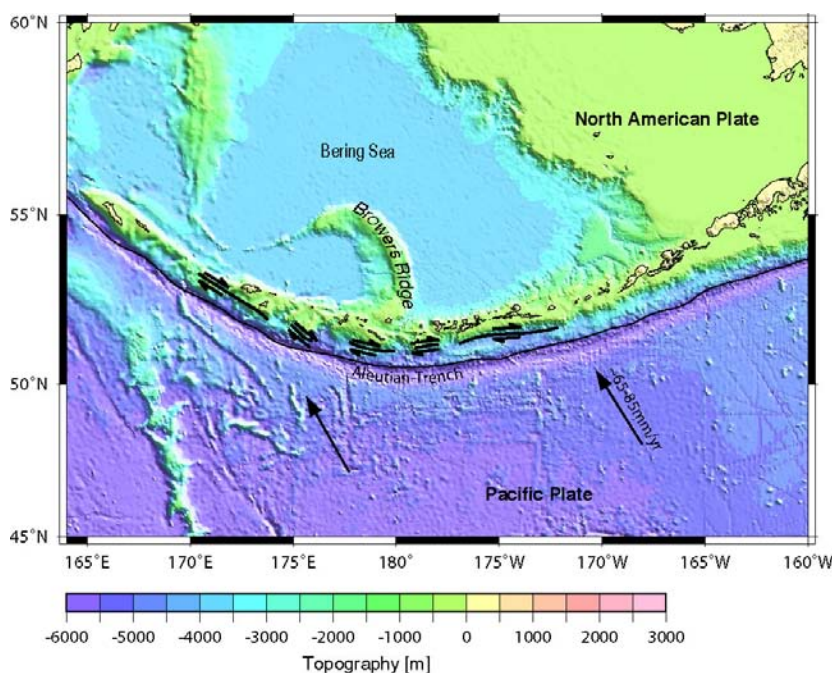

Figure A2.1: Topographic map of the Aleutian arc and the Bering Sea; solid lines indicate the Aleutian trench and margin parallel strike slip faults; arrows show the convergence direction.

Cascadia

The Cascadia subduction zone stretches along the western coast of North America between 52°N and 40°N (Figure A2.2). At the Cascadia margin, the oceanic Juan de Fuca plate subducts underneath the North American plate with a convergence rate decreasing from ~40 mm/yr near Vancouver Island to ~28 mm/yr at 40°N (e.g., DeMets et al., 1990, McCroy, 1996, Wells et al., 2002, Wilson, 2002). The convergence vector is oblique to the trench ~25° (McCroy, 1996). The Cascadia subduction zone is characterized by lots of small thrust and strike slip faults of different orientation (e.g., Goldfinger et al., 1996, McCroy, 1996). Among these faults is a remarkable set of active WNW trending left-lateral strike slip faults, where the most pronounced are the Wecoma fault, the Daisy fault, and the Alvin fault with an average slip rate of ~7-10 mm/yr (Figure A2.2, Appelgate et al., 1992, Goldfinger et al., 1992, Goldfinger et al. 1996). These transverse structures led to the assumption of clockwise block rotation of the fore-arc region (Appelgate et al., 1992, Goldfinger et al., 1992, McCaffrey et al., 2000, Wells & Simpson, 2001).
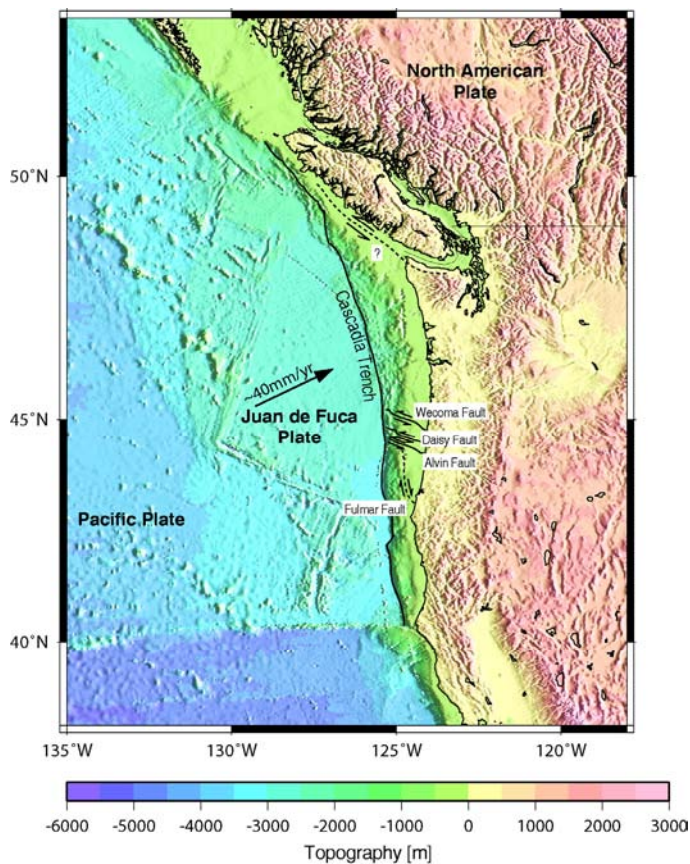

Figure A2.2: Topographic map of the Cascadia subduction zone; solid lines indicate the Cascadia trench and the strike slip faults, dashed lines show concealed strike slip faults; arrows show the convergence direction.

Ecuador-Colombia

The Ecuador-Colombia subduction zone is the northernmost part of the subduction of the Nazca plate underneath the South American plate (Figure A2.3). The oceanic Nazca plate is converging obliquely to the trench with a rate of ~65 mm/yr (e.g., Norabuena et al., 1998). The obliquity of the convergence vector to the trench changes from ~10° in the region of Ecuador to ~40° at about 5°N next to Colombia (e.g., Jarrard, 1986b, DeMets et al., 1990). The Ecuador-Colombia margin is segmented by the Carnegie Ridge (Figure A2.3). South of the Carnegie Ridge the Ecuador margin shows an erosional mass transfer behavior, whereas north of the Carnegie Ridge the Colombia margin is dominantly accretionary (Gutscher et al., 1999, Collot et al., 2002, Collot et al., 2004). The Romeral Fault Zone (also named Dolores-Guayaquil-Romeral-Fault-Zone) is a major strike slip fault and separates the continental part of the north Andean margin into two parts: the eastern province (Eastern Cordillera and east flank of the Central Cordillera) east of the Romeral Fault Zone and the western province (west flank of the Central Cordillera and the Western Cordillera) west of the Romeral-Fault-Zone (e.g., Cortés& Angelier, 2005). The deformation in the overriding plate can be considered as localized, because the deformation is concentrated within one localized shear zone (Romeral Fault Zone). The Romeral Fault Zone shows ~1cm/yr recent dextral movement (McCaffrey, 1996, Gutscher et al., 1999).
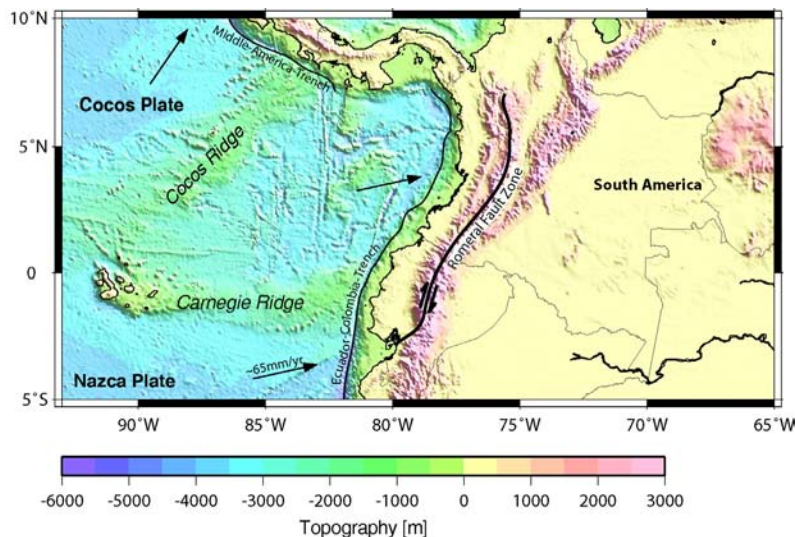

Figure A2.3: Topographic map of the Ecuador-Colombia subduction zone; solid lines indicate the Ecuador-Colombia trench and the margin parallel strike slip fault; arrows show the convergence direction.

Kuril

The central Kuril arc trench system stretches from the Kamchatka Peninsula to Hokkaido Island and is bordered by the Kamchatka trench to the north and the Japan trench to the south (Figure A2.4). At the Kuril margin, the oceanic Pacific plate subducts underneath the North American plate with a convergence rate of ~90 mm/yr (Kiruma, 1986, DeMets et al., 1990, Klaeschen et al., 1994). The convergence vector is oblique to the trench and obliquity is changing from ~10° at 50°N to ~20° at 42°N (Jarrard, 1986b, Klaeschen et al., 1994). The arc is divided into two parts, a southwestern and a northeastern part. The southwestern part is characterized by a well developed frontal arc, en echelon arranged volcanic islands, and a major strike slip fault between the volcanic and the frontal arc (Kiruma, 1986). The major strike slip fault is the Kuril-Mid-Arc Fault, accommodating ~6-11 mm/yr of dextral movement (DeMets, 1992, McCaffrey, 1996). The deformation in the overriding plate of the southwestern part of this margin can be considered as localized, because the deformation is concentrated within one localized shear zone (Kuril-Mid-Arc Fault) accommodating ~30% of the trench parallel component of the convergence vector (DeMets, 1992). The north-eastern part is characterized by a poorly developed frontal arc and no major strike slip fault (Kiruma, 1986). Unfortunately there are not sufficient reliable studies to state a style of deformation in the north-eastern part (DeMets, 1992).
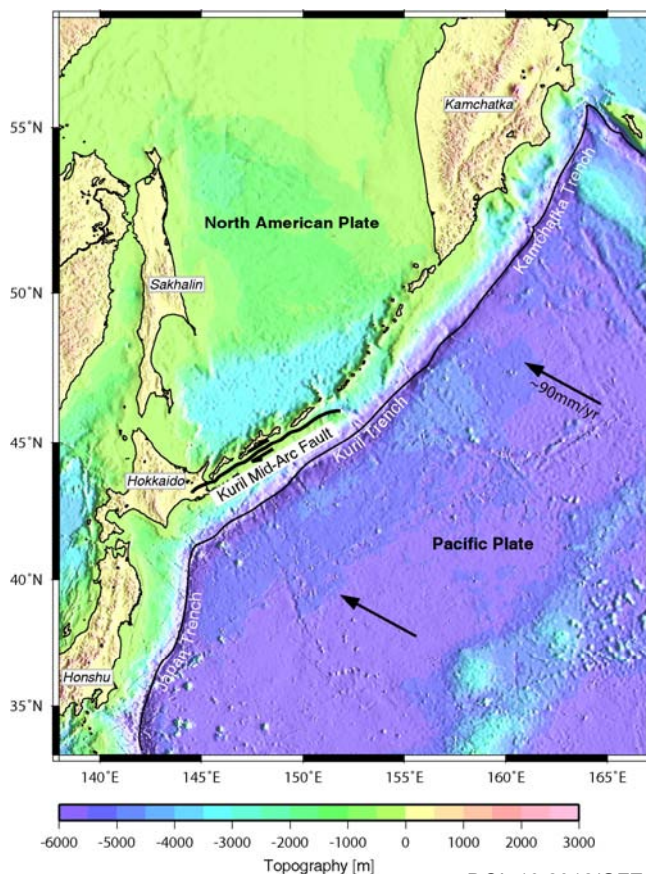

Figure A2.4: Topographic map of the Kuril subduction zone; solid lines indicate the Kuril trench and the margin parallel strike slip fault; arrows show the convergence direction.

DOI: 10.2312/GFZ.b103-07113

Sumatra

The Sumatra subduction zone stretches along the island of Sumatra (Figure A2.5). At the Sunda margin the oceanic Australian plate subducts underneath the Sunda plate with a convergence rate of ~60-70 mm/yr (e.g., Malod & Kemal, 1996). The convergence vector is oblique to the trench and changing from ~35° south of Sumatra to >50° at the northern tip of Sumatra (McCaffrey, 1992, McCaffrey et al., 2000). The Sumatra subduction zone is characterized by two major margin parallel strike slip faults: the Mentawai fault and the Sumatra fault (e.g., Malod & Kemal, 1996, Baroux et al., 1998). These two fault zones have different natures (Malod & Kemal, 1996). Whereas the Sumatra fault is an intra-continental strike slip fault coinciding with the volcanic arc, the Mentawai fault appears more like a boundary between the prism built of accreted trench fill sediments and the continental fore-arc. The Sumatra Fault Zone extends to the north along the Andaman trench as West Andaman Fault (Kamesh Raju et al., 2007). The trench parallel shear along the Sunda trench is essentially accommodated by the Sumatra fault with ~15-30 mm/yr dextral motion, only a small contribution <10 mm/yr dextral motion is assumed to be accommodated by the Mentawai fault (McCaffrey, 1992, Malod & Kemal, 1996, Baroux et al., 1998, McCaffrey et al., 2000). The Sunda trench is an excellent example for localized deformation in the vicinity of oblique convergence, where the components of the convergent motion are fully partitioned.
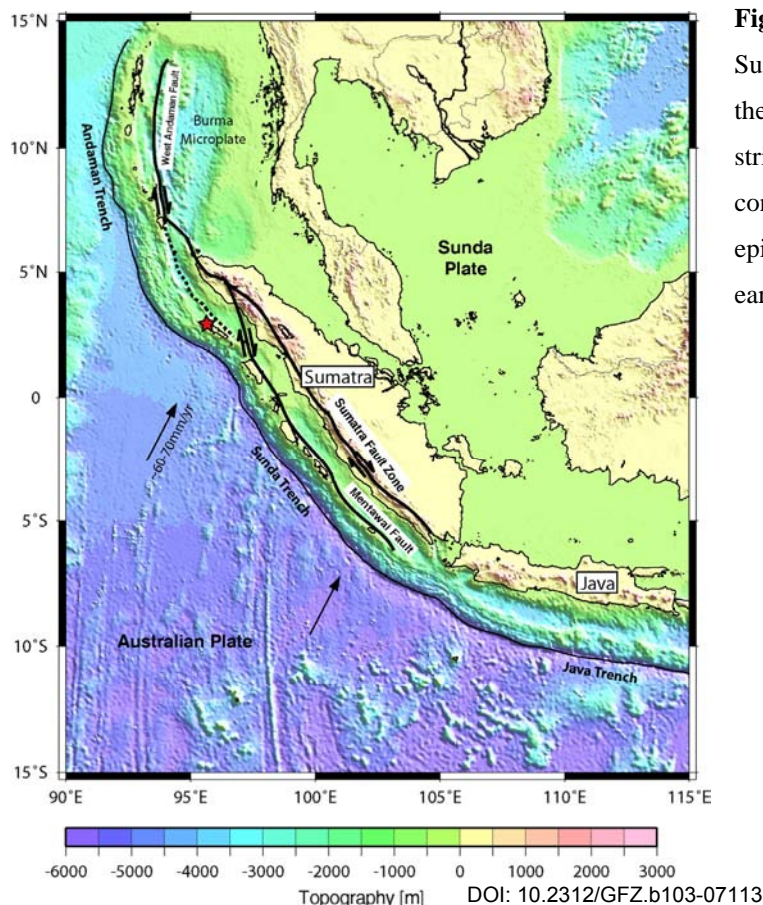

Figure A2.5: Topographic map of the Sumatra subduction zone; solid lines indicate the Sunda trench and the margin parallel strike slip faults; arrows show the convergence direction, red star indicates the epicenter of the 2004 Sumatra- Andaman earthquake.

DOI: 10.2312/GFZ.b103-07113

Tonga-Kermadec

The Tonga-Kermadec subduction zone is characterized by the westward directed subduction of the oceanic Pacific plate beneath the continental Australian plate (Figure A2.6). The Tonga and Kermadec portions of the arc are divided at the point of subduction of the Louisville Ridge (e.g., Turner & Hawkesworth, 1997). The Tonga subduction zone reveals the fasted crustal motion yet observed with convergence rates across the Tonga trench increasing northwards to a maximum of ~240 mm/yr, which results from a combination of Australian-Pacific plate convergence and the opening of the Lau Basin (Australia-Tonga divergence) (Bevis et al., 1995). The convergence vector is oblique to the trench ~10-30° at the Tonga trench and ~5° at the Kermadec trench (Bevis et al., 1995, Wallace et al., 2005). The Tonga-Kermadec subduction zone is characterized by one major EW trending sinistral strike slip fault the Fiji Fracture Zone accommodating ~80 mm/yr of slip (Millen & Hamburger, 1998, Wright et al., 2000). The Fiji Fracture Zone acts as northern transform boundary of the Pacific and Australian plates, north of this boundary remains the Pacific plate at the Earth's surface (Millen & Hamburger, 1998).
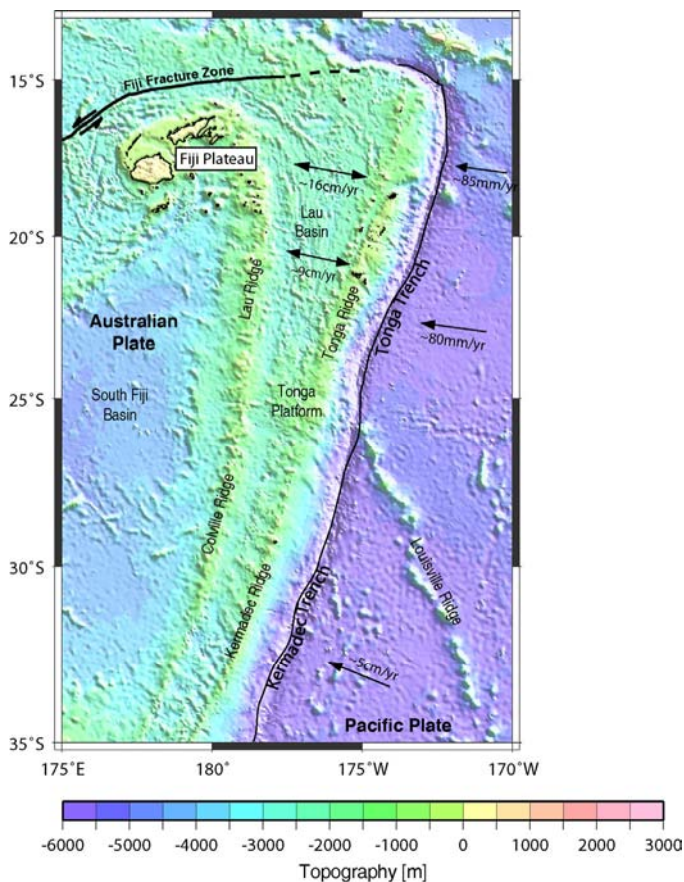

Figure A2.6: Topographic map of the Tonga-Kermadec subduction zone; solid lines indicate the Tonga-Kermadec trench and the strike slip faults; arrows show the convergence direction (single headed) and backarc spreading (double headed), respectively.

Acknowledgments

First of all, I thank my supervisors Nina Kukowski (GFZ Potsdam) and Georg Dresen (GFZ Potsdam) for giving me the opportunity to join the SFB 267, for their continued support, and for their patience during the rather long time needed to finish this thesis. The work has benefited from many interesting discussions with both of them. I really enjoyed a very good working environment and having the possibility to participate in numerous international workshops and conferences. I also thank Nina Kukowski for inviting me to participate in the TIPTEQ project and encouraging me to gain an insight into thermal modeling which significantly improved the thesis. I thank Nina for having a sympathetic ear for my problems and questions.

I wish to thank Sergei Medvedev (now at PGP, University of Oslo) for always being ready to help with advice or proofreading. His continuous encouragement has been feeding my motivation and gave me strength to finish this work.

Katrin Huhn (now at University of Bremen) is thanked for providing input for the initial numerical models in NISA. Kasper Fischer (Ruhr-University of Bochum) and Gabriele Morra (ETH Zurich) provided valuable help in overcoming problems encountered during realization of the numerical models using ABAQUS. I would like to thank Yuri Podladchikov (PGP, University of Oslo) giving me the opportunity to join a software training course in Oslo and several valuable discussions. Frank R. Schilling (GFZ Potsdam) is thanked for his helpful comments during the work on the thermal models of the Chilean subduction zone. I wish to thank Susann Wienecke (now at Statoil, Norway), Arne Hoffmann-Rothe (BGR Hannover), and Beatrice Cailleau (GFZ Postdam) for inspiring discussions and collaboration. Claudia Prezzi (University of Buenos Aires) and Daniel Melnick (University of Potsdam) are thanked for providing the density model for northern Chile and the geological map of the southern Andes, respectively. I thank Susanne Buiter (Geological Survey of Norway) for giving me the opportunity to participate in the numerical benchmark initiated within GeoMod 2004. The thesis benefited from discussions with Arno Zang (GFZ Potsdam) and Christoph Janssen (GFZ Potsdam), both are also thanked for proofreading of earlier stages of the thesis. I thank Onno Oncken (GFZ Potsdam) and Kirsten Elger for organizing the field trip to Chile which

relates my work more to nature. Andrés Tassara (Universidad de Chile) and Petra Paschke (GFZ Potsdam) are thanked for the translation of the abstract into Spanish.

Thanks to all colleagues at GFZ Potsdam for creating a pleasant working atmosphere. In particular, I would like to thank my room-mates Christoph Janssen, Kerstin Schemmann, and Uli Micksch.

I would like to thank Susan Ellis (GNS, New Zealand) and Kelin Wang (Geological Survey of Canada) for agreeing to be external reviewers of this thesis.

This thesis was accomplished with the financial support of the German Research Foundation (DFG) and the Federal Ministry of Education and Research (BMBF) within the framework of the collaborative research project "Deformation Processes in the Andes" and the project "from The Incoming Plate to mega-Thrust EarthQuake processes (TIPTEQ)" within the German Geotechnology Program. I thank Manfred Strecker (University of Potsdam) providing financial support for the period from January to June 2005.

Last, but not least I wish to warmly thank members of my family for their continuous trust and support. Their encouragement and love vitally contributed to the success of this work.

Curriculum vitae

Name: Antje Kellner

Born: 10.02.1976, Stollberg, Germany

Citizenship: German

School

1982 – 1990   Grammar school (Oberschule) in Stollberg, Germany

1990 – 1994   Secondary school (Gymnasium) in Stollberg, Germany, Degree: Abitur

University

1994 – 1995   Technical University of Dresden, Germany, Department of Geodesy

1995 – 2002   Freiberg University of Mining and Technology, Department of Mine
              Surveying and Geodesy, Degree: Diploma
              Diploma Thesis (german): Untersuchung systematischer Fehler im
              Netzvergleich SNREF 95 - STN 63

Career

2002 – 2007   Scientist at the GeoForschungsZentrum Potsdam, Germany; Department
              3.2 "Deformation and Rheology" and Department 3.1 "Lithosphere
              Dynamics"